Imaging and analytical tools to study the spatiotemporal dynamics of protein export

Jessica Angulo Capel

Imaging and Analytical Tools to Study the Spatiotemporal Dynamics of Protein Export

PhD Thesis

Jessica Angulo Capel

September 2024

Supervised by:

Prof. Dr. Maria F. Garcia-Parajo

Dr. Fèlix Campelo

ICFO – Institut de Ciències Fotòniques

UPC – Universitat Politècnica de Catalunya

Abstract

Intracellular trafficking, particularly protein secretion, faces numerous unresolved challenges. This thesis aims to provide and evaluate tools for quantitative investigation of these processes using fluorescent microscopy. Quantitative analysis offers two main benefits: detailed characterization of molecular dynamics for mechanistic understanding and objective measurements for accurate comparisons across experiments.

In Chapter 1, we introduced the secretory pathway, a cellular pathway responsible for the synthesis, processing, sorting and delivery of secretory proteins to the extracellular environment. In Chapter 2, we provided a thorough description of the methodologies used in this thesis. They included various fluorescence microscopy techniques, automated image analysis, and biological methods tailored to the secretory pathway. The tools were selected to achieve high spatial and temporal resolution, enable quantitative analysis, and allow live-cell characterization.

In Chapter 3, we used fluorescence imaging to objectively evaluate results in four projects addressing protein secretion and intracellular trafficking. These included quantifying colocalization and proximity of structures, measuring fluorescent intensity differences, and characterizing dynamics of particles like ERGIC-derived nanotubules. Consistent sample preparation and image acquisition, coupled with computational analysis, are crucial for accurate, unbiased results.

Chapter 4 focuses on single-particle tracking (SPT) in the secretory pathway, proposing control experiments and parameter descriptors to maximize data quality. We emphasized labeling strategies, imaging, and data analysis considerations for reliable results.

Chapter 5 applied these methodologies to study protein sorting at the TGN, examining the role of ER-Golgi membrane contact sites (MCS) in TGN-derived carrier biogenesis. Using super-resolution fluorescence microscopy, we identified cargo accumulation regions and conducted SPT experiments, revealing confined, slow motion of cargo proteins near MCS. This effect was inhibited by the lipid transfer blocker 25-HC, indicating upstream regulation of cargo localization preferences by MCS.

Resum

El tràfic intracel·lular, particularment la secreció de proteïnes, presenta nombrosos qüestions no resoltes. Aquesta tesi té com a objectiu proporcionar i avaluar eines per a la investigació quantitativa d'aquests processos mitjançant microscòpia fluorescent. L'anàlisi quantitativa ofereix dos avantatges principals: la caracterització detallada de les dinàmiques moleculars per a la comprensió mecànica i les mesures objectives per a comparacions precises entre experiments.

Al Capítol 1, hem introduït la via secretora, una via cel·lular responsable de la síntesi, processament, classificació i lliurament de proteïnes secretòries a l'entorn extracel·lular. Al Capítol 2, hem proporcionat una descripció exhaustiva de les metodologies utilitzades en aquesta tesi. Inclouen diverses tècniques de microscòpia de fluorescència, anàlisi d'imatges automatitzada i mètodes biològics adaptats a la via secretora. Les eines es van seleccionar per aconseguir una alta resolució espacial i temporal, permetre l'anàlisi quantitativa i permetre la caracterització en cèl·lules vives.

Al Capítol 3, hem utilitzat la imatge de fluorescència per avaluar objectivament els resultats en quatre projectes que aborden la secreció de proteïnes i el tràfic intracel·lular. Aquests inclouen quantificar la colocalització i la proximitat d'estructures, mesurar diferències en intensitat de fluorescència i caracteritzar dinàmiques de partícules com nanotúbuls derivats de l'ERGIC. La preparació consistent de mostres i l'adquisició d'imatges, juntament amb l'anàlisi computacional, són crucials per obtenir resultats precisos i imparcials.

El Capítol 4 se centra en el seguiment de partícules individuals (SPT) en la via secretora, proposant experiments de control i descriptors de paràmetres per maximitzar la qualitat de les dades. Hem posat èmfasi en les estratègies de marcatge, la imatge i les consideracions d'anàlisi de dades per a resultats fiables.

Al Capítol 5 hem aplicat aquestes metodologies per estudiar la classificació de proteïnes al TGN, examinant el paper dels llocs de contacte de membranes ER-Golgi (MCS) en la biogènesi dels transportadors derivats del TGN. Utilitzant microscòpia de fluorescència de super-resolució, vam identificar regions d'acumulació de proteïna i vam dur a terme experiments de SPT, revelant el moviment confinat i lent de les proteïnes de càrrega a prop dels MCS. Aquest efecte va ser inhibit pel bloquejador de transferència de lípids 25-HC, indicant una regulació ascendent de les preferències de localització de proteïna per part dels MCS.

Table of Contents

List of Abbreviations

AnDi: anomalous diffusion

ATTM: annealed transient time motion

CARTS: carriers of the TGN to the cell surface

CATCHR: complexes associated with tethering containing helical rods

CERT: ceramide transfer protein

COPI: coat protein complex I

COPII: coat protein complex II

CRISPR: clustered regularly interspaced short palindromic repeates

CTRW: continuous time random walks

DAG: diacylglycerol

DoG: difference of Gaussians

ECM: extracellular matrix

EMCCD: electron-multiplied charge couple device

EosFP: Eos fluorescent protein

EQ-SM: equinatoxin sphingomyelin

ER: endoplasmic reticulum

ERES: ER exit sites

ERGIC: ER-Golgi intermediate compartment

FA: focal adhesion

FBM: fractional brownian motion

FCS: fluorescence correlation spectroscopy

FFAT: two phenylalanine in an acidic tract

FRAP: fluorescence recovery after photobleaching

FRET: Förster Resonance Energy Transfer

FWHM: full width half maximum

GA-ERGIC: Golgi-associated ERGIC

GFP: green fluorescent protein

GPI: glycosylphosphatidyl inositol

HA: hemagglutinin

HeLa: Henrietta Lacks

HILO: highly inclined and laminated optical sheet

HIV-1: human immunodeficiency virus type 1

JF: Janelia Fluor

KI: knock-in

LW: Lévy walks

MCS: membrane contact sites

MDCK: Madin-Darby canine kidney cells

MINFLUX: minimal photon fluxes

mRNA: messenger ribonucleic acid

MSD: mean squared displacement

NSF: N-ethylmaleimide-sensitive factor

NSOM: near-field scanning optical microscopy

ORP: OSBP-related proteins

OSBP: oxysterol-binding protein

PALM: photoactivated localization microscopy

p-ERGIC: peripheral ERGIC

PH: pleckstrin homology

PI4P: phosphatidylinositol 4-phosphate

PKD: protein kinase D

PSF: point spread function

PtdCho: phosphatidylcholine

PtdEtn: phosphatidylethanolamine

PtdIns: phosphatidylinositol

ROI: region of interest

RPE-1: human retinal epithelial cells

RUSH: retention using selective hooks

S. cerevisiae: Saccharomyces cerevisiae

SBM: scaled Brownian motion

SBP: streptavidin binding peptide

SCAP: SREBP cleavage activating protein

SD: standard deviation

shRNA: short hairpin ribonucleic acid

SiR: silicon-rhodamine

siRNA: small interfering ribonucleic acid

SM: sphingomyelin

SMS: SM synthase

SNR: signal-to-noise ratio

sptPALM: single particle tracking PALM

SREBP: sterol regulatory element-binding protein

SRP: signal recognition particle

STED: stimulated emission depletion

STORM: stochastic optical reconstruction microscopy

TA-MSD: time-averaged mean squared displacement

TANGO1: transport and Golgi organization protein 1

TGN: *trans*-Golgi network

TIR: total internal reflection

TIRF: total internal reflection fluorescence

TMR: tetramethylrhodamine

*ts*VSV-G: temperature sensitive vesicular stomatitis virus G protein

VAMP: vesicle-associated membrane protein

VAP: VAMP-associated membrane protein

VLDL: very-low-density lipoproteins

VSV-G: vesicular stomatitis virus G protein

Chapter 1

Introduction to the Secretory Pathway

This chapter presents an introduction to the secretory pathway, a cellular pathway responsible for the synthesis, processing, sorting and delivery of secretory proteins to the extracellular environment. Following the journey of newly synthesized proteins, we provide an overview on the path through the different organelles involved in this pathway, and get an introduction to the most relevant molecular players. Additionally, the chapter examines the most accepted mechanistic models at the different stages, the unknown questions that remain unanswered, and explores possible new paradigms that have recently been suggested.

Part of this work has been published as:

Angulo-Capel, J.*, Lujan, P.*, Chabanon, M.*, Campelo, F., (2021) Interorganelle communication and membrane shaping in the early secretory pathway. *Current Opinion in Cell Biology*. 71:95-1002. doi: 10.1016/j.ceb.2021.01.010

*These authors contributed equally.

1. INTRACELLULAR TRAFFICKING

Intracellular trafficking is a broad term that encompasses the highly regulated processes of transport, sorting and delivery of molecules to specific destinations within the cell. Two examples are the transport of vesicles between the endoplasmic reticulum (ER) and the Golgi apparatus, as well as the internalization and recycling of molecules through endocytic pathways.

The regulation of intracellular trafficking involves a wide range of factors and mechanisms due to the diverse nature of cargo molecules and organelle dynamics within the cell. Therefore, understanding such a general concept requires detailed study, focusing on its different components. There are two main intracellular trafficking routes: the biosynthetic pathway, by which newly synthesized proteins are produced, and targeted to their final destination; and the endocytic pathway, by which proteins are internalized from the cell surface and further processed. The scope of this thesis focuses on the biosynthetic pathway, with strong emphasis on those that lead to protein secretion.

2. THE SECRETORY PATHWAY

The secretory pathway is a fundamental cellular process, responsible for the secretion of proteins into the extracellular environment. It represents a highly coordinated network of organelles and molecular processes, each playing distinct roles in the synthesis, modification, and transport of proteins destined for secretion. This finely tuned cellular machinery is essential for maintaining cellular homeostasis and facilitating communication with the extracellular environment.

Beginning with synthesis and translocation into the ER, proteins are transported to the Golgi for processing, followed by packaging into transport carriers. These carriers then navigate to and fuse with the plasma membrane for secretion (see **Figure 1**). Alternatively, proteins can reach the PM after first passing the endolysosomal system. It was George Palade's model of vesicular transport, that laid the foundational understanding of the secretory pathway in cells, proposing that newly-synthesized secretory proteins are transported as explained above by encapsulation into small vesicles that budded from a donor compartment and fused with an acceptor compartment at each step of the secretory pathway.[1,2] In 2013, James Rothman, Randy Schekman and Thomas Südhof were awarded the Nobel Prize in Physiology or Medicine "for their discoveries of machinery regulating vesicle traffic, a major transport system in our cells".

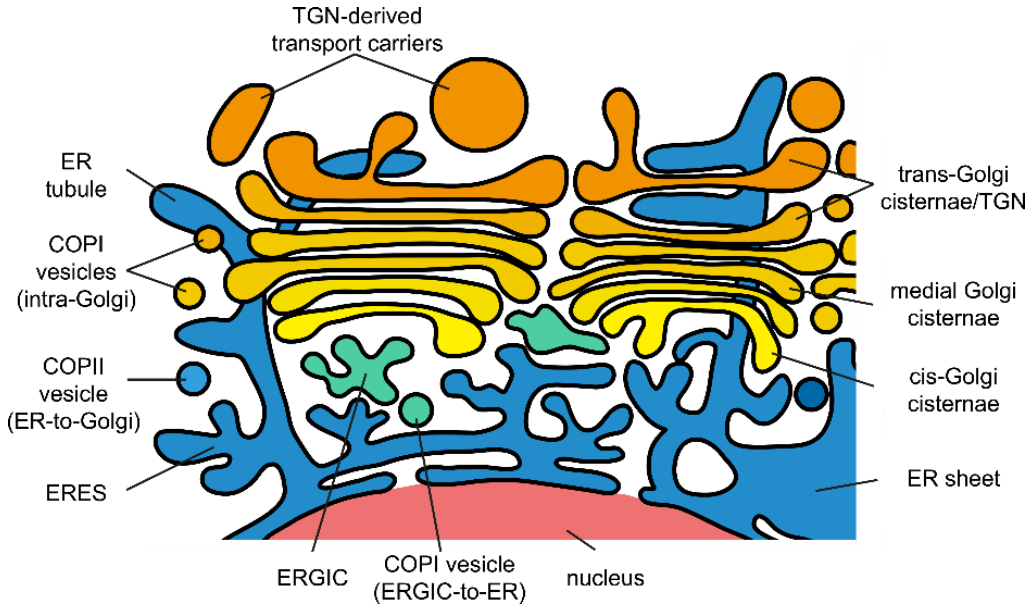

Figure 1. The early secretory pathway. Schematic visualization of the cellular structures of the endomembranous system that are involved in the early secretory pathway. Proteins are synthesized and translocated to the ER, then they travel from the ER to the Golgi apparatus through COPII vesicles. Once in the Golgi, they get post-translational modifications, and they get packed into transport carriers at the TGN. (Modified from J. Angulo-Capel et al. Current Opinion in Cell Biology (2021)[3]).

3. PROTEIN SYNTHESIS

Central to the secretory pathway is the process of protein synthesis, which occurs at the ribosomes. In the event an N-terminal ER targeting signal sequence in the nascent polypeptide is recognized by the signal recognition particle (SRP), ribosomes attach to ER membranes, and proceed protein synthesis in the vicinity of the Sec61p (or SecYEG in prokaryotes) translocon.[4] Other signaling sequences determine whether the protein stays embedded in the ER membrane, or it is completely released within the lumen. The ER provides a specific environment that enables nascent proteins undergo folding and oligomerization. At this stage, post-translational modifications such as addition of N-linked oligosaccharide chains, establishment of disulfide bonds, and hydroxylation of prolines also take place.

While the processes of protein synthesis, ER targeting, and post-translational modifications in the secretory pathway encompass several well-understood mechanisms and components, there remain several unanswered questions and areas for future research in this field:

(i) Mechanisms of co-translational targeting and translocation. While the co-translational protein targeting to the endoplasmic reticulum (ER) is a well-characterized process[5,6], the detailed molecular mechanisms by which proteins are recognized at the ribosome by the SRP and delivered to the ER protein translocation channel are still being elucidated.[7]

(ii) Integration and post-translational modifications of nascent proteins. The role of the ER in signal peptide cleavage, oligosaccharide addition and modification, and specific amino acid residue modifications needs further exploration in order to find out the efficiency of these reactions and their impact on protein function.[8]

(iii) Novel roles of the SRP. Recent findings suggest that in addition to its targeting function, the SRP plays a role in protecting secretory protein mRNAs from degradation.[9]

Moreover, the ER is not only responsible for protein synthesis, but it also produces the vast majority of cellular lipids. Some key lipid components are phosphatidylcholine (PtdCho) and phosphatidylethanolamine (PtdEtn), along with less common membrane lipids like phosphatidylinositol (PtdIns) and fundamental sphingolipid precursors. Additionally, the ER hosts enzymes involved in cholesterol synthesis and the formation of triacylglycerides for energy reserves. These lipids, synthesized within the ER, are transported to other cellular organelles either through the secretory pathway or ER contact sites, and keep the cell homeostasis.[10]

4. ER TO GOLGI TRANSPORT

The exit from the ER occurs in specific landmarks named ER exit sites (ERES)[11], characterized by the presence of coat protein complex II (COPII) components. Classically, it has been accepted that COPII controls the transport from the ER to the ER-Golgi intermediate compartment (ERGIC), while COPI is in charge of the subsequent sorting in the ERGIC towards the Golgi, as well as transport back to the ER.[12–15] The ERGIC is a membrane bound organelle, placed in between the ER and the *cis*-Golgi cisternae, which was identified following several studies that characterized its distinct biochemical composition.[16–19] However, it still remains unclear how the ERGIC structure is dynamically maintained in relation to the overall functional organization of the early secretory pathway.

The traditional understanding is that at ERES, the COPII protein complex initiates vesicle formation to transport materials to the ERGIC in a process that involves five key proteins - Sar1, Sec23, Sec24, Sec13, and Sec31. They collaboratively build a

dual-layered coat. This structure not only selects cargo, but also molds the membrane into a cargo-containing vesicle of 60-90 nm size.[20]

Although the formation of COPII vesicles is a very well-studied process, one of the major incognita is how can large cargoes be embedded within such small vesicles. Some examples of bulky cargoes include collagen, mucins, some lipoproteins, chylomicrons, and very-low-density lipoproteins (VLDLs). This conundrum has inevitably led to the formulation of new models.

This was further supported by the discovery of the protein transport and Golgi organization 1 (TANGO1).[21] This protein is necessary for the export of collagens[22,23], mucins[24] and apolipoproteins[25,26]. Its mechanism of action involves a role as a cargo receptor[27]; reorganization of COPII machinery[28]; formation of ring-like structures[29]; and interaction with the COPI-coated ERGIC membranes.[30–33] A physical model of TANGO1-mediated ER export explained how various physical properties, such as membrane tension, dynamically contribute to the formation of procollagen-containing transport intermediates that match the size of the cargo they transport.[33]

Technological advancements in 3D correlative light and electron microscopy[34,35], and in fluorescence super-resolution microscopy[36,37] are also challenging the classical paradigm of vesicular transport in the secretory pathway, leaning towards a model with more continuity between the ER and the ERGIC membranes. It has been proposed that a transient tunnel is created in between the ER and the ERGIC for the direct passage of the cargo (see **Figure 2a**).[34] On the other hand, it has also been observed a more dynamic network of tubules of variable size that remodels.[37,38] Along these lines, it is to be highlighted the work performed in the field of ADP-ribosylation factors (ARF) GTPases. Experiments on live fluorescence super-resolution microscopy show that anterograde cargo transport between the ER and the Golgi is mediated by a dynamic interconnected network of tubular ERGIC structures that defined by the small GTPase ARF4.[36]

In addition, it should also be mentioned an alternative mechanism of transfer of cargoes between the ER and the Golgi. It involves the direct trafficking between the two organelles (omitting the ERGIC) through a *hug-and-kiss* mechanism (see **Figure 2b**). *cis*-Golgi cisternae wrap around and tether ERES (*hug*), after which ER cargo is directionally transferred to the Golgi complex (*kiss*). This was observed in *S. cerevisiae*, and thus should not be completely disregarded in mammalian cells.[39]

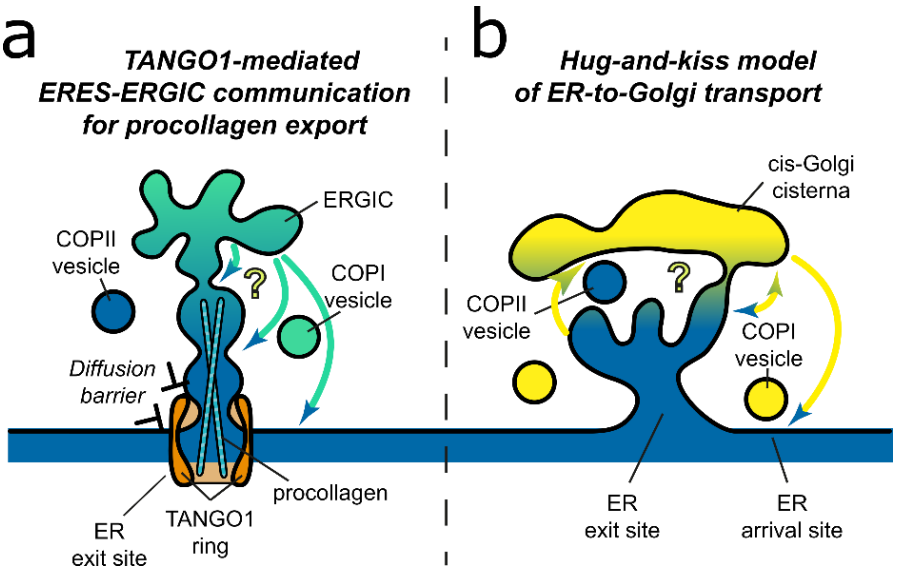

Figure 2. Two modes of communication between ERES and early Golgi elements. (a) Mechanisms of ERES/ERGIC communication for procollagen export in mammalian cells. A TANGO1 ring (orange) links procollagen (cyan-striped poles) to COPII coats (not shown). TANGO1, by binding to a tethering complex (not shown), recruits ERGIC/COPI membranes (green) to a nascent transport intermediate. Fusion of these membranes triggers carrier growth. The precise fusion site is yet to be revealed. Finally, TANGO1 creates a diffusion barrier at the carrier base to prevent membrane mixing. **(b)** Hug-and-kiss model for proximity-based ER-to-Golgi transport in yeast. A dynamic contact between ERES (blue) and cis-Golgi cisternae (yellow) enhances the efficiency of anterograde trafficking. Whether COPII vesicles are fully formed and travel the short distance within the contact or alternatively a transient fusion of the ERES with a *cis*-Golgi cisterna occurs remains unresolved. An ER arrival site where Golgi-derived COPI vesicles fuse to the ER is shown proximal to the ERES. (Modified from J. Angulo-Capel et al. Current Opinion in Cell Biology (2021)[3]).

5. GOLGI PROCESSING

The Golgi apparatus, also known as the Golgi complex or Golgi body, is an essential organelle found in most eukaryotic cells. It was named after the Italian scientist Camillo Golgi, who discovered it in 1898.[40] The Golgi apparatus plays a key role in processing and packaging proteins and lipids that are synthesized in the ER. These molecules are then sorted, modified, packaged into vesicles, and transported to their destination sites within or outside the cell.

In mammalian cells, this organelle is formed by a series of sac-like, membrane-bound cisternae, which group in stacks of 4-12, and which in turn laterally bind forming the so-called Golgi ribbon.[41,42] The biochemical composition changes across the stack, allowing for the division between *cis*-, *medial*- and *trans*-cisternae.[41] In consequence, cargo proteins travel from *cis*- to *trans*-cisternae, and the polarized

distribution of resident enzymes ensures its sequential glycosylation. The outermost region, the *trans*-Golgi network (TGN) serves as the exit station from where different cargo proteins leave the Golgi to different intracellular destination or for secretion outside the cell.

How proteins travel from *cis* to *trans* is still not fully understood, and has led to different molecular models. Two of the most important are the anterograde vesicular transport between stable compartments, and the cisternal progression/maturation. Both models have strengths and weaknesses when trying to explain the observed experimental results.[43,44]

The vesicular transport model, which gained wide acceptance from the early 1980s until the late 1990s, depicts the Golgi as a series of stable compartments working in synchronization.[45–48] Each compartment harbors a distinct set of Golgi proteins, including glycosylation enzymes, responsible for processing secretory cargoes in a sequential fashion.[49–51] Initially, newly synthesized secretory cargoes are delivered to the cis-Golgi via COPII-coated vesicles, and then moved sequentially in the anterograde (forward) direction through the Golgi compartments in COPI-coated vesicles.[52] Resident Golgi proteins are kept within specific Golgi compartments by not being incorporated into these COPI vesicles. More recent interpretations of this model suggest that COPI vesicles move bidirectionally, with anterograde COPI vesicles transporting secretory cargoes forward, while retrograde COPI vesicles recycle trafficking components.[53,54]

By contrast, in the cisternal progression/maturation model, cisternae are seen as transient carriers.[55,56] It suggests that the formation of a new *cis*-cisterna begins with the fusion of COPII vesicles or other carriers from the ER. The new *cis*-cisterna gradually matures into a TGN cisterna, ultimately breaking down into secretory vesicles and other carriers.[57–59] As cisternae themselves are the carriers that transport secretory cargoes forward, COPI vesicles recycle resident Golgi proteins from older (more *trans*) to younger (more *cis*) cisternae.[60,61] Differential recycling efficiencies for different Golgi proteins may account for the distinct biochemical characteristics or functions associated with different parts of the Golgi apparatus.[62,63] Later, it was proposed that the various Golgi compartments represent distinct kinetic stages of maturation, regulated by Rab GTPases.[64] It also needs to be mentioned that cisternal maturation has been visualized in live yeast cells, making this hypothesis stronger.[65,66]

6. EXITING THE TGN

Once at the level of the TGN, proteins are sorted for export into specific transport carriers with different destinations: the cell surface, the endo-lysosomal system, secretory granules (in the case of professional secretory cells), or back to the Golgi. The TGN emerged as a single entity in studies over the 20th century, but it was in the influential publication by Griffiths and Simons in 1986, that described it as a designated organelle on the *trans* side of the Golgi stack, responsible for the routing of proteins to lysosomes, secretory vesicles and the PM.[67]

Nowadays, it is known that transport from the TGN to the PM takes place through different carriers, which were firstly described as "pleomorphic tubular-vesicular carriers", for being heterogeneous in size and shape. First studies were performed with temperature sensitive vesicular stomatitis virus G protein (*ts*VSV-G), characterized for having a folding defect at 40 °C that allows for the synchronization of the secretion. In contrast to other types of vesicles in the endo-membranous system, no protein coat has been identified on post-Golgi carriers containing *ts*VSV-G, and their size ranges between 300 and 1700 nm.[68] These values are at least one order of magnitude larger than for example clathrin-coated vesicles, involved in PM endocytosis (60 – 100 nm), as in those cases the size is controlled by the polymerized spherical structure of the coat.[69]

Further research on protein secretion revealed that the firstly-described heterogeneous population of post-Golgi carriers indeed represent a myriad of different carriers, with both shared and distinctive molecular machinery. **Table 1** presents the classification of TGN-to-PM carriers done by Stalder and Gershlick (2020).[70] This labeling is based on experimental data, meaning that secretion pathways independently characterized in the literature, could actually correspond to common transport routes. For instance, this could be suggested for carriers of the TGN to the cell surface (CARTS)[71] and sphingomyelin (SM)-rich vesicles[72], given that specifically sorted cargos in SM-rich vesicles (i.e. lysozyme C) are also associated with CARTS. However, the fact that some cargo proteins could exit the TGN through different pathways, as suggested for VSV-G, hinders the differentiation between them.

Table 1. TGN-to-PM transport carrier classification. The information has been extended by literature search, based on the differentiation made by Stalder and Gerhlick (2020).[70] Carrier types are not combined unless there is strong experimental data to support it.

Transport Carrier	**Cargo Protein**	**Molecular Machinery**		
		Name	**Suggested Role**	**References**
ARF1-positive carriers	*ts*VSV-G	Microtubule	Transport to PM	[73]
		ARF1	Budding	[74]
		PKD	Fission	[75]
		FAPP2	Budding	[76–78]
		PI(4)KIIIβ	Not reported	[79]
		Dynamin II	Fission	[80,81]
		Actin	Not reported	[80,81]
Lamp1-RUSH carriers	VSV-G^{RUSH} LAMP1^{RUSH} TfNR^{RUSH}	Not reported	-	-
Rab6-positive carriers	ts/VSV-G^{RUSH} CD59^{RUSH} TNFα^{RUSH} ColX^{RUSH} NPY BDNF	Microtubule	Transport to PM	[82]
		Rab6	Transport to PM and fission	[82,83]
		Actin	Fission	[83]
		Myosin II	Fission	[83]
		KIF5B	Transport to PM	[82]
		KIF20A	Fission	[84]
		ELKS	Docking to exocytic hotspots	[82,85]
CtBP1-S/BARS carriers	tsVSV-G	PKD2	Fission	[86]
		PI(4)KIIIβ	Fission	[87]
		PAK	Fission	[86]
		CtBP1-S/BARS	Fission	[87]
		14-3-3γ	Fission	[87]

SM carriers	EQ-SM	ADP/Cofilin	Sorting	[88]
	GPI-protein	Actin	Sorting	[89]
	LYZ^{RUSH}	SPCA1	Sorting	[88–91]
	LPL	Cab45	Sorting	[92]
	COMP	Syndecan-1	Sorting	[93]
CARTS	LYZ PAUF SYT2	Microtubule	Transport to PM	[89]
		PKD	Fission	[71]
		Actin	Transport to PM	[71]
		Myosin II	Transport to PM	[71]
		VAP-A/B	Not reported	[94]
		Eg5/KIF11	Transport to PM	[95]
		TGN46	Sorting	[96]
		Rab6A	Not reported	[71]
		Rab8A	Not reported	[71]

Regardless of the export route, the steps leading to transport carrier biogenesis are conserved: *(i)* protein sorting, *(ii)* budding of the carrier, and *(iii)* fission from the TGN membrane (see **Figure 3)**. Accordingly, the suggested roles of each component of the carrier biogenesis machinery, as well as other identified proteins involved in the subsequent steps of carrier secretion have been indicated in **Table 1**. In the next subsection, we provide further detail about the different steps that lead to transport carrier biogenesis.

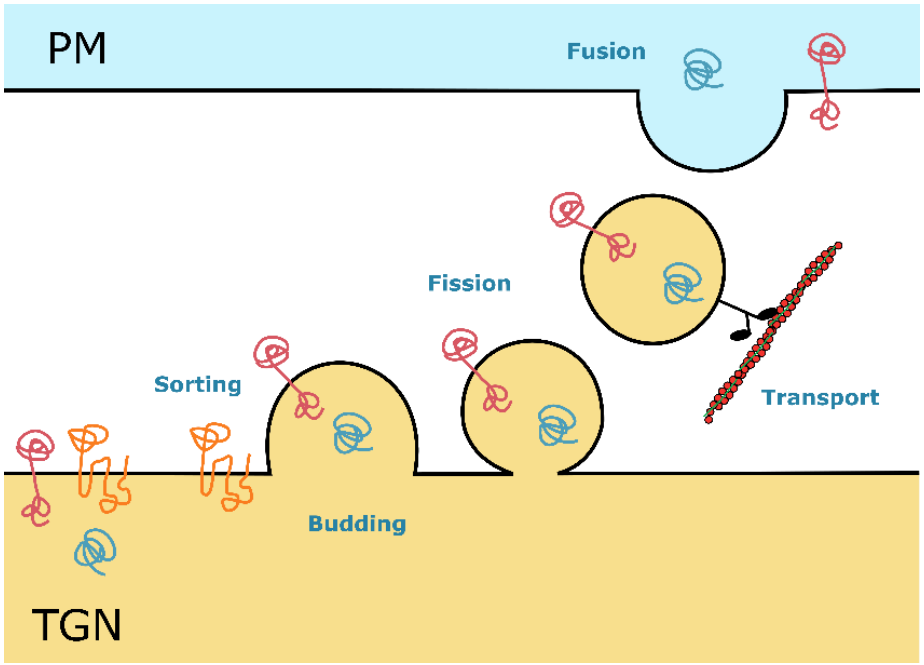

Figure 3. TGN-to-PM transport carrier formation. During the sorting step, some proteins (red and blue) are packed into the nascent carrier, while other proteins are excluded (orange). Budding consists on the bending of the membrane, where the carrier will be formed. In fission, the carrier is released. Transport to the PM is illustrated with an example, where a myosin protein (black molecule) carries the vesicle along actin filaments (red filament). Finally, fusion involves the merge of the carrier membrane with the PM, and thus releasing of the cargoes.

6.1. PROTEIN SORTING

Sorting consists on the selective segregation and packaging of cargo proteins. Although protein secretion was firstly proposed to be "in bulk", and Golgi resident proteins were suggested to rather be the ones having specific retention signals[97,98], secretion of some proteins has been proved to be regulated at the TGN level. For instance, lysozyme C is sorted into SM-rich vesicles in a Ca^{2+}-regulated mechanism.[89] Or in CARTS, the luminal domain of TGN46 is responsible of the sorting of cargos within this type of carriers.[96]

6.2. MEMBRANE BUDDING

Budding consists on the bending of the membrane on the site where the carrier will be formed. Remodeling of the membrane is achieved by the combination of a very complex lipid mixture and the interplay of proteins. Making use of these two elements, the cell has different mechanisms for membrane curvature generation.[99] One strategy is the deformation by scaffolding of peripheral membrane proteins, as

suggested for the protein FAPP2.[76–78] Given that budding at the TGN level, especially for uncoated carriers, is still and obscure process, other mechanisms of membrane curvature generation that have been proposed in the context of budding of coated vesicles should also be considered. These include: changes in the lipid composition, given that the different chemical properties favor different membrane curvatures; the influence of integral membrane proteins; or the force generation by cytoskeleton proteins.

The previously mentioned ARF proteins are also involved in regulating carrier biogenesis at the TGN. These proteins actively contribute to the generation of membrane curvature[74], and recruit different adaptor proteins. ARF1, ARF3 and ARF4 have been implicated in TGN export. However, pinpointing the exact place of action of these ARFs has proven challenging.[100]

ARF1 is known to recruit the adaptor protein AP-1 to the TGN[101], and the dissociation of AP-1 from the Golgi membranes requires ARF4[102]. Furthermore, ARF1 and ARF4 facilitate TGN export of the β-secretase BACE1 but not the amyloid precursor protein (APP), suggesting that specific ARFs may be necessary for the trafficking of different cargoes (see **Table 1**).[103] ARF3 could also play a role in TGN carrier biogenesis, since it is only localized to the TGN. Nevertheless, its high sequence similarity with Arf1 has made it hard to discern their functional differences.

A more recent study performed by Bottanelli et al. showed the role of ARF1 in the formation of tubular vesicular trafficking intermediates, that contain secretory cargoes.[73] This was further characterized with live super-resolution microscopy, as well as with correlative light and electron microscopy. The researchers observed clathrin-decorated ARF1 compartments emerging from the TGN. They suggest that this network of tubular vesicular intermediates form a new compartment for cargo transfer to endosomes or the PM.[104]

6.3. MEMBRANE FISSION

Membrane fission relies on similar mechanisms to those of membrane curvature generation, which compromise the structural integrity of the lipid bilayer at the neck to trigger the scission of the carrier. At the TGN, the catalytic activity of protein kinase D (PKD) – a cytosolic protein that is recruited by binding to the lipid diacylglycerol (DAG) – is required for the fission of some carriers, such as CARTS. It has been shown that when expressing a kinase inactive form of PKD, some cargo proteins are retained on tubes emanating from the TGN, and their transport is

impaired.[75] However, the specific mechanism is still not known. Another example is the role of Rab6 and myosin II in fission of Rab6-positive carriers, which can contain CD59, TNFα and collagen X.

6.4. ER-GOLGI MCS IN TRANSPORT CARRIER BIOGENESIS

In the classical view of eukaryotic cells, organelles are intracellular compartments that act independently to fulfill specific functions (see **Figure 4A**). The correct functioning of the cell requires the exchange of signals between them. A new communication mechanism was observed in the 1960's, which is nowadays challenging the classical model of "one organelle – one cellular function": direct contact between organelle's membranes. In the so-called membrane contact sites (MCS), membranes of different organelles or compartments come to close apposition (~10 - 30 nm apart) by protein-protein and/or protein-lipid interactions, without fusing together.[105]

Given the transient and dynamic nature of MCS, their characterization has been hampered by the lack of suitable techniques with sufficient spatial and temporal resolution. Therefore, it was not until the last decade, thanks to advances in super-resolution fluorescence microscopy techniques, that MCS have been revealed as a more widely spread mode of intracellular communication than expected (see **Figure 4B**). As more studies are being published and more functions are attributed to MCS it is becoming clear that they are key for cell metabolism coordination and for the cell to respond to environmental changes.

MCS between the ER and the Golgi form between the ER and the *trans*-Golgi cisternae and/or the TGN, two sub-compartments of the Golgi. Given the dense environment where the Golgi mainly localizes, this type of contacts has been more difficult to study, and much less is known as compared to other MCS. In the recent years, research mainly focused on the identification of the proteins involved in these MCS. ER-Golgi MCS are established by the tethering between the ER-localized components VAMP-associated protein A (VAP)–A and –B, and a number of Golgi-associated proteins, such as the oxysterol-binding protein (OSBP), different OSBP-related proteins (ORPs)[106], and the ceramide transfer protein (CERT)[107] (see **Figure 5**). Common to these Golgi-associated proteins is their ability to transfer lipids between these two organelles. In particular, CERT transports ceramide from the ER to the TGN[107], whereas OSBP shuttles cholesterol from the ER to the TGN and PI4P in the opposite direction[108]. PI4P can then be dephosphorylated by the phosphatase activity of Sac1 at the ER side.[109] This PI4P cycle creates a gradient of lipids (such as

cholesterol and ceramide) in the membranes of the early secretory pathway, thereby contributing to maintain organelle identity. Therefore, the main function of ER-Golgi MCS known to date is the regulation of Golgi lipid homeostasis.

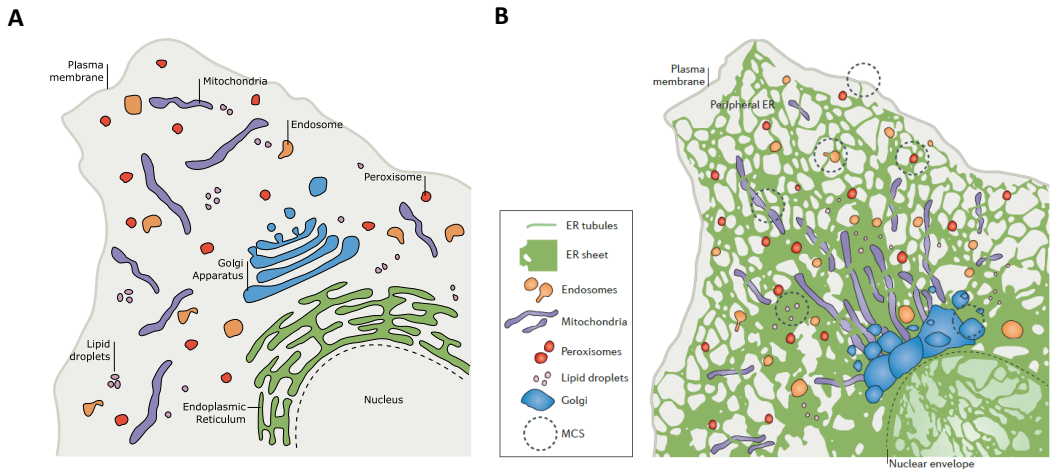

Figure 4. Model of a mammalian cell, organelle organization. A. Classical view of the cell, where each organelle is an independent entity in charge of a specific function. (Modified from Phillips, M. J. and Voeltz, G. K. *Nat Rev Mol Cell Biol.* (2016))[110]. **B.** The cell is a very crowded environment. Organelles communicate with each other and work together for the survival of the cell. A newly discovered mechanism is the establishment of MCS. The ER stands out, as it makes multiple contact sites with many organelles in the cell, behaving as a regulator of other organelles. (Taken from Phillips, M. J. and Voeltz, G. K. *Nat Rev Mol Cell Biol.* (2016))[110].

However, further studies are being performed in order to identify further roles of ER-Golgi MCS. We focus on their role in transport carrier biogenesis. Indeed, a specific type of carriers, the already mentioned CARTS, has been shown to require the establishment of ER-Golgi MCS. Silencing of the MCS components VAP-A and VAP-B[111], as well as stabilizing OSBP and CERT with the PH-FFAT domain (pleckstrin homology domain and two phenylalanine in an acidic tract motiv), results in lower secretion of the protein PAUF, and reduced formation of CARTS.[112] Similar observations have been made when using 25-hydroxycholesterol (25-HC), an oxysterol that is able to bind OSBP with high affinity, and block it in the bound conformation to VAP. This binding inhibits the VAP/OSBP-mediated sterol transfer.[108] We have yet to determine the specific role that MCS play in CARTS formation and the impact of their lipid transfer function. They may be involved in protein sorting, or the successive steps of membrane budding and/or carrier fission.

A direct link can be established between this lipid transport function and fission of the carriers. OSBP facilitates CERT-mediated ceramide transfer[113], which together

with phosphatidylcholine, can then be converted into sphingomyelin and diacylglycerol (DAG).[107,114] DAG not only promotes negative curvature in membranes[115], but also recruits and activates PKD.[116] As already mentioned in this section, PKD is required for CARTS fission at the TGN.[71,117–120]

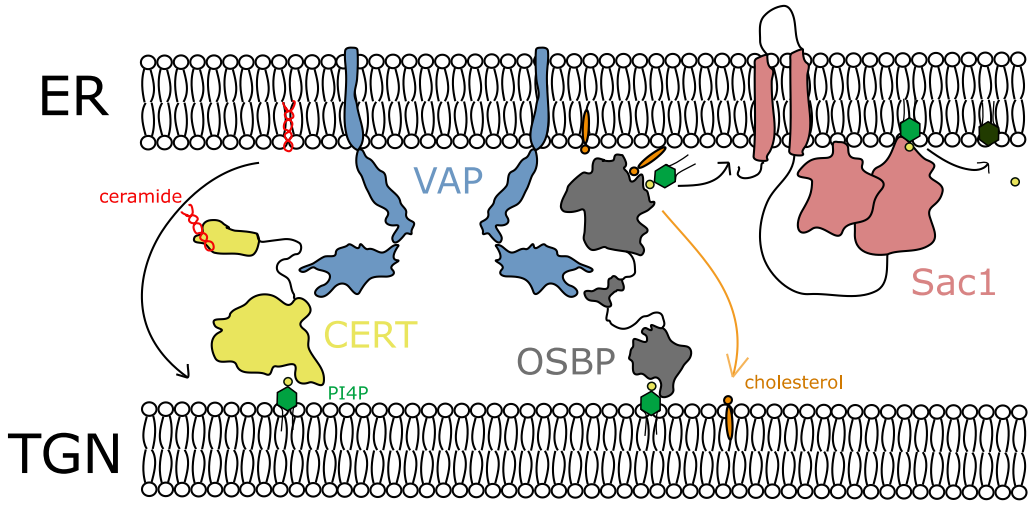

Figure 5. Proteins localized to ER-Golgi MCS. VAP-A/B is an ER transmembrane protein that serves as a picket for other MCS proteins. CERT binds to VAP-A/B and to PI4P at the TGN side, and transports ceramide from the ER to the TGN. OSBP also binds to VAP proteins and to PI4P at the TGN side. It transports cholesterol from the ER to the TGN, and PI4P in the opposite direction. PI4P at the ER can then be dephosphorylated by Sac1. (Modified from Masone, M. C. et al., *FEBS Letters* (2019)[121]).

7. TRANSPORT AND FUSION AT THE PLASMA MEMBRANE

The above-mentioned carriers need to be physically transported to the PM, and motor proteins are known to facilitate this transport. In the past, it was suggested that vesicle movement across long distances occurs via microtubules, facilitated by kinesin and dynein motors, while transport over short distances is carried out on actin filaments, driven by myosin motors.[122]

More recent studies have tried to link the different types of cargo and receptors with each motor protein (see **Table 1**). For instance, actin and myosin II are essential for PM export for CARTS,[71] while Rab6-positive carriers depend on microtubules.[82] Yet, several critical questions remain unanswered in this field, including how motor protein activity is regulated, whether specific motor proteins are required at each membrane sorting step, and if so, which ones are involved.[123]

Once at the PM, vesicles tether at the delivery sites. This capture of the arriving vesicles is essential for a correct vesicle targeting and fidelity of cargo delivery. On

the plasma membrane, two molecular tethers have been identified: ELKS protein (also reported as ERC, RAB6IP2 or CAST), and the CATCHR protein complex exocyst. The first is implicated in the secretion of neuropeptide Y in Rab6, MICAL3 and Rab8 positive carriers, and synaptic vesicle tethering to the plasma membrane in neuronal cell model.[82,85]

On the other hand, the CATCHR protein complex exocyst localizes to the Golgi, and plasma membrane, as well as at vesicle fusion points. Although the role of the exocyst complex in the secretory pathway had already been well established in *S. cerevisiae*, studies had been hampered by the fact that loss of the exocyst complex is lethal in cultured cells. It was a recent study performed by Pereira et al. that showed the importance of the exocyst complex in the mammalian constitutive secretory pathway. Consecutive transient depletion of multiple exocyst subunit resulted in cargo accumulation in post-Golgi cariers.[124]

The core machinery for vesicle fusion with the plasma membrane involves a family of proteins known as SNAREs (Soluble NSF Attachment Protein Receptors). Although the best-known SNAREs and other fusogenic complexes have been studied in the context of transport from the ER to the Golgi[125], there is a lot of interest in depicting the molecular mechanism at the PM level. There are two types of SNARE proteins; v-SNAREs (vesicle SNAREs) located on the vesicle; and t-SNAREs (target SNAREs), located on the target membrane. The interaction between these two types of proteins, drives a zippering action, that brings the vesicle close to the membrane, facilitating fusion.[126] It has been reported that a single SNARE complex is enough to trigger liposome fusion.[127] However, fast vesicle fusion in living cells requires at least three SNARE complexes.[128]

This whole process of vesicle docking, SNARE complex formation and fusion is regulated by Rab GTPases, a large family of small GTP-binding proteins. In this context it needs to be outlined the role of the protein Rab6A/A', which is associated with secretory vesicles that fuse directly with the plasma membrane.[82,83]

8. CONCEPT OF THE THESIS

Intracellular trafficking, and more specifically protein secretion, remains a field with numerous unanswered questions and challenges. At each step of this route, there are models that are being constantly challenged, and processes that are still not fully understood. The aim of this thesis is to provide tools and evaluate the already

available ones for a quantitative investigation of these processes through fluorescent microscopy. Such a quantitative approach benefits from two sides:

(i) The capacity to provide a detailed quantitative characterization of molecular dynamics, interactions, and spatial distributions can help to the mechanistic understanding.

(ii) It contributes with objective measurements that removes subjective biases and it allows for accurate comparisons between different experiments and conditions.

A detailed description of the fluorescence microscopy techniques, the computational analysis and the biological tools is provided in **Chapter 2**. The first chapter with our original results, **Chapter 3**, is focused in the second point above. By using image analysis and quantification, we helped evaluate fluorescence microscopy datasets in an objective and unbiased manner. Very similar but complementary approaches were used in four different projects that aimed to resolve specific questions in the field of protein secretion and intracellular trafficking. The approaches included: *(i)* quantification of the colocalization and proximity of structures recorded in different fluorescent channels; (ii) measurement of the fluorescent intensity differences at different cell compartments, and under different experimental conditions; and (iii) characterization of the dynamics of different subcellular structures important for membrane trafficking such as transport nanotubule carriers or secretory transport carriers.

Chapters 4 and **5** are rather centered in the first objective, aiming to develop new experimental and imaging approaches for the characterization of protein dynamics within the ER and the Golgi apparatus, that can help unravel the molecular mechanism behind protein secretion. **Chapter 4** aims at describing the possible challenges associated to the application of single particle tracking (SPT) in the secretory pathway, and proposes control experiments and analysis pipelines for an unbiased and artifact-free analysis. Building from that, **Chapter 5** applies the previously developed methodology for the characterization of the protein distribution in the TGN. As a complementary tool, we also used STED microscopy in fixed and live-conditions. The aim is to bring light into the process of protein sorting by quantitatively describing the motion and the ratio of molecules in each kinetic state.

9. REFERENCES

1. Palade, G. Intracellular aspects of the process of protein synthesis. *Science (1979)* **189**, (1975).
2. Bonifacino, J. S. Vesicular transport earns a Nobel. *Trends in Cell Biology* vol. 24 Preprint at https://doi.org/10.1016/j.tcb.2013.11.001 (2014).
3. Lujan, P., Angulo-Capel, J., Chabanon, M. & Campelo, F. Interorganelle communication and membrane shaping in the early secretory pathway. *Current Opinion in Cell Biology* vol. 71 Preprint at https://doi.org/10.1016/j.ceb.2021.01.010 (2021).
4. Akopian, D., Shen, K., Zhang, X. & Shan, S. O. Signal recognition particle: An essential protein-targeting machine. *Annual Review of Biochemistry* vol. 82 Preprint at https://doi.org/10.1146/annurev-biochem-072711-164732 (2013).
5. Saraogi, I. & Shan, S. ou. Molecular Mechanism of Co-translational Protein Targeting by the Signal Recognition Particle. *Traffic* vol. 12 Preprint at https://doi.org/10.1111/j.1600-0854.2011.01171.x (2011).
6. Pool, M. R. Signal recognition particles in chloroplasts, bacteria, yeast and mammals. *Molecular Membrane Biology* vol. 22 Preprint at https://doi.org/10.1080/09687860400026348 (2005).
7. Nyathi, Y., Wilkinson, B. M. & Pool, M. R. Co-translational targeting and translocation of proteins to the endoplasmic reticulum. *Biochimica et Biophysica Acta - Molecular Cell Research* vol. 1833 Preprint at https://doi.org/10.1016/j.bbamcr.2013.02.021 (2013).
8. Ramazi, S. & Zahiri, J. Post-translational modifications in proteins: Resources, tools and prediction methods. *Database* vol. 2021 Preprint at https://doi.org/10.1093/database/baab012 (2021).
9. Wolin, S. L. & Maquat, L. E. Cellular RNA surveillance in health and disease. *Science* vol. 366 Preprint at https://doi.org/10.1126/science.aax2957 (2019).
10. Jacquemyn, J., Cascalho, A. & Goodchild, R. E. The ins and outs of endoplasmic reticulum-controlled lipid biosynthesis. *EMBO Rep* **18**, (2017).
11. Balch, W. E., McCaffery, J. M., Plutner, H. & Farquhar, M. G. Vesicular stomatitis virus glycoprotein is sorted and concentrated during export from the endoplasmic reticulum. *Cell* **76**, (1994).

12. Stephens, D. J., Lin-Marq, N., Pagano, A., Pepperkok, R. & Paccaud, J. P. COPI-coated ER-to-Golgi transport complexes segregate from COPII in close proximity to ER exit sites. *J Cell Sci* **113**, (2000).

13. Scales, S. J., Pepperkok, R. & Kreis, T. E. Visualization of ER-to-Golgi transport in living cells reveals a sequential mode of action for COPII and COPI. *Cell* **90**, (1997).

14. Aridor, M., Bannykh, S. I., Rowe, T. & Balch, W. E. Sequential coupling between copII and copI vesicle coats in endoplasmic reticulum to Golgi transport. *Journal of Cell Biology* **131**, (1995).

15. Barlowe, C. *et al.* COPII: A membrane coat formed by Sec proteins that drive vesicle budding from the endoplasmic reticulum. *Cell* **77**, 895–907 (1994).

16. Schweizer, A., Fransen, J. A. M., Bachi, T., Ginsel, L. & Hauri, H. P. Identification, by a monoclonal antibody, of a 53-kD protein associated with a tubulo-vesicular compartment at the cis-side of the Golgi apparatus. *Journal of Cell Biology* **107**, (1988).

17. Schweizer, A. *et al.* Identification of an intermediate compartment involved in protein transport from endoplasmic reticulum to Golgi apparatus. *Eur J Cell Biol* **53**, (1990).

18. Saraste, J. & Svensson, K. Distribution of the intermediate elements operating in ER to Golgi transport. *J Cell Sci* **100**, (1991).

19. Schweizer, A., Matter, K., Ketcham, C. M. & Hauri, H. P. The isolated ER-Golgi intermediate compartment exhibits properties that are different from ER and cis-Golgi. *Journal of Cell Biology* **113**, (1991).

20. Peotter, J., Kasberg, W., Pustova, I. & Audhya, A. COPII-mediated trafficking at the ER/ERGIC interface. *Traffic* vol. 20 Preprint at https://doi.org/10.1111/tra.12654 (2019).

21. Bard, F. *et al.* Functional genomics reveals genes involved in protein secretion and Golgi organization. *Nature* **439**, (2006).

22. Wilson, D. G. *et al.* Global defects in collagen secretion in a Mia3/TANGO1 knockout mouse. *Journal of Cell Biology* **193**, (2011).

23. Saito, K. *et al.* TANGO1 Facilitates Cargo Loading at Endoplasmic Reticulum Exit Sites. *Cell* **136**, (2009).

24. Zhang, L. *et al.* O-Glycosylation regulates polarized secretion by modulating Tango1 stability. *Proc Natl Acad Sci U S A* **111**, (2014).

25. Pitman, J. L., Bonnet, D. J., Curtiss, L. K. & Gekakis, N. Reduced cholesterol and triglycerides in mice with a mutation in Mia2, a liver protein that localizes to ER exit sites. *J Lipid Res* **52**, (2011).

26. Santos, A. J. M., Nogueira, C., Ortega-Bellido, M. & Malhotra, V. TANGO1 and Mia2/cTAGE5 (TALI) cooperate to export bulky pre-chylomicrons/VLDLs from the endoplasmic reticulum. *Journal of Cell Biology* **213**, (2016).

27. Saito, K. & Katada, T. Mechanisms for exporting large-sized cargoes from the endoplasmic reticulum. *Cellular and Molecular Life Sciences* vol. 72 Preprint at https://doi.org/10.1007/s00018-015-1952-9 (2015).

28. Saito, K. & Maeda, M. Not just a cargo receptor for large cargoes; An emerging role of TANGO1 as an organizer of ER exit sites. *Journal of Biochemistry* vol. 166 Preprint at https://doi.org/10.1093/jb/mvz036 (2020).

29. Raote, I. *et al.* TANGO1 assembles into rings around COP II coats at ER exit sites. *Journal of Cell Biology* **216**, (2017).

30. Liu, M. *et al.* Tango1 spatially organizes ER exit sites to control ER export. *Journal of Cell Biology* **216**, (2017).

31. Santos, A. J., Raote, I., Scarpa, M., Brouwers, N. & Malhotra, V. TANGO1 recruits ERGIC membranes to the endoplasmic reticulum for procollagen export. *Elife* **4**, (2015).

32. Nogueira, C. *et al.* SLY1 and syntaxin 18 specify a distinct pathway for procollagen VII export from the endoplasmic reticulum. *Elife* **2014**, (2014).

33. Raote, I. *et al.* A physical mechanism of tango1-mediated bulky cargo export. *Elife* **9**, (2020).

34. Weigel, A. V. *et al.* ER-to-Golgi protein delivery through an interwoven, tubular network extending from ER. *Cell* **184**, (2021).

35. Shomron, O. *et al.* Copii collar defines the boundary between er and er exit site and does not coat cargo containers. *Journal of Cell Biology* **220**, (2021).

36. Wong-Dilworth, L. *et al.* Nanoscale imaging reveals the mechanisms of ER-to-Golgi transport via a dynamic tubular-vesicular network. *bioRxiv* (2023).

37. Ben-Takaya, H., Miura, K., Pepperkok, R. & Hauri, H. P. Live imaging of bidirectional traffic from the ERGIC. *J Cell Sci* **118**, (2005).

38. Simpson, J. C., Nilsson, T. & Pepperkok, R. Biogenesis of tubular ER-to-golgi transport intermediates. *Mol Biol Cell* **17**, (2006).

39. Kurokawa, K., Okamoto, M. & Nakano, A. Contact of cis-Golgi with ER exit sites executes cargo capture and delivery from the ER. *Nat Commun* **5**, (2014).

40. Bentivoglio, M. & Mazzarello, P. One hundred years of the Golgi apparatus: History of a disputed cell organelle. *Ital J Neurol Sci* **19**, (1998).

41. Klumperman, J. Architecture of the mammalian Golgi. *Cold Spring Harb Perspect Biol* **3**, a005181 (2011).

42. Emr, S. *et al.* Journeys through the Golgi - taking stock in a new era. *Journal of Cell Biology* **187**, 449–453 (2009).

43. Glick, B. S. & Luini, A. Models for Golgi traffic: A critical assessment. *Cold Spring Harb Perspect Biol* **3**, (2011).

44. Lujan, P. & Campelo, F. Should I stay or should I go? Golgi membrane spatial organization for protein sorting and retention. *Arch Biochem Biophys* **707**, 108921 (2021).

45. Rambourg, A., Daraspe, J., Képès, F. & Verbavatz, J. M. Morphodynamics of the yeast Golgi apparatus. in *The Golgi Apparatus: State of the Art 110 Years after Camillo Golgi's Discovery* (2008). doi:10.1007/978-3-211-76310-0_37.

46. Rothman, J. E. The Golgi apparatus: Two organelles in tandem. *Science* vol. 213 Preprint at https://doi.org/10.1126/science.7268428 (1981).

47. Farquhar, M. G. Progress in unraveling pathways of Golgi traffic. *Annual review of cell biology* vol. 1 Preprint at https://doi.org/10.1146/annurev.cb.01.110185.002311 (1985).

48. Dunphy, W. G. & Rothman, J. E. Compartmental organization of the golgi stack. *Cell* vol. 42 Preprint at https://doi.org/10.1016/S0092-8674(85)80097-0 (1985).

49. Kleene, R. & Berger, E. G. The molecular and cell biology of glycosyltransferases. *BBA - Reviews on Biomembranes* vol. 1154 Preprint at https://doi.org/10.1016/0304-4157(93)90003-7 (1993).

50. Rabouille, C. *et al.* Mapping the distribution of Golgi enzymes involved in the construction of complex oligosaccharides. *J Cell Sci* **108**, (1995).

51. Nilsson, T., Au, C. E. & Bergeron, J. J. M. Sorting out glycosylation enzymes in the Golgi apparatus. *FEBS Letters* vol. 583 Preprint at https://doi.org/10.1016/j.febslet.2009.10.064 (2009).

52. Rothman, J. E. & Wieland, F. T. Protein sorting by transport vesicles. *Science (1979)* **272**, (1996).

53. Orci, L., Amherdt, M., Ravazzola, M., Perrelet, A. & Rothman, J. E. Exclusion of Golgi residents from transport vesicles budding from Golgi cisternae in intact cells. *Journal of Cell Biology* **150**, (2000).

54. Pelham, H. R. B. & Rothman, J. E. The debate about transport in the golgi - Two sides of the same coin? *Cell* vol. 102 Preprint at https://doi.org/10.1016/S0092-8674(00)00060-X (2000).

55. Grasse, P. P. Ultrastructure, polarité et reproduction de l'appareil de Golgi. *C R Hebd Seances Acad Sci* **245**, (1957).

56. Morre, D. J. & Ovtracht, L. Dynamics of the Golgi apparatus: membrane differentiation and membrane flow. *International Review of Cytology* vol. suppl. 5 Preprint at (1977).

57. Bannykh, S. I. & Balch, W. E. Membrane dynamics at the endoplasmic reticulum-golgi interface. *Journal of Cell Biology* vol. 138 Preprint at https://doi.org/10.1083/jcb.138.1.1 (1997).

58. Mironov, A. *et al.* ER-to-Golgi carriers arise through direct en bloc protrusion and multistage maturation of specialized ER exit domains. *Dev Cell* **5**, (2003).

59. Bonfanti, L. *et al.* Procollagen traverses the Golgi stack without leaving the lumen of cisternae: Evidence for cisternal maturation. *Cell* **95**, (1998).

60. Glick, B. S. & Malhotra, V. The curious status of the Golgi apparatus. *Cell* vol. 95 Preprint at https://doi.org/10.1016/S0092-8674(00)81713-4 (1998).

61. Rabouille, C. & Klumperman, J. The maturing role of COPI vesicles in intra-Golgi transport. *Nature Reviews Molecular Cell Biology* vol. 6 Preprint at https://doi.org/10.1038/nrm1735 (2005).

62. Glick, B. S., Elston, T. & Oster, G. A cisternal maturation mechanism can explain the asymmetry of the Golgi stack. *FEBS Lett* **414**, (1997).

63. Weiss, M. & Nilsson, T. Protein sorting in the Golgi apparatus: A consequence of maturation and triggered sorting. *FEBS Lett* **486**, (2000).

64. Glick, B. S. & Nakano, A. Membrane traffic within the Golgi apparatus. *Annual Review of Cell and Developmental Biology* vol. 25 Preprint at https://doi.org/10.1146/annurev.cellbio.24.110707.175421 (2009).

65. Matsuura-Tokita, K., Takeuchi, M., Ichihara, A., Mikuriya, K. & Nakano, A. Live imaging of yeast Golgi cisternal maturation. *Nature* **441**, (2006).

66. Losev, E. *et al.* Golgi maturation visualized in living yeast. *Nature* **441**, (2006).

67. Griffiths, G. & Simons, K. The trans Golgi network: Sorting at the exit site of the Golgi complex. *Science (1979)* **234**, (1986).

68. Polishchuk, R. S. *et al.* Correlative Light-Electron Microscopy Reveals the Tubular-Saccular Ultrastructure of Carriers Operating between Golgi Apparatus and Plasma Membrane. *Journal of Cell Biology* **148**, 45–58 (2000).

69. Kirchhausen, T., Owen, D. & Harrison, S. C. Molecular Structure, Function, and Dynamics of Clathrin-Mediated Membrane Traffic. *Cold Spring Harb Perspect Biol* **6**, a016725–a016725 (2014).

70. Stalder, D. & Gershlick, D. C. Direct trafficking pathways from the Golgi apparatus to the plasma membrane. *Semin Cell Dev Biol* **107**, 112–125 (2020).

71. Wakana, Y. *et al.* A new class of carriers that transport selective cargo from the trans Golgi network to the cell surface. *EMBO J* **31**, 3976–3990 (2012).

72. Deng, Y., Rivera-Molina, F. E., Toomre, D. K. & Burd, C. G. Sphingomyelin is sorted at the trans Golgi network into a distinct class of secretory vesicle. *Proc Natl Acad Sci U S A* **113**, (2016).

73. Bottanelli, F. *et al.* A novel physiological role for ARF1 in the formation of bidirectional tubules from the Golgi. *Mol Biol Cell* **28**, 1676–1687 (2017).

74. Beck, R. *et al.* Membrane curvature induced by Arf1-GTP is essential for vesicle formation. *Proceedings of the National Academy of Sciences* **105**, 11731–11736 (2008).

75. Liljedahl, M. *et al.* Protein Kinase D Regulates the Fission of Cell Surface Destined Transport Carriers from the Trans-Golgi Network. *Cell* **104**, 409–420 (2001).

76. Godi, A. *et al.* FAPPS control Golgi-to-cell-surface membrane traffic by binding to ARF and PtdIns(4)P. *Nat Cell Biol* **6**, (2004).

77. Cao, X. *et al.* Golgi protein FAPP2 tubulates membranes. *Proceedings of the National Academy of Sciences* **106**, 21121 LP – 21125 (2009).

78. Lenoir, M. *et al.* Structural basis of wedging the Golgi membrane by FAPP pleckstrin homology domains. *EMBO Rep* **11**, 279–284 (2010).

79. Godi, A. *et al.* ARF mediates recruitment of PtdIns-4-OH kinase-β and stimulates synthesis of PtdIns(4,5)P2 on the Golgi complex. *Nat Cell Biol* **1**, 280–287 (1999).

80. Schnoor, M., Stradal, T. E. & Rottner, K. Cortactin: Cell Functions of A Multifaceted Actin-Binding Protein. *Trends Cell Biol* **28**, 79–98 (2018).

81. Cao, H. *et al.* Actin and Arf1-dependent recruitment of a cortactin–dynamin complex to the Golgi regulates post-Golgi transport. *Nat Cell Biol* **7**, 483–492 (2005).

82. Grigoriev, I. *et al.* Rab6 Regulates Transport and Targeting of Exocytotic Carriers. *Dev Cell* **13**, 305–314 (2007).

83. Miserey-Lenkei, S. *et al.* Rab and actomyosin-dependent fission of transport vesicles at the Golgi complex. *Nat Cell Biol* **12**, 645–654 (2010).

84. Miserey-Lenkei, S. *et al.* Coupling fission and exit of RAB6 vesicles at Golgi hotspots through kinesin-myosin interactions. *Nat Commun* **8**, (2017).

85. Grigoriev, I. *et al.* Rab6, Rab8, and MICAL3 cooperate in controlling docking and fusion of exocytotic carriers. *Current Biology* **21**, (2011).

86. Pagliuso, A. *et al.* Golgi membrane fission requires the CtBP1-S/BARS-induced activation of lysophosphatidic acid acyltransferase δ. *Nat Commun* **7**, 12148 (2016).

87. Valente, C. *et al.* A 14-3-3γ dimer-based scaffold bridges CtBP1-S/BARS to PI(4)KIIIβ to regulate post-Golgi carrier formation. *Nat Cell Biol* **14**, 343–354 (2012).

88. von Blume, J. *et al.* ADF/Cofilin Regulates Secretory Cargo Sorting at the TGN via the Ca2+ ATPase SPCA1. *Dev Cell* **20**, 652–662 (2011).

89. Kienzle, C. *et al.* Cofilin recruits F-actin to SPCA1 and promotes Ca2+-mediated secretory cargo sorting. *Journal of Cell Biology* **206**, 635–654 (2014).

90. Crevenna, A. H. *et al.* Secretory cargo sorting by Ca2+-dependent Cab45 oligomerization at the trans-Golgi network. *Journal of Cell Biology* **213**, 305–314 (2016).

91. Deng, Y. *et al.* Activity of the SPCA1 Calcium Pump Couples Sphingomyelin Synthesis to Sorting of Secretory Proteins in the Trans-Golgi Network. *Dev Cell* **47**, (2018).

92. Von Blume, J. *et al.* Cab45 is required for Ca2+-dependent secretory cargo sorting at the trans-Golgi network. *Journal of Cell Biology* **199**, 1057–1066 (2012).

93. Sundberg, E. L., Deng, Y. & Burd, C. G. Syndecan-1 Mediates Sorting of Soluble Lipoprotein Lipase with Sphingomyelin-Rich Membrane in the Golgi Apparatus. *Dev Cell* **51**, 387-398.e4 (2019).

94. Wakana, Y. *et al.* CARTS biogenesis requires VAP–lipid transfer protein complexes functioning at the endoplasmic reticulum–Golgi interface. *Mol Biol Cell* **26**, 4686–4699 (2015).

95. Wakana, Y. *et al.* Kinesin-5/Eg5 is important for transport of CARTS from the trans-Golgi network to the cell surface. *Journal of Cell Biology* **202**, 241–250 (2013).

96. Lujan, P. *et al.* Sorting of secretory proteins at the trans-Golgi network by human TGN46. *Elife* **12**, (2024).

97. Kelly, R. B. Pathways of protein secretion in eukaryotes. *Science (1979)* **230**, 25 LP – 32 (1985).

98. Wieland, F. T., Gleason, M. L., Serafini, T. A. & Rothman, J. E. The rate of bulk flow from the endoplasmic reticulum to the cell surface. *Cell* **50**, 289–300 (1987).

99. Mcmahon, H. T. & Gallop, J. L. Membrane curvature and mechanisms of dynamic cell membrane remodelling. *Nature* **438**, 590–596 (2005).

100. Adarska, P., Wong-Dilworth, L. & Bottanelli, F. ARF GTPases and Their Ubiquitous Role in Intracellular Trafficking Beyond the Golgi. *Frontiers in Cell and Developmental Biology* vol. 9 Preprint at https://doi.org/10.3389/fcell.2021.679046 (2021).

101. Stamnes, M. A. & Rothman, J. E. The binding of AP-1 clathrin adaptor particles to Golgi membranes requires ADP-ribosylation factor, a small GTP-binding protein. *Cell* **73**, (1993).

102. Nakai, W. *et al.* ARF1 and ARF4 regulate recycling endosomal morphology and retrograde transport from endosomes to the Golgi apparatus. *Mol Biol Cell* **24**, (2013).

103. Tan, J. Z. A. *et al.* Distinct anterograde trafficking pathways of BACE1 and amyloid precursor protein from the TGN and the regulation of amyloid-β production. *Mol Biol Cell* **31**, (2020).

104. Stockhammer, A. *et al.* Multi-functional ARF1 compartments serve as a hub for short-range cargo transfer to endosomes. *bioRxiv* (2023).

105. Scorrano, L. *et al.* Coming together to define membrane contact sites. *Nat Commun* **10**, 1–11 (2019).

106. Venditti, R. *et al.* Molecular determinants of ER–Golgi contacts identified through a new FRET–FLIM system. *Journal of Cell Biology* **218**, 1055–1065 (2019).

107. Hanada, K. *et al.* Molecular machinery for non-vesicular trafficking of ceramide. *Nature* **426**, 803–809 (2003).

108. Mesmin, B. *et al.* A Four-Step Cycle Driven by PI(4)P Hydrolysis Directs Sterol/PI(4)P Exchange by the ER-Golgi Tether OSBP. *Cell* **155**, 830–843 (2013).

109. Kim, Y. J., Hernandez, M.-L. G. & Balla, T. Inositol lipid regulation of lipid transfer in specialized membrane domains. *Trends Cell Biol* **23**, 270–278 (2013).

110. Phillips, M. J. & Voeltz, G. K. Structure and function of ER membrane contact sites with other organelles. *Nat Rev Mol Cell Biol* **17**, 69–82 (2016).

111. Wakana, Y. *et al.* CARTS biogenesis requires VAP–lipid transfer protein complexes functioning at the endoplasmic reticulum–Golgi interface. *Mol Biol Cell* **26**, 4686–4699 (2015).

112. Wakana, Y. *et al.* The ER cholesterol sensor SCAP promotes CARTS biogenesis at ER–Golgi membrane contact sites. *Journal of Cell Biology* **220**, (2021).

113. Perry, R. J. & Ridgway, N. D. Oxysterol-binding protein and vesicle-associated membrane protein-associated protein are required for sterol-dependent activation of the ceramide transport protein. *Mol Biol Cell* **17**, (2006).

114. Huitema, K., Van Den Dikkenberg, J., Brouwers, J. F. H. M. & Holthuis, J. C. M. Identification of a family of animal sphingomyelin synthases. *EMBO Journal* **23**, (2004).

115. Shemesh, T., Luini, A., Malhotra, V., Burger, K. N. J. & Kozlov, M. M. Prefission Constriction of Golgi Tubular Carriers Driven by Local Lipid Metabolism: A Theoretical Model. *Biophys J* **85**, (2003).

116. Baron, C. L. & Malhotra, V. Role of diacylglycerol in PKD recruitment to the TGN and protein transport to the plasma membrane. *Science (1979)* **295**, (2002).

117. Yeaman, C. *et al.* Protein kinase D regulates basolateral membrane protein exit from trans-Golgi network. *Nat Cell Biol* **6**, (2004).

118. Maeda, Y., Beznoussenko, G. V., Lint, J. Van, Mironov, A. A. & Malhotra, V. Recruitment of protein kinase D to the trans-Golgi network via the first cysteine-rich domain. *EMBO Journal* **20**, (2001).

119. Bossard, C., Bresson, D., Polishchuk, R. S. & Malhotra, V. Dimeric PKD regulates membrane fission to form transport carriers at the TGN. *Journal of Cell Biology* **179**, (2007).

120. Liljedahl, M. *et al.* Protein Kinase D Regulates the Fission of Cell Surface Destined Transport Carriers from the Trans-Golgi Network. *Cell* **104**, 409–420 (2001).

121. Masone, M. C., Morra, V. & Venditti, R. Illuminating the membrane contact sites between the endoplasmic reticulum and the trans -Golgi network. *FEBS Lett* **593**, 3135–3148 (2019).

122. Atkinson, S. J., Doberstein, S. K. & Pollard, T. D. Moving off the beaten track. *Current Biology* **2**, (1992).

123. Kamal, A. & Goldstein, L. S. Connecting vesicle transport to the cytoskeleton. *Current Opinion in Cell Biology* vol. 12 Preprint at https://doi.org/10.1016/S0955-0674(00)00123-X (2000).

124. Pereira, C. *et al.* The exocyst complex is an essential component of the mammalian constitutive secretory pathway. *J Cell Biol* **222**, (2023).

125. Malsam, J. & Söllner, T. H. Organization of SNAREs within the Golgi stack. *Cold Spring Harb Perspect Biol* **3**, (2011).

126. Jahn, R. & Scheller, R. H. SNAREs - Engines for membrane fusion. *Nature Reviews Molecular Cell Biology* vol. 7 Preprint at https://doi.org/10.1038/nrm2002 (2006).

127. Van Den Bogaart, G. *et al.* One SNARE complex is sufficient for membrane fusion. *Nat Struct Mol Biol* **17**, (2010).

128. Mohrmann, R., De Wit, H., Verhage, M., Neher, E. & Sørensen, J. B. Fast vesicle fusion in living cells requires at least three SNARE complexes. *Science (1979)* **330**, (2010).

Chapter 2

Introduction to the Techniques

This chapter details and places in context the diverse set of experimental and analytical tools as well as methodologies employed in the thesis. These include *(i)* different fluorescence microscopy techniques that enable a quantitative characterization of the spatio-temporal dynamics of cellular components, *(ii)* automated image analysis and quantification algorithms, and *(iii)* biological methods tailored to the study of the secretory pathway. The fundamentals of each technique are explained in detail, highlighting the technical advancements that led to the tools that we are able to use today.

The selection criteria for these modern tools were guided by three main objectives: *(i)* achieving the highest spatial and temporal resolution possible, *(ii)* enabling quantitative and automated analysis for objective and reproducible outcomes, and, when feasible, *(iii)* allowing for live-cell characterization of the biological processes under investigation.

1. SELECTION OF THE METHODOLOGY

The set of tools used in this thesis include different fluorescence microscopy techniques, different image analysis and quantification algorithms, as well as the biological tools tailored for this study's needs. The selection of these tools has been made to fulfill the following requirements:

(i) Achieving the highest resolution possible by the microscopy techniques. We aim for techniques that are capable of capturing details of the cellular structures – as for the case of stimulated emission depletion (STED) microscopy – or very precisely determining the position of single protein molecules – as it is the case for single particle tracking (SPT).

(ii) Enabling a quantitative and automated analysis for non-biased and reproducible results. Quantitative data analysis is nowadays more crucial than ever before to better understand and rationalize microscopy datasets. Current computational advancements are allowing to extract more and more meaningful information, and therefore allow us to drive further conclusions and formulate new hypotheses. Moreover, automation in data analysis helps to standardize the quantification process, reducing human biases and variability in interpreting the results.

(iii) Compatible with live-cell characterization of the biological processes. The biological methods and the microscopy techniques should allow to monitor the biological processes in living cells, in order to get an insight to their functioning in a state similar to their natural environment.

2. INTRODUCTION TO OPTICAL MICROSCOPY

Despite the advancements in terms of resolution of electron microscopy, a vast amount of the research in cell biology is still performed with microscopes that utilize light and conventional lenses. There are several reasons that can make this strategy a preferable one for multiple studies. The first one is that visible or far-red wavelength light is not invasive, meaning that these types of light do not damage or interfere with cellular processes, and are therefore compatible with live-cell imaging. Secondly, cells are optically transparent, and therefore it is possible to image the intracellular compartments by means of light. Finally, it is compatible with fluorescent tagging, which allows the specific labeling of very specific molecular species, usually very specific proteins, that serve to visualize specific compartments. Moreover, it is to be mentioned its versatility, ease of use, and ease of implementation of optical microscopy.

However, in 1873, Abbe´s work concluded that the smallest distance that can be resolved between two points in an optical system is proportional to the wavelength of the used light (λ) and inversely proportional to the numerical aperture (NA) of the imaging lens.[1]

$$d \approx \frac{\lambda}{2NA} \quad (1)$$

This imposes a so-called diffraction limit of ~180 nm, in an ideal scenario using light of 500 nm wavelength and an oil objective with 1.4 NA. However, in practical, conventional microscopes, resolutions better than 200-250 nm are rarely achieved due to various practical limitations such as the quality of the optical components, alignment, and environmental conditions. Consequently, many efforts have been devoted over the last decades to overcome this drawback.

2.1. FLUORESCENCE MICROSCOPY

Improvements in resolution and contrast in optical microscopy were mainly given by advancements in the field of fluorescence microscopy. Fluorescent molecules have been instrumental because they emit a large number of photons upon excitation with a specific light wavelength, and they can be used to tag very specific cellular molecules. This results in very high contrast images, that report on the spatial distribution of the labeled molecules in a very specific manner. Moreover, because there are a large number of fluorescent molecules with specific excitation and emission spectrum, fluorescence microscopy allows to image multiple of these molecules simultaneously (multi-color fluorescence microscopy).

In order to understand what the phenomena of fluorescence is, we first need to make a short reference to the absorption of light. Absorption is a phenomenon that occurs when photons interact with a molecule or atom causing a change (transition) in its energy states. Radiation is absorbed when it has an energy equal to the transition energy. As different kinds of electronic transitions can exist in complex molecules, the electromagnetic radiation can trigger different kinds of transitions depending on its wavelength and, thus, its energy: electronic, vibrational, rotational or translational transitions.[2]

When irradiating a fluorescent molecule, if the incident light possesses the energy required to trigger the excitation of electrons (electronic transition) from a ground energy level (S_0 in **Figure 1**) to an excited energy level (S_1 or S_2 in **Figure 1**), then

the molecule will get excited. Once in the excited state, the electron can follow different relaxation and decay transitions before returning to the ground state S_0. Firstly, the electron reaches the lowest vibrational energy level of the excited state through the production of heat, the so-called vibrational relaxation. It can undergo internal conversion, transitioning from one excited electronic state to a lower excited electronic state (for instance from S_2 to S_1 in **Figure 1**). Then, it can reach the ground state through multiple different paths indicated in **Figure 1**. We refer to fluorescence emission, when the transition from S_1 to S_0 occurs in a radiative manner.[2] This process can be repeated multiple times, therefore emitting multiple photons.

When a fluorescent molecule loses its ability to fluoresce, one can refer to it as photobleaching. This phenomenon can also be placed within this context of energy states transitions. When the fluorophore absorbs photons, it can undergo photochemical reactions that ultimately lead to the change of the fluorophore chemical structure and the termination of fluorescence. Photobleaching is a very important concept in fluorescence microscopy, because it limits the imaging time, and indirectly the spatial resolution and contrast of images.

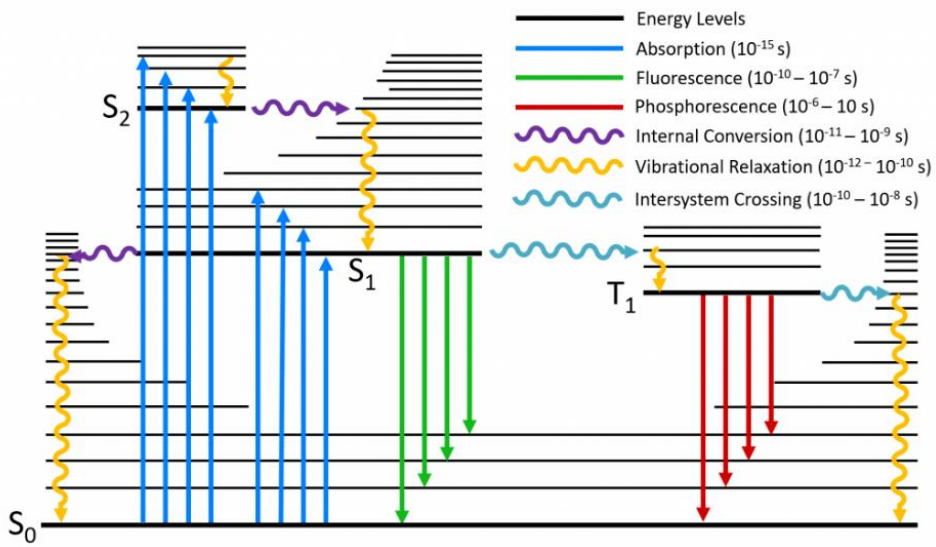

Figure 1. Jablonski diagram. The electrons can be excited by absorption of light (blue arrows), and the decay of the electron can take place through different paths: there is always vibrational relaxation (yellow arrows) followed by several alternatives that include fluorescence (green arrows that go from S1,0 to S0), non-radiative relaxation (yellow arrow, from S1,0 to S0), and quenching (not shown in the figure). The electron can also transition from a higher energy lever to a lower energy level before the mentioned decays (violet arrow from S2 to S1). The electron can also go to the triplet state by intersystem crossing (cyan arrows) and, eventually, reach the ground state though non-radiative relaxation (yellow arrow, from T1 to S0) or phosphorescence (red arrows, from T1 to S0). (Taken from [3]).

For a given fluorescent molecule, there is not a single discrete wavelength of light that triggers the transition to an excited state. Excitation by some wavelengths is more probable than others, and this is depicted by the excitation spectrum of the molecule. Similarly, the wavelength of the emitted fluorescent photons is not discrete, but rather presents a range of emitted wavelengths, each with a given probability, as shown by the emission spectrum. Importantly, the emission spectrum is independent of the excitation wavelength that is used. The reason for it is that, though while exciting with light of different wavelengths the electrons go to different excited energy levels, the vibrational relaxation makes that the fluorescence takes place from the lowest excited state S_1. And a similar explanation can be given to understand why the emission spectrum does not consist in a single peak: it is possible to go to a range of S_0 vibrational levels from the S_1 level.[2]

Considering the relaxation events (associated with energy losses) that occur before fluorescence emission, it is straightforward to realize that the emitted fluorescence photon is of lower energy and, thus, its emission wavelength is longer. Therefore, the peak of the emission spectrum is red shifted. This phenomenon in called Stokes shift (see **Figure 2**).[2]

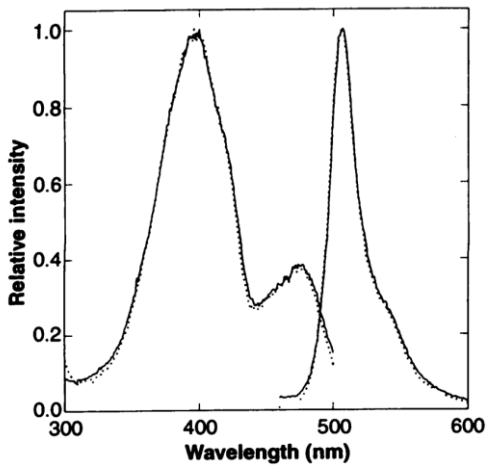

Figure 2. Excitation and emission spectra of the green fluorescent protein (GFP). E. coli-generated GFP (solid lines) and purified *A. victoria* L form GFP (dotted lines). The left spectrum corresponds to the excitation wavelengths, and the right spectrum corresponds to the emission wavelengths, which is red-shifted according to Stokes' shift. (Taken from Chalfie, M. et al., Science (1994)[4]).

There is a rate coefficient associated to each of these relaxation processes, derived from the fact that they are not equally probable. For example, the rate for the relaxation through fluorescence (i.e. by the emission of photons) is k_F, whereas the rate for a non-radiative decay is k_{nr}. Considering only these two possible decays are

the most probable, the depopulation of the excited state is described by differential equation:

$$\frac{d}{dt}N_1 = -k_F \cdot N_1 - k_{nr} \cdot N_1 \quad (2)$$

where N_1 is the number of molecules in the excited state S1. The solution of the equation is:

$$N_1(t) = N_1(0) \cdot e^{\left(\frac{-t}{\tau_F}\right)} \quad (3)$$

where $N_1(0)$ is the number of molecules that were initially in the S1 state, and τ_F is the fluorescence lifetime, given by the inverse sum of all radiative and non-radiative rates:

$$\tau_F = \frac{1}{k_F + k_{nr}} \quad (4)$$

Another important parameter in fluorescence microscopy is fluorescence intensity (I_F). It corresponds to the number of emitted photons, and is proportional to the excitation power (I_{in}), the absorption cross-section (σ) and a constant called quantum yield (ϕ).

$$I_F \sim I_{in}\sigma\phi \quad (5)$$

The absorption cross-section (σ) is a measure of the probability that a photon will be absorbed by the molecule. The quantum yield is the number of emitted photons relative to the number of absorbed photons, and it is characteristic of each fluorophore.

$$\phi_F = \frac{number\ of\ emitted\ photons}{number\ of\ absorbed\ photons} = \frac{k_F}{k_F + k_{nr}} \quad (6)$$

2.2. FAR-FIELD OPTICAL MICROSCOPY

When a beam of light is focused, the lens causes the light waves to undergo constructive interference at a point in space, creating an intensity pattern, $I(x, y, z)$, with a peak known as the point spread function (PSF). The diameter of this spot at the full width half maximum (FWHM) is approximately:

$$\Delta r \approx \lambda/(2n\ \sin\alpha) \quad (7)$$

in the focal plane, and:

$$\Delta z \approx \lambda/(n\, sin^2\alpha) \quad (8)$$

along the optical axis. λ is the wavelength of the light, α corresponds to the aperture angle of the lens, and n is the refractive index. Since all fluorescent emitters within this focal spot are illuminated, and therefore can emit light, simultaneously, distinguishing them individually becomes nearly impossible.[5]

Much of the research to overcome this limitation had initially focused on the so-called near-field scanning optical microscopy (NSOM), which detects non-propagating light waves from the sample surface with a nanosized aperture tip. However, this technique is limited to the visualization of the cell surface that is very close to the tip, and therefore research in biological sciences has continued to depend on developments in far-field optical microscopy.

Having the diffraction barrier in mind, numerous optical implementations aimed at increasing the contrast. Noise decreases the signal-to-noise ratio (SNR), effectively broadening the PSF, and consequently reducing the resolution. Two strategies, implemented in far-field optical microscopy, stand out for effectively reducing out-of-focus fluorescence, and thus noise: confocal fluorescence microscopy and total internal reflection fluorescence (TIRF) microscopy. Their contribution extends beyond contrast improvement, because they also laid the foundation for implementing some of the super-resolution microscopy techniques.

Confocal fluorescence employs a pinhole aperture at the confocal plane of the detector, which only allows light from the focal plane (or very close to it) to reach the detector. This spatial filtering significantly reduces the contribution of out-of-focus light, enhancing the axial resolution. When combined with point-wise excitation and detection with a scanning approach, the technique is called confocal laser scanning microscopy, and the overall detected intensity distribution is approximately the square of the excitation intensity distribution.[5]

$$I(x,y,z) \cdot I_{em}(x,y,z) \approx I^2(x,y,z) \quad (9)$$

being $I(x,y,z)$ the illumination intensity, and $I_{em}(x,y,z)$ the emitted intensity. This multiplicative effect arises because both the illumination and detection are confined to the same small region, enhancing the precision and clarity of the detected signal.

TIRF microscopy relies in a completely different physical mechanism, which is directly related to the refraction of light. When light propagating through a medium

of high-refracting index encounters an interface with a medium of lower refractive index, it is either reflected or refracted according to Snell's law:

$$n_1 \cdot \sin\theta_1 = n_2 \cdot \sin\theta_2 \tag{10}$$

where n_1 andn_2 are the refractive indices of the high- and low-refractive index media, respectively, and θ_1 and θ_2 are the angles of the incident and the refracted rays, respectively, both relative to the normal to the interface. When $n_1 > n_2$ and $\theta_1 > \theta_c$ (the critical angle), total internal reflection occurs in medium 1, as seen in **Figure 3**. The critical angle is given by this equation:

$$\theta_c = \sin^{-1}(n_2/n_1) \tag{11}$$

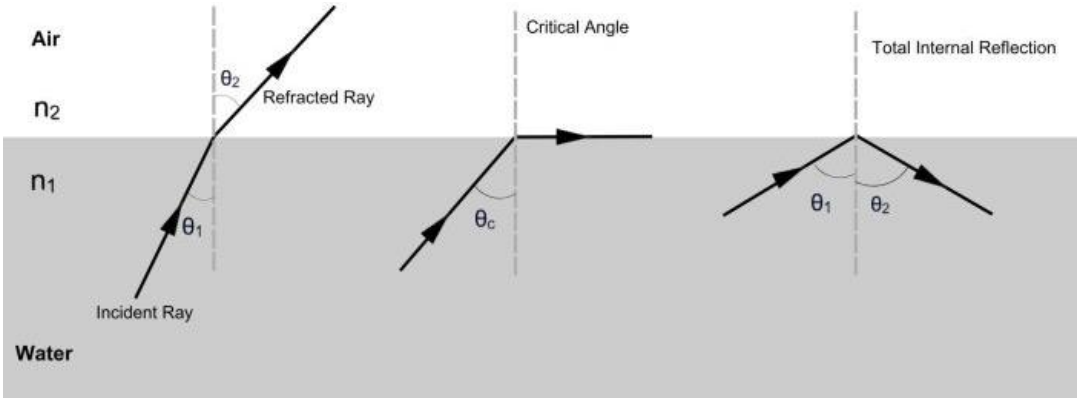

Figure 3. Schematic representation of the refraction of light at the interface between two media, including total internal reflection. (Taken from [6]).

However, some of the incident energy manages to penetrate through the interface, and propagates parallel to the surface in the plane of incidence. The created field, known as the "evanescent field", is capable of exciting fluorescent molecules that are located close to the interface between the two materials.[7] The intensity of this evanescent field decays exponentially with the distance z from the interface, as shown in this equation:

$$I(z) = I_0 \cdot e^{-z/d_p} \tag{12}$$

where d_p is the characteristic penetration depth (d_p), given by:

$$d_p = \frac{\lambda_0/n_1}{4\pi\sqrt{sin^2\theta - (\frac{n_1}{n_2})}} \tag{13}$$

where λ_0 is the wavelength of the incident light in vacuum, so before it enters the medium with refractive index n_1, n_2 is the refractive index of the medium into which the light is penetrating (water in this case), and θ is the angle of incidence of the light with respect to the normal to the interface between the two media.

TIRF manages to reduce the out-of-focus excitation, and in consequence the background, because the excitation of fluorophores far from the surface is strongly reduced. However, this also means that imaging is limited to the cell surface.

To bypass this inconvenience, another strategy was proposed: highly inclined and laminated optical sheet (HILO) illumination.[8] In this illumination scheme, the laser beam is displaced from the center of the objective so that it is refracted on the surface, similarly to TIRF. But in this case the critical angle is not reached. The inclination of the beam, creates a laminated sheet at the specimen side, that minimizes the illumination area.

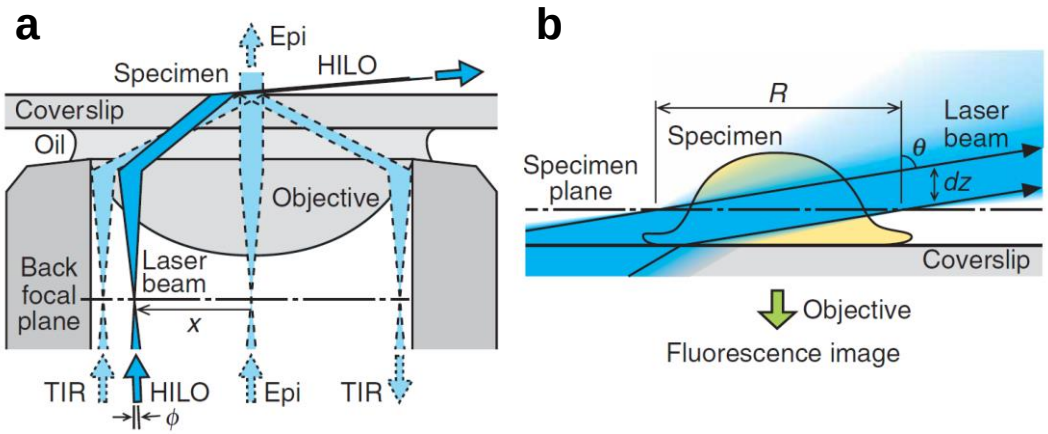

Figure 4. Highly Inclined and Laminated Optical sheet (HILO) microscopy. a. Positioning of the laser beam in HILO and Epi and TIR illumination. In HILO, the laser beam is slightly displaced (x) from the center of the objective, but not enough to TIR. **b.** Optical sheet going through a sample. dz is the thickness of the sheet, θ is the incidence angle, and R is the diameter of the illuminated area. (Taken from Tokunaga, M. et al., Nature Methods (2008)[8]).

The thickness of the sheet along the z-direction (dz) is given by:

$$dz = R / \tan\theta \tag{14}$$

where R is the diameter of the illuminated area, and θ is the incidence angle (see **Figure 4**). Another feature is that the illumination beam always passes through the center of the specimen plane, even when changing the position of the objective along the z-axis (i.e. when changing the focal plane).

3. SUPER-RESOLUTION FLUORESCENCE MICROSCOPY

The strategies explained above efficiently increase the SNR, however, they are still limited by the diffraction limit given by Abbe's equation. From the mid-late-20th century, several approaches aimed at overcoming the diffraction limit. The development of super-resolved fluorescence microscopy led Eric Betzig, Stefan W. Hell, and William E. Moerner to be awarded the Nobel Prize in Chemistry in 2014.

On the one hand, stimulated emission depletion (STED) microscopy achieved super-resolution by implementing scanning and reducing the focal spot size (further explained in the following section).[9] On the other hand, stochastic optical reconstruction microscopy (STORM)[10], and photoactivated localization microscopy (PALM)[11] simply used a time-sequential readout of the single fluorophore locations.

All of these microscopes rely on the same basic principle, some fluorophores stay on, while the surrounding ones remain off. This sequential activation (as for STORM and PALM) or depletion (as for STED) is very useful to increase spatial resolution, but inevitably limits the temporal resolution. Therefore, most of the biological research using these techniques is still performed on fixed cells, given that live-cell imaging with these methods can suffer from artifacts, reduced resolution, and phototoxicity, making it challenging to study fast or transient biological events effectively. However, while challenging, the use of super-resolution microscopy techniques for live-cell imaging is becoming more and more feasible, as we will show in this Thesis."

3.1. STIMULATED EMISSION DEPLETION MICROSCOPY

Stimulated emission depletion (STED) microscopy was proposed in 1994 by Stefan W. Hell.[9] The initial publication claimed a gain in the resolution by a factor of 4.5, but nowadays this factor is considered to be around 10 (from 200 nm to 20 nm spatial resolution).

STED is based on a conventional confocal laser scanning configuration, with an additional doughnut-shaped laser beam overlapped with the excitation one that depletes the fluorescence by transitioning excited fluorophores to the ground state via stimulated emission. This way, fluorophores within the rims of the STED laser doughnut will have a longer-wavelength fluorescence emission as compared to the central fluorophores, and therefore can be filtered out. Only the photons coming from a sub-diffraction spot on the center of the doughnut will reach the detector. Theoretically the spatial resolution is only limited by the intensity of the STED laser, the higher the intensity, the smaller the effective excitation area:[12]

$$d \approx \frac{\lambda}{NA\sqrt{1+\frac{I}{I_S}}} \tag{15}$$

where NA is the numerical aperture of the objective, I is the intensity of the STED depletion laser, and I_S is the saturation intensity (which accounts for the absorption cross-section and lifetime of the molecules).

However, instrument and dye limitations usually result on an x and y resolution higher than 20 nm (see **Figure 5**). It is to be highlighted, though, that the trade-off for a good spatial resolution in a scanning-based technique, is a decrease in the temporal resolution to the order of seconds. Moreover, the use of very high excitation and depletion laser powers enhances spatial resolution significantly but also introduces challenges like photobleaching and photodamage. The development of fluorescent molecules with superior photophysical properties, but also other innovations such as time-gated detection[13] have allowed to mitigate photodamage and photobleaching by reducing the needed average intensity.

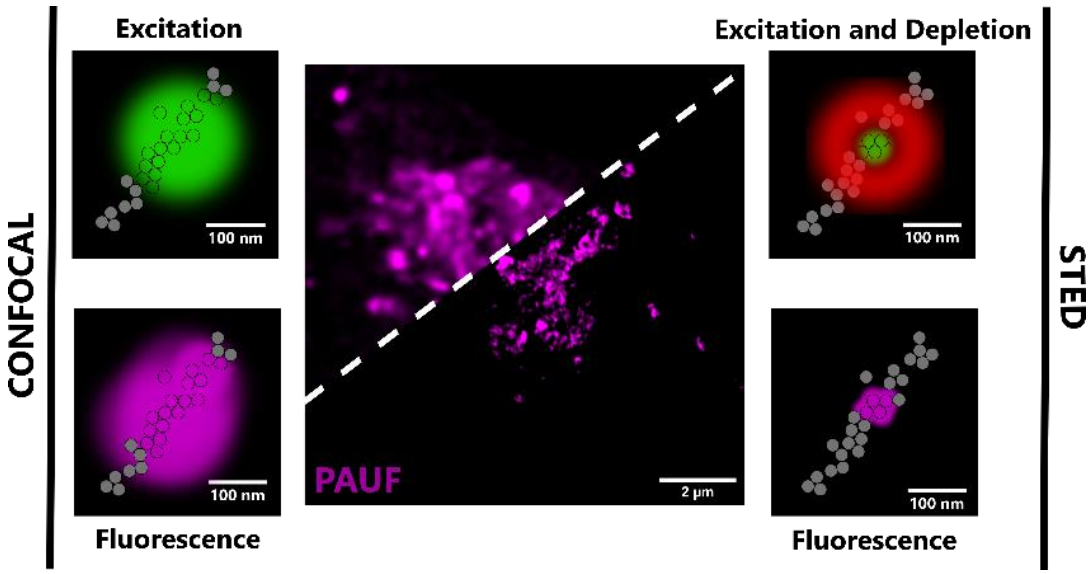

Figure 5. Comparison between the image acquisition in confocal laser scanning microscopy and STED microscopy. Grey spots represent non-emitting fluorescent molecules. The size of the fluorescent molecules is larger than reality for a proper representation. **Left:** Confocal laser scanning microscopy. Effective illuminated area (green) and resulting fluorescence (magenta). The effective PSF has a width of about 250 nm. **Right:** STED microscopy. Effective illuminated area (green) and resulting fluorescence (magenta). The doughnut-shaped depletion laser (red) reduces the effective excitation area to about 50 nm. **Middle:** Example image of PAUF protein within the Golgi apparatus. The top left corner shows the imaging performed with confocal laser scanning microscopy, and the lower right corner shows the imaging performed with STED microscopy.

Although initially applied on fixed cells using antibody labeling, the introduction of silicon-rhodamine (SiR), a far-red, cell permeable, and STED compatible organic fluorophore pushed STED nanoscopy to live-cell imaging.[14] Nowadays, there is a range of commercially available probes designed for multicolor live-cell STED imaging.[15] They are commercially available from Abberior GmbH and freely available for research uses from Howard Hughes Medical Institute (Janelia Fluor dyes). Moreover, these can be found conjugated to the ligands of the self-labeling tags Halo and SNAP. This strategy is key for intracellular labeling in live-cell imaging (further explained in **Section 6**).[16]

Since STED is implemented in a confocal configuration, is has 3D capabilities, allowing the visualization of internal cell compartments. Recent implementations allow to increase the resolution not only in the xy plane, but also in the z direction. This has been achieved by using a phase mask that creates a ring-shaped depletion profile, with two additional high-intensity lobes above and below the center of the ring.[17] The latest commercial STED setups, such as the INFINITY platform from Abberior, achieve an isotropic resolution better than 75 nm in all directions in the 3D mode. However, it is to be noted that given it is a scanning-based technique, a 3D image is obtained by sequentially stacking thin 2D planes, which again compromises the temporal resolution.

4. FLUORESCENCE MICROSCOPY FOR THE STUDY OF PROTEIN DYNAMICS

Fluorescence microscopy has been crucial not just for obtaining high-resolution images, but also for advancing a significant area of biophysics research interested in the dynamics of molecules within cells. The ability to visualize and distinguish individual molecules in the native environment of living cells provides a more quantitative and precise understanding of the spatiotemporal dynamics that govern cellular functions.

One of these techniques is fluorescence recovery after photobleaching (FRAP), used from the 1970s, which measures the rate of recovery of fluorescence after photobleaching a uniformly distribution of fluorescent molecules.[18–20] The velocity at which the surrounding fluorescent molecules re-populate the bleached spot is directly proportional to their diffusion coefficient and the instantaneous velocity. It has led to multiple contributions on the understanding of protein and lipid dynamics, organelle communication and directionality of intracellular trafficking

pathways.[21] Its main limitation, though, is that it only provides information about the ensemble dynamics of the molecules.

Fluorescence correlation spectroscopy (FCS) is also widely used to investigate the mobility, interactions, aggregation and polymerization of molecules. Broadly, FCS analyzes the fluctuations of the fluorescence intensity when the fluorescent molecules diffuse through a small illumination volume. The autocorrelation function of the fluorescence fluctuations allows to extract the mean dwell time of the molecules, that is directly linked to the diffusion coefficient.[22] However, this technique is still limited by diffraction. It is to be noted though, that the combination of FCS with NSOM or STED microscopy has allowed to use excitation volumes smaller than the diffraction limit.[23,24]

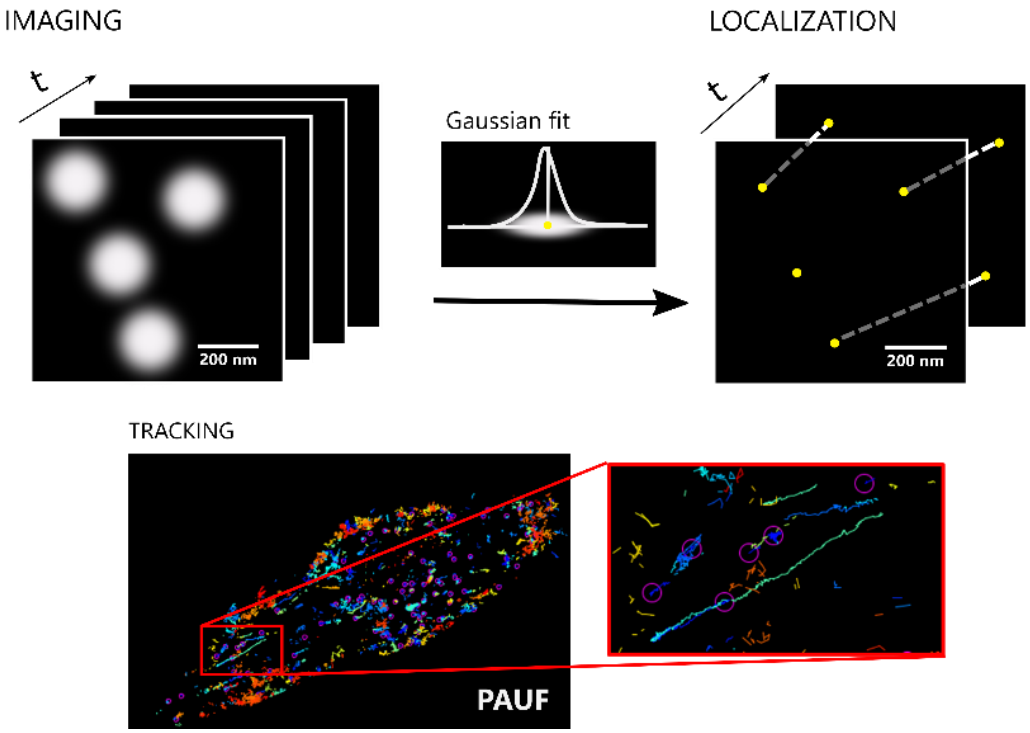

Figure 6. Single particle tracking. Top left: Images of sparsely distributed, diffraction-limited spots are taken over time. **Top right:** The center of mass is determined commonly by Gaussian fitting. **Bottom:** The spots are connected in a frame-to-frame basis to reconstruct the trajectories (colored lines).

A different technique that has been extensively used for the study of individual molecular dynamics within cells is single particle tracking (SPT). It relies on the spatial isolation of the individual fluorophores, usually by sub-labeling of the molecule of interest with lower concentrations of the fluorescent probe. Although this technique

does not physically overcome the barrier of the diffraction limit, the sparse distribution of the emitters allows the determination of the centroid position of the PSF, commonly by fitting Gaussian functions. Therefore, the positional precision of this technique is far beyond the resolution limit – typically between 20 to 50 nm –, mainly depending on the SNR of each spot. After spot detection and centroid position determination, localizations obtained over time are linked in a frame-to-frame basis (see **Figure 6**).[25] The temporal resolution is also in the order of tens of ms, basically limited by the integration time of the camera, and the brightness of the fluorophore, since the brighter the fluorophore the shorter it is necessary to integrate the signal and achieve the desired localization precision.

A recent development worth noting combines the principles of STED microscopy and single particle tracking. Minimal photon fluxes (MINFLUX) microscopy localizes photon emitters in space by probing the emitter with doughnut-shaped excitation beam, with a central intensity minimum. Since the fluorescence intensity drops to 0 at the exact molecular position, it is possible to very precisely localize it. The initial publication reported a ~1 nm localization precision, and 6 nm spatial resolution, with 22 times fewer photons than for centroid localization.[26] MINFLUX has been recently used to observe the movement of the molecular motor kinesin-1 on microtubules, and it was possible to discern up to 1.7 nm displacements with 1 ms time resolution.[27] The same protein was also tracked within living cells, and in 3D.[28] This technique, thus, outperforms traditional centroid fitting. However, using a single doughnut-shaped excitation beam to follow the movement of a molecule has an obvious drawback: the low throughput. Until new implementations are developed, it is hard to believe that MINFLUX will replace classical SPT, which is valued for its simplicity, ease of implementation, and high throughput.

4.1. SINGLE PARTICLE TRACKING

SPT was first presented as "nanovid microscopy", which consisted on the tracking of 40 nm size gold nanoparticles on the surface of living cells.[29,30] Rapidly, this method allowed milestones such as the tracking of kinesin along microtubules[31] or glycoproteins on cell membranes.[32] Due to this technique´s straightforward implementation, many research groups worldwide focused on developing algorithms for reconstructing trajectories and analyzing diffusion in two- and three-dimensional systems.

Nowadays, this technique is performed using fluorescent reporters, that are excited using a laser beam. The emitted fluorescence is filtered out from the excitation light

and detected using a camera detector with high quantum yield and fast frame transfer, such as electron-multiplied charge couple device (EMCCD) cameras. A high NA objective (higher than 1.2) collect the largest possible number of emitted of photons. Moreover, TIRF illumination is commonly used to reduce the out-of-focus fluorescence and increase the SNR. The same illumination scheme usually allows the displacement of the laser beam to achieve HILO, and therefore illuminate higher planes inside the cell. Alternatively, light sheet illumination can be used to provide a better optical sectioning.[25]

As highlighted before, the performance of SPT is closely linked to the performance of the fluorescent reporters. Brightness and photobleaching rate determine the localization precision and the tracking time, respectively. When using fluorescent dyes attached to antibodies, or fluorescent proteins encoded within the protein of study, the localization precision is restricted to around 20 to 50 nm, and the number of photons before photobleaching is in the order of 10^5 to 10^6.[25] General strategies to improve these two parameters are the addition of multiple fluorescent molecules to a single antibody, or the conjugation of quantum dots to antibodies, semiconductor nanocrystals that have superior photostability and brightness.[33] However, all these tools require the use of antibodies, which cannot cross living cells' membrane, and therefore limit the study to membrane molecules, and from the extracellular side. Luckily, this technique is also benefiting from the continuous development of fluorescent organic dyes compatible with in super-resolution microscopy. As mentioned before, it is possible to find commercial organic dyes of a wide range of absorption and emission spectra, which can be conjugated to the Halo or SNAP ligands.[15,16]

SPT also requires the sparse distribution of fluorescent molecules for the proper fitting of the centroid position. This is usually achieved by labeling a small subset of the molecules, also referred to as sub-labeling conditions, with nano molar concentrations of dye, or by waiting for the photobleaching of most of the fluorescent molecules (either fluorescent dyes or expressed fluorescent proteins). A different approach that combined PALM with SPT, named sptPALM, was presented in 2008 by Manley et al. The sequential photoactivation of the fluorescent protein EosFP allowed to track the proteins VSV-G and HIV-1 Gag on the plasma membrane. Though each trajectory was lasting around 1 second, the sequential photoactivation of the fluorescent protein allowed to harvest many more trajectories, and to even reconstruct a spatial map of diffusion coefficients.[34] These fluorescent proteins are

nowadays being replaced by the photoactivatable versions of the JF dyes, that as we mentioned before can be synthesized as Halo and SNAP ligands.[16,35]

Finally, it is worth mentioning the many efforts that have been devoted to track molecules in 3D, which can be especially important for intracellular dynamics. The initial methods used confocal set ups and stacked multiple z-planes.[36] However, temporal resolution was a drawback. Keeping the simplicity of wide-field illumination, combined with TIRF, HILO or light sheet illumination, PSF engineering approaches managed to achieve higher temporal resolution. A cylindrical lens generates axial astigmatism in the collected image, and therefore the 3D information is encoded in the detected PSF shape. However, these approaches are complex in terms of both optical implementations and algorithms to analyze the 3D trajectories. Another method, developed by Sims et al., named single molecule light field microscopy, segments the back focal plane with microlenses to capture multiple 2D views of the same fluorophore, enabling precise 3D localization through parallax and a fitting algorithm. This technique achieves up to 20 nm precision over a 6 μm depth and improves imaging speed and density, demonstrated in whole-cell imaging and high-density volumetric datasets.[37,38]

4.2. QUANTIFICATION OF SINGLE MOLECULE MOTION

As already mentioned, studying the motion patterns of molecules within cells is of high interest in biophysics, since they are a read-out of the medium properties in which they move, and report on interactions of this molecule with the system. The motion of molecules has been long studied as random walks, a mathematical model characterized by an erratic change of position over time.[39,40] The space explored by a random walker over time can be measured by the mean squared displacement (MSD), which describes the average extent of space explored by a particle as a function of time.

$$MSD(\mathrm{t}) = \frac{1}{N-m}\sum_{i=1}^{N-m}[x_j(t_i + m\Delta t) - x_j(t_i)]^2 \qquad (16)$$

where x_j is the position of the j-th particle at time t_i.[25,41]

The MSD grows linearly for Brownian walkers, and can be calculated as the variance of the diffusion equation:

$$MSD(t) = 2dD\mathrm{t} \qquad (17)$$

where d is the dimensionality of the space, and D is the diffusion coefficient.[25,41]

Deviations from such linear behavior have been experimentally observed and referred to as anomalous diffusion. It is described by a power-law with an exponent called anomalous exponent or alpha coefficient (α): with $0 < \alpha < 1$ for subdiffusion, $\alpha = 1$ for Brownian motion, and $\alpha > 1$ for superdiffusion.

$$MSD(t) = 2dKt^{\alpha} \tag{18}$$

where K is the generalized diffusion constant.[25,41]

Calculating the diffusion coefficient (or the generalized diffusion constant) and the anomalous exponent is key to characterizing the motion of molecules. An approximation in order to get the diffusion properties of single trajectories assumes that the ensemble-averaged MSD and the time-averaged MSD (TA-MSD) are equivalent, and therefore can use the information contained within a single trajectory to fit alpha and the diffusion coefficient.

$$TA - MSD\left(t_{lag} = m\Delta t\right) = \frac{1}{N-m}\sum_{i=1}^{N-m}[x_j(t_i + m\Delta t) - x_j(t_i)]^2 \tag{19}$$

where x_j is the position of the j-th particle at time t_i or $(t_i + m\Delta t)$, and t_{lag} is the interval over which the displacement is measured. It is defined as $t_{lag} = m\Delta t$, where m is an integer multiple of the time step Δt.[25,41]

And the diffusion coefficient and alpha exponent can still be extracted with:

$$MSD\left(t_{lag}\right) = 2dK{t_{lag}}^{\alpha} \tag{20}$$

Fitting these two parameters with the MSD equation seems a feasible task. However, there are some associated difficulties:[42]

(i) Finite statistics within a single trajectory. To perform accurate fitting, it is necessary to have a significant number of datapoints. The time-averaging performed for each single trajectory, establishes a direct link between quality of the fitting and trajectory length.

(ii) Localization error or precision. The position of the fluorophore at each time point is determined by fitting the observed point spread function (PSF) to a model. The accuracy of this position is quantified by the localization error, which is given by the standard deviation of the fitted positions. This standard deviation reflects the precision of the measurement, indicating how much the determined position of the fluorophore varies around the true position due to factors like noise and fitting accuracy. The standard deviation scales with the inverse square root of the number

of detected photons. The localization error sets a minimum diffusion coefficient that the system is able to distinguish.

(iii) Dynamic localization error. Each acquisition is taken while the molecule is moving, and therefore it is only possible to measure a temporal mean position. This introduces a negative bias to the position.

(iv) Non-ergodic processes. Ergodicity breaking refers to the non-equivalence of time-averaged properties of a single particle's trajectory, and ensemble-averaged properties of many particles in the same system. This discrepancy arises due to various reasons, such as heterogeneous dynamics, energy barriers, or long-term correlations in the particle's movement. In non-ergodic systems, the TA-MSD can exhibit a linear behavior in the long-time limit, even when α is not equal to 1.[43]

(v) Heterogeneity in the diffusion behavior. It is possible that the tracked molecule changes its diffusion behavior during the image acquisition, as a result of transient changes in the interaction of the molecule with its environment. This can lead to changes in the diffusion coefficient, in the anomalous exponent, in both, or even in the underlying diffusion model (explained below). Therefore, averaging over the whole trajectory can lead to completely wrong estimates.

Moreover, anomalous diffusion can arise due to multiple reasons. Indeed, deviation from Brownian motion can be given by multiple different types of interactions with the system. Depending on the underlying physical mechanism, the calculation of the MSD might not be very informative because very different diffusion models can lead to similar curves (see **Figure 7**). Some examples of diffusion models are: *(i)* continuous time random walks (CTRW), in which the timing and magnitude of each step are governed by probability distributions. *(ii)* fractional Brownian motion (FBM), which extends classical Brownian motion by allowing for long-range dependence or memory in the increments (such as displacements) of the process. Large displacements or changes in position tend to be followed by smaller displacements, and vice versa. *(iii)* Lévy walks (LW), which are characterized by intermittent long steps interspersed with short steps or periods of rest. *(iv)* annealed transient time motion (ATTM), in which the movement properties change over time. The changes in speed and the time that the particle spends moving at each speed follow certain probability distribution.[41,43]

Therefore, there are other parameters, different from the diffusion coefficient and the anomalous diffusion exponent, that can provide with complementary

information, and therefore help to interpret the underlaying physical mechanism. These include:

(i) the instantaneous velocity, as the frame-by-frame displacement multiplied by the frame time.

(ii) the instantaneous diffusion coefficient ($D_{1\text{-}4}$), calculated from the TA-MSD, but the linear fit is computed using the first four time lags. It is a measure of the diffusion at short time scales.

(iii) the diffusion radius, calculated as the mean distance to the mean centroid position of the trajectory.

(iv) the angle distribution, obtained by the calculation of the angle formed by triplets of consecutive time points. It is a measure of confinement, since confined molecules have a tendency to jump back, and therefore the distribution of angles is shifted to 180°.

(v) transient confinement zones detection, performed with temporal sliding windows that calculate the probability to be within a certain region of given radius over time. Confinement within a trajectory is detected when the particle is within this region longer than a random diffusant would stay.[44,45]

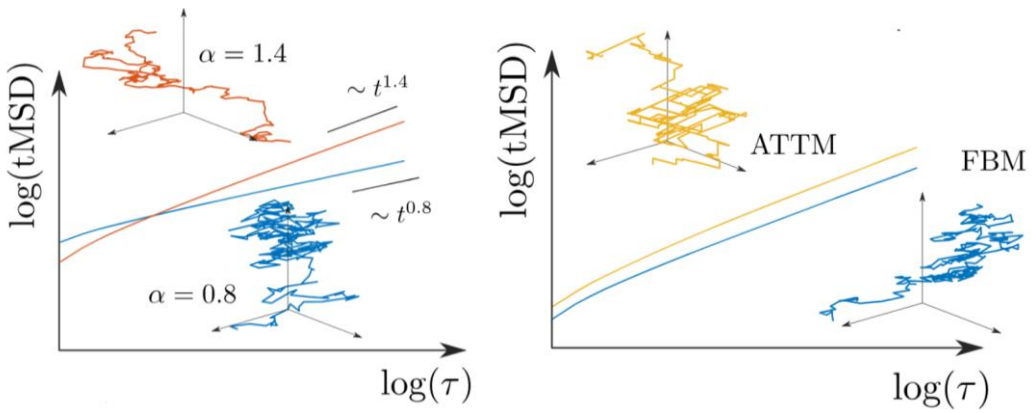

Figure 7. TA-MSD of trajectories with different diffusion model. TA-MSD calculated from single trajectories. In the left panel, one can observe two trajectories corresponding to molecules that display different anomalous exponents (α), despite belonging to the same underlying diffusion model. In the right panel, the anomalous exponent is the same despite having two different diffusion models (ATTM and FBM). (Taken from G. Muñoz-Gil et al., *New Journal of Physics* (2020)[46]).

However, a better characterization could be done, if it would be possible to identify the underlying physical model that describes the molecule's motion. In 2020, the anomalous diffusion (AnDi) challenge aimed at finding the best algorithm for: *(i)* the

prediction of the α exponent, *(ii)* classification of the underlying diffusion model, and *(iii)* trajectory segmentation (see **Figure 8**). After the submission by 13 participating teams, which used either classical statistics or machine learning methods, the authors compared the obtained results. Although there was no method that outperformed in all tasks, machine learning approaches provided the best results overall.[40]

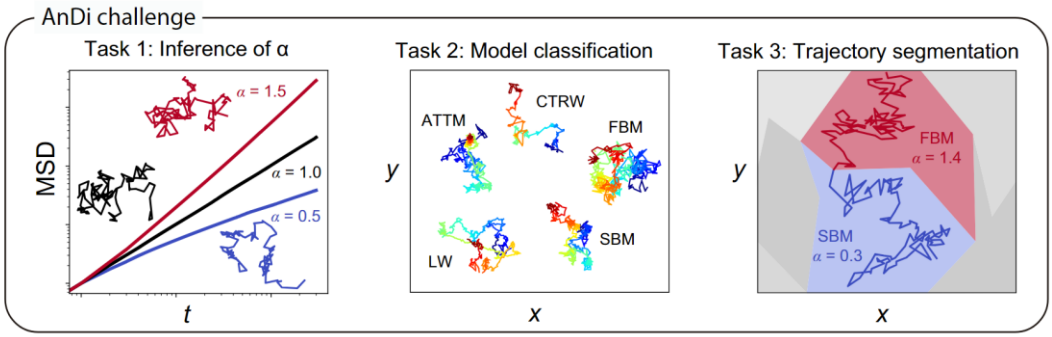

Figure 8. 1st AnDi challenge tasks and datasets. Task 1 – Inference of the anomalous diffusion exponent. Representative trajectories and corresponding MSD for diffusive (α = 1, blacklines), subdiffusive (0 < α < 1, blue lines), and superdiffusive (1 < α < 2, red lines) motion. **Task 2 –** Classification of the underlying anomalous diffusion model. Representative trajectories for a continuous-time random walk (CTRW), fractional Brownian motion (FBM), Lévy walk (LW), annealed transient time motion (ATTM), and scaled Brownian motion (SBM). Different diffusion models produce subtle changes. **Task 3 –** Segmentation and characterization of a trajectory with changepoint. Trajectory switching diffusion model and/or exponent as a result of diffusion in a spatially heterogeneous environment, represented by the colored patches. (Taken from G. Muñoz-Gil et al. Nature Communications (2021)[40]).

The algorithm that best identified the alpha coefficient in 2D trajectories was the one presented by A. Gentili and G. Volpe, which combined feature engineering based on classical statistics with supervised deep learning.[47] The best algorithm for the classification of the underlying diffusion model, presented by A. Argun, G. Volpe and S. Bo, used machine learning, and was based on recurrent neural networks.[48]

The trajectory segmentation proved to be the most challenging task in the AnDi challenge, even in minimalistic setting with a single change point. Indeed, characterizing trajectories with time-dependent diffusive properties remains an open research question, which has motivated the organization of a second AnDi challenge. This new challenge, that has just been launched, not only aims to distinguish changepoints in the diffusion model (as in the first AnDi challenge), but also changes in the diffusion coefficient and the anomalous diffusion exponent.[49] It also aims at identifying multiple of these changepoints, as compared with the first

challenge, in which a maximum of one changepoint was introduced in the simulated data.

It is precisely from these changes in diffusive properties that we can extract the most meaningful information about the different interactions in our systems. While we still need to wait to see the results of these 2nd AnDi challenge, this thesis uses one of the algorithms that is participating: STEP, presented by B. Requena et al.[50] The reason of this choice is essentially given by the short length of the trajectories and the ambition to extract the most meaningful quantitative information from the data. Indeed, STEP is a machine learning method able to predict the diffusion coefficient and the anomalous diffusion exponent, at each time step of the input trajectory. It is shown that STEP outperforms TA-MSD in the prediction of both parameters for short trajectories. Finally, an interesting feature is that the pointwise prediction of the diffusion coefficient and the anomalous exponent can be used for the identification of changepoints within the same trajectory (see **Figure 9**).

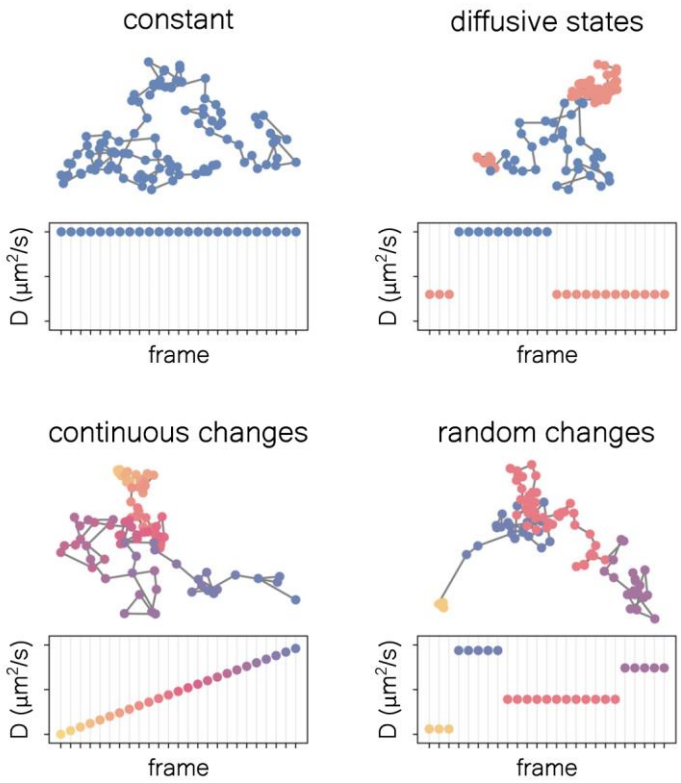

Figure 9. STEP's ability to detect changes in the diffusion coefficient. Examples of trajectories and the corresponding diffusion coefficient D as a function of time for constant D, changes within a discrete set of states with fixed D, continuous and monotonous change of D, and switch between random Ds. (Taken from B. Requena et al., Biophysical Journal (2023)[50]).

The authors of the publication evaluated STEP's performance on simulated trajectories of different underlaying diffusion models, and show that it is indeed able to predict the diffusion coefficient with very small error (see **Figure 10A**). However, this error changes with the trajectory length, given that, despite its point-wise output, STEP still needs the surrounding displacements to make accurate predictions. In **Figure 10B** we can see the comparison in mean relative error ($|D_{true} - D_{pred}|/D_{true}$) between STEP and classical TA-MSD. It is to be noted that, given that the trajectories had changes in the diffusion coefficient, the MSD could only be calculated for the already separated fragments (referred to "TA-MSD + segments"). Otherwise, the TA-MSD would yield an effective parameter for the whole trajectory that would not represent the actual phenomena, which already justifies the use of STEP. One can appreciate that STEP's prediction ("STEP", blue) on very short trajectories has similar results that TA-MSD on already splitted trajectories ("TA-MSD + segments", yellow), with a slightly higher error on STEP's prediction. However, for trajectories with uniform diffusion properties, a fairer comparison can be done between the "STEP + segments" (orange) and the "TA-MSD + segments" (yellow). For those uniform trajectories, we can see that those smaller of about 50 frames are better predicted with STEP. For longer trajectories with uniform diffusion coefficient, TA-MSD is a more suitable method. Nevertheless, the probability of observing diffusion changes in these longer trajectories is higher, and TA-MSD would lead to wrong estimations of the diffusive properties. Therefore, it is better to use STEP overall, given its better performance in short trajectories that are unlikely to present changes, and its flexibility to study longer trajectories with multiple changes.

Regarding the alpha coefficient, **Figure 10C** highlights some discrepancies between the true and predicted values. This should be taken into account when studying diffusion processes where directed motion plays a key role. As for the mean absolute error, calculated as $|\alpha_{true} - \alpha_{pred}|$, STEP outperforms TA-MSD in all segment lengths, independently of whether the trajectory has uniform diffusion properties or not (see **Figure 10D**). It also shows a comparable performance to CONDOR, the deep learning algorithm that, as already mentioned, best-performed in the 1st AnDi challenge.[47] For short trajectories smaller than about 25 frames, STEP still gave slightly better predictions.

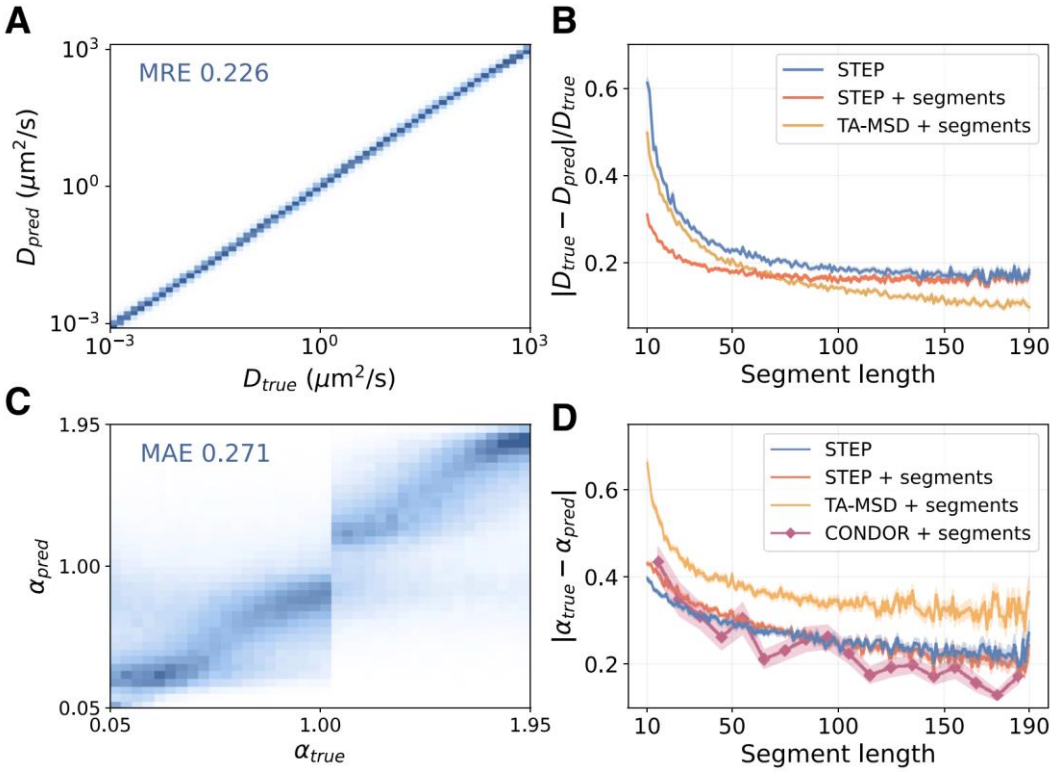

Figure 10. Time-dependent diffusion properties prediction. (Taken from B. Requena et al., Biophysical Journal (2023)[50]). **A.** 2D histogram of the predicted diffusion coefficient D compared to the ground truth. The mean relative error (MRE) over the whole test set is 0.226. **B.** Relative error for the prediction of D as a function of the segment length. **(C)** 2D histogram of the predicted anomalous diffusion exponent (α) as compared to the ground truth. The MAE over the whole test set is 0.271. **(D**) MAE for the prediction of a as function of the segment length.

5. IMAGE ANALYSIS

The rise of new microscopy techniques that enable the visualization of cellular structures with increasingly higher spatial and temporal resolution has triggered a boost on image analysis algorithms. Image analysis consists in the extraction of meaningful quantitative information from images. In order to properly interpret the extracted data, it is necessary to understand where does the information come from and how images are treated by the different software.

In image analysis, the different tasks can usually be classified as: *(i)* object detection, *(ii)* classification, *(iii)* segmentation, and *(iv)* tracking. However, image analysis usually requires previous image processing, which involves changing the image in ways that will help the later extraction of quantitative information.[51]

5.1. IMAGE PROCESSING

Image processing involves tasks aimed at cleaning up the image, such as subtracting background signal or applying filters to reduce noise. Although it is beyond the scope of this thesis to review all types of operations that can be performed, we highlight some that we find particularly important for this thesis:

(i) Point operations. They are mathematical operations applied to individual pixel values. Point operations can be performed using a single image, an image and a constant, or two images of the same size. An example can be image inversion, which involves reversing the intensity values; making the higher values lower, and the lower values higher. Another example is contrast enhancement, in which the intensity ranges are adjusted to make the features more distinguishable. Binarization can also be considered a point operation, since certain selected values are set to zero, whereas the others are set to 1.[51]

(ii) Filtering with filter kernels. Filtering can make segmentation much easier by enhancing features and reducing noise. It basically consists in the modification of a pixel intensity values according to the neighboring pixels. To do so, it makes use of filter kernels or convolution masks, which are small matrix arrays that slide over an image, and at each position, the pixel values are multiplied by the kernel values. An example are mean filters, that replace the pixel value by the mean of the defined area. Another very important one is Gaussian filter. The Gaussian function is characterized by its bell-shaped curve, which ensures that pixels near the center of the filter have higher weights than those farther away. This results in a gentle blurring effect (see **Figure 11**). Two variants of the Gaussian filter, that are used for edge detection and feature extraction are:

(i) *Difference of Gaussians (DoG) filtering*. It is based on the principle of subtracting two Gaussian-blurred versions of an image, each with a different standard deviation (σ). We are left with an image that contains the information between the two smoothing scales. This highlights the areas of the image where there are rapid changes in intensity, effectively identifying edges and other important features.[51,52]

(ii) *Laplacian of Gaussian (LoG) filtering*. It combines a Gaussian filter with a Laplacian operator, which is a second-order derivative operator that highlights regions of rapid intensity change (edges).[51,52] The appearance

of a LoG filter is like an upside-down DoG filter, and leads to comparable results.

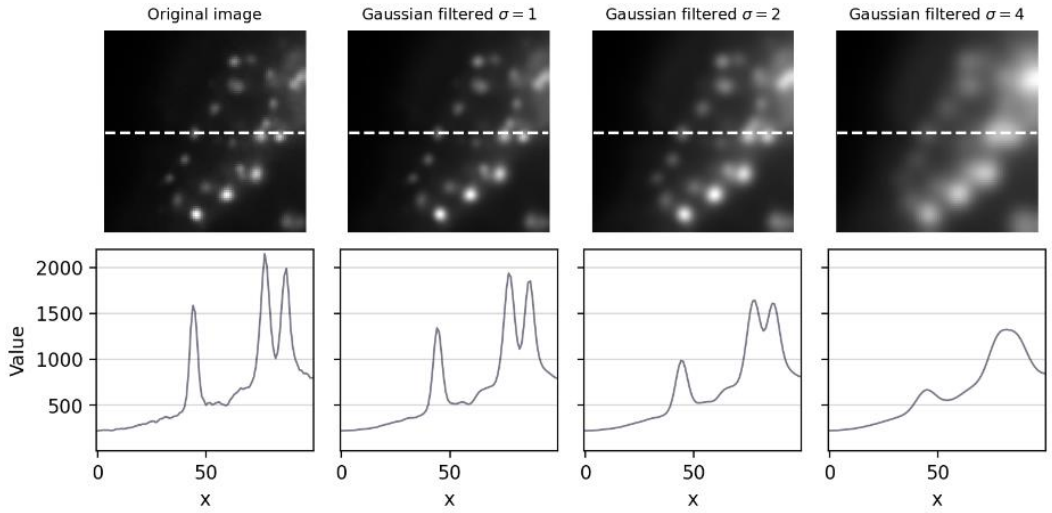

Figure 11. Gaussian filtering. An example of smoothing with Gaussian filters of different size. The lower images show the intensity distribution over the line drawn on the top images. (Taken from [51]).

(iii) Morphological transformations. They are used to modify the shapes of features in images. Many are used on binary images to improve image segmentation. They apply a structuring element (i.e. a kernel) to the input image. Some important ones are:

(i) *Erosion and dilation*. Erosion operation reduces the boundaries of regions of foreground pixels (typically white), reducing the size of objects and eliminating small noise. On the contrary, dilation expands the boundaries of the foreground objects in an image. This operation is particularly useful for connecting disjoint objects, filling small holes, and enhancing specific features in the image.[51,52]

(ii) *Opening and closing*. Opening consists of an erosion followed by a dilation, shrinking the object first, to then expand it again to its approximately original size. It can be useful to separate very close neighboring structures. Closing does this process the other way around. It can serve to connect closely placed neighboring structures.[51,52]

(iii) *Watershed*. It treats the greyscale image as a topographic surface. If we imaging water flowing through this landscape, local minima are

gathered, drawing lines that represent the boundaries between different objects.[52,53]

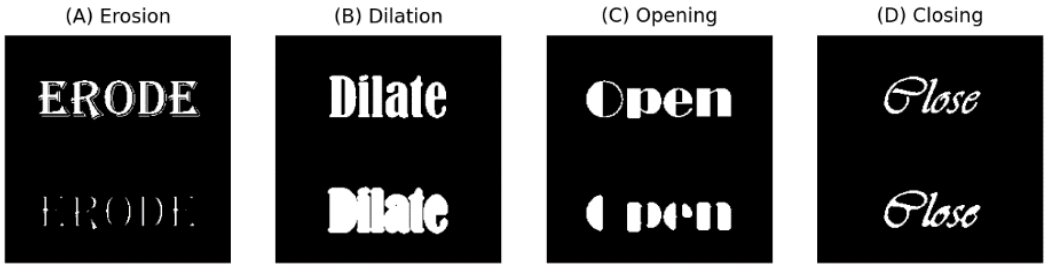

Figure 12. Overview of erosion, dilation, opening and closing. The original image is show on top, whereas the processed image is below. (Taken from [51]).

(iii) Deconvolution. Given diffraction, an image obtained with an optical system is convolved with the PSF, which results in blurring and distortion. Therefore, when one has a good understanding of the optics and noise, it is possible to try to reverse blurring to a certain extent by performing image deconvolution.[52] Classical approaches, such as Richardson-Lucy deconvolution, require knowledge of the PSF of the microscope, and assume Poisson noise statistics.[54] Otherwise, a theoretical PSF, based on known microscopic parameters can also be used. Nowadays, new deep-learning algorithms, that do not require a previous characterization of the PSF, are being developped.[55]

5.2. OBJECT DETECTION AND CLASSIFICATION

The purpose of object detection is identifying and localizing specific objects within an image. Object detection algorithms typically operate by scanning the image with a bounding box or region proposal mechanism to identify potential object locations. Classification is performed simultaneously.

Robust results, appropriate for real world applications, are mainly being given by deep learning algorithms.[56] A recent contribution of deep learning to this field, related to microscopy images, is the development of the so-called artificial labeling. Based on the information of other microscopy images, it is possible to recognize the different cellular structures, and therefore label them differently. This approach is very attractive since it avoids chemical labeling in live imaging.[57,58]

5.3. SEGMENTATION

Segmentation involves separating parts of an image to facilitate further analysis. Therefore, whereas in object detection some type of object is identified, in

segmentation it is the pixels of an image which are classified. Two of the simplest methods are:

(i) Thresholding. It converts a greyscale image into a binary image, separating image regions of interest based on the pixel intensity.[51] This threshold that determines the selected regions can be manually selected, or automatically selected following some criteria. For instance, Otsu's method minimizes intra-class intensity variance, and performs well identifying objects of two different intensities, so when the intensity histogram has a bimodal distribution.[59]

(ii) Local-maxima. It identifies and isolates objects based on local intensity peaks.[51] It can be possible to identify whole objects once the image has been pre-processed and this operation is applied on a binary image.

In the context of cellular biology, developments in cell segmentation are continuously being made. The cell tracking challenge has been following the developments of cell segmentation, and they claim that that machine learning-based algorithms outperform traditional algorithms. One should refer to this publication to find the latest algorithm that best suits the specific application.[60]

A simpler task is the segmentation of diffracted limited spots, such as those coming from single molecules. Therefore, it is usually performed with the two segmentation methods described above. According to the single particle tracking challenge, all participating methods included a series of pre-processing steps to reduce noise, and enhance objects using median, wavelet-based, Gaussian, LoG, watershed, or other filters. Then, spots are segmented using local-maxima or thresholding. Finally, the center coordinates of these spots are found using Gaussian fitting or intensity-based centroid calculation.[61]

5.4. TRACKING

Tracking refers to the process of following objects or features over a sequence of images or frames. The simplest approach is nearest-neighbors, that links the closest pairs of objects, usually based on the Euclidean distance. However, some limitations arise in crowded scenarios, when the object moves significantly between frames, when they temporary overlap, or when they split or fuse.

According to the single particle tracking challenge, the best-in-class algorithms used multiframe and multitrack optimization.[52,61] It can be highlighted the use of Kalman filtering, which uses a predictive model to estimate the object's position and velocity, updating with each frame to correct it (see **Figure 12**).[62,63]

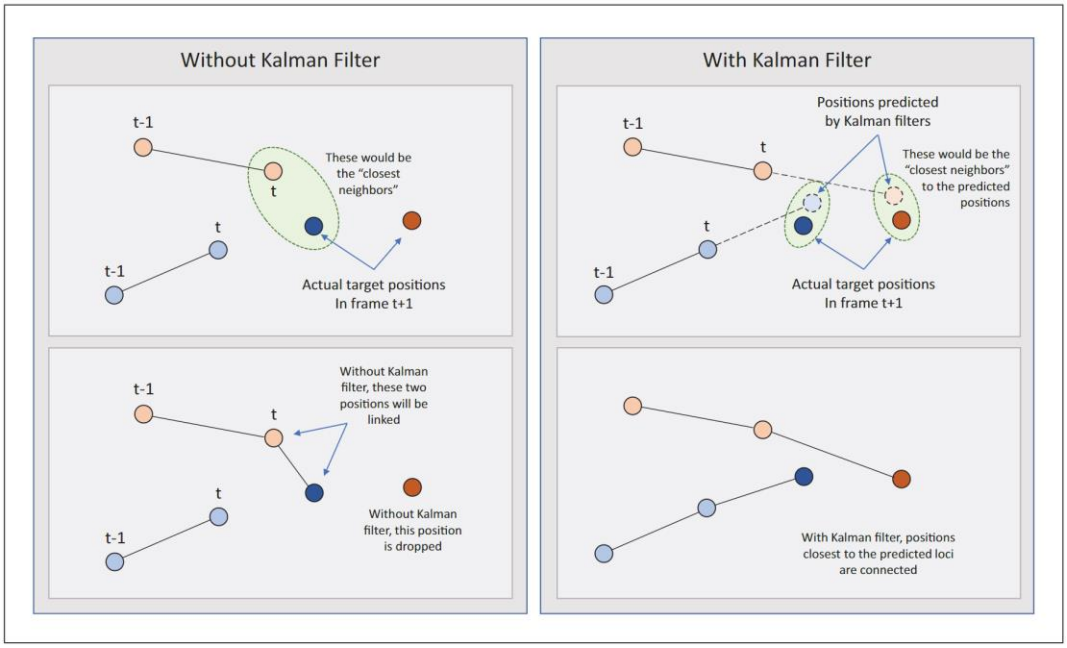

Figure 12. Kalman filter. Left panel. Linking without using a Kalman approach. Two nascent particle tracks are shown in light orange and light blue. The light orange particle at time *t* is linked to the dark blue particle at time *t+1*. The light orange track is not linked. **Right panel.** Linking with the Kalman approach. The predicted changes in position of the light orange and the light blue are found from time *t* to *t+1*. These predicted positions are then compared to the actual particle positions at *t+1*. This way, position linking proceeds by extending both the orange and the blue trajectories, on the basis of their prior behavior. (Taken from J. Aaron et al. (2019)[52]).

The cell tracking challenge, which is a more recent publication, and in which more machine learning approaches participated, did not find remarkable differences in the performance of machine learning-based and traditional linking techniques.[60]

6. BIOLOGICAL TOOLS

6.1. FLUORESCENT LABELING

There are two types of fluorescent molecules that are mostly used in cell biology: *(i)* organic dyes and *(ii)* fluorescent proteins. The first consist on chemical species that can be synthesized in the lab, and have fluorescent properties. Many times, changing the chemical structure can improve the fluorescent properties. As for the fluorescent proteins, they were discovered as natural proteins in living organisms. The first one was the green fluorescent protein (GFP), discovered in *A. victoria*, a bioluminescent jellyfish, and led to the Nobel Prize in Chemistry in 2008. The discovery of new fluorescent proteins, and their multiple modifications has led to a plethora of

variants with different excitation and emission spectra, quantum yields and photostabilities.[64]

There are multiple strategies to target these fluorescent molecules to our protein of interest. The two classical labeling strategies are:

(i) Antibody labeling. Antibodies are proteins able to very specifically recognize other molecules, especially other proteins. The organic dyes are covalently attached to antibodies through distinct chemical groups. Many times, a so-called primary antibody is used to recognize the protein of interest. These antibodies are produced by immunization of an animal (such as sheep, goats, mouses, or donkeys) with such proteins, and the produced antibodies are extracted from the animal and purified. A so-called secondary antibody is usually the one that is attached to the fluorescent molecule. These antibodies can recognize any antibody of certain animal. For this reason, in this thesis, we refer to mouse anti-sheep for a secondary antibody produced by a mouse, that is able to recognize sheep antibodies. This sequential labeling avoids to self-label each of the primary antibodies, and any store-bought secondary antibody with different fluorescent dyes can be used for all primary. It is to be noted that antibodies are not cell permeable, and therefore it is necessary to fix and permeabilize membranes for intracellular labeling.

(ii) Fluorescent tagging. The cells need to be genetically modified to express the protein of interest fused to the fluorescent protein of choice. There are multiple strategies to do so in mammalian cells. In this Thesis, gene transient transfection was the mostly used procedure, which consists in the delivery of purified nucleic acid to the cells using different chemical reagents, electroporation, or viruses. This results in an overexpression of the protein, that gets lost after a short time. Another strategy is the generation of stable cell lines, which include markers that allow the selection, such as antibiotic resistances. These cells also overexpress the plasmid, but the selective conditions avoid the loss of the expression by the population of cells. Other more sophisticated strategies include CRISPR Cas9 knock-in (KI) strategies.[65] It is to be noted that fluorescent tagging is compatible with live cell imaging, and therefore it has been a widely used strategy.

However, the brightness and photostability of fluorescent proteins is lower than for the organic dyes, especially the ones that have been recently developed, such as the Janelia Fluor dyes.[66] However, as already mentioned, intracellular tagging with organic dyes is very challenging, and the use of antibodies is not compatible with life imaging, unless labeling membrane proteins from the extracellular side. Luckily,

a combination of both genetical intracellular tagging and organic dyes has been recently developed: the so-called self-labeling proteins tags. They come from proteins present in living organisms, that have certain catalytic activity, that can be used to covalently bind the organic dye to their protein sequence. This way, these tags can be expressed in cells and, upon addition of the organic dye (modified to have certain chemical group), they are covalently bound. The three most popular are: HaloTag[67], SNAP-tag[68] and CLIP-tag[69].

6.2. BIMOLECULAR FLUORESCENCE COMPLEMENTATION

In order to be able to visualize the MCS we used bimolecular fluorescence complementation (BiFC), a technique used to visualize protein-protein interactions in living cells. It is based on the principle that two non-fluorescent fragments of a fluorescent protein can reconstitute to form a fluorescent complex when brought together by an interaction between proteins fused to these fragments. These split versions exist for the venus and the cerulean fluorescent proteins, amongst others.[70]

6.3. SYNCHRONIZATION OF PROTEIN SECRETION

In many of the experiments, it will be necessary to control the localization of the protein within the secretory pathway. We used 20°C block, that is known to block protein transport out of the ER to the TGN.[71] In many cases, the protein synthesis inhibitor cycloheximide as also used to create a protein secretion pulse.[72]

Another strategy that allows for the synchronized release and transport of proteins from one cellular compartment to another, facilitating the study of protein trafficking in real-time, is retention using selective hooks (RUSH).[73] A protein of interest is fused to streptavidin-binding peptide (SBP), that binds to streptavidin fused to KDEL. Streptavidin-KDEL serves as a "hook" of the protein, and retains it in the ER until biotin is added. However, there are some inconveniences associated such as the need to overexpress both the hook and the prey protein, which are quite big constructs.

7. REFERENCES

1. Abbe, E. Beiträge zur Theorie des Mikroskops und der mikroskopischen Wahrnehmung: I. Die Construction von Mikroskopen auf Grund der Theorie. *Archiv für mikroskopische Anatomie* **9**, (1873).

2. Lakowicz, J. R. *Principles of Fluorescence Spectroscopy*. *Principles of Fluorescence Spectroscopy* (Springer, 2006). doi:10.1007/978-0-387-46312-4.

3. Edinburgh Instruments Ltd. What is a Jablonski Diagram (Perrin-Jablonski Diagram)? *https://www.edinst.com/blog/jablonski-diagram-2/*.

4. Chalfie M., Tu Y., Euskirchen G., Ward W. W. & Prasher D. C. Green fluorescent protein as a marker gene expression. *Science (1979)* **263**, 802–805 (1994).

5. Hell, S. W. Far-field optical nanoscopy. *Science* vol. 316 Preprint at https://doi.org/10.1126/science.1137395 (2007).

6. Avantier, Inc. What is Total Internal Reflection (TIR). *https://avantierinc.com/resources/knowledge-center/what-is-total-internal-reflection-tir/* (2023).

7. Axelrod, D. Cell-substrate contacts illuminated by total internal reflection fluorescence. *Journal of Cell Biology* **89**, (1981).

8. Tokunaga, M., Imamoto, N. & Sakata-Sogawa, K. Highly inclined thin illumination enables clear single-molecule imaging in cells. *Nat Methods* **5**, 159–161 (2008).

9. Hell, S. W. & Wichmann, J. Breaking the diffraction resolution limit by stimulated emission: stimulated-emission-depletion fluorescence microscopy. *Opt Lett* **19**, 780–782 (1994).

10. Hess, S. T., Girirajan, T. P. K. & Mason, M. D. Ultra-high resolution imaging by fluorescence photoactivation localization microscopy. *Biophys J* **91**, (2006).

11. Betzig, E. *et al*. Imaging intracellular fluorescent proteins at nanometer resolution. *Science (1979)* **313**, (2006).

12. Eggeling, C., Willig, K. I., Sahl, S. J. & Hell, S. W. Lens-based fluorescence nanoscopy. *Q Rev Biophys* **48**, (2015).

13. Vicidomini, G. *et al*. Sharper low-power STED nanoscopy by time gating. *Nat Methods* **8**, (2011).

14. Lukinavičius, G. *et al.* A near-infrared fluorophore for live-cell super-resolution microscopy of cellular proteins. *Nat Chem* **5**, 132–139 (2013).

15. Grimm, J. B. *et al.* A general method to improve fluorophores for live-cell and single-molecule microscopy. *Nat Methods* **12**, 244–250 (2015).

16. Grimm, J. B., Brown, T. A., English, B. P., Lionnet, T. & Lavis, L. D. Synthesis of Janelia Fluor HaloTag and SNAP-Tag Ligands and Their Use in Cellular Imaging Experiments. in *Methods in Molecular Biology* 179–188 (Springer New York, 2017). doi:10.1007/978-1-4939-7265-4_15.

17. Klar, T. A., Jakobs, S., Dyba, M., Egner, A. & Hell, S. W. Fluorescence microscopy with diffraction resolution barrier broken by stimulated emission. *Proceedings of the National Academy of Sciences* **97**, 8206–8210 (2000).

18. Edidin, M., Zagyansky, Y. & Lardner, T. J. Measurement of membrane protein lateral diffusion in single cells. *Science (1979)* **191**, (1976).

19. Jacobson, K., Derzko, Z., Wu, E. S., Hou, Y. & Poste, G. Measurement of the lateral mobility of cell surface components in single, living cells by fluorescence recovery after photobleaching. *Journal of Supramolecular and Cellular Biochemistry* **5**, (1977).

20. Axelrod, D., Koppel, D. E., Schlessinger, J., Elson, E. & Webb, W. W. Mobility measurement by analysis of fluorescence photobleaching recovery kinetics. *Biophys J* **16**, (1976).

21. Kenworthy, A. K. What's past is prologue: FRAP keeps delivering 50 years later. *Biophysical Journal* vol. 122 Preprint at https://doi.org/10.1016/j.bpj.2023.05.016 (2023).

22. Elson, E. L. Fluorescence correlation spectroscopy: Past, present, future. *Biophysical Journal* vol. 101 Preprint at https://doi.org/10.1016/j.bpj.2011.11.012 (2011).

23. Eggeling, C. *et al.* Direct observation of the nanoscale dynamics of membrane lipids in a living cell. *Nature* **457**, (2009).

24. Manzo, C., Van Zanten, T. S. & Garcia-Parajo, M. F. Nanoscale fluorescence correlation spectroscopy on intact living cell membranes with NSOM probes. *Biophys J* **100**, (2011).

25. Manzo, C. & Garcia-Parajo, M. F. A review of progress in single particle tracking: From methods to biophysical insights. *Reports on Progress in Physics* vol. 78 Preprint at https://doi.org/10.1088/0034-4885/78/12/124601 (2015).

26. Balzarotti, F. *et al.* Nanometer resolution imaging and tracking of fluorescent molecules with minimal photon fluxes. *Science (1979)* **355**, (2017).

27. Wolff, J. O. *et al.* MINFLUX dissects the unimpeded walking of kinesin-1. *Science (1979)* **379**, (2023).

28. Deguchi, T. *et al.* Direct observation of motor protein stepping in living cells using MINFLUX. *Science (1979)* **379**, (2023).

29. De Brabander, M., Nuydens, R., Geerts, H. & Hopkins, C. R. Dynamic behavior of the transferrin receptor followed in living epidermoid carcinoma (A431) cells with nanovid microscopy. *Cell Motil Cytoskeleton* **9**, (1988).

30. Geerts, H. *et al.* Nanovid tracking: a new automatic method for the study of mobility in living cells based on colloidal gold and video microscopy. *Biophys J* **52**, (1987).

31. Gelles, J., Schnapp, B. J. & Sheetz, M. P. Tracking kinesin-driven movements with nanometre-scale precision. *Nature* **331**, (1988).

32. Sheetz, M. P., Turney, S., Qian, H. & Elson, E. L. Nanometre-level analysis demonstrates that lipid flow does not drive membrane glycoprotein movements. *Nature* **340**, (1989).

33. Dahan, M. *et al.* Diffusion Dynamics of Glycine Receptors Revealed by Single-Quantum Dot Tracking. *Science (1979)* **302**, (2003).

34. Manley, S. *et al.* High-density mapping of single-molecule trajectories with photoactivated localization microscopy. *Nat Methods* **5**, (2008).

35. Grimm, J. B. *et al.* Bright photoactivatable fluorophores for single-molecule imaging. *Nat Methods* **13**, 985–988 (2016).

36. Levi, V. & Gratton, E. Three-Dimensional Particle Tracking in a Laser Scanning Fluorescence Microscope. in *Single Particle Tracking and Single Molecule Energy Transfer* (2009). doi:10.1002/9783527628360.ch1.

37. Daly, S. *et al.* High-density volumetric super-resolution microscopy. *Nat Commun* **15**, (2024).

38. Sims, R. R. *et al.* Single molecule light field microscopy. *Optica* **7**, (2020).

39. Pearson, K. The problem of the random walk [3]. *Nature* vol. 72 Preprint at https://doi.org/10.1038/072342a0 (1905).

40. Muñoz-Gil, G. *et al.* Objective comparison of methods to decode anomalous diffusion. *Nat Commun* **12**, (2021).

41. Metzler, R., Jeon, J. H., Cherstvy, A. G. & Barkai, E. Anomalous diffusion models and their properties: Non-stationarity, non-ergodicity, and ageing at the centenary of single particle tracking. *Physical Chemistry Chemical Physics* **16**, (2014).

42. Sposini, V. *et al.* Towards a robust criterion of anomalous diffusion. *Commun Phys* **5**, (2022).

43. Massignan, P. *et al.* Nonergodic subdiffusion from brownian motion in an inhomogeneous medium. *Phys Rev Lett* **112**, (2014).

44. Simson, R., Sheets, E. D. & Jacobson, K. Detection of temporary lateral confinement of membrane proteins using single-particle tracking analysis. *Biophys J* **69**, (1995).

45. Helmuth, J. A., Burckhardt, C. J., Koumoutsakos, P., Greber, U. F. & Sbalzarini, I. F. A novel supervised trajectory segmentation algorithm identifies distinct types of human adenovirus motion in host cells. *J Struct Biol* **159**, (2007).

46. Muñoz-Gil, G., Garcia-March, M. A., Manzo, C., Martín-Guerrero, J. D. & Lewenstein, M. Single trajectory characterization via machine learning. *New J Phys* **22**, (2020).

47. Gentili, A. & Volpe, G. Characterization of anomalous diffusion classical statistics powered by deep learning (CONDOR). *J Phys A Math Theor* **54**, (2021).

48. Argun, A., Volpe, G. & Bo, S. Classification, inference and segmentation of anomalous diffusion with recurrent neural networks. *J Phys A Math Theor* **54**, (2021).

49. Muñoz-Gil, G. *et al.* Quantitative evaluation of methods to analyze motion changes in single-particle experiments. *ArXiv* (2023).

50. Requena, B. *et al.* Inferring pointwise diffusion properties of single trajectories with deep learning. *Biophys J* **122**, (2023).

51. Pete Bankhead. *Introduction to Bioimage Analysis. Https://Bioimagebook.Github.Io/*. (Jupyter Book, 2022).

52. Aaron, J., Wait, E., DeSantis, M. & Chew, T. L. Practical Considerations in Particle and Object Tracking and Analysis. *Current Protocols in Cell Biology* vol. 83 Preprint at https://doi.org/10.1002/cpcb.88 (2019).

53. Vincent, L., Vincent, L. & Soille, P. Watersheds in Digital Spaces: An Efficient Algorithm Based on Immersion Simulations. *IEEE Trans Pattern Anal Mach Intell* **13**, (1991).

54. Richardson, W. H. Bayesian-Based Iterative Method of Image Restoration*. *J Opt Soc Am* **62**, (1972).

55. Pylvänäinen, J. W., Gómez-de-Mariscal, E., Henriques, R. & Jacquemet, G. Live-cell imaging in the deep learning era. *Current Opinion in Cell Biology* vol. 85 Preprint at https://doi.org/10.1016/j.ceb.2023.102271 (2023).

56. Lorente, Ò., Riera, I. & Rana, A. Image Classification with Classic and Deep Learning Techniques. *ArXiv* (2021).

57. Christiansen, E. M. *et al.* In Silico Labeling: Predicting Fluorescent Labels in Unlabeled Images. *Cell* **173**, (2018).

58. Ounkomol, C., Seshamani, S., Maleckar, M. M., Collman, F. & Johnson, G. R. Label-free prediction of three-dimensional fluorescence images from transmitted-light microscopy. *Nat Methods* **15**, (2018).

59. Otsu, N. THRESHOLD SELECTION METHOD FROM GRAY-LEVEL HISTOGRAMS. *IEEE Trans Syst Man Cybern* **SMC-9**, (1979).

60. Maška, M. *et al.* The Cell Tracking Challenge: 10 years of objective benchmarking. *Nat Methods* **20**, (2023).

61. Chenouard, N. *et al.* Objective comparison of particle tracking methods. *Nat Methods* **11**, (2014).

62. Godinez, W. J. & Rohr, K. Tracking multiple particles in fluorescence time-lapse microscopy images via probabilistic data association. *IEEE Trans Med Imaging* **34**, (2015).

63. Kalman, R. E. A new approach to linear filtering and prediction problems. *Journal of Fluids Engineering, Transactions of the ASME* **82**, (1960).

64. Zimmer, M. GFP: From jellyfish to the Nobel prize and beyond. *Chem Soc Rev* **38**, (2009).

65. Zhang, F., Wen, Y. & Guo, X. CRISPR/Cas9 for genome editing: Progress, implications and challenges. *Hum Mol Genet* **23**, (2014).

66. Yan, Q. & Bruchez, M. P. Advances in chemical labeling of proteins in living cells. *Cell and Tissue Research* vol. 360 Preprint at https://doi.org/10.1007/s00441-015-2145-4 (2015).

67. Los, G. V. *et al.* HaloTag: A novel protein labeling technology for cell imaging and protein analysis. *ACS Chem Biol* **3**, (2008).

68. Keppler, A. *et al.* A general method for the covalent labeling of fusion proteins with small molecules in vivo. *Nat Biotechnol* **21**, (2003).

69. Gautier, A. *et al.* An Engineered Protein Tag for Multiprotein Labeling in Living Cells. *Chem Biol* **15**, (2008).

70. Kerppola, T. K. Visualization of molecular interactions by fluorescence complementation. *Nature Reviews Molecular Cell Biology* vol. 7 Preprint at https://doi.org/10.1038/nrm1929 (2006).

71. Matlin, K. S. & Simons, K. Reduced temperature prevents transfer of a membrane glycoprotein to the cell surface but does not prevent terminal glycosylation. *Cell* **34**, (1983).

72. Schneider-Poetsch, T. *et al.* Inhibition of eukaryotic translation elongation by cycloheximide and lactimidomycin. *Nat Chem Biol* **6**, (2010).

73. Boncompain, G. *et al.* Synchronization of secretory protein traffic in populations of cells. *Nat Methods* **9**, (2012).

Chapter 3

Image Analysis for the Study of Intracellular Trafficking

This chapter presents four different projects in which we applied image analysis and quantification tools to fluorescence microscopy images. These projects were carried out in collaboration with scientists at ICFO and other research institutions. All the projects are set in the context of intracellular trafficking, and more specifically the formation of cargo-containing transport carriers both at the TGN and the ER. Generally, these pipelines aim to calculate meaningful parameters such as colocalization and proximity between point-like or tubular structures, diffusion parameters of these structures, and fluorescence intensity quantification on structures such as the TGN and the plasma membrane.

Part of this work has been published in:

Wakana, Y., Hayashi, K., Nemoto, T., Watanabe, C., Taoka, M., **Angulo-Capel, J.**, Garcia-Parajo, M. F., Kumata, H., Umemura, T., Inoue, H., Arasaki, K., Campelo, F., Tagaya, M. (2020) The ER cholesterol sensor SCAP promotes CARTS biogenesis at ER–Golgi membrane contact sites. Journal of Cell Biology. 220 (1): e202002150; doi: 10.1083/jcb.202002150

Wong-Dilworth, L., Bregu, G., Restel, S., Rodilla-Ramirez, C., Ebeling, S., Harel, S., Leupold, P., Grimm, J., Lavis, L.D., **Angulo-Capel, J.**, Campelo, F., Bottanelli, F. (2023) Nanoscale imaging reveals the mechanisms of ER-to-Golgi transport via a dynamic tubular vesicular network. BioRxiv 2023.10.27.563951; doi: 10.1101/2023.10.27.563951

1. INTRODUCTION

When performing quantifications on microscopy images obtained with fluorescence microscopy, several key factors need to be considered to ensure accurate, unbiased, and reproducible results. For instance, sample preparation and image acquisitions need to be consistent. On the image analysis side, one needs to understand how the data has been obtained, as well as how it is processed. Otherwise, the quantifications can lead to artifacts and misinterpretation of the results.

Despite this cautionary note, it is still highly recommended to use computational approaches to extract meaningful quantitative descriptors of the microscopy data, even when they might appear obvious by eye inspection. Utilizing computational pipelines can significantly enhance the accuracy and reliability of the quantifications for many reasons:

(i) Standardization and consistency. Automated pipelines reduce the user-to-user variability introduced by manual inspection, ensuring that all images are analyzed the same way. Moreover, the analysis can be repeated, making it easier to replicate results across different experiments and labs.[1]

(ii) Efficiency and throughput. Automated analysis can handle large datasets quickly and efficiently.

(iii) Allow for more sophisticated analyses. Automated pipelines can incorporate sophisticated algorithms for calculation of the desired parameters.

In this section, we describe four different projects where image analysis and quantification have been applied to fluorescence microscopy images. In general, the pipelines aimed at calculating meaningful parameters such as: *(i)* colocalization and proximity between point-like or tubular structures, *(ii)* diffusion parameters of these structures, and *(iii)* fluorescence intensity measurement on structures such as the TGN and the plasma membrane.

2. PROXIMITY AND COLOCALIZATION QUANTIFICATION OF PUNCTATE STRUCTURES

The first contribution was to the publication: Wakana, Y., Hayashi, K., Nemoto, T., Watanabe, C., Taoka, M., Angulo-Capel, J., Garcia-Parajo, M. F., Kumata, H., Umemura, T., Inoue, H., Arasaki, K., Campelo, F., Tagaya, M. (2020) The ER cholesterol sensor SCAP promotes CARTS biogenesis at ER–Golgi membrane contact sites. Journal of Cell Biology. 220 (1): e202002150

The publication is in the context of ER-Golgi MCS, and how they play a role in the formation of CARTS, a specific type of carriers that form at the TGN. As a reminder, both the silencing of the MCS components VAP-A and VAP-B, as well as the stabilization of the MCS with the PH-FFAT construct, results in reduced secretion of the protein PAUF, and inhibition of the formation of CARTS.[2,3] Similar observations have been made when using 25-hydroxycholesterol (25-HC), an oxysterol that is able to bind OSBP with high affinity, and block it in the bound conformation to VAP. This binding inhibits the VAP/OSBP-mediated sterol transfer.[4] However, it is still not known the specific role that MCS play in CARTS formation, nor the impact of their lipid transfer function in this respect.

Wakana and Campelo suggested that the non-vesicular transport of cholesterol and ceramide at ER-Golgi MCS could provide the necessary lipids for the formation at the TGN of liquid-ordered membrane nanodomains, segregated from other lipids and that could function as a platform for specific proteins involved in glycosylation, cargo sorting, and transport carrier biogenesis (see **Figure 1**).[5]

In Wakana et al., Journal of Cell Biology (2020), another player was brought to these MCS platforms, the so-called sterol regulatory element-binding protein (SREBP) cleavage activating protein (SCAP), which is a cholesterol sensor in the ER.[6] It is known that, when the cholesterol in the ER is low, SCAP escorts SREBPs transcription factors into COPII vesicles for traffic from the ER to the Golgi. In the Golgi, SREBPs are cleaved by proteases, and the transcriptionally active domain enters the nucleus, promoting the expression of genes involved in cholesterol synthesis and uptake.[7] The main important points of the publication are:

(i) SCAP is a novel component of Sac1-positive ER-Golgi MCSs.

(ii) In cholesterol-fed conditions, ER-localized SCAP interacts through Sac1 with the VAP-A-OSBP complex at the ER-Golgi MCSs.

(iii) SCAP is important for PI4P turnover and VAP-A-OSBP complex distribution at the ER-Golgi MCSs

(iv) SCAP is required for the biogenesis of CARTS at the TGN.

(v) SCAP regulates CARTS biogenesis in a cholesterol-dependent manner

(vi) The SCAP-SREBP complex functions in CARTS biogenesis.

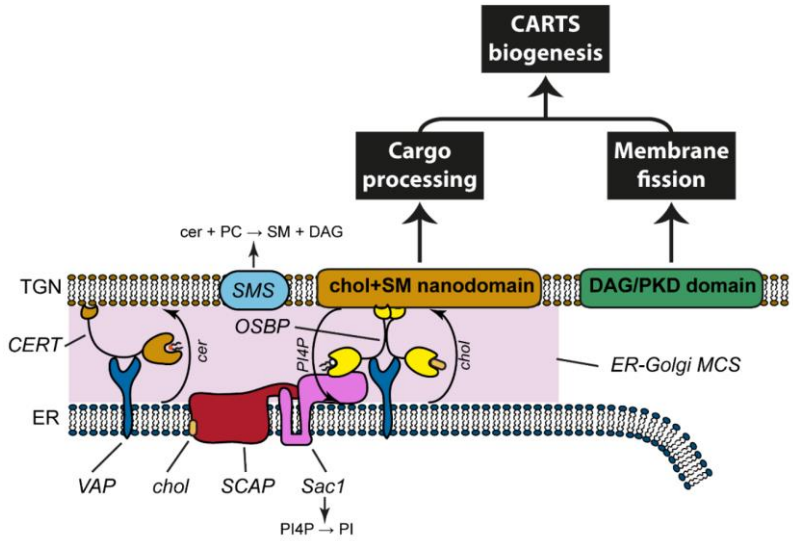

Figure 1. Lipid homeostasis at ER-Golgi MCSs for CARTS biogenesis. ER-Golgi MCSs serve as platforms for the non-vesicular transport of lipids and mediate the PI4P cycle at the ER-Golgi interface, as well as DAG, SM, and cholesterol homeostasis. cer: ceramide; chol: cholesterol; DAG: diacylglycerol; MCS: membrane contact site; PC: phosphatidylcholine; PI: phosphatidylinositol; PI4P: PI 4-phosphate; PKD: protein kinase D; SM: sphingomyelin; SMS: SM synthase. (Taken from Y. Wakana, F. Campelo, Cells (2021))[5].

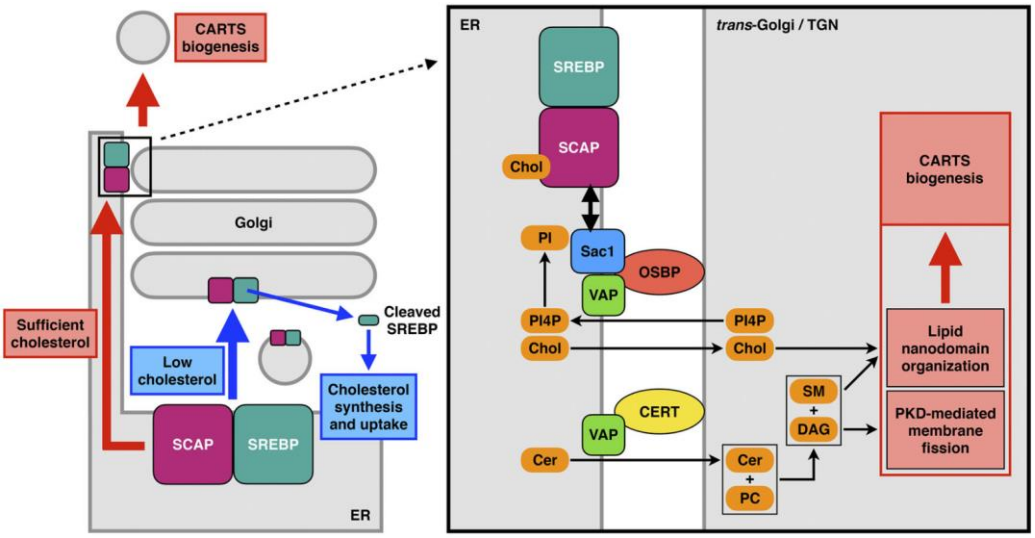

Figure 2. Working model for the facilitation of CARTS biogenesis by the SCAP–SREBP complex at ER–Golgi MCSs. Low cholesterol (Chol) levels: SCAP escorts SREBP transcription factors from the ER to the Golgi complex for cholesterol synthesis and uptake (left panel, blue arrows). Sufficient cholesterol levels: a complex of cholesterol-bound SCAP and SREBP interacts with the VAP–OSBP complex via Sac1 and functions in the counter-transport of ER cholesterol and Golgi PI4P at ER–Golgi MCSs to promote CARTS biogenesis at the TGN domains immediately adjacent to the ER MSCs (left panel, red arrows, and right panel). PC, phosphatidylcholine. (Taken from Wakana, Y. et al., Journal of Cell Biology (2021)[2]).

The proposed model resulting from this study is shown in **Figure 2**. The model proposes that in sufficient cholesterol levels, SCAP and SREBP interact with ER-Golgi MCS proteins via Sac1. There, cholesterol and ceramide are transported to the Golgi. At the *trans*-Golgi membranes, cholesterol and SM are involved in lipid nanodomain organization, which can function as a platform for molecular machineries responsible for processing and sorting of cargoes.

My contribution in this publication included the development and use of image analysis and quantification tools that provided quantitative support to the conclusions highlighted in points *(i)* and *(v)*, as well as super-resolution imaging of CARTS formation adjacent to MCS (to be described in **Chapter 5**). The first quantification entailed the distances between Golgi ministacks in different channels in nocodazole-treated of HeLa cells. The distance was measured between two ER-Golgi MCS proteins: Sac1, either as a mutant variant or as wild type, and VAP-A. The second quantification was a colocalization quantification between carriers in different channels. More specifically, colocalization between the SM sensor equinatoxin-SM (EQ-SM)[8], and the CARTS cargo PAUF.

2.1. METHODS

The experimental part of this project was performed by Y. Wakana (School of Life Sciences, Tokyo University of Pharmacy and Life Sciences, Japan).

Cell culture and transfection

Plasmid transfection into HeLa cells was performed using X-tremeGENE 9 DNA transfection reagent (Roche), according to the manufacturers' protocols.

PAUF-MycHis plasmid was donated by S.S. Koh (Korea Research Institute of Bioscience and Biotechnology, Daejeon, Korea). The plasmid encoding EQ-SM (tagged with oxGFP) was generous gifts from C.G.Burd (Yale School of Medicine, New Haven, CT). The plasmids encoding the GFP-Sac1 WT and K2A mutant were generous gifts from P. Mayinger (Oregon Health and Science University, Portland, Oregon).

Immunofluorescence and imaging

HeLa cells were fixed with 4% PFA in PBS at room temperature for 20 min, permeabilized with 0.2% Triton X-100 in PBS for 30 min, and then blocked with 2% bovine serum albumin (BSA) in PBS for 30 min. The cells were labeled with the indicated primary antibodies:

- VAP-A: rabbit anti-GST-VAP-A, donated by D. Ridgway (Atlantic Research Center, Canada), see publication [9]
- PAUF-MycHis: mouse anti-c-Myc (clone 9E10, Sigma-Aldrich)

The secondary antibodies were conjugated to Alexa Fluor 488, 594, 633, or 647 in the blocking buffer.

The samples were imaged with an Olympus Fluoview FV1000 or FV1200 confocal microscope with a UPLSAPO 60× O NA 1.35 apochromat objective, that fully compensates for both spherical and chromatic aberrations, and FV10-ASW software. The two-color images have been taken sequential frame-by-frame. Pixel dwell time was set to 2 µs, i.e. 2 seconds per frame. The pixel size was 59 nm, in 1024x1024 pixel images.

Nocodazole treatment

HeLa cells were transfected either with GFP-Sac1 WT or K2A as explained above. After 20 hours, they were treated with 2 µg/ml 25-HC for 1 h. Then, they were treated with 5 µg/ml nocodazole (to depolymerize microtubules and create Golgi mini-stacks) or DMSO (control) for 2 h. The cells were then fixed and visualized with GFP and antibodies against GM130 and VAP-A as explained above.

PAUF secretion assay

HeLa cells were transfected with PAUF-MycHis and EQ-SM. 20 h later, the medium was replaced with Opti-MEM, and cells were incubated at 20 °C for 2 hours. Cells were placed back to 37°C for 30 minutes, and then fixed and immunolabeled against PAUF-MycHis as explained above.

2.2. DEVELOPED ANALYSIS

Individual cells were used as experimental repeats, versus different samples containing data from several cells, to better capture the intrinsic biological variability present within the cell population. This enhanced the statistical power of our analyses by providing a larger number of data points. We ensured that each cell contained sufficient information (i.e. high number of punctate structures), and that each one was independently processed and analyzed. Since there are no comparisons between different experimental conditions, we did not consider that this data representation could lead to pseudoreplication and artificial decrease of the p-values.[10]

Proximity analysis of Golgi ministacks

The detection of punctate structures and Golgi ministacks was performed with Fiji, by setting an intensity threshold and segmenting the particles from the binary mask using the "Analyze Particles" command. The proximity between the structures detected in the two channels was then calculated with a self-written MATLAB code. It uses the centroid position of the Sac1 punctate structures to find the nearest-neighbor centroid in the opposite channel (GM130 or VAP-A-positive structures). The maximum allowed connecting distance was 1 µm.

Colocalization of transport carriers

The detection of Golgi ministacks was performed with ComDet, a Fiji Plugin that detects particles and calculates the colocalization between channels (https://github.com/UU-cellbiology/ComDet.git). The Golgi area was excluded by manually selecting an ROI of the cytoplasm without the perinuclear area. The detection included larger particles, and the segmentation of larger particles. The approximate particle size was set to 3 pixels (177 nm), and the intensity threshold (in standard deviation) was set to 80. The colocalization is just defined by a user-defined distance. The maximum distance between colocalized spots was set to 4 pixels (236 nm).

2.3. RESULTS

Sac1 colocalizes with ER-Golgi MCSs

In the publication, it was shown that there is a good overlap of Sac1's signal with VAP-A (ER-localized) and close proximity to TGN46 (TGN-localized) (see **Figure 3**), suggesting that Sac1 is prominently localized to ER-Golgi MCSs. This pattern was also observed for the mutant Sac1 K2A, which has two lysins replaced by two alanines in the COPI-interacting motif. This motif serves for retrograde transport from the *cis*-Golgi to ER,[11] and some ER integral membrane proteins also use this signal for their movement along the ER from the cell center to the periphery.[12,13] Therefore, mutation of this lysine in principle results in a higher localization of the protein Sac1 to the perinuclear area. If so, this mutant could be used as a bait to identify new candidates that interact with it at the Golgi membranes.

In order to quantify the colocalization of Sac1 with TGN46 and VAP-A, cells were treated with nocodazole, a microtubule-depolymerizing agent that induces the formation of dispersed Golgi ministacks in the cytoplasm.[14] This allowed us to study the individual components and spatial organization of Golgi proteins without the

complex architecture of a fully formed Golgi apparatus. Although Sac1 is an ER localized protein, we observed the formation of signal puncta (both for the wild-type and the mutant K2A proteins) that were in close apposition with VAP-A (see **Figure 4**).

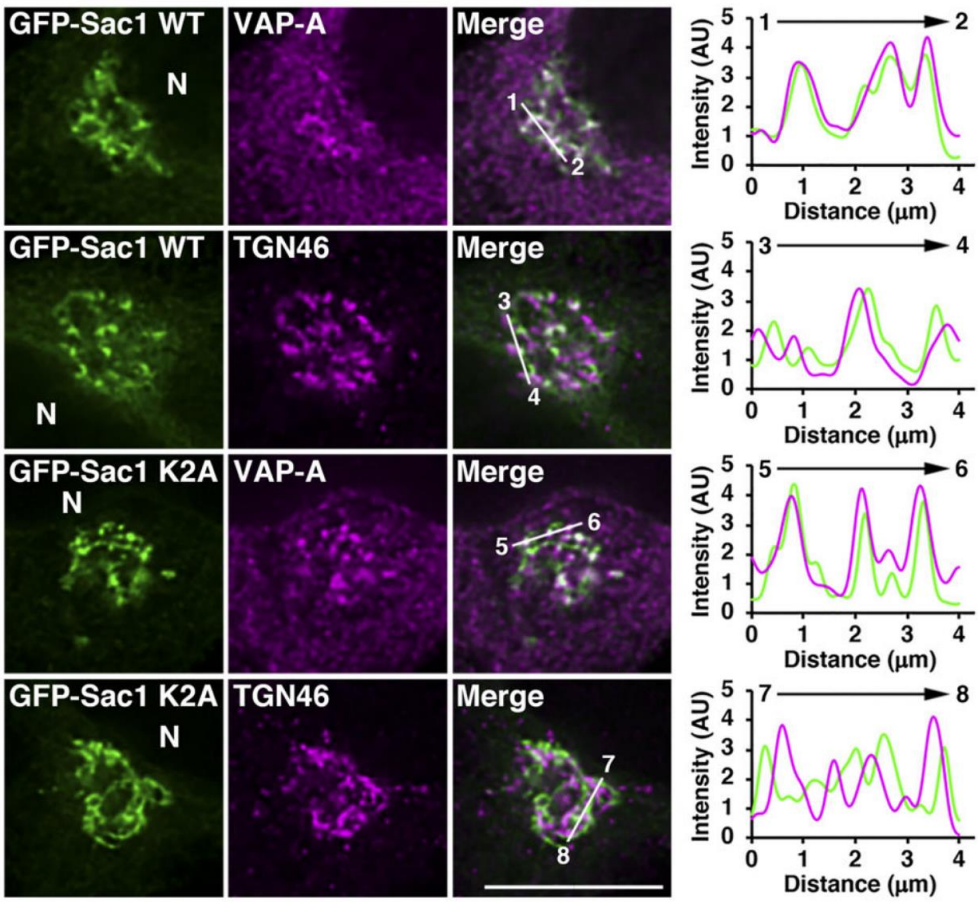

Figure 3. Colocalization of GFP-Sac1 WT or K2A with VAP-A and their proximity to TGN46. HeLa cells expressing GFP-Sac1 WT or K2A were treated with 2 μg/ml 25-HC for 1 h. The graphs on the right show the fluorescence intensity of GFP-Sac1 WT or K2A (green), and VAP-A or TGN46 (magenta) along the respective white lines shown in the merged images. N: nucleus. Scale bar, 10 μm. (Taken from Wakana, Y. et al., Journal of Cell Biology (2021)[2]).

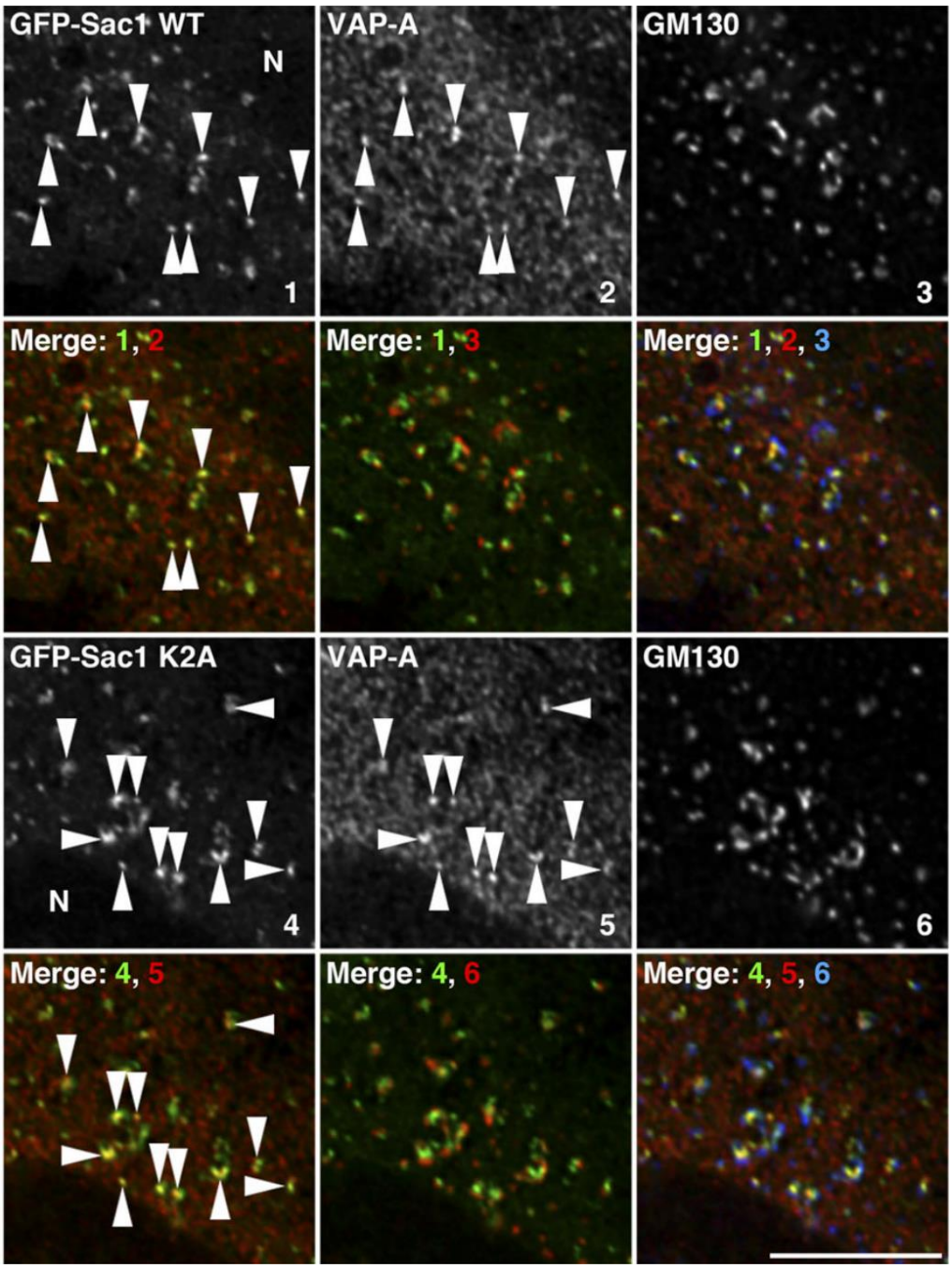

Figure 4. Colocalization between Golgi ministacks, labeled for Sac1 WT or Sac K2A. HeLa cells expressing GFP-Sac1 WT or K2A, and treated with 2 µg/ml 25-HC for 1 h and with 5 µg/ml nocodazole for 2 h. Representative images of the immunofluorescence against GFP (panels 1 and 4), VAP-A (panels 2 and 5), and GM130 (panels 3 and 6). Merged images of the first and third rows are shown in the second and fourth rows, respectively, with color coding corresponding to the numbering of the individual panels. Arrowheads indicate the small punctate elements containing both GFP-Sac1 and VAP-A. Scale bar, 10 µm. (Taken from Wakana, Y. et al., Journal of Cell Biology (2021)[2])

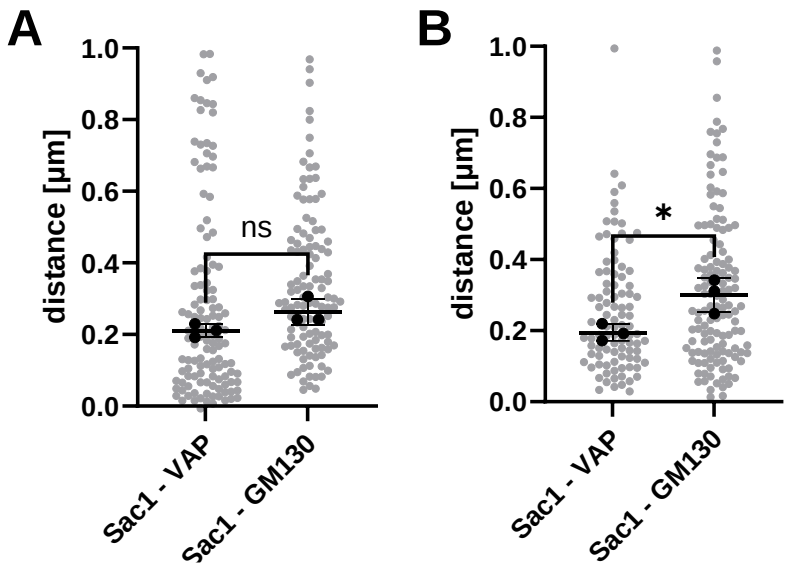

Figure 5. Median distance between Golgi mini-stacks. HeLa cells expressing GFP-Sac1 WT or K2A, and treated with 2 µg/ml 25-HC for 1 h and with 5 µg/ml nocodazole for 2 h. They were then labeled against VAP-A and GM130. Median distance between Sac1 puncta and GM130 ministacks. Grey points represent all distance values, and black points represent the median value per cell (each one with more than 60 Sac1 ministacks). Error bars represent mean and SD of the cell median values (black dots). **A.** Distance between Sac1 WT and VAP positive puncta, and between Sac1 WT and GM130 puncta. The difference is not statistically significant (two-tailed paired t-test, p-value = 0.1599). **B.** Quantification in mutated Sac1. Distance between Sac1 K2A and VAP positive puncta, and between Sac1 K2A and GM130 puncta (two-tailed paired t-test, p-value = 0.0198).

Given that the structures were not perfectly overlapping, we found that, rather than colocalization, a better measure of the proximity between the different structures was the nearest neighbor distance of their centroid positions, which was performed as described in the **Methods** section. **Figure 5** represents the median distance between the Sac1 puncta to the nearest neighbor in each of the other channels. One can observe that Sac1 is closer to VAP-A than to the *cis*-Golgi marker GM130. However, this is only statistically significant for the K2A mutant. According to these measurements, this mutant was then used to identify interacting candidates. Immunoprecipitation and mass spectrometry revealed SCAP as a possible interacting protein.

CARTS are enriched in cholesterol and SM

In the same publication, it is shown that CARTS contain glycosylphosphatidyl inositol (GPI)-anchored proteins, indicating that the membranes are probably enriched in cholesterol and sphingolipids. This established a possible link between CARTS and the SM-rich carriers. This latter type of carriers is very interesting because some of

their cargoes have shown to be sorted by different mechanisms. For instance, the common cargo LyzC is sorted through Ca^{2+}-dependent oligomerization, mediated by Cab45 and the Ca^{2+} pump SPCA1.[15]

To strengthen the hypothesis that CARTS are enriched with these lipids, SM in the luminal leaflet of the secretory pathway membranes was labeled with the SM reporter protein EQ-SM. We quantified the number of colocalizing vesicles in HeLa cells overexpressing both EQ-SM and PAUF-MycHis. As shown in **Figure 6**, 74 ±15% of PAUF-MycHis-positive CARTS contained EQ-SM[8]. In the first publication that reported this new distinct SM-rich vesicles, they measure that at 86 ±5% of GPI–positive exocytic vesicles were EQ-SM-positive, which is in agreement with the values that we measured.[8]

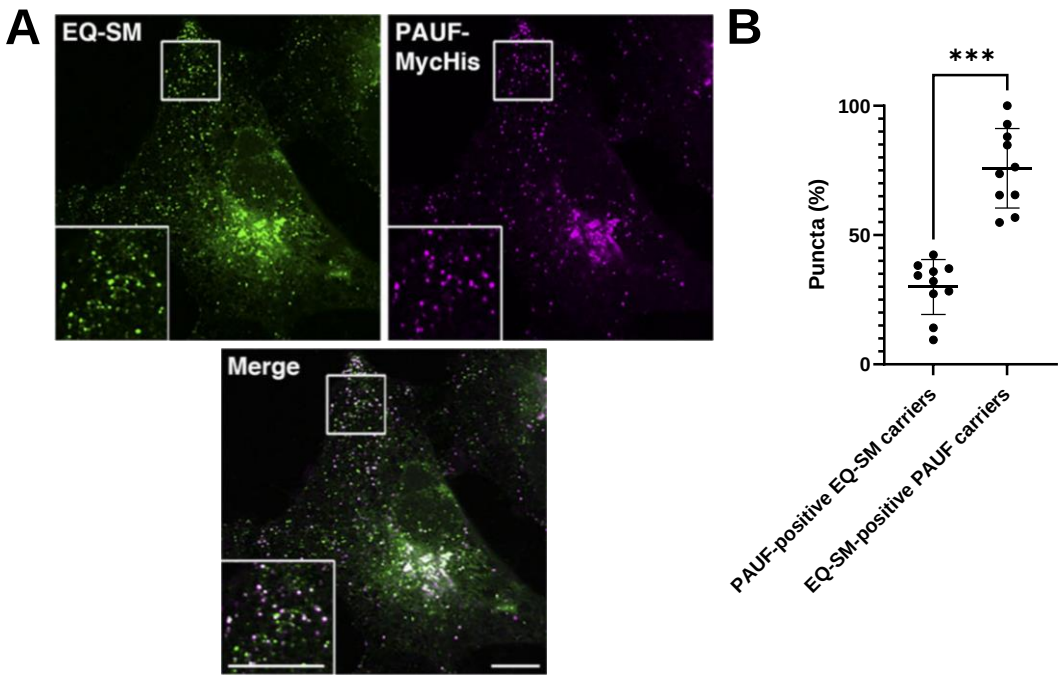

Figure 6. Colocalization of EQ-SM and PAUF-MycHis. A. Representative image of a cell co-transfected with EQ-SM (green) and PAUF-MycHis (magenta). High magnifications of the boxed areas are shown in the insets. Scale bar, 10 µm. **B.** Quantification of EQ-SM-positive puncta containing PAUF-MycHis (left) and PAUF-MycHis-positive puncta containing EQ-SM (right). Each spot represents the mean percentage per cell, each one with 20-180 puncta. The difference is significative (two-tailed paired t-test, p-value=0.0002). (Published in Wakana, Y. et al., Journal of Cell Biology (2021)[2]).

3. HEMAGGLUTININ SECRETION QUANTIFICATION

Our collaborator Y. Wakana (School of Life Sciences, Tokyo University of Pharmacy and Life Sciences, Japan) identified hemagglutinin (HA) as new transmembrane

cargo whose transport to plasma membrane also seems to require OSBP and PKD, common molecular machinery in the formation of CARTS (unpublished work). In order to robustly quantify if there is indeed secretion under different inhibiting conditions, we developed a pipeline to quantify fluorescence intensity of HA both in the Golgi and the plasma membrane. This work is in preparation for submission.

HeLa cells overexpressing HA were treated with different siRNAs: one that inhibited the expression of OSBP, two that inhibited the expression of PKD2, and two control RNAs with no effect. A similar study was performed on Madin-Darby canine kidney (MDCK) cells, a polarized cells model that express high amounts of heparan sulfate and HA.[16] These cells were treated with the inhibitor CRT0066101, an inhibitor of all isoforms of PKD.[17]

3.1. METHODS

The experimental part of this project was performed by Y. Wakana (School of Life Sciences, Tokyo University of Pharmacy and Life Sciences, Japan).

Plasmids and stable cell lines

The plasmid encoding influenza-FPV-HA-mEGFP was a generous gift from S. Chiantia (Institute of Biochemistry and Biology, University of Potsdam, Germany) (Addgene plasmid #127810).[18] ss-mKate2-FM4-HA plasmid was cloned by Y. Wakana (School of Life Sciences, Tokyo University of Pharmacy and Life Sciences, Japan) from the plasmid mKate2-FM4-GPI (generous gift from C.G.Burd, Yale School of Medicine, New Haven, CT).

For establishment of stable cell lines expressing ss-mKate2-FM4-HA, cDNA encoding the signal sequence (ss) of human growth hormone 1 (GH1) (aa 1-26), mKate2, FM4, and influenza-FPV-HA (aa 491-563) was inserted into pCX4-IRES-Bsr. For establishment of HeLa and MDCK cells stably expressing ss-mKate2-FM4-HA, PLAT-A packaging cells were transfected with pCX4-ss-mKate2-FM4-HA-IRES-Bsr, and 48 h later, the medium containing retrovirus was collected and used for infection of HeLa and MDCK cells, respectively. Selection of HeLa and MDCK cells stably expressing ss-mKate2-FM4-HA was performed with 10 μg/ml blasticidin. For establishment of Tet-On HeLa cells expressing HA-mEGFP, PLAT-A packaging cells were transfected with pRetroX-Tet-On Advanced or pRetroX-HA-mEGFP-Tight-Pur, and 48 h later, the medium containing retrovirus was collected and used for infection of HeLa cells. Selection of Tet-On HeLa cells expressing HA-mEGFP was performed

with 500 µg/ml G418 and 1 µg/ml puromycin. All the stable cell lines were obtained without single-cell cloning.

Cell culture and transfection

HeLa and MDCK cells were grown in DMEM supplemented with 10% FCS. PLAT-A packaging cells were grown in DMEM supplemented with 10% FCS, 10 µg/ml blasticidin S, and 1 µg/ml puromycin.

Transfection of siRNA into HeLa cells were carried out using Oligofectamine reagent (Thermo Fisher Scientific), according to the manufacturers' protocols.

Silencing RNA (siRNA and shRNA)

The targeting sequences of siRNA and shRNA were as follows:

Control (GL2 luciferase): 5'-AACGTACGCGGAATACTTCGA-3'

OSBP: 5'-AAGGAGTTAACCCATATTTAT-3'

PKD2 (882): 5'-ATGCAAAGACTGCAAGTTTAA-3'

PKD2 (1303): 5'-AACAGATACTATAAGGAAATT-3'

HA-mEGFP localization in OSBP and PKD2 knockdown cells

Tet-On HeLa cells expressing HA-mEGFP were transfected with control siRNA or siRNA oligos targeting OSBP or PKD2. At 48 h after siRNA transfection, the medium was replaced with DMEM containing 10% FCS and 1 µg/ml doxycycline to induce expression of HA-mEGFP. After 24 h, cells were fixed an immunolabeled against GM130 and TGN46, as explained above.

mKate2-FM4-HA transport in polarized MDCK cells

MDCK cells stably expressing ss-mKate2-FM4-HA were seeded onto Transwells (costar, #3413) for polarization. After 96 h, the medium was replaced with DMEM containing 10% FCS, 20 mM HEPES-KOH, pH 7.4, 1 µM D/D solubilizer, and 20 µg/mL cycloheximide, and then the cells were incubated in a water bath at 20°C for 45 min, followed by pretreatment with DMSO (control) or 20 µM CRT0066101 for 15 min. The cells were then incubated in a water bath at 37°C for 5 or 30 min, followed by fixation with 4% PFA. The samples were processed as indicated for immunofluorescence microscopy. They were then fixed and immunolabeled against GM130 and the tight junction protein ZO-1, both at the plasma membrane plane, and the Golgi plane.

Immunofluorescence

Cells were fixed with 4% PFA in PBS at room temperature for 20 min, permeabilized with 0.2% Triton X-100 in PBS for 30 min, and then blocked with 2% bovine serum albumin (BSA) in PBS for 30 min. The cells were labeled with the indicated primary antibodies and secondary antibodies conjugated to Alexa Fluor 488, 594, or 647 in the blocking buffer.

- GM130: mouse anti-GM130 (#810823, BD Biosciences), secondary antibody AF488.
- TGN46: rabbit anti-TGN46 (Wakana et al. JCB 2021[5]), secondary antibody AF594.
- ZO-1: rabbit anti-ZO-1 (#21773-1-AP, Proteintech), secondary antibody AF647.

The samples (Tet-on HeLa-HA-mEGFP) were analyzed with an Olympus Fluoview FV1200 confocal microscope with a UPLSAPO 60x O NA 1.35 apochromat objective, that fully compensates for both spherical and chromatic aberrations, and FV10-ASW software. The samples (MDCK-mKate2-FM4-HA) were analyzed or with an Olympus Fluoview FV3000 confocal microscope with a UPLANXAPO 60x O NA 1.42 objective and FV31S-SW software. The two-color images have been taken sequential frame-by-frame. Pixel dwell time was set to 2 µs, i.e. 2 seconds per frame. The pixel size was 52 nm, in 1024x1024 pixel images.

The samples were imaged with an Olympus Fluoview FV1000 or FV1200 confocal microscope with a UPLSAPO 60× O NA 1.35 apochromat objective, that fully compensates for both spherical and chromatic aberrations, and FV10-ASW software. The two-color images have been taken sequential frame-by-frame. Pixel dwell time was set to 2 µs, i.e. 3 seconds per frame. The pixel size was 59 nm, in 1024x1024 pixel images.

The fluorescence signal of HA, GM130 and TGN46 was measured at two different planes, at the plasma membrane height, and at a middle plane that included the Golgi (identified by TGN46 and GM130 channels).

3.2. DEVELOPED ANALYSIS

Individual cells were used as experimental repeats, versus different samples containing data from several cells, to better capture the intrinsic biological variability present within the cell population. This enhanced the statistical power of our

analyses by providing a larger number of data points. We ensured that each cell was independently processed and analyzed. However, it is important to note that in this specific case, it would have been more appropriate to represent the mean values per sample (rather than by individual cell) as data points, especially when comparing different experimental conditions, in order to avoid pseudoreplication and artificial decrease of the p-values.[10] The primary reason for not doing so was the lack of sufficient data. Despite this, I chose to highlight the developed image analyses in this section, acknowledging that the published data should ideally contain more comprehensive datasets. These data are preliminary and unpublished, and further experiments will aim to address these limitations and provide a more robust dataset.

Quantification of fluorescence intensity on HeLa cells

The analysis was performed with a custom-written MATLAB code, available in the following Github link: https://github.com/JessicaAngulo/Hemagglutinin_secretion.git

HeLa cells were segmented from the microscopy images by hand, given that there was no marker to automatically do so. It was performed with the *drawpolygon* MATLAB function, since there was no channel that allowed an easy segmentation of the whole cell area. For the segmentation of the TGN46, an intensity threshold of 120 over 256 grey values was applied on the TGN46 channel imaged at the Golgi plane. This thresholded signal was used for the detection of the TGN structures (see **Figure 7**). The image was contrast adjusted with the function *imadjust*, and Gaussian filtered with *imgaussfilt*, which uses a 2-D Gaussian smoothing kernel of standard deviation 2. The obtained binary mask was used for the identification of the structures' boundaries, using the function *bwboundaries* ('noholes' option).

To calculate the HA intensity density signal at the plasma membrane, the intensity was integrated over the selected cell ROI, and divided by the area of that same ROI. Similarly, for the HA intensity density signal at the TGN, the fluorescence was integrated over the segmented TGN46 mask, and divided by the TGN area.

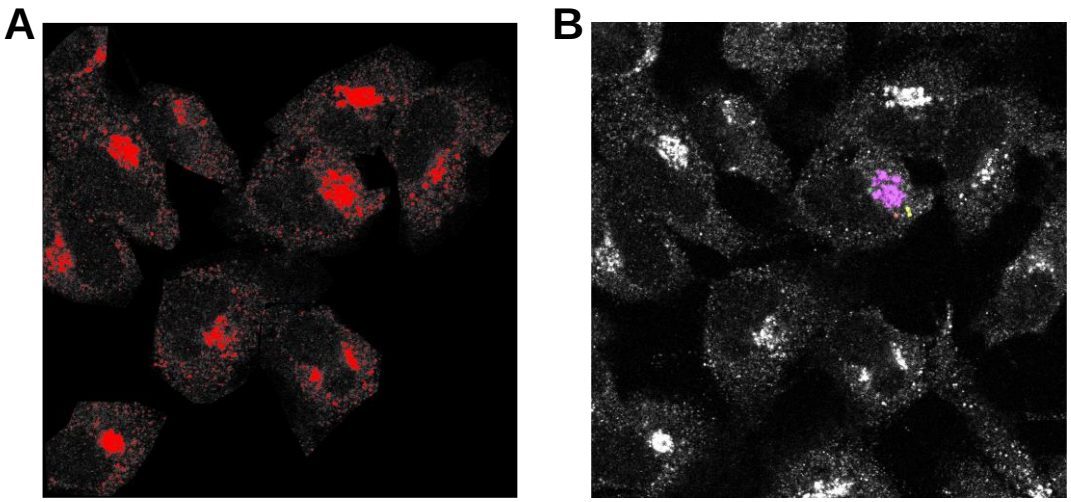

Figure 7. TGN segmentation in HeLa cells. HeLa cells labeled against the TGN marker TGN46 and imaged by confocal microscopy. The field of view is 105.47 µm. **A.** Intensity threshold applied for the segmentation of the TGN46 signal on HeLa cells. The greyscale image represents the raw TGN46 detected signal of the selected cells, and the red pixels label the segmented TGN structures within those cells. **B.** The same field of view as in (a), highlighting a single example of a segmented TGN structure. The segmentation allows the separation of structures which are apart from one another, shown by the different coloring of the structures.

Quantification of fluorescence intensity in MDCK cells

The analysis was performed with a self-written MATLAB code, available in the following Github link: https://github.com/JessicaAngulo/Hemagglutinin_secretion.git

The MDCK cells were segmented making use of the tight junction fluorescence channel (ZO-1 positive). A series of morphological operations to identify the cell edges were applied. The noise was filtered out using a Wiener filter of 10x10 (*wiener2* function). Then, we performed a top-hat filtering with a disk-shaped structuring element of radius 15 to enhance bright features (function *imtophat*). Minima shallower than 3000 units were suppressed with the *imhmin* function. This filtered function was segmented with the *watershed* algorithm. This segmentation also allowed to discard cells that were out of focus, to prevent incorrect measurements of the fluorescence intensity values.

An intensity threshold of 70 over 256 grey values was applied on the GM130 channel imaged at the Golgi plane. This thresholded signal was used for the detection of the Golgi structures (see **Figure 8**). The image was contrast adjusted with the function *imadjust*, and Gaussian filtered with *imgaussfilt*, using a 2-D Gaussian smoothing

kernel of standard deviation 2. The obtained binary mask was used for the identification of the structures' boundaries, using the function *bwboundaries* ('noholes' option).

To calculate the HA fluorescence intensity density signal at the plasma membrane, the intensity was integrated over the selected cell ROI, and divided by the area of the same ROI. For the HA intensity density signal at the Golgi, the fluorescence was integrated over the segmented GM130 mask, and divided by the Golgi area.

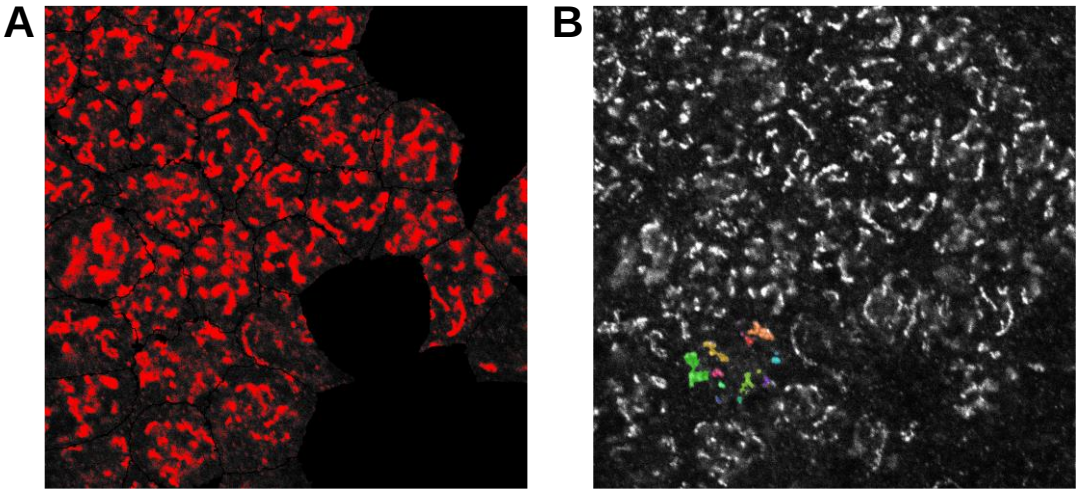

Figure 8. Golgi segmentation in MDCK cells. MDCK cells labeled against the Golgi marker GM130. The field of view is 53.03 μm. **A.** Intensity threshold applied for the segmentation of the GM130 signal on MDCK cells. The greyscale image represents the raw GM130 detected signal, and the red pixels label the segmented Golgi structures. Cells that are out of focus are discarded from the analysis. **B.** The same field of view as in (a), and an example of segmented Golgi structures in one single cell. The segmentation allows the separation of structures which are apart from one another, shown by the different coloring of the structures.

3.3. RESULTS

Quantification of the HA traffic between the TGN and the plasma membrane in HeLa cells

The fluorescence intensity at the plasma membrane was calculated by integration of the HA fluorescence intensity divided by the cell area. The fluorescence intensity at the Golgi was calculated by integration of the fluorescence intensity at the segmented Golgi structures (obtained from the GM130 channel), divided by the Golgi area (GM130 mask). From these values, the mean intensity ratio of HA-mEGFP was calculated as:

$$mean\ intensity\ ratio = \frac{I_{PM}/I_{Golgi}}{\overline{I_{ratio}}} \quad (1)$$

being I_{Golgi} the fluorescence intensity per pixels at the Golgi, I_{PM} the fluorescence intensity at the plasma membrane, and $\overline{I_{ratio}}$ the mean of the intensity ratio for normalization.

Figure 9 shows the results for the control conditions and 3 different gene silencing conditions. One can appreciate that indeed there is a decrease of HA at the plasma membrane in all knockdowns of PKD2 and OSBP as compared to the control. This indicates that there is possibly a TGN export defect for HA in HeLa cells when silencing PKD2 or OSBP.

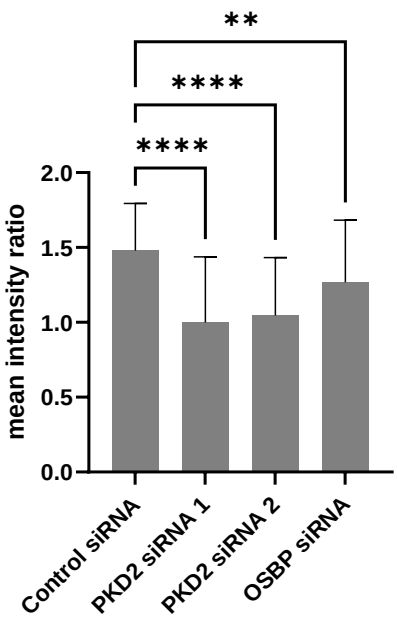

Figure 9. Mean fluorescence intensity ratio of HA at the plasma membrane of HeLa cells. The mean fluorescence intensity ratio is calculated as the fluorescence intensity per pixel in the plasma membrane, divided by the fluorescence intensity per pixel at the Golgi. Comparison between a control and the inhibition using 2 different PKD2 silencing RNAs, or an OSBP silencing RNA. N of the control siRNA = 90 cells, N of the PKD2 siRNA 1 = 95 cells, N of the PKD2 siRNA 2 = 79 cells, N of the OSBP siRNA = 97 cells. Statistical significance calculated with one-way ANOVA test: ** for p-value 0.0332 to 0.0021, **** for p-value <0.0001.

Quantification of HA traffic between the Golgi and the plasma membrane in MDCK cells

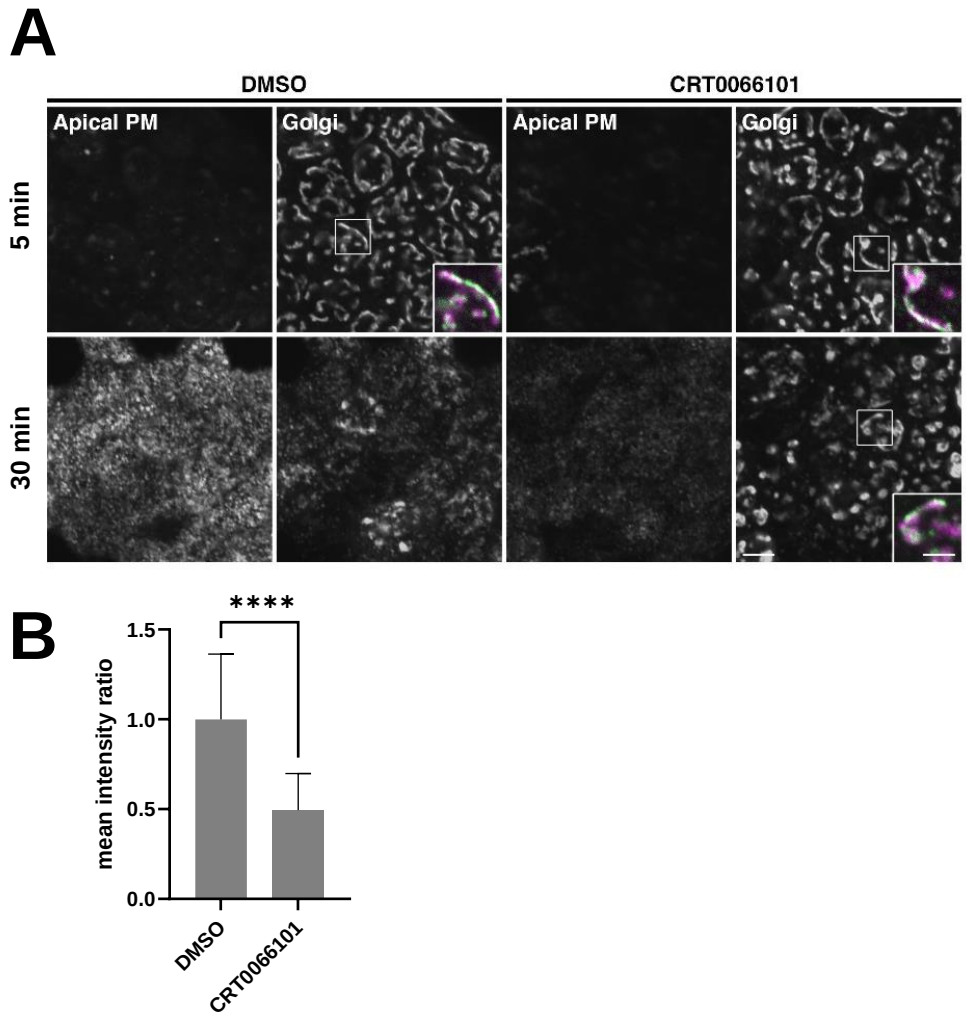

Figure 10. Effect of CRT0066101 in the secretion of HA in MDCK cells. A. Representative images of multiple MDCK cells overexpressing mKate2-FM4-HA. The greyscale images show mKate2's signal at a plasma membrane plane or at a Golgi plane, at 5 min and 30 min after addition of the D/D solubilizer. Zoom ins show the signal of GM130 (immunolabeled) in green, and HA signal (reported by mKate2) in magenta. Scale bar 3µm. (Unpublished data shared by Y. Wakana). **B.** Mean fluorescence intensity ratio of HA at the plasma membrane of MDCK cells. Comparison between a control (DMSO), and the inhibitor CRT0066101. N of the DMSO = 451 cells, N of the PKD2 siRNA 1 = 378 cells. Statistical significance calculated with two-tailed Welch's t-test, p-value < 0.0001.

Figure 10 shows the mean fluorescence intensity ratio of HA at the plasma membrane, calculated as explained in equation (1). The fluorescence intensity at the plasma membrane was calculated by integration of the HA fluorescence intensity divided by the cell area. The fluorescence intensity at the Golgi was calculated by integration of the fluorescence intensity at the segmented Golgi structures (obtained from the TGN46 channel), divided by the Golgi area (TGN46 mask). One

can appreciate that the inhibition of all PKD isoforms with CRT0066101[17] results in lower secretion of HA, indicating that PKD activity is necessary for the secretion of this protein.

4. MECHANO-REGULATED CARGO TRANSPORT TO FOCAL ADHESIONS

The following project has been in collaboration with J. Vera (ICFO-Institute of Photonic Sciences, Spain) (unpublished work). This project is framed within the broader context of a research in which mechanotransduction by cell adhesions is investigated. Cell adhesions are plasma membrane regions enriched in integrins ad other adhesion proteins that are used by cells to attach to their substrate. In cell migration, actin, microtubules, and intermediate filaments are regulated by common signaling cascades that initiate and coordinate their polarization and extension toward the region where the cell front is formed.[19] Mechanotransduction, which refers to the series of mechanism by which cells convert mechanical stimuli from their environment into intracellular biochemical signals, is essential for cell migration. Cells with strong matrix adhesions and high contractility migrate in a mesenchymal manner, adhering to the extracellular matrix (ECM) via integrin-mediated focal adhesions (FAs).[19] FAs play a crucial role interacting with the actin cytoskeleton and microtubules to mediate force transmission and signal transduction.[20]

Mechanotransduction occurs via: *(i)* integrin activation and FA formation[21], *(ii)* force transmission through biochemical signals by mechanosensitive proteins like the focal adhesion kinase (FAK)[22], *(iii)* cytoskeletal reorganization[23], and *(iv)* changes in gene expression.[24]

One needs to consider that most of the plasma membrane proteins come from the secretory pathway, and are therefore processed through the ER and the Golgi apparatus.[25] Moreover, these two organelles are key to determine the lipid composition of the plasma membrane, through coordinated lipid synthesis, modification, and transfer mechanisms, involving both vesicular and non-vesicular pathways.[26] It is therefore logical to think that the secretory pathway might be in high synchrony with the mechanical sensing pathways that regulate cell adhesion and migration.

Indeed, it has been shown that Rab6-positive carriers, which transport CD59, TNFα and collagen X, are delivered to so-called "exocytosis hotspots" very close to FAs,

and contribute to FA turnover during directed cell migration.[27,28] The trafficking to FAs of these Rab6-positive carriers is Rho- and PKD-dependent.[29] Given that PKD is also necessary for CARTS fission at the TGN, we wanted to assess whether CARTS are also trafficked to FAs. This could establish a first link between CARTS and mechanosensation at FAs.

To do so, we analyzed the spatial delivery of CARTS at the plasma membrane and looked at the distance of these carriers to FAs. We used PAUF-mKate2-FM4 to synchronize protein secretion, and looked at the presence of PAUF-positive carriers by TIRF microscopy. FAs were imaged by overexpression of Paxillin-eGFP, a bona fide marker protein of these structures. We looked at the mean distance to FA boundaries of the last 5 seconds of the traces of PAUF-mKate2-FM4 before disappearance, to quantify whether there was a spatial preference for the delivery of CARTS to FAs.

4.1. METHODS

Cell culture and molecular biology

mKate2-FM4-PAUF plasmid was cloned by Y. Wakana (School of Life Sciences, Tokyo University of Pharmacy and Life Sciences, Japan) from the plasmid mKate2-FM4-GPI (generous gift from C.G.Burd, Yale School of Medicine, New Haven, CT).

HeLa cells were grown in DMEM supplemented with 10% FBS, and 1% penicillin and streptavidin. Cells were seeded on 35 mm cell imaging dishes with glass bottom (#81218-200, Ibidi) the previous day. The imaging dishes had been previously coated with fibronectin by incubation with a solution at 10 µg/ml for 30 minutes at 37ºC. Overexpression was performed with X-tremeGENE 9 DNA transfection reagent (Roche), 20 hours before the experiment, and according to the manufacturers' protocol.

Secretion synchronization

Cells were incubated at 20ºC for 45 minutes with the 1 µM of D/D solubilizer (to dissolve mKate2-FM4-PAUF aggregates and allow this protein to leave the ER) and 100 nM of cycloheximide (to inhibit new protein synthesis)[30]. Afterwards, the medium was exchanged for the same solution with D/D solubilizer and cycloheximide, but also including 25 mM HEPES pH 7.4. Cells were moved to the microscope for incubation at 37ºC. Imaging was started after 45 min incubation.

Imaging with TIRF microscopy

Imaging was performed on a Nikon Eclipse Ti system using a 100x oil objective with NA of 1.49, equipped with an ANDOR technology EMCCD iXon 897 camera, with a 256x256 field of view, and 156.7 nm pixel size. The system has 4 laser lines of wavelength: 405 nm, 488 nm, 560 nm and 647 nm. Imaging at 37°C was achieved with a custom-built incubator. The lasers were placed in TIRF. Videos were recorded at a frame rate of 1 frame/second with continuous illumination at 10% laser power (~18.25 W/cm^2) of the 560 nm laser. Before and after the imaging, one screenshot of the paxillin-labeled focal adhesions was taken using the 488 nm laser at 5% laser power (~1.55 W/cm^2), 1 frame/second integration time.

4.2. DEVELOPED ANALYSIS

Diffusion data from all cells was integrated as single histograms to better identify trends. This enhanced the statistical power of our analyses by providing a larger number of data points. However, we would like to note that it would have been more appropriate to select a descriptor such as the mean or the median values per experimental repeat, which ideally would be different samples containing multiple cells. The primary reason for not doing so was the lack of sufficient data. Despite this, I chose to highlight the developed image analyses in this section, acknowledging that the published data should ideally contain more comprehensive datasets. This data is preliminary and unpublished, and further experiments will aim to address these limitations and provide a more robust dataset.

Carrier detection and tracking

Detection and tracking were performed using TrackMate.[31] Spot detection with TrackMate was performed using the LoG (Laplacian of Gaussian) detector, an estimated object diameter of 0.6 µm, a quality threshold of 1, and subpixel localization was allowed. No further quality thresholding was applied. The tracking was performed with the LAP tracker, allowing a linking distance of 1.2 µm, a gap-closing max distance of 1.2 µm, and 1 gap-closing max frame gap.

Diffusion analysis

The diffusion analysis was performed with a self-written MATLAB user interface (described in **Chapter 4**). It can be found in the following Github repository link: https://github.com/JessicaAngulo/SPT_analysis_UI.git

This user interface allowed the selection of an ROI containing the cell area, and therefore excludes trajectories laying outside. For each identified trajectory, we computed the diffusion radius, as a measure of the mean distance explored by the

particle to the mean centroid position. The mean centroid position for a given set of coordinates (x_i, y_i) is:

$$\bar{x} = \frac{1}{N}\sum_{i=1}^{N} x_i \ \ and \ \bar{y} = \frac{1}{N}\sum_{i=1}^{N} y_i \quad (1)$$

The diffusion radius (R_{diff}) is the mean distance to the centroid position calculated as:

$$R_{diff} = \frac{1}{N}\sum_{i=1}^{N} \sqrt{(x_i - \bar{x})^2 + (y_i - \bar{y})^2} \quad (2)$$

We considered for the analysis only those trajectories longer than 20 frames, and the diffusion radius was only calculated for the last 5 seconds of the trajectory (which selects the number of N), in order to select the fusing events as much as possible.

Detection of FAs

The detection of the fluorescent FAs was performed with the same custom-written MATLAB user interface as mentioned before, which can be found in the following repository link: https://github.com/JessicaAngulo/SPT_analysis_UI.git

First, the FA marker (paxillin-eGFP) channel image (contrast adjusted) is Gaussian filtered with the MATLAB function *imgaussfilt*, which uses a 2-D Gaussian smoothing kernel of standard deviation 2. Then, this filtered image is used for the user selection of an intensity threshold, which in turn is used on the original image. The obtained binary mask is already used for the identification of the structures' boundaries, using the function *bwboundaries* ('noholes' option).

Measurement of the distances to FA

The distance of all localizations (of the PAUF channel) to the boundaries of these identified structures (segmented FA channel) was calculated using k-nearest neighbors. This function finds the closest boundary point for each localization, and computes the distance (function *knnsearch*). Only the last 5 seconds were used for the calculation of a mean distance value.

4.3. RESULTS

We calculated the probability to disappear, by simply measuring the number of trajectories, with respect to the FA distance, as a read-out of carrier fusion with the plasma membrane. In **Figure 11A**, one can appreciate that this probability decays

with the distance to FAs, although it still remains quite high for distances larger than 5µm. In an earlier publication, S. Stehbens et al. reported similar measurements, yet tracking a different type of carriers, the Rab6-positive carriers.[28] Our distribution is broader than that reported by. S. Stehbens et al. (see **Figure 11B**). These differences may arise from many of the carriers fusing at places far from FA boundaries because they do not carry proteins important for FA turnover and mechanosensing. However, it is also possible that many of these carriers disappeared because of photobleaching or because they went out of the focal plane.

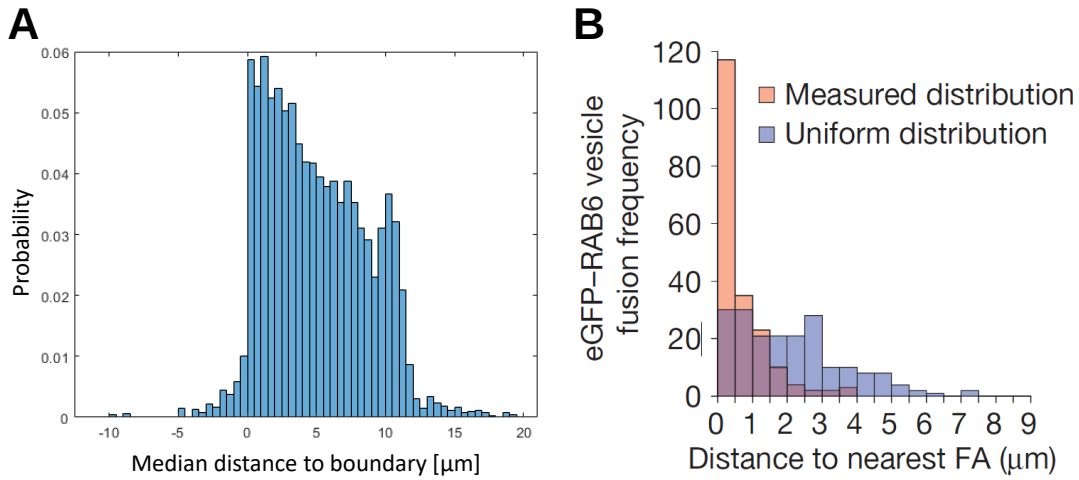

Figure 11. Probability to disappear with respect to FA distance. A. Distribution of disappearance events with respect to the distance to the FA boundaries. The distance to the FAs is calculated as the mean distance of the last 5 seconds before disappearance. N= 6 cells. **B.** Distribution of disappearance reported by S. Stehbens et al., Nature Cell Biology (2014).[28] Overexpression of EGFP-Rab6A and paxillin-mCherry on HaCaT cells. Histogram of the fusion events in a 10 min time-lapse sequence compared with a uniform distribution (20x20 pixel grid).

In order to select as much as possible, the carriers that are fusing, rather than the ones that disappeared for other reasons (photobleaching or out-of-plane movement), we computed the diffusion radius. We expect that carriers display a rather confined motion before fusing with the plasma membrane due to the docking mechanisms. This was quantified by examining at the diffusion radius of the last 5 seconds of the trajectory. **Figure 12A** shows the distribution of the mean diffusion radius over these 5 last seconds with respect to the distance to FA boundaries. Carriers with very small diffusion radius (i.e. relatively confined trajectories) disappear very close to FAs, mostly within a 5µm region. They have a very defined diffusion radius, which could indicate a relative size of the delivery hotspot, or a spatial confinement within the carrier before delivery. The diffusion radius,

understood as the mean distance to centroid position, could indicate that the protein moves within a carrier of about 200 nm in diameter, which fits with the measured size of CARTS.[2]

If we again look at the distribution of diffusion radius, but we separate carriers that exhibit very small diffusion radius (smaller than 0.15 µm) from the ones that have a higher diffusion radius (higher than 0.15 µm), one can appreciate that the more confined carriers (i.e. small diffusion radius) are located very close the FA boundaries before disappearing, whereas the highly mobile carriers (i.e. large diffusion radius) uniformly disappear at all distances to FAs (see **Figure 12B**).

Taken together, these data indicate that there is a preference for CARTS fusion at plasma membrane sites very close to FAs. So far, it seems that CARTS contain molecules that are important for cell adhesion and migration. It would be interesting to report which of the proteins transported through CARTS might be related to this cellular activity. Also, whether these proteins travel exclusively through this carrier, and whether the Rab6-positive carriers investigated previously were CARTS. J. Vera is also performing experiments in cells mechanically stretched, to see whether there is a feedback loop that promotes cargo delivery at FAs upon mechanical stress.

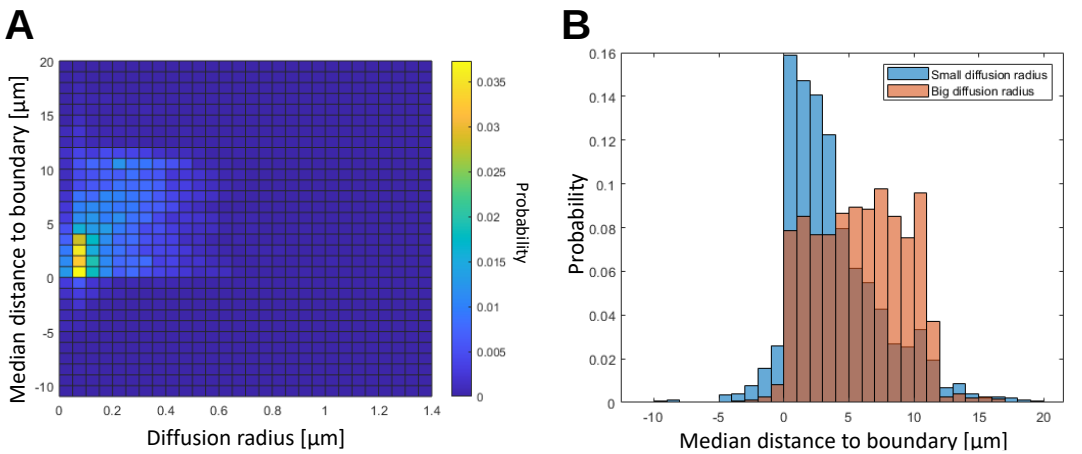

Figure 12. Diffusion radius of the carriers before disappearance. Both the diffusion radius and the distance to the FA boundaries are calculated with the last 5 seconds of the trajectory. N = 6 cells. **A.** Heatmap of the diffusion radius with respect to the mean distance to the FA boundaries. **B.** Distribution of the diffusion radius with respect to FA distance. Diffusion radius smaller than 0.15 µm are considered small (blue), and diffusion radius larger than 0.15 µm are considered large (orange).

5. DYNAMICS OF ER-TO-GOLGI TUBULAR TRANSPORT

This contribution was published in: Wong-Dilworth, L., Bregu, G., Restel, S., Rodilla-Ramirez, C., Ebeling, S., Harel, S., Leupold, P., Grimm, J., Lavis, L.D., Angulo-Capel, J., Campelo, F., Bottanelli, F. (2023) Nanoscale imaging reveals the mechanisms of ER-to-Golgi transport via a dynamic tubular vesicular network. bioRxiv 2023.10.27.563951

The publication investigates the process of ER-to-Golgi transport. As already explained in **Chapter 1**, the classical ER-to-Golgi transport model involves the formation of small COPII vesicles, that bud from ERES and travel to the Golgi via the intermediate compartment (the ERGIC). However, a number of processes cannot be simply explained within the framework of this model, such as how large and rigid cargo proteins, such as collagens, are trafficked from the ER to the Golgi. It has been suggested that cargoes could instead travel through larger tubules rather than vesicles. These tubules have been shown to either be structurally separated from the ER and Golgi[32,33], or to fuse both membranes.[34] In this paper, Wong-Dilworth et al. bring experimental evidence that is compatible with a model in which there is more continuity between the ER and the ERGIC membranes. With live-cell super-resolution STED microscopy, the authors show the step-by-step cargo transfer from the ER to the Golgi through an interconnected tubular network that is positive for the small GTPase ARF4, the ERGIC-receptor protein ERGIC53, and partially decorated by COPI components. The main points of the publication include:

(i) ARF4 and COPI define a highly dynamic tubular-vesicular network of ER-Golgi

intermediate compartments.

(ii) The ARF4 network dynamically remodels around static ERES.

(iii) Anterograde cargo, visualized by secretion synchronization using the RUSH assay, percolates through the ARF4 tubular network.

(iv) Acute degradation of ARF4 triggers COPI dissociation and mis-regulation of ER-Golgi transport.

Figure 13 shows how this tubular network could serve as an intermediate compartment between the ER and the ERGIC or *cis*-Golgi cisternae, and that functions for cargo sorting to either anterograde or retrograde transport. While this network is decorated with ARF4 and COPI components, COPI is only present in some subdomains of the carriers, possibly acting as retrograde transport sorting domains.

Retrieval to the ER could be then mediated by COPI, also present in the tubules, through COPI vesicles or direct tubular connections with the ER. Anterograde transport could travel to ERGIC structures or directly to the *cis*-Golgi through these transport tubules, or by direct contact with the ER.

My contribution in this publication included 3 different quantifications needed to support the conclusions laid down in points *(i)* and *(ii)*. The first one was a quantitative measurement of the mobility of peripheral ERGIC tubular structures, as seen by live-cell confocal fluorescence microscopy; as well as a comparison of this measure between more rounded tubules, and more elongated tubules. This was performed both in HeLa and human retinal epithelial (RPE-1) cells. The second contribution was the measurement of the movement of peripheral ERGIC tubular structures as compared to ERES. Finally, I performed a quantification of the proximity between ARF4 tubules and ERES.

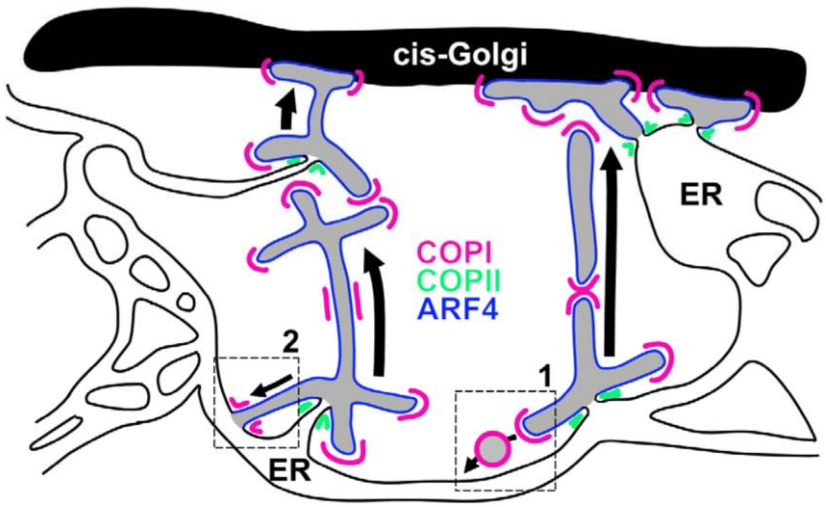

Figure 13. ER-to-Golgi transport occurs via a dynamic network or ARF4 tubules. A tubular network decorated with COPI and ARF4, and with no COPII serves as an intermediate compartment that regulates cargo destination. Cargo could travel through this ERGIC structures through intermediate tubules or by direct contact with the ER. ERGIC-to-ER retrieval could be mediated by either 1) COPI vesicles forming from ERGICs and fusing with the ER network below or 2) direct tubular connections with the ER. (Taken from Wong-Dilworth, L. et al., BioRxiv (2023)[35]).

5.1. METHODS

Performed by L. Wong-Dilworth (Institute of Biochemistry, Freie Universität Berlin, Germany) and other members of F. Bottanelli's laboratory.

CRISPR-Cas9 gene editing

ARF4 endogenous Halo tagging is described in Wong-Dilworth, L. et al., Journal of Cell Biology (2023).[36] Sec13 endogenous SNAP tagging is described in Wong-Dilworth, L. et al., BioRxiv (2023).[35]

Sample preparation

Imaging of live-cell samples was carried out on glass-bottom dishes (3.5 cm diameter, No. 1.5 glass; Cellvis) coated with fibronectin (Sigma-Aldrich). Live cells were labeled for 1 h using HaloTag and SNAP substrates at a concentration of 1 µM. To remove the excess of dye, cells were washed three times with growth medium after the staining and left for 1 h in an incubator at 37°C and 5% CO2. Imaging was done in FluoBrite DMEM (Gibco) supplemented with 10% FBS, 20 mM Hepes (Gibco), and 1× GlutaMAX (Gibco). Live-cell experiments were performed at 37°C. For confocal imaging of ARF4 and Sec13, the combinations of Janelia Fluor dyes were:

- ARF4-Halo: JF552-HaloTagligand
- Sec13-SNAP: JFX650-SNAPTagligand

Laser-scanning confocal microscopy

Imaging was carried out on an Abberior Expert Line STED microscope supplied with 485, 561 and 646 nm laser lines and an Olympus Objective UPlanSApo 100x, NA 1.40, WD 0.13. Two-color images were acquired sequentially line by line. The detection was performed using avalanche photodiodes with detection windows set to 571-630 nm and 650-756 nm. Acquisition was done using the Instruments Development Team, Imspector Image Acquisition & Analysis Software v16.3.16118 (http://www.imspector.de). The pixel size was set to 60 nm or 80 nm. For live-samples, the temporal resolution was 2 seconds. Live-cell imaging was carried out at 37°C.

5.2. DEVELOPED ANALYSIS

Calculation of the proximity of ARF4 tubules to ERES

The spatial proximity between ARF4-positive structures and ERES (detected by using the COPII component Sec13 as a marker protein) was quantified from images acquired with laser-scanning confocal microscopy was quantified with a custom-made MATLAB code, available on the following Github link: https://github.com/JessicaAngulo/Tubules_proximity_analysis.git

The structures in each channel (ARF4 and Sec13 channels) were detected by firstly applying a dehazing technique (*imreducehaze* function), Gaussian filtering (*imgaussfilt* fuction), and contrast adjusted (*imadjust* function) to enhance image quality. Second, an automatic intensity threshold was applied, defined as the mean pixel intensity plus 2 times the standard deviation, for the images on HeLa cells, or the mean intensity plus 1 time the standard deviation, for images on the RPE-1 cells. Structures were detected using the *bwboundaries* function on the binary image. Only structures with a minimum area of 10 pixels and a maximum area of 400 pixels were retained (pixel size was 0.06 µm). The upper size limit allowed for the exclusion of those large structures found in the ARF4-labeled perinuclear area (see **Figure 14**). Next, the distances between the centroid positions of the ARF4- and Sec13-labeled structures (center-to-center distance) were calculated using the nearest neighbor distance approach (*knnsearch* function). Based on visual inspection, ERES found within 6 pixels (360 nm) to their nearest ARF4-positive structure were considered to be adjacent.

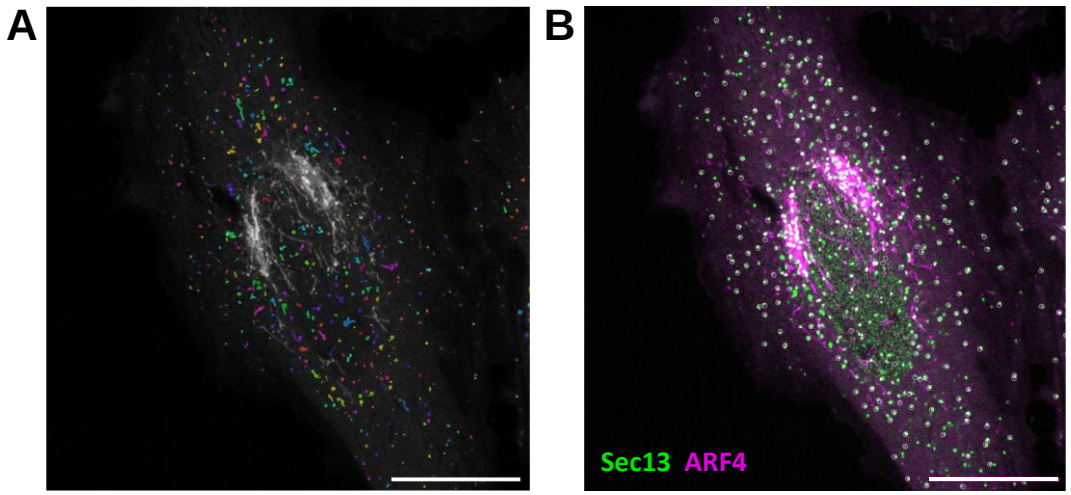

Figure 14. Proximity analysis between ARF4 tubules and ERES on HeLa cells. ERES were labeled with endogenously SNAP-tagged Sec13. ARF4 was endogenously Halo-tagged, and labeled with JF552 fluorophore. Scalebar 20 µm. **a.** Detection of ARF4 tubules. Only the ARF4 channel is shown in the greyscale image for simplicity. Segmented structures are colored in different colors to distinguish each individual structure. **b.** Proximity between Sec13 puncta (green) and ARF4 tubules (magenta). When the structures are closer than 6 pixels, they were considered to be adjacent (labeled as white circles).

Individual cells were used as experimental repeats, versus different samples containing data from several cells, to better capture the intrinsic biological variability present within the cell population. This enhanced the statistical power of our analyses by providing a larger number of data points. Since different conditions were

not compared, we considered that there would not be pseudoreplication.[10] We ensured that each cell contained sufficient information (i.e. high number of punctate structures), and that each one was independently processed and analyzed.

Detection and tracking of Sec13 puncta

The detection and tracking of the ERES (imaged with the COPII component Sec13), which generally appeared as round structures, was performed using TrackMate.[31] Spot detection with TrackMate was performed using the LoG (Laplacian of Gaussian) detector, with an estimated object diameter of 0.6 µm, a quality threshold of 1, and subpixel localization was allowed. No further quality thresholding was applied. The tracking was performed with the LAP tracker, allowing a linking distance of 1.2 µm, a gap-closing max distance of 1.2 µm, and 1 gap-closing max frame gap.

Detection and tracking of ARF4 tubules

TrackMate did not perform satisfactorily on the ARF4 structures, due to their heterogeneous shape (from round structures to rather elongated tubules; see **Figure 15A**). To circumvent this, we leveraged the morphological resemblance between ARF4 structures and mitochondria and used MitoMeter, an algorithm for segmentation and tracking of elongated structures such as mitochondria.[37] MitoMeter segmentation was performed with a minimum structure area of 0.3 µm, and a maximum structure area of 200 µm. No custom Gaussian filtering and no threshold were applied. For the tracking, the maximum velocity threshold was set to 1 µm/s. Fission and fusion events were considered.

Using the shape characterization provided by Mitometer, the aspect ratio of the ARF4 tubules was used for the classification of the diffusion parameters. The aspect ratio is defined as the major axis length divided by the minor axis length. Structures with an aspect ratio smaller than 1.5 were categorized as rounded, while those with a larger aspect ratio were considered elongated. When considering entire trajectories, the criterion to classify them as rounded or elongated was based on a majority rule, that is if more than half of the frames were assigned to either of these categories, then the entire trajectory was assigned to that category (see **Figure 15A**).

Characterization of ARF4 and Sec13 dynamics

Further analysis of the tracking data was performed using a custom-made script coded in MATLAB (available on: https://github.com/JessicaAngulo/Tracking_tubules.git).

The ARF4-labeled perinuclear area was excluded from the analysis. For each identified structure, we computed *(i)* the instantaneous velocity in every frame as the frame-by-frame displacement divided by the frame time and *(ii)* the diffusion coefficient (also referred to as instantaneous diffusion coefficient, D_{1-4}), which was calculated from the time-averaged mean square displacement (TA-MSD). Specifically, for a particle trajectory with coordinate position vectors $\boldsymbol{x}_j$, sampled in time N times, the TA-MSD at time lag t_{lag} is calculated as:

$$TA\text{-}MSD\left(t_{lag} = m\Delta t\right) = \frac{1}{N-m}\sum_{i=1}^{N-m}\left[\boldsymbol{x}_j(t_i + m\Delta t) - \boldsymbol{x}_j(t_i)\right]^2 \quad (3)$$

where $t_{lag} = m\Delta t$, for $m = 1\ to\ 4$, where Δt is the frame time. From here the diffusion coefficient, D_{1-4}, was computed by a linear fit of:

$$TA\text{-}MSD\left(t_{lag}\right) = 4D_{1-4}t_{lag} + b \quad (4)$$

using the first four time lags. The "y" intercept (b) is also fitted for each trajectory. For these computations, we used only those trajectories with a minimum trajectory length of 12 frames.

Different samples containing data from several cells were used to compare differences between different experimental conditions, and avoid pseudoreplication.

5.3. RESULTS

Diffusion properties of peripheral ARF4-positive ERGICs

In this publication, thanks to the high spatial resolution of live-cell STED microscopy time-lapse movies, we were able to distinguish between different subclasses of ARF4-positive ERGICs in both HeLa and RPE-1 cell types. Those tethered to the cis-Golgi cisternae are named in this publication Golgi-associated ERGICs (GA-ERGICs), whereas those located at the cell periphery are named peripheral ERGICs (p-ERGICs). Moreover, ARF4 forms highly mobile tubules that emanate from static p-ERGICs. In order to provide an unbiased quantitative assessment as whether it is true that there are two populations of ARF4-positive p-ERGICs, we looked at their diffusion properties according to their shape (i.e. their aspect ratio). **Figure 15A** shows two examples of ARF4-positive structures with either a more elongated shape (left) or a more circular shape (right). When plotting the distributions of instantaneous velocity or diffusion coefficient with respect to their aspect ratio, we observed a clear correlation following a linear relationship, that is, the more elongated the structure is, the faster it moves (**Figure 15B-C**).

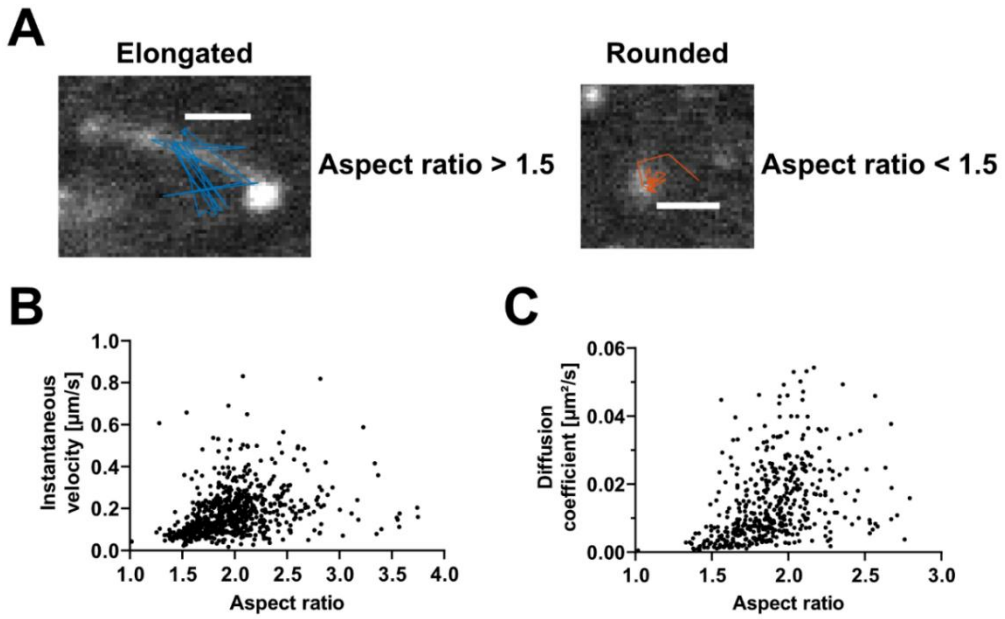

Figure 15. ARF4-positive p-ERGICs are characterized by elongated and rounded tubular-vesicular structures. A. Classification of ARF4 structures. The aspect ratio was used to determine whether a structure is elongated or rounded. Structures with an aspect ratio above 1.5 are considered elongated and structures with an aspect ratio below 1.5 are considered rounded. The aspect ratio was determined as described in the methods. Scale bar 1 µm. **B-C.** Dynamic properties of ARF4 structures detected in one representative HeLa cell with respect to the mean aspect ratio. **B.** Instantaneous velocity. **C.** Diffusion coefficient. (Published in Wong-Dilworth, L. et al., BioRxiv (2023)[35]).

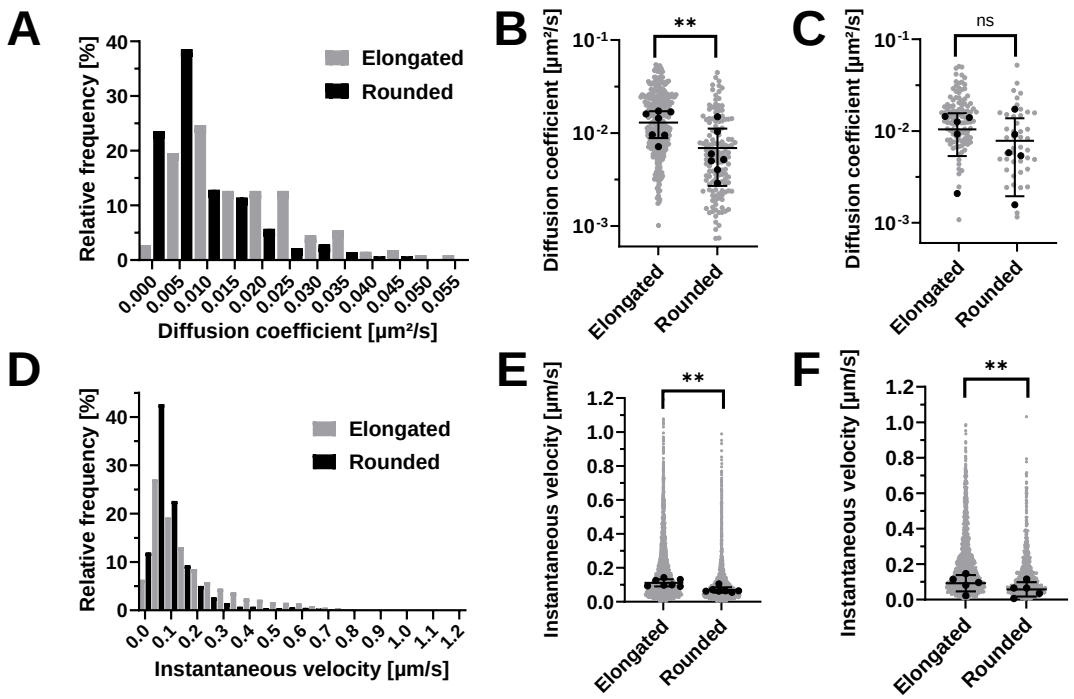

Figure 16. Diffusion properties of the elongated and rounded ARF4-positive p-ERGIC structures. A. Relative frequency of the diffusion coefficient from elongated (grey bars) and rounded (black bars) ARF4 structures. Analysis on HeLa cells. **B-C.** Scatter dot plot of the diffusion coefficient of elongated and rounded ARF4 structures. Error bars represent mean and SD of the cell median values (black dots). Significance calculated between the median values per cell with a paired t-test. **B.** Analysis on HeLa cells. Black dots represent median value for each cell (N = 7 cells), and grey dots represent individual structure values (Elongated N = 335, rounded N = 143 structures). P-value = 0.0032. **C.** Analysis on RPE-1 cells. Black dots represent median value for each cell (N = 5 cells), and grey dots represent individual structure values (Elongated N = 108, rounded N = 45 structures). p-value = 0.2052. **D.** Relative frequency of the instantaneous velocity from elongated (grey bars) and rounded (black bars) ARF4 structures. Analysis on HeLa cells. **E-F.** Scatter dot plot of the instantaneous velocity of elongated and rounded ARF4 structures. Error bars represent mean and SD of the cell median values. Significance calculated between the median values per cell with a paired t-test. **E.** Analysis on HeLa cells. Black dots represent median value for each cell (N = 7 cells), and grey dots represent individual displacement values (Elongated N = 6548, rounded N = 3617 displacements). P-value = 0.0016. **F.** Analysis on RPE-1 cells. Black dots represent median value for each cell (N = 5 cells), and grey dots represent individual displacement values (Elongated N = 1960, rounded N = 979 displacements). P-value = 0.0046. (Published in Wong-Dilworth, L. et al., BioRxiv (2023)[35]).

Figure 16 shows the calculated diffusion coefficients and instantaneous velocities of the detected elongated and rounded structures both for HeLa and RPE-1 cells. In HeLa cells, we observed that ARF4 elongated structures have a higher diffusion coefficient and instantaneous velocities than the rounded ones. In the case of RPE-

1 cells, the differences in the diffusion coefficient between rounded and elongated structures is not significant, but the instantaneous velocity is higher on elongated structures as compared to rounded ones. However, it is to be noted that the statistics for the RPE-1 cell line are smaller. This suggests that there are different populations of p-ERGICs of different shape and dynamics, that could have distinct cellular functions. A possible working hypothesis would be that the rounded and more immobile structures could be stable ERGICs specialized in the transport to different destinations, whereas the more mobile tubular structures may connect the rounded ones transferring cargo from one to another.

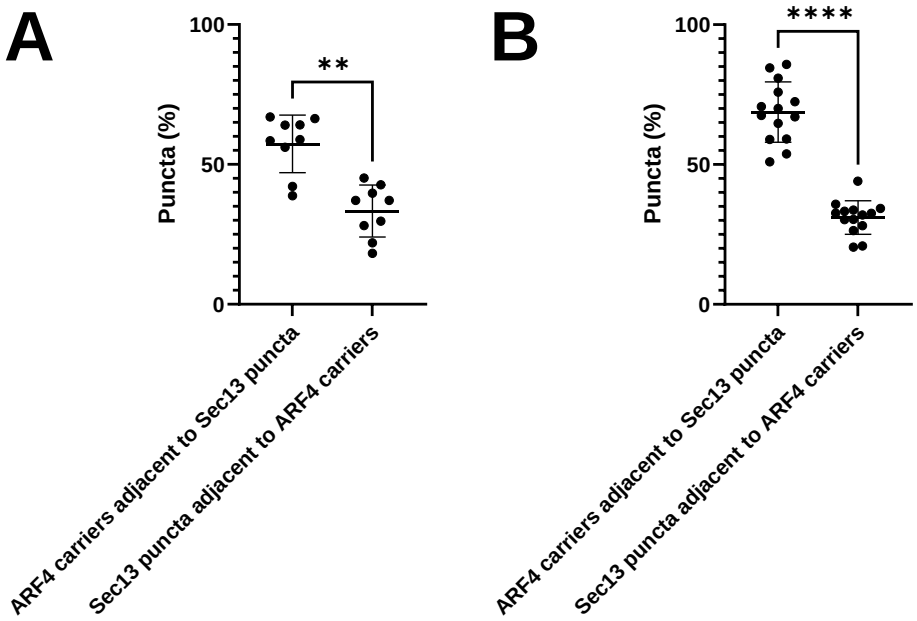

Figure 17. Colocalization of ARF4 and Sec13. Quantification of ARF4-positive carriers adjacent to Sec13-labeled ERES and Sec13-labeled ERES adjacent to ARF4-positive carriers. Each spot represents the mean percentage per cell, each one with 200-700 puncta. **A.** Quantification on HeLa cells. Significance calculated with a 2-tailed paired t-test, p-value=0.0013. **B.** Quantification on RPE-1 cells. Significance calculated with a 2-tailed paired t-test, p-value<0.0001. (Published in Wong-Dilworth, L. et al., BioRxiv (2023)[35])

Proximity between ARF4 tubules and ERES

The authors showed that, both in HeLa and RPE-1 cells, observed with confocal time-lapse microscopy, the majority of the ARF4-positive p-ERGICs appeared to be associated with ERES puncta, marked by endogenously SNAP-tagged Sec13. To quantitatively assess this observation, we computed the percentage of ARF4 structures that are adjacent to Sec13 puncta, and the percentage of Sec13 puncta that are adjacent to ARF4 structure (see **Figure 17**). Our data revealed that, indeed,

most of ARF4-positive carriers are adjacent to ERES. We suggest that, in those cases, the transfer of cargo from ERES to p-ERGICs is taking place. However, most of the ERES are not associated with ARF4-positive p-ERGICs, possibly because not all of them are active in a given time point.

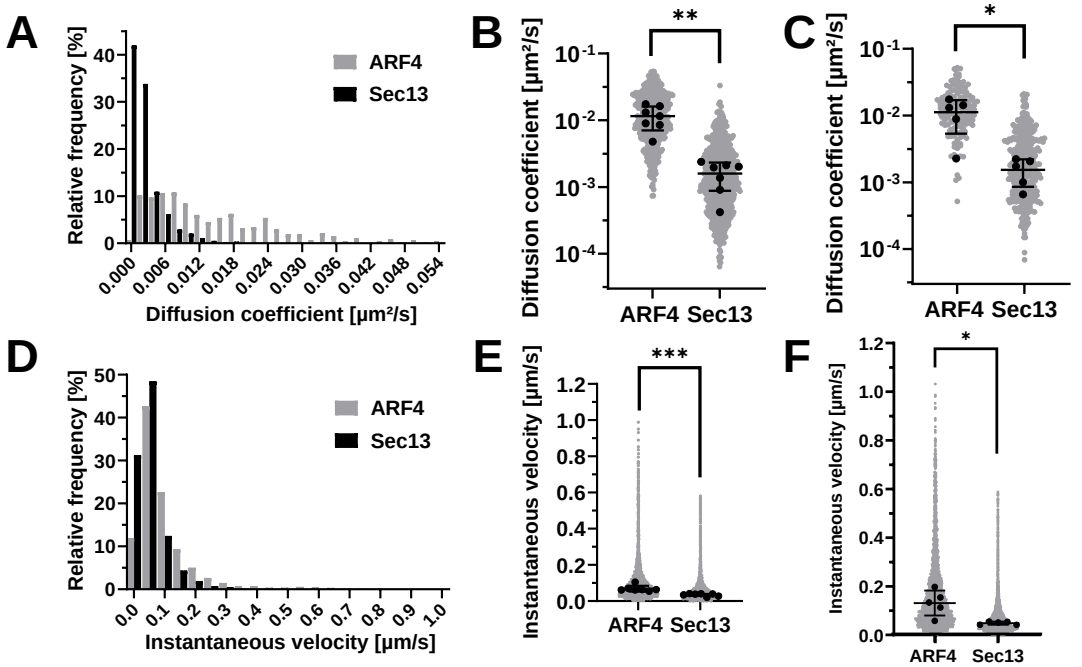

Figure 18. Diffusion properties of the p-ERGICs structures and ERES. P-ERGIC tubules are labeled with ARF4, and ERES are labeled with Sec13. **A.** Relative frequency of the diffusion coefficient from ARF4 (grey bars) and Sec13 (black bars) structures. Analysis on HeLa cells. **B-C**. Scatter dot plot of the diffusion coefficient of ARF4 and Sec13 structures. Error bars represent mean and SD of the cell median values (black dots). Significance calculated between the median values per cell with a paired t-test. **B.** Analysis on HeLa cells. Black dots represent median value for each cell (N = 7 cells), and grey dots represent individual structure values (ARF4 N = 464, Sec13 N = 586 structures). P-value = 0.0012. **C.** Analysis on RPE-1 cells. Black dots represent median value for each cell (N = 5 cells), and grey dots represent individual structure values (ARF4 N =143, Sec13 N = 360 structures). p-value =0.0194. D. Relative frequency of the instantaneous velocity from ARF4 (grey bars) and Sec13 (black bars) structures. Analysis on HeLa cells. **E-F.** Scatter dot plot of the instantaneous velocity of ARF4 and Sec13 structures. Error bars represent mean and SD of the cell median values (black dots). Significance calculated between the median values per cell with a paired t-test. **E.** Analysis on HeLa cells. Black dots represent median value for each cell (N = 7 cells), and grey dots represent individual displacement values (ARF4 N = 3614, Sec13 N = 25391 displacements). P-value = 0.0010. **F.** Analysis on RPE-1 cells. Black dots represent median value for each cell (N = 5 cells), and grey dots represent individual displacement values (ARF4 N = 2726, Sec13 N = 11047 displacements). P-value = 0.0231. (Published in Wong-Dilworth, L. et al., BioRxiv (2023)[35]).

Diffusion properties of peripheral Sec13-positive ERGICs

Visual inspection of the microscopy time-lapse movies suggested that ARF4 tubules rapidly remodel around the stationary ERES. We therefore examined the dynamics of ARF4 tubules and Sec13 puncta. **Figure 18** shows the calculated diffusion coefficients and instantaneous velocities of the detected structures both for HeLa and RPE-1 cell lines. Both for cell lines, ARF4 tubules have a higher diffusion coefficient and instantaneous velocities than Sec13 puncta (ERES).

6. DISCUSSION

In this chapter, we have highlighted the importance of using computational approaches for quantification. Computational pipelines offer several benefits in terms of: *(i)* standardization and consistency, *(ii)* efficiency and throughput, and *(iii)* sophisticated analysis. I have performed different image quantifications in four different projects, all of them in the context of intracellular trafficking and confocal fluorescence microscopy.

The first project was in collaboration with Y. Wakana and was published in Journal of Cell Biology. My contributions included:

(i) Quantifying distances between Golgi ministacks in different channels in nocodazole-treated HeLa cells, focusing on the ER-Golgi MCS proteins Sac1 and VAP-A. In our results, the mutant Sac1 K2A is closer to VAP-A than to the cis-Golgi marker GM130. This was then useful to identify interacting partners through immunoprecipitation and mass spectrometry, particularly the identification of SCAP as a new ER-Golgi MCS protein.

(ii) Conducting colocalization quantification between carriers in different channels, particularly between the SM sensor equinatoxin-SM (EQ-SM) and the CARTS cargo PAUF. Our quantification showed that 74 ±15% of PAUF-MycHis-positive CARTS contained EQ-SM, suggesting that they CARTS and SM-rich carriers could be the same.

The second project, also in collaboration with Y. Wakana, was a quantification of the secretion of HA, after inhibiting ER-Golgi MCS components in different ways. In HeLa cells, the inhibition was performed with siRNAs against PKD2 and OSBP. In MDCK cells, the inhibition was performed with the PKD inhibitor CRT0066101. In all cases, the mean relative fluorescence intensity at the plasma membrane was reduced. This presents HA as another possible CARTS-specific cargo. Future work will focus on finding whether it can exit through other TGN-derived carrier formation pathways.

The third project was in collaboration with J. Vera, and was in the context of FA formation. It was shown that Rab6-positive carriers deliver to "exocytosis hotspots" near focal adhesions (FAs) and contribute to FA turnover during directed cell migration. We wanted to assess whether CARTS also show a similar preference, since both Rab6-positive carriers and CARTS are PKD-dependent. Therefore, we analyzed the spatial delivery of CARTS at the plasma membrane and their proximity to FAs. Using PAUF-mKate2-FM4 to synchronize protein secretion, we observed PAUF-positive carriers with TIRF microscopy. FAs were imaged by overexpressing Paxillin-eGFP. We measured the mean distance of PAUF-mKate2-FM4 carriers to focal adhesion boundaries during the last 5 seconds before their disappearance. We concluded that CARTS preferentially fuse at plasma membrane sites near focal adhesions (FAs), suggesting they contain molecules crucial for cell adhesion and migration. Future research should identify which proteins transported by CARTS are related to these activities, determine if these proteins travel exclusively via CARTS, and ascertain whether previously studied Rab6-positive carriers were actually CARTS.

The last project was in collaboration with L. Wong-Dilworth, and the results have been published in BioRxiv. This study challenges the classical model of small COPII vesicles transporting cargo from the ER to the Golgi, and proposes that larger cargoes travel through a dynamic tubular network. Using live super-resolution STED microscopy, the authors demonstrated step-by-step cargo transfer via an interconnected network marked by ARF4, ERGIC53, and partially COPI components. My contributions included quantifying:

(i) The mobility of peripheral ERGIC tubular structures, from live-cell confocal fluorescence microscopy videos, comparing rounded and elongated tubules in HeLa and RPE-1 cells. In HeLa cells, we observed that ERGIC elongated structures (labeled by ARF4) have higher diffusion coefficients and instantaneous velocities than the rounded ones. This suggests distinct populations of p-ERGICs with different shapes and dynamics, potentially serving unique cellular functions. A hypothesis is that rounded, more immobile structures are stable ERGICs specialized in transport to various destinations, while the more mobile tubular structures transfer cargo between them.

(ii) The movement of peripheral ERGIC tubular structures relative to ERES, from live-cell confocal fluorescence microscopy videos. Both in HeLa and RPE-1 cells, ARF4 tubules have a higher diffusion coefficient and instantaneous velocities than Sec13

puncta (ERES), suggesting that ARF4 tubules rapidly remodel around the stationary ERES.

(iii) The proximity between ARF4 tubules and ERES. Our data revealed that most ARF4-positive carriers are adjacent to ERES, suggesting cargo transfer from ERES to p-ERGICs at these sites. However, most ERES are not associated with ARF4-positive p-ERGICs, likely because not all are active simultaneously.

7. REFERENCES

1. Waters, J. C. Accuracy and precision in quantitative fluorescence microscopy. *Journal of Cell Biology* vol. 185 Preprint at https://doi.org/10.1083/jcb.200903097 (2009).
2. Wakana, Y. *et al.* The ER cholesterol sensor SCAP promotes CARTS biogenesis at ER–Golgi membrane contact sites. *Journal of Cell Biology* **220**, (2021).
3. Wakana, Y. *et al.* CARTS biogenesis requires VAP–lipid transfer protein complexes functioning at the endoplasmic reticulum–Golgi interface. *Mol Biol Cell* **26**, 4686–4699 (2015).
4. Mesmin, B. *et al.* A Four-Step Cycle Driven by PI(4)P Hydrolysis Directs Sterol/PI(4)P Exchange by the ER-Golgi Tether OSBP. *Cell* **155**, 830–843 (2013).
5. Wakana, Y. & Campelo, F. The PKD-Dependent Biogenesis of TGN-to-Plasma Membrane Transport Carriers. *Cells* **10**, 1618 (2021).
6. Hua, X., Nohturfft, A., Goldstein, J. L. & Brown, M. S. Sterol resistance in CHO cells traced to point mutation in SREBP cleavage-activating protein. *Cell* **87**, (1996).
7. Brown, M. S., Radhakrishnan, A. & Goldstein, J. L. Retrospective on Cholesterol Homeostasis: The Central Role of Scap. *Annual Review of Biochemistry* vol. 87 Preprint at https://doi.org/10.1146/annurev-biochem-062917-011852 (2018).
8. Deng, Y., Rivera-Molina, F. E., Toomre, D. K. & Burd, C. G. Sphingomyelin is sorted at the trans Golgi network into a distinct class of secretory vesicle. *Proc Natl Acad Sci U S A* **113**, (2016).

9. Wyles, J. P., McMaster, C. R. & Ridgway, N. D. Vesicle-associated membrane protein-associated protein-A (VAP-A) interacts with the oxysterol-binding protein to modify export from the endoplasmic reticulum. *J Biol Chem* **277**, (2002).

10. Zweifach, A. Determining how many cells to average for statistical testing of microscopy experiments. *Journal of Cell Biology* **223**, e202401074 (2024).

11. Gomez-Navarro, N. & Miller, E. Protein sorting at the ER-Golgi interface. *Journal of Cell Biology* **215**, (2016).

12. Lavieu, G. *et al.* Induction of cortical endoplasmic reticulum by dimerization of a coatomer-binding peptide anchored to endoplasmic reticulum membranes. *Proc Natl Acad Sci U S A* **107**, (2010).

13. Wakana, Y. *et al.* Bap31 is an itinerant protein that moves between the peripheral endoplasmic reticulum (ER) and a juxtanuclear compartment related to ER-associated degradation. *Mol Biol Cell* **19**, (2008).

14. Cole, N. B., Sciaky, N., Marotta, A., Song, J. & Lippincott-Schwartz, J. Golgi dispersal during microtubule disruption: Regeneration of Golgi stacks at peripheral endoplasmic reticulum exit sites. *Mol Biol Cell* **7**, (1996).

15. Deng, Y. *et al.* Activity of the SPCA1 Calcium Pump Couples Sphingomyelin Synthesis to Sorting of Secretory Proteins in the Trans-Golgi Network. *Dev Cell* **47**, (2018).

16. Shamoto, M. & Leighton, J. Cell Surface Glycosaminoglycans of Cell Line MDCK Derived from Canine Kidney. *Cancer Res* **37**, (1977).

17. Harikumar, K. B. *et al.* A novel small-molecule inhibitor of protein kinase D blocks pancreatic cancer growth in vitro and in vivo. *Mol Cancer Ther* **9**, (2010).

18. Dunsing, V. *et al.* Optimal fluorescent protein tags for quantifying protein oligomerization in living cells. *Sci Rep* **8**, (2018).

19. Seetharaman, S. & Etienne-Manneville, S. Cytoskeletal Crosstalk in Cell Migration. *Trends in Cell Biology* vol. 30 Preprint at https://doi.org/10.1016/j.tcb.2020.06.004 (2020).

20. Geiger, B. & Bershadsky, A. Assembly and mechanosensory function of focal contacts. *Current Opinion in Cell Biology* vol. 13 Preprint at https://doi.org/10.1016/S0955-0674(00)00255-6 (2001).

21. Goldmann, W. H. Mechanotransduction and focal adhesions. *Cell Biol Int* **36**, (2012).

22. Mitra, S. K. & Schlaepfer, D. D. Integrin-regulated FAK-Src signaling in normal and cancer cells. *Current Opinion in Cell Biology* vol. 18 Preprint at https://doi.org/10.1016/j.ceb.2006.08.011 (2006).

23. Wehrle-Haller, B. & Imhof, B. A. Actin, microtubules and focal adhesion dynamics during cell migration. *International Journal of Biochemistry and Cell Biology* vol. 35 Preprint at https://doi.org/10.1016/S1357-2725(02)00071-7 (2003).

24. Wang, Y. X., Wang, D. Y., Guo, Y. C. & Guo, J. Zyxin: A mechanotransductor to regulate gene expression. *Eur Rev Med Pharmacol Sci* **23**, (2019).

25. Gilchrist, A. *et al.* Quantitative Proteomics Analysis of the Secretory Pathway. *Cell* **127**, (2006).

26. Marie, M., Sannerud, R., Avsnes Dale, H. & Saraste, J. Membrane traffic in the secretory pathway: Take the 'A' train: On fast tracks to the cell surface. *Cellular and Molecular Life Sciences* vol. 65 Preprint at https://doi.org/10.1007/s00018-008-8355-0 (2008).

27. Fourriere, L. *et al.* RAB6 and microtubules restrict protein secretion to focal adhesions. *Journal of Cell Biology* **218**, (2019).

28. Stehbens, S. J. *et al.* CLASPs link focal-adhesion-associated microtubule capture to localized exocytosis and adhesion site turnover. *Nat Cell Biol* **16**, (2014).

29. Eisler, S. A. *et al.* A rho signaling network links microtubules to PKD controlled carrier transport to focal adhesions. *Elife* **7**, (2018).

30. Schneider-Poetsch, T. *et al.* Inhibition of eukaryotic translation elongation by cycloheximide and lactimidomycin. *Nat Chem Biol* **6**, (2010).

31. Tinevez, J.-Y. *et al.* TrackMate: An open and extensible platform for single-particle tracking. *Methods* **115**, 80–90 (2017).

32. Simpson, J. C., Nilsson, T. & Pepperkok, R. Biogenesis of tubular ER-to-golgi transport intermediates. *Mol Biol Cell* **17**, (2006).

33. Ben-Takaya, H., Miura, K., Pepperkok, R. & Hauri, H. P. Live imaging of bidirectional traffic from the ERGIC. *J Cell Sci* **118**, (2005).

34. Weigel, A. V. *et al.* ER-to-Golgi protein delivery through an interwoven, tubular network extending from ER. *Cell* **184**, (2021).

35. Wong-Dilworth, L. *et al.* Nanoscale imaging reveals the mechanisms of ER-to-Golgi transport via a dynamic tubular-vesicular network. *bioRxiv* (2023).

36. Wong-Dilworth, L. *et al.* STED imaging of endogenously tagged ARF GTPases reveals their distinct nanoscale localizations. *Journal of Cell Biology* **222**, (2023).

37. Lefebvre, A. E. Y. T., Ma, D., Kessenbrock, K., Lawson, D. A. & Digman, M. A. Automated segmentation and tracking of mitochondria in live-cell time-lapse images. *Nat Methods* **18**, (2021).

Chapter 4

Methodological Proposal for SPT in the Secretory Pathway

To ensure accurate single-particle tracking (SPT) in the secretory pathway, several considerations must be addressed, and optimization of both the experimental conditions and the analysis are crucial to acquire enough and meaningful data. This chapter does not aim to identify the best experimental conditions in all possible scenarios, but rather to propose control experiments and identify parameter descriptors so that any user can maximize data quality and quantity while avoiding artifacts. The focus is on the labeling strategy, the imaging, and the data analysis. Moreover, we highlight the aspects to be taken into account when comparing diffusion parameters in different studies.

1. INTRODUCTION

Thanks to technical advances, SPT is experiencing a surge in intracellular applications. Over the last decade, it has been extensively used to study nuclear proteins.[1–3] More recently, a few studies have ventured into other organelles, such as the ER. The first SPT experiments in the ER were presented by Holcman et al., which followed calreticulin, an ER localized protein, and the ER localized signal sequence KDEL, and showed that the diffusion of these proteins in the ER tubes is different from those in the tube junctions.[4] More recently, Obara et al. performed SPT of the ER protein VAP-B, and correlated its movement with ER-mitochondria contact sites.[5] It seems that SPT can begin to illuminate many intracellular molecular processes by visualizing the motion of the different molecular players.

However, SPT is still a highly specialized technique that requires significant expertise and experience from the scientist. It involves numerous details both from the experimental and analytical side that must be meticulously managed to achieve accurate results. Due to its complexity, the technique is challenging to reproduce consistently, and there is a high risk of introducing artifacts and biases, which can compromise the reliability and validity of the outcomes. To make this highly specialized technique more accessible, several steps need to be taken:

(i) Clear documentation and manuals. The specific steps need to be carefully detailed in the research articles so that they can be reproduced and/or adapted by other researchers, even by those with less experience in the technique. Although the details about the labeling, washing of the free dye, and analysis of the data are usually described in the materials and methods sections, we have identified a general gap in the literature, namely, that it is usually not explained the rationale behind the selection of that methodology, nor the type of artifacts that can be produced as a result of an incorrect handling. Hence, an unexperienced user could adopt blindly a published SPT protocol for their own protein of interest without adapting it to the specific needs, obtaining a suboptimal at best, or artefactual at worst, performance. For instance, if the unbound dye is not properly washed before imaging the protein of interest, it will result in the inaccurate determination of the diffusion properties, as free dye trajectories would be erroneously ascribed to real protein trajectories.

(ii) Standardization of protocols. Many details both in the experimental and the analytical part are very differently chosen across research articles. This could result in different effective results of the calculated parameters, making it difficult to

compare them among different studies. For instance, the selection of the imaging frame rate varies widely across different research articles. This could yield different effective diffusion coefficients for the same protein and experimental conditions.[6] From the analysis side, many different diffusion parameters are usually calculated to report changes upon different conditions. Even when the reported parameter is the diffusion coefficient calculated with the TA-MSD, this calculation is implemented differently by different scientists (e.g., the fitting has been performed using different number of time lags), adding confusion in the interpretation of the experimental data.

(iii) Quality control and validation. In order to identify possible artifacts and biases, scientific works should include negative controls, in order to account for non-specific and background signals; as well as positive controls, i.e., use samples with well-characterized molecules with known diffusion properties to validate the accuracy of the SPT setup.[7] For this validation to be performed by other scientists in the community, it would be also interesting that the raw data were freely and openly available through cloud-based platforms for data storage, sharing, and collaborative analysis.

(iv) Use of automation and technology. Analysis pipelines should be available and easy to use, not only for the community to check the published data, but also so that they can be used on new data and the results can be compared. Nowadays, the analysis pipelines are often not available in public repositories such as Github, or they are not easy to implement. It is therefore necessary to implement integrated real-time data processing and analysis software that can track particles and calculate diffusion properties on-the-fly. This allows for immediate feedback and adjustment of experimental conditions if necessary.

1.1. CONSIDERATIONS FOR THE IMPLEMENTATION IN THE SECRETORY PATHWAY

There are specific challenges when using SPT in the context of the secretory pathway. Following the recommendations described above, one should adopt specific strategies to enhance the reliability and reproducibility of results. The first challenge is that, to visualize single molecules within intracellular compartments, one cannot generally use TIRF or widefield illumination, as they do not reach deep enough into the cell, or have enough signal-to-background for proper single molecule detection, respectively. For intracellular SPT, one typically uses HILO

illumination. By contrast to TIRF, HILO illumination allows the imaging of intracellular targets well enough above the cover glass. HILO also reduces background fluorescence and enhances contrast as compared to widefield illumination, although to a lesser extent as when using TIRF illumination. Another level of complexity of intracellular SPT is that HILO illumination only captures a thin sheet volume (an almost 2D space), so tracking this reduced space often produces fewer and shorter trajectories, as proteins can move away from the illuminated volume. It is thus paramount to optimize the methods as much as possible to acquire meaningful data of the highest possible quality and quantity.

In this chapter, we aimed at proposing a full experimental pipeline for intracellular SPT, in which we describe the necessary control experiments, and identify the parameter descriptors that should be computed and measure in order to maximize the amount and quality of the collected data without major artifacts. The focus is on three critical steps in SPT: *(i)* the labeling strategy, *(ii)* the imaging strategy, and *(iii)* the analysis of the data.

First, intracellular labeling usually comes in hand with the use of self-labeling tags (such as HaloTag or SNAP-tag) and conjugated organic dyes. Self-labeling tags allow the use of fluorophores of superior photophysical properties to those of fluorescent proteins, as well as a straightforward means to obtain a sparse sampling of the molecules of interest. Despite these indisputable advantages over fluorescent proteins, they still present their own set of challenges, that we will describe below. Here, we propose a set of experiments that will help SPT users to rationally select the most convenient dye, minimize free dye (and therefore maximize the labeling specificity), and optimize the labeling concentration (which will depend on different factors that are intrinsic to the protein of interest, such as its characteristic instantaneous velocities).

Second, from the imaging point of view there are also multiple parameters that need to be optimized for each protein of interest. These parameters include the excitation laser power, the imaging frame rate, etc., which highly depend on the optical system, the selected dyes, and the protein being investigated. Therefore, we do not aim at choosing the best parameters for all possible scenarios (as this is something impossible), but rather propose a set of experiments and measurements that will serve any user to identify the best experimental conditions for their own research.

And third, regarding the analysis of the collected data, we compare the output from different analysis strategies. Motion parameters are calculated in various ways,

leading to different values even for the same parameters in similar experimental conditions. We emphasize a few considerations for comparing results from different studies. As a key takeaway message, comparing absolute values between studies is often unreliable due to the many specific details of experimental conditions and analysis strategies.

2. METHODS

2.1. EXPERIMENTAL METHODS

Cell culture and molecular biology

HeLa cells were grown in DMEM supplemented with 10% FBS (without antibiotics). Cells were seeded on 35 mm cell imaging dishes with glass bottom (#81218-200, Ibidi). The following day, plasmid transfection was performed using X-tremeGENE 9 DNA transfection reagent (Roche), 20 hours before fixation, and according to the manufacturers' protocol.

The plasmid used in this chapter is Halo-CALR (encoding calreticulin) gifted by E. Avezov (UK Demential Research Institute, Cambridge, UK).

The cell line HeLa Cab45 RUSH was gifted by D. Gershlick (Cambridge Institute for Medical Research, The University of Cambridge, UK).[8] It stably expresses Strep-KDEL and SBP-Cab45-Halo.

Sample preparation

For fixed samples, cells were fixed 20 hours after transfection by a 20-minute incubation with 4% PFA, and the PFA was quenched incubating with 0.1% $NaBH_4$ (w/v in PBS, Fischer Scientific, #S/2560148) for 7 minutes. This was performed to avoid that the leftover PFA would immobilize the free dye. NaBH4 reacts with the free aldehyde groups of unreacted PFA, reducing them to alcohols, thereby preventing them from reacting with other components in the sample, including free dye molecules.[9,10] Cells were then labeled with either 1, 0.1, or 0.01 nM JF646, JF549, by incubation for 15 minutes at 37°C and 5% CO_2.[11] Alternatively, we also labeled with 1 µM of the photoactivatable PA-JF646, or PA-JF549-HaloTag ligands, by incubation for 15 minutes at 37°C and 5% CO_2.[12] They were washed by incubation with DMEM (10% FBS, without antibiotics, without Phenol red) for different amounts of times (from 15 min to 2 hours, specified in the results), at 37°C and 5% CO_2. Finally, the medium was changed to imaging medium consisting of DMEM (10% FBS, without antibiotics, without Phenol red) with 25 mM HEPES pH 7.4 and cells were

taken for imaging. After each of these steps, the samples were washed 3 times with PBS.

For live samples, cells were labeled with either 1, 0.1, or 0.01 nM JF646, JF549, by incubation for 15 minutes at 37°C and 5% CO_2.[11] Or with 1 µM of the photoactivatable PA-JF646, or PA-JF549-HaloTag ligands, also incubation for 15 minutes at 37°C and 5% CO_2.[12] Cells were washed by incubation with DMEM (10% FBS, without antibiotics, without Phenol red) for 2 hours, at 37°C and 5% CO_2. Finally, the medium was changed to imaging medium consisting of DMEM (10% FBS, without antibiotics, without Phenol red) with 25 mM HEPES pH 7.4 and cells were taken for imaging. After each step, the samples were washed 3 times with PBS.

SPT imaging

Imaging was performed on a Nikon Eclipse Ti system using a 100x oil objective with NA of 1.49, equipped with an ANDOR technology EMCCD iXon 897 camera, with a 512x512 pixels field of view, 156.7 nm pixel size, and an EM gain of 100. The system has 4 laser lines of wavelength: 405 nm, 488 nm, 560 nm and 647 nm. Imaging at 37°C was achieved with a custom-built incubator. The selected recorded field of view was 150x150 pixel size. The illumination was HILO.

Excitation of the Janelia fluor dye JF646-HaloTag ligand was continuous, performed with 10-30% laser power (~96 - 805 W/cm^2)* of the 647 nm wavelength laser, and acquisition was at 10-30 ms frame integration time. Excitation of the JF549-HaloTag ligand was continuous, performed with 10-30% laser power (~18 - 147 W/cm^2)* of the 560 nm wavelength laser, and acquisition was at 10-30 ms frame integration time.

Excitation of the photoactivatable PA-JF646-HaloTag ligand and -SNAPtag ligand dyes was performed with 10-30% laser power of the 647 nm laser (~96 - 804 W/cm^2)*. Excitation of the photoactivatable PA-JF549-HaloTag ligand and -SNAPtag ligand dyes was performed with 10-30% laser power of the 560 nm laser (~18 - 147 W/cm^2)*. Photoactivation was induced for all dyes with a 10 ms pulse of the 405 nm laser at 1-5% (from ~124 – 1547 mW/cm^2)* every 20 seconds, which was considered enough time for the complete photobleaching of the previously photoactivated subset of molecules.

*The laser powers were measured in epifluorescence illumination mode at the specimen side.

2.2. DEVELOPED ANALYSIS

Spot detection and tracking

Spot detection and tracking were performed with Trackit, an SPT software implemented in MATLAB.[13] This software uses two wavelet filters for the detection of particles, and the candidate spots can be selected with a used defined threshold based on the SNR. The localization of the spots are refined using a 2D gaussian fit. The linking is performed with nearest neighbor algorithm. The tracking algorithm can bridge gaps in detections to account for fluorophore blinking, based on user-defined parameters.

The spot detection was performed with a thresholding value SNR = 1 or 2. It was set to SNR = 1 when measuring changes in the SNR in different laser power conditions, to ensure detection of all molecules; and it was set to SNR = 2, in all other experiments. The tracking was performed with nearest neighbors, using different values for the tracking radius, according to the optimization performed for each condition (see **Section 4**). We selected a minimum tracking length of 2 frames, 1 gap frames, and a minimum track length before gap of 0 frames.

Analysis with MATLAB

The analyses are integrated into a custom-written MATLAB user interface, that allows to load the videos in .tiff format and the tracking data coming from TrackMate[14] or Trackit[13] (see **Figure 1A**). The interface also allows to visualize all the videos with the trajectories, and filter them by drawing an ROI, or according to other criteria such as the trajectory length or the diffusion coefficient (see **Figure 1B**). It is also possible to visualize a second channel single image, or image sequence as a composite. One can also upload and visualize a bright field image, meant to help drawing the boundaries of the cells with the "Select ROI" tool.

In the Analysis tab, one can get the results for different types of analysis (see **Figure 1C**). It is also possible to use a second channel corresponding to a fluorescence image of a specific cellular structure, and use that to obtain measurements of the distance of each SPT localization to the structure boundaries. In addition, we can use this second channel to classify the diffusion properties according to the distance to these boundaries. This type of analysis is not used or discussed in this chapter but in **Chapter 5**. The codes can be found in the following Github repository link: https://github.com/JessicaAngulo/SPT_analysis_UI.git

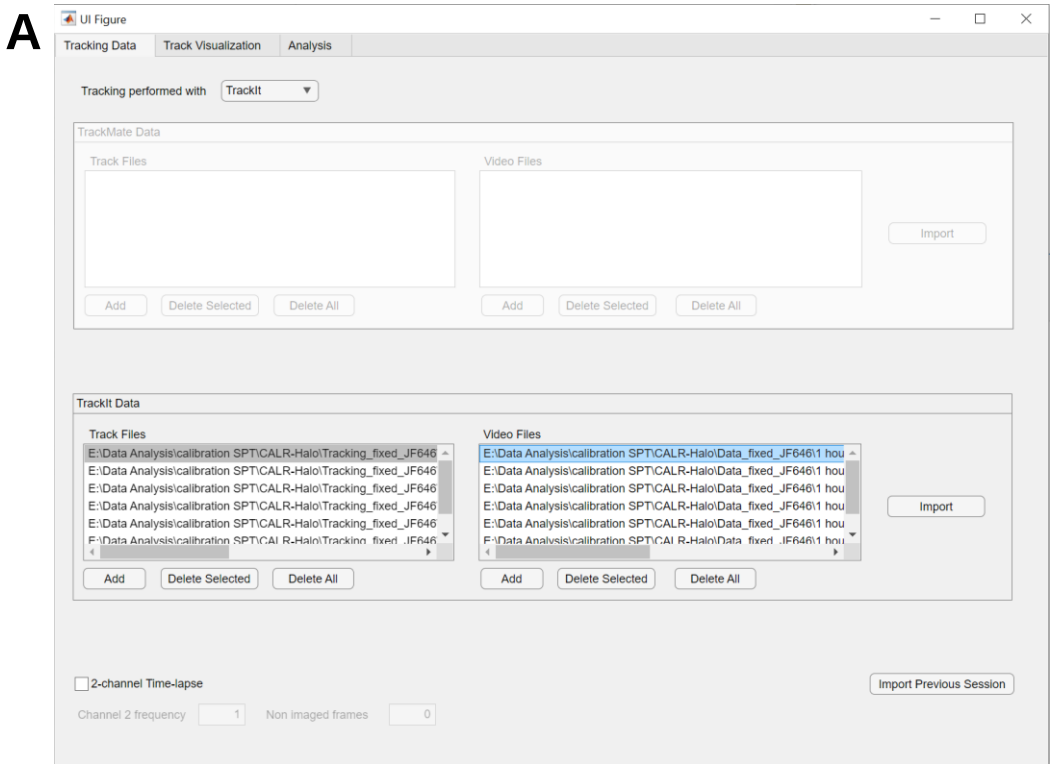
A
UI Figure
Tracking Data
Track Visualization
Analysis
Tracking performed with
TrackIt
TrackMate Data
Track Files
Video Files
Import
Add
Delete Selected
Delete All
TrackIt Data
Track Files
Video Files
Import
2-channel Time-lapse
Import Previous Session
Channel 2 frequency
Non imaged frames

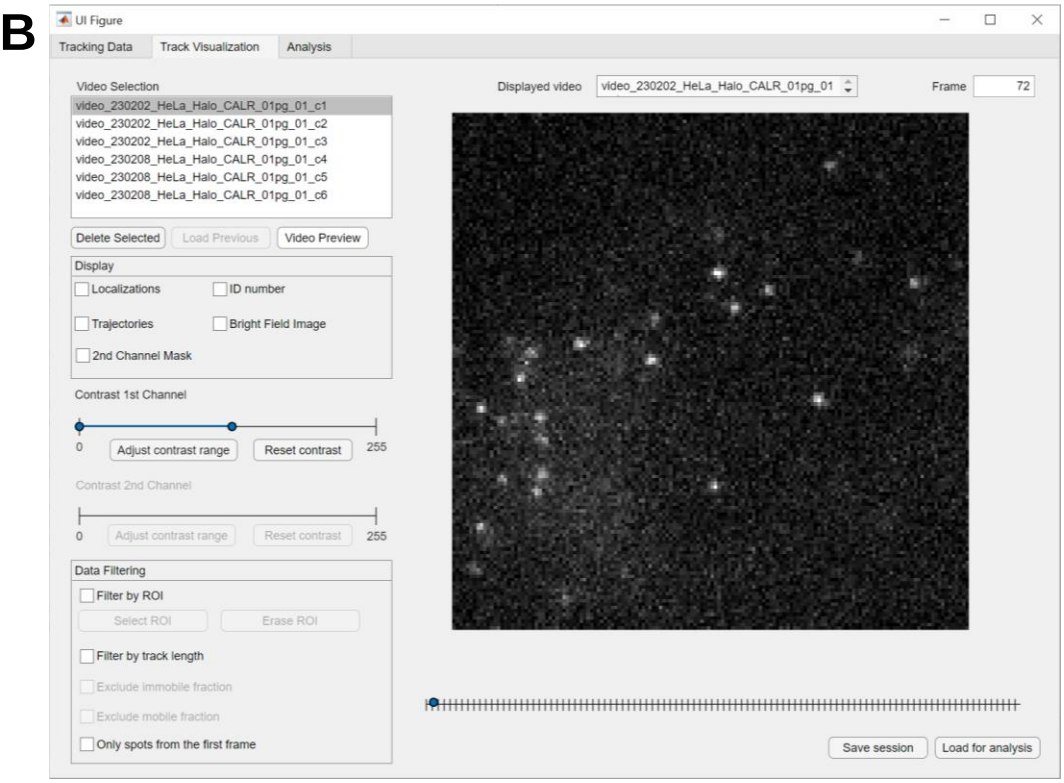
B
UI Figure
Tracking Data
Track Visualization
Analysis
Video Selection
video_230202_HeLa_Halo_CALR_01pg_01_c1
video_230202_HeLa_Halo_CALR_01pg_01_c2
video_230202_HeLa_Halo_CALR_01pg_01_c3
video_230208_HeLa_Halo_CALR_01pg_01_c4
video_230208_HeLa_Halo_CALR_01pg_01_c5
video_230208_HeLa_Halo_CALR_01pg_01_c6
Delete Selected
Load Previous
Video Preview
Display
Localizations
ID number
Trajectories
Bright Field Image
2nd Channel Mask
Contrast 1st Channel
Adjust contrast range
Reset contrast
Contrast 2nd Channel
Data Filtering
Filter by ROI
Select ROI
Erase ROI
Filter by track length
Exclude immobile fraction
Exclude mobile fraction
Only spots from the first frame
Displayed video
video_230202_HeLa_Halo_CALR_01pg_01
Frame
72
Save session
Load for analysis

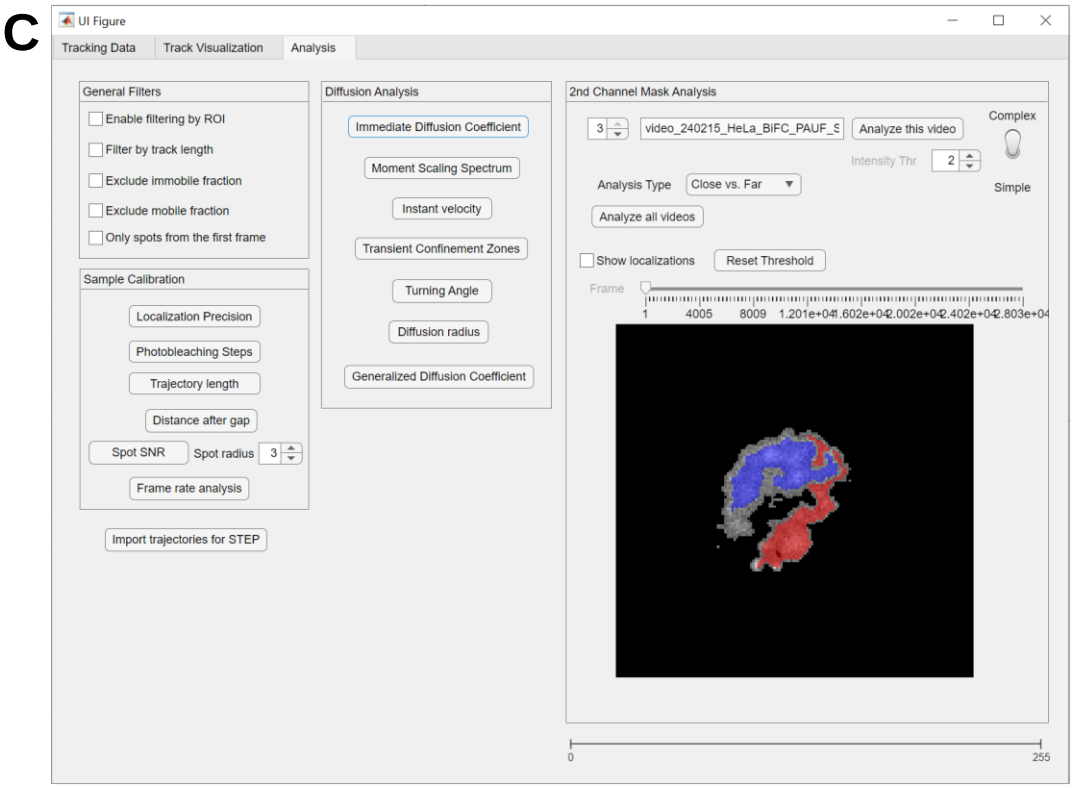

Figure 1. Developed user interface for the analysis of SPT data. A. Tracking data loading tab. It is necessary to load the tracking data obtained from TrackMate or Trackit. One can choose whether interlaced imaging have been performed. **B.** Track visualization tab. One can visualize the trajectories and the localizations in different manners. It is possible to visualize a second channel and bright field images. The data can also be filtered according to different parameters. **C.** Analysis tab. The data can be uniformly filtered and analyzed with different algorithms. If a second channel image or image sequence is present, it is possible to detect the structures and get the diffusion parameters classified by boundary proximity.

The analyses that have been used in this chapter are:

(i) Signal-to-noise ratio (SNR).

A window of 16 pixels around each spot detected by Trackit was defined, ensuring that the boundaries of this window remained within the image dimensions. A mask was created to isolate the pixels within a user-defined radius around the spot's center. In this analysis, the selected spot radius was 3 pixels. Two sub-images were then extracted from the original image: one representing the background, where pixels within the spot mask were excluded, and one representing the spot, where only pixels within the spot mask were included. The SNR was calculated as the difference between the peak intensity and the mean background intensity, divided by the background standard deviation.

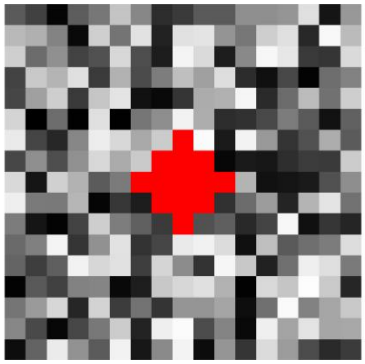

Figure 2. Zoomed-in view of the selected window for Signal-to-Noise Ratio (SNR) calculation. The displayed region illustrates the specific pixels involved in the SNR calculation process. The red pixels indicate the spot area used for calculating the peak intensity (3 pixels radius), while the surrounding pixels are the ones used for the calculation of the background.

(ii) Photon budget.

The photon count of each spot was calculated by summing the spot pixel values ($counts$), adjusting for an offset of the counts in dark pixels, and normalizing by the sensitivity and gain of the imaging system.

$$photon\ count = \frac{(counts - offset) \cdot sensitivity}{EM\ gain} \quad (1)$$

For this ANDOR technology EMCCD iXon 897 camera, the sensitivity, also known as quantum efficiency is 0.95, the offset is 100 counts and the EM gain was 100x.

The photon budget was the result of summing photon counts of all spots of a single trajectory (in fixed samples). Only immobile trajectories (i.e. with a diffusion coefficient smaller than 0.04 $\mu m^2/s$) and that were present in the first frame were included in the analysis of the photon budget.

(iii) Instantaneous diffusion coefficient (D1-4).

This parameter was calculated from the TA-MSD. Specifically, for a particle trajectory with coordinate position vectors $\boldsymbol{x}_j$, composed of N time steps, the TA-MSD at time lag t_{lag} is calculated as:

$$TA\text{-}MSD\left(t_{lag} = m\Delta t\right) = \frac{1}{N-m}\sum_{i=1}^{N-m}\left[\boldsymbol{x}_j(t_i + m\Delta t) - \boldsymbol{x}_j(t_i)\right]^2 \quad (2)$$

and from here the diffusion coefficient, D_{1-4}, was computed by a linear fit of $TA\text{-}MSD\left(t_{lag}\right) = 4D_{1-4}t_{lag} + b$ using the first four time lags, $t_{lag} = m\Delta t$, for $m = 1\ to\ 4$, where Δt is the frame time. The "y" intercept (b) is also fitted for each

trajectory. For these computations, we used only those trajectories with a minimum trajectory length of 12 frames.

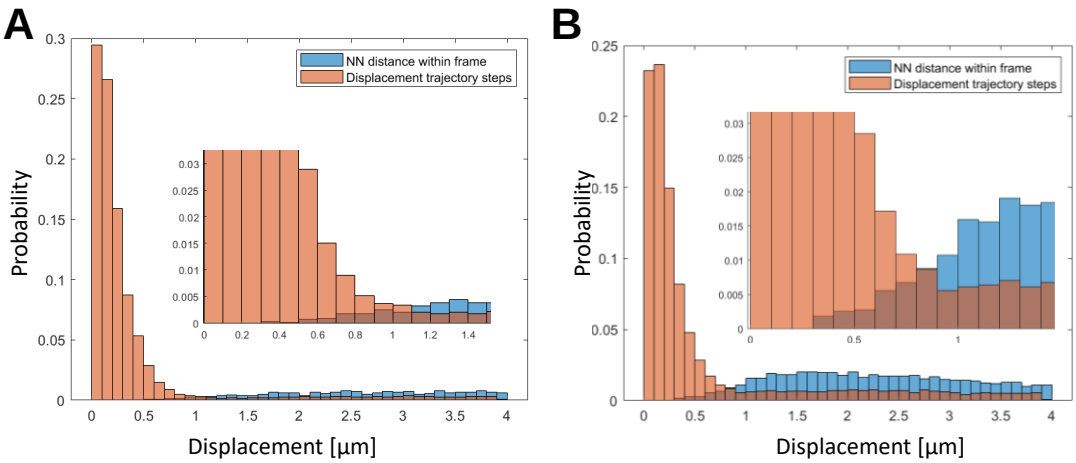

Figure 3. Distribution of the nearest neighbor distances within the same frame. Live HeLa cells overexpressing Halo-CALR, labeled with PA-JF646-Halo ligand, and washed for 2 hours with DMEM. Imaging was performed at 20 ms frame integration time. The blue histograms represent the distance to the nearest neighbor of each localization within the same frame. The orange histograms represent the distance to the nearest neighbor between consecutive frames. The overlap between the two distribution indicates connected distances in which the probability of having connected localizations from different molecules is very high. **A.** Distributions for 3 cells imaged with a photoactivation laser power of 1%. **B.** Distributions for 4 cells imaged with a photoactivation laser power of 5%.

(iv) Frame rate analysis.

In order to select a linking distance that minimizes the probability to perform a wrong connection, we calculated the distance of each localization (each detected position molecule) to the nearest neighbor within the same frame. This provides a measure of how close the detected molecules are to one another (a measure of single molecule density in each frame). The obtained distribution of these nearest neighbor distances represents an approximation to the likelihood of assigning a wrong trajectory link as a function of the distance (**Figure 3**). We selected a cut-off distance that correspond to the smallest 5% percentile of this distribution.

Each of these maximum distance cut-offs correspond to the maximum displacement that can be detected, and therefore, when dividing by the frame time, it corresponds to the maximum detected velocity. The maximum diffusion coefficient that can be detected for each maximum detectable displacement has been estimated assuming Brownian motion of a molecule, according to the Einstein relation:

$$\langle \Delta r^2(t) \rangle = 2dDt \qquad (3)$$

where $\langle \Delta r^2(t) \rangle$ is the mean squared displacement after time t, d the dimensionality of the system (in this case 2), D the diffusion coefficient, and t the time interval. One can approximate the displacement for the Brownian motion as:

$$\Delta r_{max}^2 = 2dDt \quad (4)$$

where Δr_{max} is the maximum displacement, which we approximate as:

$$\langle \Delta r^2 \rangle = \Delta r_{max}^2 \quad (5)$$

Therefore, the maximum detectable diffusion coefficient (D_{max}) can be approximated as:

$$D_{max} = 4 \cdot \Delta r_{max}^2 \cdot \Delta t \quad (6)$$

(v) Static localization uncertainty or static localization precision.

This parameter was extracted from SPT data of immobile particles in fixed cells. Only immobile trajectories (i.e. with a diffusion coefficient smaller than 0.04 $\mu m^2/s$), that were present in the first frame, and that were longer than 20 frames were included in the analysis.

For each immobile trajectory, we computed the mean x and y positions, representing the average position of the trajectory. We then calculated the deviations of each localization point from the mean position. We calculated the standard deviation of the deviations in the x (std_x) and y (std_y) directions. To combine these deviations into a single measure of precision, we computed the root mean square of the standard deviations, given by:

$$SD = \sqrt{std_x^2 + std_y^2} \quad (7)$$

Following the same estimation as for the frame rate analysis, a minimum detectable diffusion coefficient can be calculated with the equation:

$$D_{min} = 4 \cdot \Delta r_{min}^2 \cdot \Delta t \quad (8)$$

where Δr_{min} is the minimum displacement, that we approximate to the previously calculated SD (equation (7)), and Δt the frame integration time.

Diffusion analysis with STEP (Python)

We obtained the pointwise diffusion properties of the trajectories with STEP, a machine learning method able to predict the diffusion coefficient and the anomalous diffusion exponent, at each time step of the input trajectory.[15] The codes

from the original publication of STEP can be found in: https://github.com/BorjaRequena/step.git. The scripts for the specific data analysis used in this thesis can be found in: https://github.com/JessicaAngulo/step.git.

Two models were trained by B. Requena (ICFO-Institute of Photonic Sciences, Barcelona, Spain), following a standard gradient-based training procedure. One model served for the inference of the diffusion coefficient, and the other one for the alpha exponent. The training procedure for these models follows the exact same steps as the original work, incorporating three main improvements to address some of its original issues. First, the models use the logarithm of the displacements between consecutive steps and their sign, instead of working with the absolute positional data. Additionally, the models were trained using batches with different lengths, such that all trajectories within the same batch have the same length, but different batches have different lengths. Finally, the original L1 loss function was replaced by the L2 loss function or mean squared error (MSE), which is more sensitive to outliers, resulting in more consistent predictions.

$$\mathcal{L}_{MSE}(x) = \frac{1}{n\sum_i T_i}\sum_{i=1}^{n}\sum_{t=1}^{T_i}(y_{i,t} - f(x_i)_t)^2 \tag{9}$$

where $f(x_i)_t$ is the prediction of the i-th trajectory at the time step t in a batch of n trajectories. $y_{i,t}$ is the true label for the same time, and T_i denotes its length. The parameter update was performed with an Adam optimizer[16], whose learning rate was adjusted using the learning rate finder tool from the *fastai* library.[17]

The trajectories used in the training were generated following the procedure described in G. Muñoz-Gil et al. for the Fractional Brownian Motion (FBM) diffusion model.[18] With this approach, we strive for simplicity in the training process, considering only the anomalous diffusion models that are strictly needed to describe the observed experimental phenomena. It was shown in the original work that some anomalous diffusion models, such as the scaled Brownian motion (SBM), the continuous time random walk (CTRW), or the annealed transit-time model, yield to confusion in the frame-wise analysis stemming from indistinguishable or unrecognizable scenarios that result in constant predictions.[15] Therefore, FBM seems to be a useful and meaningful model that can be related to the observations, because it incorporates memory effects in the displacements, and allows for anomalous diffusion, which can be subdiffusive or superdiffusive.

For the inference, we used only those trajectories with a minimum trajectory length of 12 frames. The initial position of each trajectory was adjusted to start at the origin (i.e., coordinate [0,0]). This means that we shifted the entire trajectory such that the starting point is at (0,0). Additionally, we scaled the displacements (the changes in position between consecutive frames) by dividing them by their standard deviation. This normalization step ensures that the variations in trajectory displacements are comparable across different trajectories, making the data more consistent for analysis.

3. LABELING STRATEGY

As already mentioned, there are important aspects to be considered when using self-labeling tags, such as SNAP or HALO tags. Firstly, the 1:1 labeling ratio inherent to these tags results in lower SNR, as each protein molecule is tagged with only one molecule of dye. This makes it essential to use dyes with superior fluorescent properties. Recent work by Grimm et al. presented a new family of bright photostable small fluorescent dyes (JF dyes).[19] One of them, the JF549-HaloTag ligand, was shown to be brighter than the tetramethylrhodamine (TMR)-HaloTag ligand and Cy3-HaloTag ligand, both classically used in SPT. Another one, the JF646-HaloTag ligand also has a higher absorbance than SiR (silicon-rhodamine), though they did not show a comparison of the brightness.[19] The same group later reported photoactivatable versions of these two dyes, which both have even superior fluorescent properties, as compared to the JF549, the JF646 or a classically used photoactivatable fluorescent protein mEos3.2.[12] Moreover, all of them display scarce blinking, which makes them desirable for a proper linking of the detected spots.[12,19] These are some of the reasons why these set of dyes are being widely used nowadays for intracellular applications.

Another challenge is the presence of unbound dye, which can increase the background fluorescence and reduce the SNR of the individual molecules. This unbound dye can also be incorrectly identified as the protein of interest, resulting in inaccurate calculations of the diffusion properties of the target molecules. The protocols used in different publications are very different, ranging from few short washes with PBS, long incubations, or multiple short washes.[4–6] Moreover, many of the steps involved in the washing of unbound dye are challenging to describe and can be very highly scientist-dependent. It is therefore necessary to establish a systematic way to detect the unbound dye, so that every user can evaluate whether their labeling protocol is good enough for their needs.

Finally, the labeling density needs to be finely tuned, to avoid tracking errors and optimize the SNR. To maximize data collection and minimize background signals, one needs to improve the efficiency of our labeling techniques to minimize background signals. In the literature, very low concentrations of dyes –in the nanomolar range– have usually been used for this purpose. However, very low concentrations of dye lead to a very low throughput, highly complicating for instance the representation of diffusion maps, in which the diffusion properties are represented in space to identify regions of certain diffusion properties. Given that the varying expression levels of different proteins of interest can result in different localization densities even with the same labeling concentration, it is important to determine beforehand the optimal dye concentration for each experimental condition. In the following section, we will discuss how to select the photoactivating laser pulse in order to control de localization density, as well.

3.1. DYE SELECTION

As already mentioned, the most obvious way to maximize data collection and minimize background signal is by selecting the fluorescent dye that has the best fluorescent properties. In **Figure 4**, we show the photon budget of different dyes, measured as the number of emitted photons before photobleaching, as a measure of the photostability in our specific experimental conditions. For us, the JF646-HaloTag ligand has a higher photostability than the JF549-HaloTag. The photoactivatable versions are even more photostable, being the PA-JF646-HaloTag ligand the one that worked best in our experimental conditions. Moreover, Grimm et al. reported that the photoactivatable versions have superior absorbance cross-section coefficient, meaning that they will show higher brightness with the same laser power.

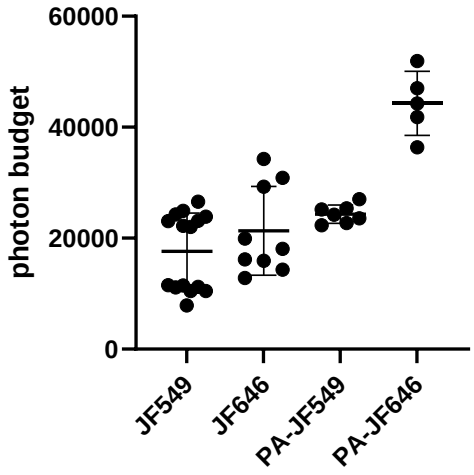

Figure 4. Photon budget of different Janelia Fluor dyes. The photon budget is the number of emitted photons before photobleaching of a dye. Error bars represent mean and SD of each cell median value (black dots). For the JF549-Halo ligand and the JF646-Haloligand, the experiments have been performed on HeLa cells overexpressing Halo-Calreticulin, labeled with 0.1 nM of dye. The PA-JF549-Halo ligand and the PA-JF646-Halo ligand dyes were imaged in the stable cell line HeLa Cab45 RUSH. They were washed for 1 or 2 hours with DMEM at 37 °C. The excitation was performed with continuous illumination at 30% laser power of the 647 nm laser, and the acquisition was at 20 or 30 ms frame time. Only the molecules present in the first frame, and with a diffusion coefficient smaller than 0.04 $\mu m^2/s$ are included in the analysis, to make sure that they are only the immobile molecules.

Given these results, we would recommend to check which fluorophore is more photostable in each specific experimental condition. The use of different imaging buffers and the location within different cellular compartments with different pH and chemical composition can influence the photon budget of the fluorophores. Although it is true that Grimm et al. reported that the quantum yields of the 549 versions are higher than for the 646 versions, and are therefore brighter, we recommend to prioritize the photostability, as the brightness can be tuned with the illumination conditions.

As new fluorophores are constantly being engineered, similar measurements should be done to find out improvements or particularities of their setups. However, it is to be noted that the selection of the dye is many times conditioned by the excitation-emission spectra of other fluorescent reporters that might also be co-imaged, such as when labeling for some cellular compartments with fluorescent proteins, or when labeling of other single molecules. For instance, the need to visualize another reporter with UV light would complicate the use of the photoactivatable dyes.

The photon budget simply reports on the number of photons that a dye emit before photobleaching, and is therefore a measure of the probability to photobleach (i.e. the photostability). One can tune how these photons are emitted. On the one hand, the excitation laser power will determine the rate of emission of these photons, and, consequently, the total imaging time before photobleaching, which impacts on the maximum duration of the single molecule trajectories. On the other hand, the frame rate serves to select over how much time is this signal integrated. In brief, it has to be slow enough so we obtain sufficient SNR for precise single molecule detection, but also fast enough so we avoid motion blur –that is, the significant movement of the single molecule within a single frame. We will therefore describe in Section 4, how to rationalize this decision.

3.2. WASH OF THE FREE DYE

A challenge that we very quickly faced was that it is sometimes difficult to distinguish whether the single molecules correspond to free dye or to dye bound to the protein of interest. This can be extremely problematic, as we have observed that the diffusion properties of the free dye have overlapping diffusion coefficients to that of the labeled protein. Incorrectly assigning free dye localizations as single protein localizations can therefore lead to miscalculation of the diffusion properties of the protein of interest. Hence, it is paramount in SPT experiments to minimize the amount of free dye in our samples, as well as to be able to detect and quantify their presence. In order to find the best experimental approach to this end, we labeled cells, after which we used different washing protocols, consisting in washing out the free dye by incubating the labeled cells in DMEM for different amounts of time. To discern experimentally between free and bound dye, we used cells fixed with PFA, and quenched it with $NaBH_4$. In fixed cells imaged by SPT, the immobile molecules correspond to specific labeling, whereas the mobile trajectories correspond to the unbound, free dye. These experiments were performed both in HeLa overexpressing Halo-CALR (which were labeled with either JF549 or JF646 dyes), and in the HeLa cell line stably expressing Cab45-Halo RUSH (in which we used the PA versions of these dyes for the labeling). Only the molecules in the first frame were considered in the analysis, to avoid overrepresentation of the free dye. This is because the fixed, immobile bound fraction is constrained to a single plane, and the molecules that appear in latter frames correspond to unbound molecules that can freely diffuse and enter the imaging plane and get excited.

Our results (**Figure 5A**) show that the diffusion coefficient displays a bimodal distribution, with a population of immobile diffusing molecules (with a peak at ~0.01 $\mu m^2/s$), and a population of highly diffusion molecules (with a peak at ~0.1 um $\mu m^2/s$). We believe that the second corresponds to the unbound dye. Although the diffusion coefficient of free dye has been reported to be in the order of 100 $\mu m^2/s$, it is to be noted that the fixation can significantly alter the cellular environment, leading to reduced diffusion coefficients.[20] Fixatives such as paraformaldehyde create cross-links between proteins, which can create a more crowded and viscous environment, hindering the movement of small molecules. However, there can be overlap in the diffusion coefficient distribution with that of labeled proteins, and therefore it is very important to get rid of this free dye as much as possible.

When washing the free dye for different amounts time, our results indicate that after 2-hour incubation there is still around a 20% of free JF646-Halo ligand dye (**Figure 5B**). Although this value is quite high, we expect the free dye to display higher diffusion coefficients, that are more probable to leave the focus plane. Moreover, we have appreciated that this is highly dependent on the dye, as these values are lower for the PA-JF646 Halo ligand, as shown in **Figure 5C**. The broad variability in the samples shows the difficulty to reproduce the washes experimentally, strengthening the need to perform controls when reproducing experimental conditions from one lab to another or from one researcher to another. While we do not claim that this type of wash is the most effective method for removing unbound dye, it proved to be the most effective in our specific experiments. Each one should perform these kind of control experiments themselves when setting up their optimal experimental conditions.

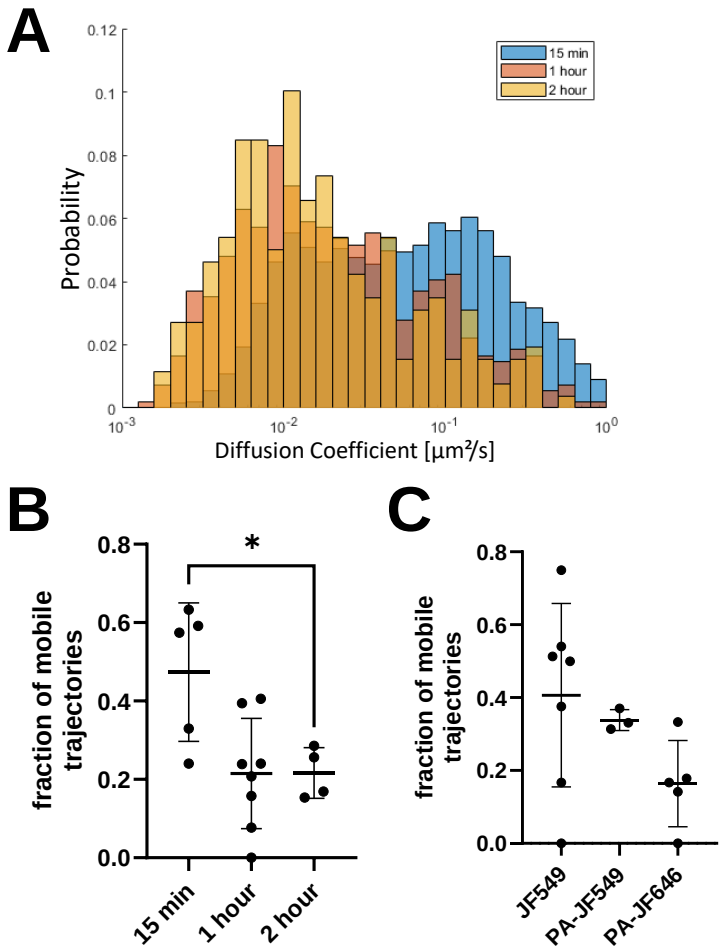

Figure 5. Wash out of the free dye. A-B. HeLa cells overexpressing Halo-CALR, labeled with 0.1 nM of JF646-Halo ligand, fixed and washed for 15 minutes, 1 hour or 2 hours with DMEM at 37 °C. The excitation was performed with continuous illumination at 30% laser power of the 647 nm laser, and the acquisition was at 20 ms frame rate. Only the molecules present in the first frame are included in the analysis, to avoid over representation of the free dye. **A.** Distribution of the D1-4 of JF646-Halo ligand fluorescent molecules, after 15-minutes, 1-hour and 2-hour wash. **B.** Fraction of the mobile molecules in the first frame, for cells washed for 15 minutes, 1 hour or 2 hours with DMEM. Molecules are considered mobile when their diffusion coefficient is higher than 0.04 $\mu m^2/s$. Error bars represent mean and SD of each cell (black dots). Significance calculated between the values per cell with an unpaired t-test. p-value(*) = 0.0288. **C.** Fraction of mobile molecules for cells labeled with JF549-Halo ligand, PA-JF549-Halo ligand, and the PA-JF646-Halo ligand, all of them fixed washed for 2 hours with DMEM at 37 °C. The last two dyes have been sampled on the stable cell line HeLa Cab45 RUSH. In these two last conditions, excitation was performed with continuous illumination at 30% laser power of the 647 nm laser, and the acquisition was at 30 ms frame rate. Photoactivation was performed at 2% of the 405 nm laser during 10 ms every 20 seconds. Only the molecules present in the first frame are included in the analysis, to avoid over representation of the free dye. Error bars represent mean and SD of each cell (black dots).

3.3. CONTROL OF THE LABELING DENSITY

The classical way to reach the single molecule regime is to add nanomolar concentrations of the dye, so that only a sparse subset of the molecules is actually labeled. In **Section 4** we will justify that this strategy is outperformed by the alternative strategy of using saturating amounts of photoactivatable dyes (and controlling the density of single molecules by fine tuning the photoactivation rate). In spite of this, an analysis on how different concentrations of dye influence the labeling density and the SPT performance is still useful to understand the effect of the different single molecule densities for the spot detection and the tracking.

In the following experiments, we used HeLa cells overexpressing calreticulin (Halo-CALR), and labeled them with different concentrations of the JF646-Halo ligand. It is important to stress that, because different cells might have different expression levels, different labeling concentrations do not always correspond to the same fluorescent molecule density (see **Figure 6**).

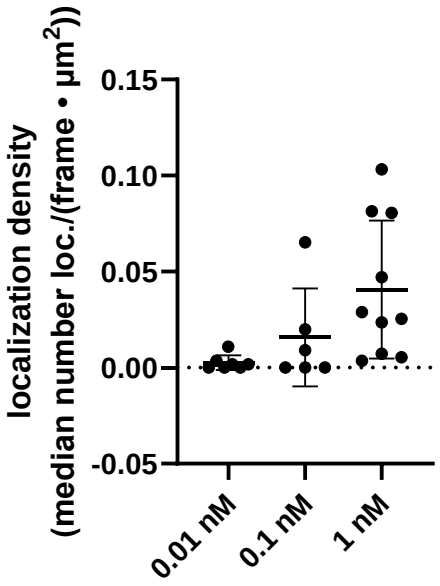

Figure 6. Localizations density for samples labeled with different concentrations of JF646 dye. The localization density is calculated as the median number of localizations per frame and per μm^2. Live HeLa cells overexpressing Halo-CALR, labeled with different concentrations of JF646-Halo ligand, and washed for 2 hours with PBS. The excitation was performed with continuous illumination at 30% laser power of the 647 nm laser, and the acquisition was at 20 ms frame rate. Detection threshold in Trackit was set to SNR = 1.

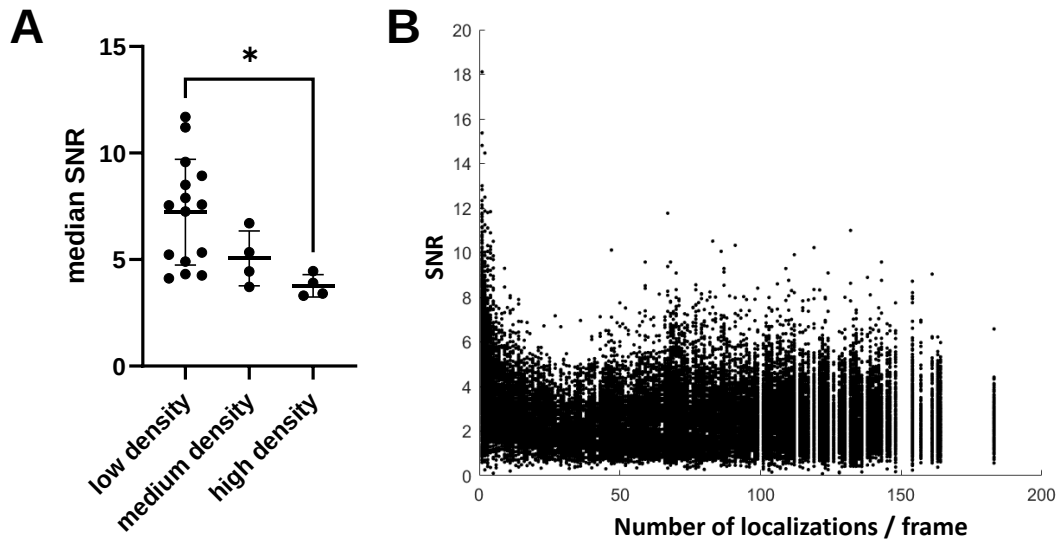

Figure 7. Relationship between the SNR and the localizations density. The SNR of each localization has been calculated as described in the **Methods Section**. Live HeLa cells overexpressing Halo-CALR, labeled with different concentrations of JF646-Halo ligand, and washed for 2 hours with DMEM. The excitation was performed with continuous illumination at 30% laser power of the 647 nm laser, and the acquisition was at 20 ms frame time. Detection threshold in Trackit was set to SNR 2. **A.** SNR of cells displaying different localizations densities. The localization density is calculated as the median number of localizations per frame and per μm^2; and considered "low" for median densities per cell smaller than 0.02 localizations/(frame·μm^2), "medium" when the median densities per cell are between 0.02 and 0.06 localizations/(frame·μm^2), and "high" when the median density per cell values larger than 0.06 localizations/(frame·μm^2). Error bars represent mean and SD of each cell median value (black dots). Significance calculated between the median values per cell with an unpaired t-test. p-value (*) = 0.0149. **B.** SNR vs. the number of localizations per frame for a representative cell. This example was labeled with 1 nM concentration of dye.

Interestingly, our results indicate that increasing the localization density parallels a decrease in the median SNR per molecule (**Figure 7A**). This is because the increase in the number of molecules in the excitation volume contribute to an increase of the background fluorescence and results in a reduced SNR of the in-plane molecules. In **Figure 7B**, we show the relationship between the SNR and the spot density, obtained from a single representative video, in which cells were labeled with 1 nM concentration of dye and imaged live. Due to photobleaching and out-of-focus protein diffusion, the video contains a wide range of single molecule densities. One can appreciate that the SNR reduces as the labeling density increases, until it reaches a plateau, in which the SNR has a constant range of values, probably because the background fluorescence remains constant. While the median spot SNR obtained in these experiments is relatively larger than 2 (which is the minimum SNR used as a detection threshold in our spot detection algorithm, see **Section 2.2**), caution

should be taken when deciding a single molecule density so it does not lead to too low SNR that can jeopardize spot detection. Otherwise, problems in the detection would result in shorter, fragmented, and reduced numbers of detected trajectories. Based on our results, we would recommend selecting a localization density smaller than 0.06 localizations/(frame·μm^2), which corresponds to the low and medium labeling densities shown in **Figure 7A**. Based on the obtained results for our specific experimental conditions and expression levels (see **Figure 6**), this condition would be met with a labeling performed with 0.01 nM and 0.1 nM of dye. While the mean localization density for the cells labeled with 1 nM of dye is below 0.06 localizations/(frame·μm^2), the span of the cell-to-cell variability leads to many cells with a localization density above this value, which precludes us from recommending the use of that labeling concentration.

4. IMAGING STRATEGY

Cells and their internal organelles are inherently 3-dimensional in nature. By contrast, with HILO illumination, we specifically image molecules localized in a relatively thin sheet that does not cover the entire cell. Hence, molecules move in and out of the plane, limiting the number and length of the acquired trajectories. Because of this, it is essential to optimize the imaging conditions to collect more and better data. In practical terms, this means that we aim to improve on the SNR of the fluorescent molecules, and increase the number of harvested trajectories. In the classical approach of using sub-labeling conditions to guarantee a sparse localization of single molecules, the dye concentration needs to be as high as possible, without compromising single molecule detection capacity, the linking fidelity between frames, or the SNR. Regarding the frame rate, it is important to select one that not only allows to fully sample the dynamics of the target protein, but also to reduce linking errors, without compromising spot detection due to the low SNR. Importantly also in practical terms is that using very fast frame rates usually occurs at the expense of reducing the field of view.

A somewhat different labeling and imaging strategy that has proved to increase drastically the number of harvested trajectories is SPT PALM. SPT PALM combines standard SPT with the use of photoactivatable fluorophores,[21] thus allowing to get sparse detection of single molecules not by using sub-labeling conditions (as in standard SPT, as explained above) but by only photoactivating a sparse number of molecules at a time. With this approach, it is possible to successively activate new subsets of fluorophores once the previous ones have photobleached, leading to

increased throughput. In this case, similar control experiments can be done to select the appropriate fluorophore density and imaging frame rate. While in standard SPT, we varied the labeling concentration to modulate the density of detected single molecules, in SPT PALM we do it by varying the photoactivation laser power and its pulse duration.

Once the optimal frame rate and photoactivation conditions have been selected, the last parameter to optimize is the excitation power. As explained before, the excitation power determines at which rate the photons are emitted. High powers will lead to high SNR of the single spots, but at the expense of the trajectory length (the photon budget of the dye will be distributed in less imaging frames). The decision of what excitation power to use is therefore a trade-off between these different factors. Again, this should be tested and optimized for each fluorophore and setup.

4.1. FRAME RATE SELECTION

As already explained above, it is necessary to choose a frame rate that allows to reliably and accurately follow the motion of the molecule of interest. In addition, the decision on the frame rate depends on other factors, such as the density of molecules in the field of view, because the higher the localization density is, the shorter the maximum allowed linking distance can be (to minimize wrong connections between frames). We therefore calculated a linking distance cut-off for which we have approximated that the probability of having a wrong linking candidate is smaller than 5% (as explained in **Section 2.2**). As shown in **Figure 8A**, this maximum linking distance decreases as the localization density increases (achieved in this case by using higher labeling concentrations of dye).

Although the distance cutoff is not affected by the frame rate used for the imaging –as it only depends on the localization density–, it reports on the maximum detectable velocity, which is in turn also a function of the frame rate. In other words, as the linking distance is a measure of the maximum molecule frame-to-frame displacement that can be detected, we can obtain the maximum detectable velocity by dividing this maximum displacement by the frame time. Altogether, our experimental results indicate, as predicted, that the maximum detectable velocity decreases with the frame time (**Figure 8B**). Specifically, as these experiments report on the dynamics of the ER chaperon calreticulin, if this protein moves at instantaneous velocities above 100 μm/s, not even the fastest frame rate (10 ms frame time) will be able to catch this motion, causing a bias in the diffusion analysis

towards slower molecules. Similarly, if we were to detect diffusion coefficients in the order of 10 $\mu m^2/s$, we would recommend to use either 10 or 20 ms frame time, and a concentration of dye smaller than 0.1 nM (see **Figure 8C**). Indeed, the maximum velocity reported by Holcman et al. for Halo-CALR was 60 µm/s, which means that in these conditions we would be capturing calreticulin's fastest reported dynamics.[4]

However, decreasing the frame time also affects (worsens) the SNR, as less photons are detected per molecule (with the same excitation power). When we measured the SNR of the molecules (**Figure 8D**) using a frame integration time of 10 ms, we obtained a median SNR per single molecule that is very close to the thresholding SNR for the detection (SNR = 2), which would imply that many molecules are not detected. Consequently, we propose that it would be recommendable to use 20 ms frame time, which increases the SNR while maintaining a decent maximum velocity and diffusion coefficient (**Figure 8B-D**). When also adding the labeling density (in this case, the concentrations of dye) into play, our results indicate similar SNR values for the tested concentrations, so we would suggest to use the highest concentration to have a higher throughput. In conclusion, for this specific protein and experimental conditions, based on all these results, we would suggest to use a frame integration time of 20 ms, and a labeling concentration of 0.1 nM, in order to capture the maximum displacements of this protein, get a proper SNR for the detection, and still have a labeling density as high as possible.

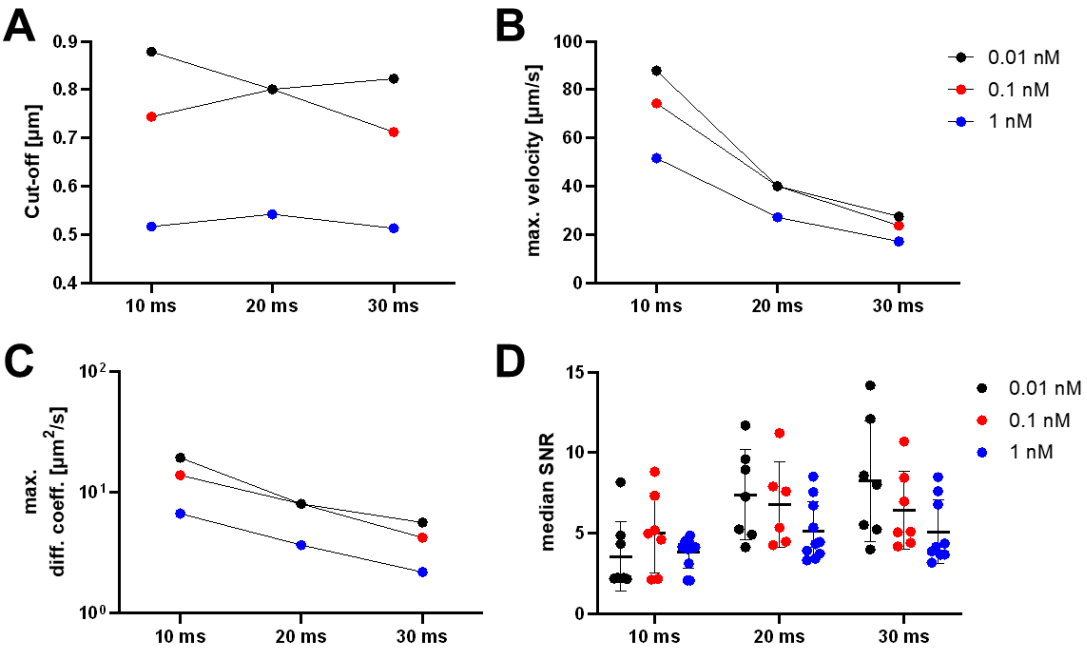

Figure 8. Selection of the frame rate and the labeling density for SPT of the protein Halo-CALR labeled with JF646. Live HeLa cells overexpressing Halo-CALR, labeled with different concentrations of JF646-Halo ligand, and washed for 2 hours with DMEM. The excitation was performed with continuous illumination at 30% laser power of the 647 nm laser, and the acquisition was at 10, 20 or 30 ms frame time. Detection threshold in Trackit was set to SNR 2 **A.** Maximum linking distance cut-off for each frame time and labeling condition. Calculated from the distribution of nearest neighbor distances within the same frame. The cut-off represents the maximum linking distance for having a probability of wrong connection smaller than 5%, obtained from the distribution of all gathered samples. **B.** Maximum detected velocity corresponding to each linking distance cut-off, obtained from the distribution of all gathered samples. **C.** Maximum detected diffusion coefficient corresponding to each linking distance cut-off, obtained from the distribution of all gathered samples. **D.** Median SNR of the detected particles for each frame time and labeling condition. Error bars represent mean and SD of each cell median value (dots).

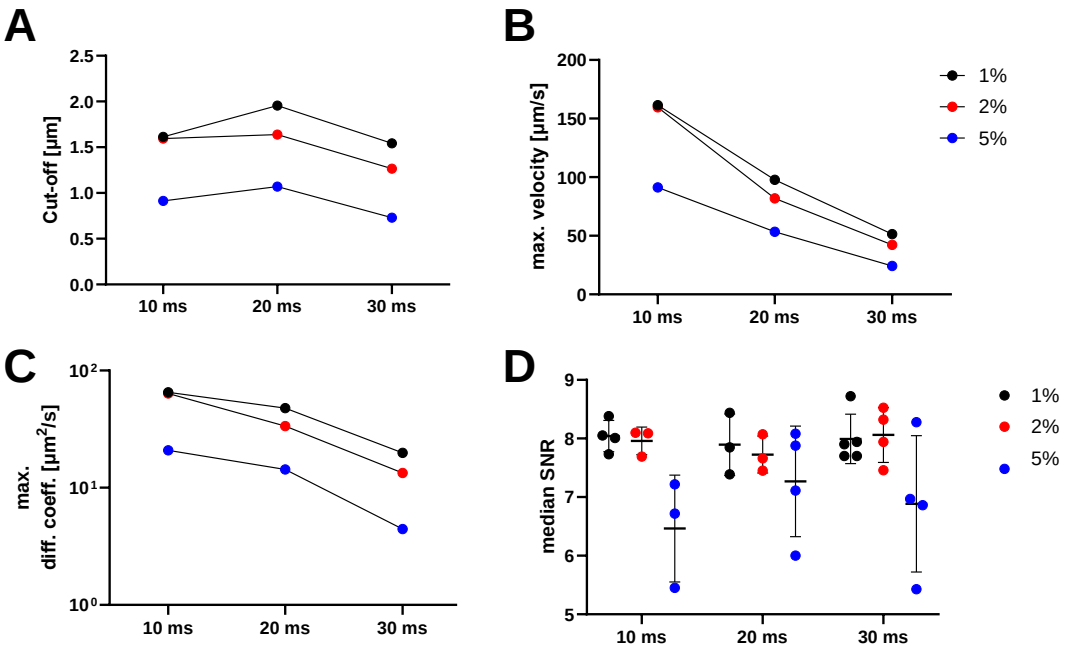

Figure 9. Selection of the frame rate and the labeling density for SPT of the protein Halo-CALR labeled with PA-JF646. Live HeLa cells overexpressing Halo-CALR, labeled with PA-JF646-Halo ligand, and washed for 2 hours with PBS. The excitation was performed with continuous illumination at 30% laser power of the 647 nm laser, and photoactivation for 10 ms with the 405 nm laser at different powers every 20 seconds. The acquisition was at 10, 20 or 30 ms frame time. Detection threshold in Trackit was set to SNR = 2 **A.** Maximum linking distance cut-off for each frame time and labeling condition. Calculated from the distribution of nearest neighbor distances within the same frame. The cut-off represents the maximum linking distance for having a probability of wrong connection smaller than 5%, obtained from the distribution of all gathered samples. **B.** Maximum detected velocity corresponding to each linking distance cut-off, obtained from the distribution of all gathered samples. **C.** Maximum detected diffusion coefficient corresponding to each linking distance cut-off, obtained from the distribution of all gathered samples. **D.** Median SNR of the detected particles for each frame time and labeling condition. Error bars represent mean and SD of each cell median value (dots).

A similar criterion can be used for photoactivatable dyes, but instead of controlling the labeling concentration, it is the photoactivation power that needs to be changed. In order to be able to increase the localization density step-wise, we always photoactivated during 10 ms every 20 seconds, independently of the used frame rate. Following the same criteria as before, imaging at a 20 ms frame integration time at all photoactivation intensities are appropriate to catch diffusion coefficients in the order of 10 $\mu m^2/s$ (see **Figure 9**). However, the SNR of samples imaged with a 5% photoactivation laser tends to be smaller, and therefore it would be recommended to use a milder photoactivation. In conclusion, for this specific

protein, and expression levels, it is recommended to use a laser power of the photoactivation laser of 1 or 2%, and a frame rate of 20 ms.

4.2. SELECTION OF THE EXCITATION POWER

As already explained, while the photon budget is an intrinsic property of a fluorescent dye in a specific environment, how fast these photons are emitted can be controlled with the excitation power. When exciting with very high laser powers, the photons are emitted at a fast rate, implying that the photon budget of each individual fluorophore is exhausted very quickly, i.e. the fluorophore transitions between its fluorescent and non-fluorescent states at an accelerated rate. As a consequence, the total fluorophore population undergoes photobleaching in a relatively short time, precluding the possibility to acquire long trajectories. Therefore, the excitation laser power should be low enough so we can record as long trajectories as needed, but also high enough to not compromise the SNR (so we can have a proper detection of the spots) or the localization precision (so we can determine the protein localization with high accuracy).

To quantify the relative contribution of these different factors, we used fixed HeLa cells to measure trajectory length, single molecule SNR, and localization precision of immobile Halo-CALR molecules labeled with the JF646-HaloTag ligand (**Figure 10A-B**). Our results confirm that the trajectory length decreases as we increase the excitation laser power (from around 3 seconds with a 20% excitation power to below 1 second for 40% excitation power, **Figure 10A**). Moreover, we appreciated a slight improvement in the localization precision when increasing the excitation laser power, although this trend is not statistically significative, possibly due to the cell-to-cell and sample-to-sample variability (**Figure 10B**). In accordance to this, we also observed no effect on the SNR of the detected spots upon varying the excitation laser power (**Figure 10C**). In conclusion, for these specific experimental conditions, it would be recommended to use the 20% laser power, as it allows to track the molecules for longer, without significantly compromising the localization precision or the SNR of the detected molecules.

Based on these results, a question that arises is whether the obtained trajectory lengths (of the order of a few seconds) are sufficiently large so we can capture protein dynamics or they are too short, becoming a limiting factor in our studies. To test that, we performed analogous experiments as those shown in **Figure 10** (with the same frame integration time of 20 ms), but in this case in live cells (**Figure 11**). Our results show that, in live cells, the distribution of trajectory lengths is highly

peaked towards short trajectories (most trajectories are below 300 ms, corresponding to trajectory lengths shorter than 15 frames), so trajectory lengths are rarely in the order of 1 second (**Figure 11**). These results indicate that a large percentage of the molecules move out of the imaging plane before photobleaching. In consequence, in this experiment, we are generally not limited by photobleaching and could thus use higher excitation laser powers to improve the SNR and the localization precision. This kind of analysis will be important in conditions in which the localization precision and/or the SNR are limiting, as one could quantitatively test whether using higher laser powers would be possible. That being said, as a general rule, we would suggest to, within these limits, use the lowest excitation laser power possible, as high powers could additionally cause cell photodamage.

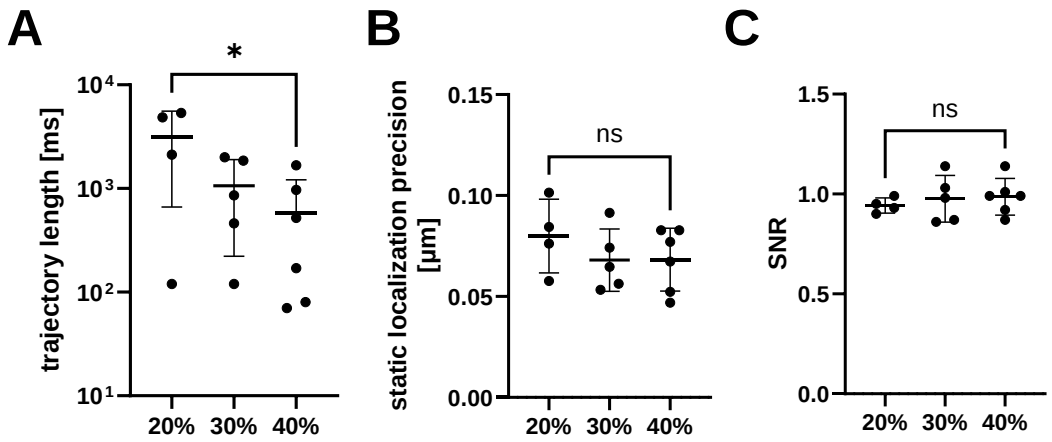

Figure 10. Selection of the excitation laser power for the JF646-HaloTag ligand. HeLa cells overexpressing Halo-CALR were labeled with 0.1 nM of JF646-HaloTag ligand, fixed and washed for 2 hours with DMEM at 37 °C. The excitation was performed with continuous illumination at different laser powers of the 647 nm laser (indicated in % of the total nominal power, see Methods section for the relationship to the actual laser power), and the acquisition was with a 20 ms frame time (50 Hz frame rate). Detection threshold was set to SNR = 1. Only the molecules present in the first frame, and with a diffusion coefficient smaller than 0.04 $\mu m^2/s$ were included in the analysis. Error bars represent mean and SD of each cell median value (dots). Significance calculated between the median values per cell calculated with an unpaired t-test. **A.** Median trajectory length of the immobilized particles. p-value(*) = 0.0381. **B.** Median values for the static localization precision of the immobilized particles. **C.** Median SNR of the immobilized particles.

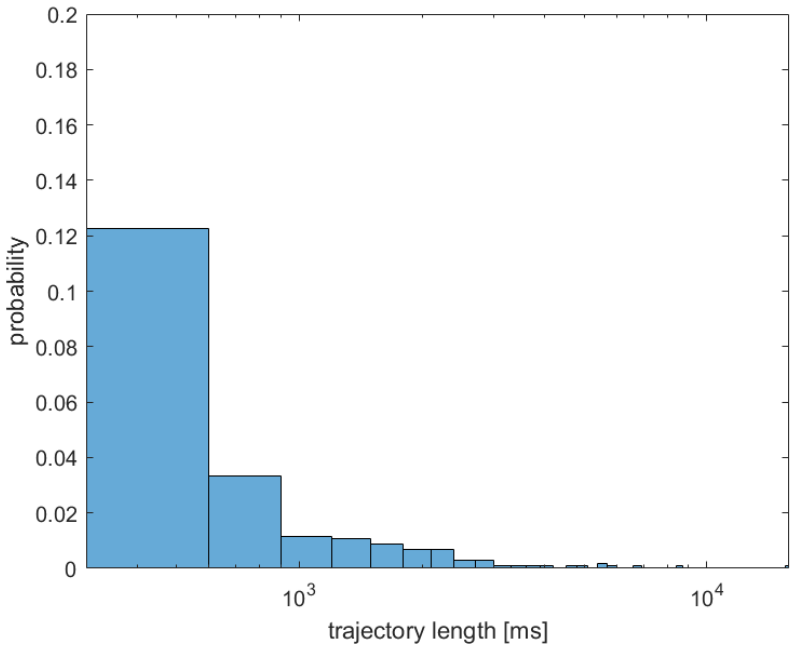

Figure 11. Distribution of the trajectory lengths for Halo-CALR imaged with the JF646-HaloTag ligand. HeLa cells overexpressing Halo-CALR, labeled with 0.1 nM of JF646-HaloTag ligand and washed for 2 hours with DMEM at 37 °C. The excitation was performed with continuous illumination at 30% laser powers of the 647 nm laser, and the acquisition was at 20 ms frame integration time. Detection threshold in Trackit was set to SNR 2.

4.3. DISCUSSION ON THE LOCALIZATION PRECISION

Independently of the measured parameter, the different imaging conditions influence the results. This is manly given by the localization precision, which arise from the noise and the camera exposure, and result in the static localization uncertainty or precision and the dynamic localization uncertainty of precision, respectively. The first arises from the fact that each coordinate has a Gaussian probability distribution function characterized by the standard deviation, that depends on the pixel size, the number of recorded photons, and noise sources. This means that when measuring the position of the same molecule, fixed in space, one does not recover the same localization position. It can be experimentally measured by imaging immobile particles, and calculating the standard deviation of the deviations from the mean position, as we have done in this thesis (see **Section 2.2.**). On the other hand, the dynamic localization uncertainty or motion blur comes from the finite camera exposure, given that the molecule keeps moving during the frame acquisition. It can be high for very fast molecules, imaged at slow frame rates. It is more difficult to calculate, as it is necessary to know the diffusion coefficient of the molecule. We have not measured it in this thesis.[22]

We want to highlight that the different localization precisions, arising from the different imaging conditions and setups, can influence differently the calculated motion parameters. The localization precision represents the minimum displacement that one can measure, and therefore, we can roughly estimate a minimum detectable velocity and diffusion coefficient. We have seen in **Figure 10**, that the static localization precision in our setup is between 50 and 90 nm. This means that we are not able to capture displacements smaller than these values. The challenge comes from the fact that slower or immobile molecules will show this degree of displacements due to the localization precision. What we want to highlight again, is that this should be taken into account when comparing different diffusion coefficient values. Moreover, experiments performed for the comparison between different conditions should be done at the same frame rate.

5. SPT DATA ANALYSIS

In the SPT literature, we can find a wide array of quantitative parameters that describe the motion and dynamics of the single molecules, some of which can be even calculated in many different ways. Moreover, different experimental conditions or different equipment can sometimes lead to different values for the same parameters. We would like to highlight a few considerations that should be taken into account when comparing the results obtained from different studies.

Despite using the same imaging conditions, it may be sometimes difficult or even meaningless to compare the results from different studies because the calculated diffusion parameters might be different. The parameter that is arguably the most commonly used to describe the motion of SPT trajectories is the diffusion coefficient, which is usually calculated by fitting the TA-MSD. However, there are different procedures and even definitions to compute this parameter, and so the name "diffusion coefficient" might have different meanings in different studies. Here, we described some of these "small" details that are sometimes hidden in the literature and that can affect how the diffusion coefficient is calculated:

(i) The fraction of time lags used for the fitting of the TA-MSD. Given the finite length of experimental trajectories, the MSD is calculated with less datapoints as the time lag increases (for time lag m frames, the number of data points in the summatory is $N-m$, where N is the trajectory length in frames, see **Eq. 2**). This results in a very high uncertainty at large time lags. Moreover, diffusion of molecules within cells rarely follows a purely Brownian motion, so the TA-MSD is not linear with respect to the time lag. For these reasons, the fitting of the diffusion coefficient using the TA-MSD

curve is usually performed with only a fraction of the curve (the initial time lags). Strategies to determine which fraction of the curve to use for the fit have been developed,[22] but, in practice, this is usually performed using the first 4 time lags. One should pay attention as some research articles use the time lags 1 to 4, while others use the 2 to 4, or even other ranges. Using just the initial 4 time lags is a conservative approach for the fitting, and somewhat an approximation because the obtained value does not correspond to the generalized diffusion coefficient (that is, the diffusion coefficient for a general anomalous diffusion model, see **Chapter 2**), but it is rather a measure that approximates the diffusion as purely Brownian for short time ranges. As a consequence, these $D_{1\text{-}4}$ or $D_{2\text{-}4}$ coefficients do not inform us about the type of motion (e.g., Brownian vs. anomalous diffusion), so in order to test whether the SPT data corresponds to different types of motion, other types of analysis are needed. Nonetheless, the trajectory length is a limitation for those analyses, making it challenging to obtain accurate predictions of the type of single molecule motion from short trajectories, as the ones usually acquired in intracellular SPT.

(ii) The "y" intercept of the TA-MSD fit. The offset of the MSD curve at zero lag time is indicative of the localization precision. Therefore, for realistic experimental conditions, in which the localization precision is not perfect, the Einstein relation needs to be modified as:

$$\langle \Delta r^2(t) \rangle = 4\sigma^2 + 2dDt \tag{9}$$

being σ the static localization uncertainty, or the localization precision. Therefore, this "y" intercept is a parameter than can also be fitted. In some research articles this intercept is forced at exactly 0, which is something we would not recommend.

When the trajectories are long enough, it is possible to fit, not only the diffusion coefficient, but also the alpha exponent. However, we have already seen in **Chapter 2, Section 4.2**, in the analysis performed by Requena et al., that the relative error in the estimation of the alpha exponent can be pretty high, even for long trajectories. For trajectories smaller than 100 points, the relative error can be from 0.4 to 0.6.[15]

A much simpler parameter that describes particle dynamics is the instantaneous velocity, calculated as the frame-wise displacement multiplied by the frame rate. In processes where the velocity changes over time, instantaneous velocity allows for the analysis of these fluctuations, giving a more detailed picture of the motion at any given moment. However, the single displacement data is highly sensitive to

noise. Moreover, the usefulness of instantaneous velocity can be limited in systems where the motion is highly irregular or where long-term diffusion behavior is of primary interest. In those cases, the diffusion coefficient and the alpha coefficient are more useful parameters.

In this thesis, we have used a novel deep learning approach (named STEP) that provides the step-wise diffusion coefficient and alpha exponent values from single molecule trajectories.[15] We have explained in **Chapter 2** why this approach performs better than the classical TA-MSD. Moreover, STEP combines the step-wise information provided by the instantaneous diffusion, and includes a further layer of information, as the represented motion properties are the diffusion and the type of motions (whether it is confined, Brownian or super diffusive motion).

Having these parameters predicted for each trajectory link (and not only a single average value for the whole trajectory) allows us to monitor how these dynamic properties are distributed in space. Thus, we build what we call diffusion maps (**Figure 12**), which are representations of any frame-wise dynamic parameter (not only of the diffusion coefficient, but also of, e.g., the instantaneous velocity, or the alpha exponent). In **Figure 12A-C**, we show diffusion maps of the ER protein Halo-CALR for a representative cell, in which the localizations are color-coded by the value of the instantaneous velocity, the frame-wise diffusion coefficient obtained with STEP, and the alpha coefficient also obtained with STEP, respectively. First of all, our results indicate that the experimental conditions used allowed us to reconstruct part of the ER network. We noticed that the instantaneous velocity, as previously reported by Holcman et al., changes over this network, with the smallest values found in highly confined regions (possibly ER sheets or junctions), and the higher instantaneous velocities preferentially localized into regions that appear to form more elongated shapes (possibly ER tubules) (see **Figure 12A**). These qualitative results are in agreement with the reported differential dynamics of Halo-CALR, which shows slow dynamics in ER junctions, and faster dynamics in ER tubules.[4]

Our STEP analysis allowed us to perform a similar diffusion map using the values of the frame-wise diffusion coefficient map, showing a similar trend (see **Figure 12B**). However, we qualitatively saw that the local diffusion coefficient values are more uniform in space with respect to these two types of regions. Moreover, we could clearly identify the appearance of punctate regions of very small diffusion coefficient, which highlight the complementarity of our analysis using STEP, as the

instantaneous velocity does not report on the long-term diffusion behavior, which the local diffusion coefficient does.

When representing the alpha exponent, one can also identify the same regions of high confinement and small diffusion coefficient. On top, there are regions of high confinement and higher diffusion coefficient. It would be interesting to check with another fluorescent reporter whether these molecules are within different regions of the ER. There are some localizations labeled as highly diffusive (alpha exponent larger than 1) that could correspond to directional motion within the ER, or tubes being pulled out of the ER. Taken together, we believe that our data underscores the significance of obtaining diffusion maps from SPT trajectories, which could be especially useful to identify spatial regions of uniform diffusion properties.

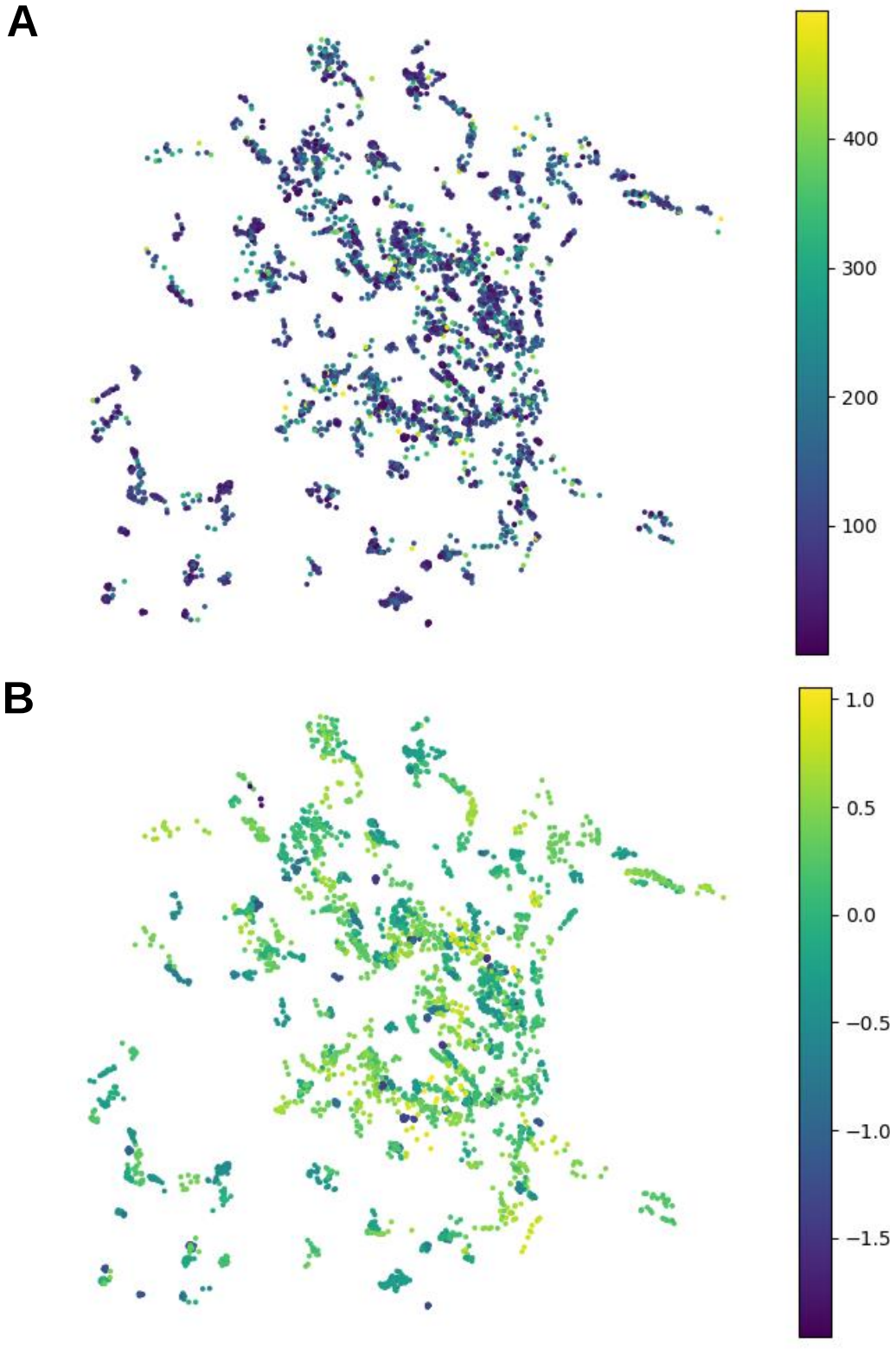
A
400
300
200
100
B
1.0
0.5
0.0
−0.5
−1.0
−1.5

Figure 11. Diffusion maps of Halo-CALR imaged with the PA-JF646-HaloTag ligand. Live HeLa cells overexpressing Halo-CALR, labeled with PA-JF646-Halo ligand, and washed for 2 hours with DMEM. The excitation was performed with continuous illumination at 30% laser power of the 647 nm laser, and photoactivation for 10 ms with the 405 nm laser at different powers every 20 seconds. The acquisition was at 20 ms frame time. Detection threshold in Trackit was set to SNR 2. Localizations are displayed in space and colored according to: **A.** the instantaneous velocity. **B.** the frame-wise diffusion coefficient obtained with STEP. **C.** The frame-wise alpha exponent obtained with STEP.

6. DISCUSSION

To address the specific challenges that SPT in the secretory pathway poses, it is essential to adopt a comprehensive approach that includes optimizing labeling strategies, imaging parameters, and data analysis methods. By conducting control experiments and identifying the best experimental conditions for each step, researchers can maximize the quality and reliability of their SPT data while minimizing experimental and analytical artefacts. This process involves iterative testing and refinement to tailor the techniques to the specific needs of the molecules and cellular context being studied.

We have shown that the photoactivatable versions of the JF646 and JF549 dyes have superior fluorescent properties as compared to their non-photoactivatable versions.

Although PA-JF549 has objectively better fluorescent properties, the specific requirements for each protein of interest and each experimental condition may lead to choosing one dye over the other. Factors such as the available excitation laser lines and the presence of other fluorescent reporters come into play in this decision.

Our results and analyses showed that when labeling the molecules with a fluorophore, it is essential to minimize the number of unbound fluorescent molecules, as they can be very difficult to distinguish from the protein under investigation. We proposed to conduct control experiments on fixed cells to minimize the remaining mobile fraction, which corresponds to unbound dye. We have observed that this process strongly depends on the dye, suggesting that the chemical groups of the dye may influence how effectively it can be washed away.

Although the quantifications are not included in this thesis, we conducted control experiments to investigate potential non-specific binding of the dye. Labeling fixed samples of mixed populations containing transfected and non-transfected cells revealed that non-transfected cells never exhibited bound immobile dye (data not shown).

We have also proposed a strategy to make rational decisions regarding localization density. This can be controlled by using different concentrations of standard non-photoactivatable dyes or by varying the power of the 405 nm laser during photoactivation. The decision should aim to maximize the number of localizations per frame while ensuring sufficient SNR for precise particle detection.

For the imaging conditions, we emphasized the importance of selecting a frame rate that can capture the entire range of molecular speeds. The localization density should be adjusted to enable choosing a frame rate capable of capturing the full diffusion dynamics of the protein of interest while maintaining a high enough SNR for molecule detection. Finally, we have shown how to optimize the selection of a proper excitation power to guarantee molecule visualization at the selected frame rate for an extended period. However, within the range of laser powers tested, we did not observe significant differences.

Regarding the analysis of trajectories, multiple motion parameters are calculated using various measurement methods. We have emphasized that absolute values are not directly comparable between studies due to specific experimental conditions influencing the results. This underscores the importance of conducting positive

control experiments to validate the employed methodology against previously established standards.

7. REFERENCES

1. Cisse, I. I. *et al.* Real-time dynamics of RNA polymerase II clustering in live human cells. *Science (1979)* **341**, (2013).
2. Gebhardt, J. C. M. *et al.* Single-molecule imaging of transcription factor binding to DNA in live mammalian cells. *Nat Methods* **10**, (2013).
3. Elf, J., Li, G. W. & Xie, X. S. Probing transcription factor dynamics at the single-molecule level in a living cell. *Science (1979)* **316**, (2007).
4. Holcman, D. *et al.* Single particle trajectories reveal active endoplasmic reticulum luminal flow. *Nat Cell Biol* **20**, 1118–1125 (2018).
5. Obara, C. J. *et al.* Motion of VAPB molecules reveals ER–mitochondria contact site subdomains. *Nature* **626**, (2024).
6. Hansen, A. S. *et al.* Robust model-based analysis of single-particle tracking experiments with spot-on. *Elife* **7**, (2018).
7. Calderon, C. P. Motion blur filtering: A statistical approach for extracting confinement forces and diffusivity from a single blurred trajectory. *Phys Rev E* **93**, (2016).
8. Pereira, C. *et al.* The exocyst complex is an essential component of the mammalian constitutive secretory pathway. *J Cell Biol* **222**, (2023).
9. Axthelm, M. K. & Krakowka, S. Immunocytochemical methods for demonstrating canine distemper virus antigen in aldehyde-fixed paraffin-embedded tissue. *J Virol Methods* **13**, (1986).
10. Clancy, B. & Cauller, L. J. Reduction of background autofluorescence in brain sections following immersion in sodium borohydride. *J Neurosci Methods* **83**, (1998).
11. Grimm, J. B., Brown, T. A., English, B. P., Lionnet, T. & Lavis, L. D. Synthesis of Janelia Fluor HaloTag and SNAP-Tag Ligands and Their Use in Cellular Imaging Experiments. in *Methods in Molecular Biology* 179–188 (Springer New York, 2017). doi:10.1007/978-1-4939-7265-4_15.

12. Grimm, J. B. *et al.* Bright photoactivatable fluorophores for single-molecule imaging. *Nat Methods* **13**, 985–988 (2016).

13. Kuhn, T., Hettich, J., Davtyan, R. & Gebhardt, J. C. M. Single molecule tracking and analysis framework including theory-predicted parameter settings. *Sci Rep* **11**, (2021).

14. Tinevez, J.-Y. *et al.* TrackMate: An open and extensible platform for single-particle tracking. *Methods* **115**, 80–90 (2017).

15. Requena, B. *et al.* Inferring pointwise diffusion properties of single trajectories with deep learning. *Biophys J* **122**, (2023).

16. Kingma, D. P. & Ba, J. L. Adam: A method for stochastic optimization. in *3rd International Conference on Learning Representations, ICLR 2015 - Conference Track Proceedings* (2015).

17. Howard, J. & Gugger, S. Fastai: A layered api for deep learning. *Information (Switzerland)* **11**, (2020).

18. Hanada, K. *et al.* Molecular machinery for non-vesicular trafficking of ceramide. *Nature* **426**, 803–809 (2003).

19. Grimm, J. B. *et al.* A general method to improve fluorophores for live-cell and single-molecule microscopy. *Nat Methods* **12**, 244–250 (2015).

20. Sigaut, L., Villarruel, C., Ponce, M. L. & Ponce Dawson, S. Fluorescence correlation spectroscopy experiments to quantify free diffusion coefficients in reaction-diffusion systems: The case of Ca2+ and its dyes. *Phys Rev E* **95**, (2017).

21. Manley, S. *et al.* High-density mapping of single-molecule trajectories with photoactivated localization microscopy. *Nat Methods* **5**, (2008).

22. Michalet, X. Mean square displacement analysis of single-particle trajectories with localization error: Brownian motion in an isotropic medium. *Phys Rev E Stat Nonlin Soft Matter Phys* **82**, (2010).

Chapter 5

Characterization of Protein Sorting at ER- Golgi MCS

In this chapter we applied the methodology established in Chapters 3 and 4 to characterize protein sorting at the TGN. We used super-resolution STED microscopy and SPT to characterize cargo protein distribution in the regions of the TGN enriched in ER-Golgi MCS. First, STED microscopy performed on fixed cells allowed us to distinguish regions of cargo accumulation. These inhomogeneities are compatible with the suggested hypothesis in which ER-Golgi MCS might be creating sphingomyelin- and cholesterol-rich nanodomains, that serve as sorting domains in the TGN. Using live-cell STED imaging we observed that these cargo accumulations form punctate structures, which are dynamic in terms of movement, appearance and disappearance, and fusion. The movement appears in synchrony with the MCS structures, which sometimes wrap them. Finally, we performed SPT experiments to monitor the dynamics of individual cargo proteins both within and outside these putative cargo sorting regions. By a quantitative characterization of the dynamics of these cargo proteins, we revealed that a large number of these proteins follow a very confined and slow motion when they are in close proximity to the MCS. Interestingly, this effect is inhibited when the ER-Golgi MCS were stabilized by the addition of the lipid transfer blocker 25-HC. However, the fraction within and outside of protein in these cargo accumulations is conserved across proteins and MCS destabilizing conditions, indicating that this is regulated upstream and that MCS only regulate the location preference of these cargo accumulations.

Part of this work has been published as:

Wakana, Y., Hayashi, K., Nemoto, T., Watanabe, C., Taoka, M., **Angulo-Capel, J.**, Garcia-Parajo, M. F., Kumata, H., Umemura, T., Inoue, H., Arasaki, K., Campelo, F., Tagaya, M. (2020) The ER cholesterol sensor SCAP promotes CARTS biogenesis at ER–Golgi membrane contact sites. Journal of Cell Biology. 220 (1): e202002150. doi: 10.1083/jcb.202002150

1. INTRODUCTION

1.1. ER-GOLGI MCS IN THE SECRETORY PATHWAY

As already explained in Chapter 1, membrane contact sites (MCS) are platforms for communication between cell compartments. A particular type of MCS occupies this chapter, ER-Golgi MCS, which form between the ER and the *trans*-Golgi cisternae and/or the TGN. Some proteins at both sides of the contact interact, such as VAP–A and –B, OSBP[1], and CERT[2] (see **Chapter 1, Section 6.4**). Some of them are lipid transfer proteins. In particular, CERT transports ceramide from the ER to the TGN[2], whereas OSBP shuttles cholesterol from the ER to the TGN and PI4P in the opposite direction[3]. PI4P can then be dephosphorylated by the phosphatase activity of Sac1 at the ER side.[4] This PI4P cycle helps sustain a gradient of lipids (such as cholesterol and ceramide) in the membranes of the early secretory pathway, thereby contributing to maintain organelle identity.

Although the main function of ER-Golgi MCS known to date is the regulation of Golgi lipid homeostasis, it has been shown that the formation of ER-Golgi MCs is required for CARTS formation. As a reminder, silencing of the MCS components VAP-A and VAP-B[5], as well as stabilizing OSBP and CERT with the PH-FFAT domain, results in lower secretion of the protein PAUF, and reduced formation of CARTS.[6] Similar observations have been made when using 25-HC, an oxysterol that is able to bind OSBP with high affinity, and block it in the bound conformation to VAP. This binding inhibits the VAP/OSBP-mediated sterol transfer.[3] However, the specific role that MCS play in CARTS formation, as well as the impact of their lipid transfer function still remains as an unanswered question. Furthermore, whether ER-Golgi MCS are necessary for protein sorting, and/or the successive steps of membrane budding and/or carrier fission is also unknown.

1.2. AIM OF THE PROJECT

Given the inhibitory effect of 25-HC in CARTS biogenesis, it is logical to assess the potential role(s) of lipid transport at MCS. Based in our current knowledge, a direct link can be hypothesized between this lipid transport function and fission of the carriers. In MCS, OSBP facilitates activation of CERT-mediated ceramide transfer.[7] Ceramide and phosphatidylcholine, can then be converted into sphingomyelin and diacylglycerol (DAG).[2,8] DAG not only promotes negative curvature in membranes, therefore possibly facilitating neck narrowing during fission[9], but also recruits and

activates PKD.[10] As already mentioned in **Chapter 1**, PKD is required for CARTS fission at the TGN.[11–15]

However, the formation of local lipid inhomogeneities at the TGN by MCS can also be linked to sorting processes. Indeed, it has long been recognized that one of the primary mechanisms of protein sorting at the TGN is lipid-dependent, through the formation of sphingolipid-rich lipid nanodomains, or rafts.[16,17] It has been observed that disturbing sphingomyelin metabolism inhibits sorting and transport carrier biogenesis.[18,19] Therefore, ER-Golgi MCS might generate distinct nanodomains, rich in cholesterol and sphingomyelin, that could serve as sorting regions. This chapter aims at bringing light into this possibility.

In order to observe protein sorting at the TGN, we looked at the protein distribution in regions enriched in ER-Golgi MCS. For this purpose, we used a stable cell line co-expressing OSBP and VAP-A fused to the split version of the Venus fluorescent protein (Vn-OSBP and Vc-VAP-A), named HeLa BiFC in this thesis for short.[6] The cargo protein distribution was compared between the PAUF-SNAP construct, and a control construct of SNAP with a signal sequence for targeting to the secretory pathway (termed ss-SNAP in this work). As this latter protein is merely the SNAP sequence brought to the secretory pathway by a signal peptide, it should not have any specific endogenous sorting signals for TGN export. Therefore, this cargo protein can be used as an example of protein that leaves the TGN in a non-specific manner, maybe through the so-called "bulk secretion". Additionally, cells were treated with the previously mentioned 25-HC, in order to both stabilize the MCS and inhibit OSBP's lipid transfer. The resultant effects can reveal more information about the molecular mechanism underlying CARTS biogenesis.

Two techniques were used: STED microscopy (both in fixed cells and in live-conditions) and SPT. The first one provides a super-resolved picture of the protein cargo distribution, while SPT provides the dynamics of the single molecules in the same context. While STED allowed us to distinguish regions of accumulation of cargo, SPT allowed us to distinguish regions of distinct mobility, in terms of velocity and type of motion, therefore bringing complementary information.

2. CHARACTERIZATION OF PAUF AND SS-SNAP SECRETION

In order to study CARTS biogenesis, it is necessary to establish a protocol for protein secretion synchronization. Cells were seeded, transfected with the corresponding tagged protein cargoes, and incubated at 20°C for 2 hours to block general TGN

export, without blocking ER-to-Golgi traffic.[20,21] After accumulation at the Golgi with the 20°C block, TGN export was activated again by shifting the temperature back to 37°C.

It is to be noted that synchronization using the 20°C block is far from a perfect approach, because trafficking from the ER to the Golgi can be rather slow and it is difficult to accumulate all the proteins at the Golgi, even after 2 hours incubation. We tried to implement the RUSH assay[22] with the protein PAUF as a cargo, but the different approaches did not work in our hands. We tried to use the stable HeLa cell lines stably expressing Strep-KDEL combined with either SBP-Halo or SBP-Halo-PAUF, implemented in D. Gershlick's lab (Cambridge Institute for Medical Research, The University of Cambridge, UK).[23] We also performed stable CRISPR knock-in of PAUF-SBP-EGFP and PAUF-SBP-Halo on multiple cell lines: HeLa wild type, HeLa TGN46-SNAP KI, HeLa BiFC, and the HeLa Strep-KDEL from D. Gershlick's lab. Cells never survived the antibiotic selection. It is interesting that the KI didn't work either for simply PAUF-Halo or PAUF-SNAP on the same cell lines (data not shown). Further work will be necessary to investigate the cause of these effects.

2.1. METHODS

Cell culture and molecular biology

HeLa BiFC (Vn-OSBP and Vc-VAP-A) cells and the plasmid encoding PAUF-SNAP were established by Y. Wakana (School of Life Sciences, Tokyo University of Pharmacy and Life Sciences, Japan).[6] The plasmid encoding PAUF-MycHis was donated by S.S. Koh (Korea Research Institute of Bioscience and Biotechnology, Daejeon, Korea).

Cloning of ss-SNAP construct was performed by PCR amplification of the PAUF-SNAP construct, excluding the sequence encoding for PAUF (primers 5'-GGCTTAATTAAGGACAAAGACTGCGAAATGAAGCGCAC-3' and 5'-GCCTTAATTAAATACATCTTCCCTGCCCAGGTGG-3'). The PCR was performed with DNA polymerase KOD Hot Start (Novagen), according to the manufacturer's protocol. The template DNA was digested with DpnI (New England Biolabs), and the resulting sequence was then digested with PacI restriction enzyme (New England Biolabs). Finally, it was ligated with the T4 DNA ligase (New England Biolabs).

HeLa cells were grown in DMEM supplemented with 10% FBS (without antibiotics). HeLa BiFC stable cells were grown in DMEM supplemented with 10% FBS, 2.5 L-glutamine, 1 µg/ml puromycin, and 10 µg/ml blasticidin. Cells were seeded the

previous day on 12 mm size #1.5H–thickness cover glasses (ThorLabs) placed in 6-well plates. Plasmid transfection was performed using X-tremeGENE 9 DNA transfection reagent (Roche), 20 hours before fixation, and according to the manufacturers' protocol.

Secretion synchronization

20 hours after transfection, the medium of the cells was changed to DMEM (10% FBS, 2.5 mM L-glutamine, without antibiotics, without Phenol Red) with 25 mM HEPES pH 7.4, 100 µM of cyclohexamide (CHX). Cells were then incubated for 2h at 20°C.[20,21] After the 20°C block, cells were washed 3 times with PBS, and the medium was changed to DMEM (10%FBS, 2.5mM L-glutamine, without antibiotics, without phenol red) for the incubation at 37°C. Coverslips were taken at different stages of the protocol, and fixed with 3.7% formaldehyde in PBS (v/v) for 20 minutes.

In the cases in which the overexpressed plasmid was SNAP-tagged, cells were labeled with 1 µM JF549-SNAPligand or JF646-SNAPligand (Promega)[24] in DMEM (10% FBS, 2.5 mM L-glutamine, without antibiotics, without phenol red) for 15 min at 37°C, and washed 3 times with PBS previous to the 20°C block. The 2 hours incubation at 20°C also served as washing time for the Janelia fluorophore.

Immunofluorescence

After fixation and wash with PBS, all coverslips were permeabilized with 0.1% TritonX in PBS (v/v), blocked with 4% BSA in PBS (w/v) for 30 minutes, and immunolabeled. For the visualization of PAUF-MycHis, we used a mouse anti-c-Myc (clone 9E10, Sigma-Aldrich) primary antibody (1:200 dilution) and a goat anti-mouse Abberior STAR RED–conjugated goat anti-mouse IgG secondary antibody (Abberior) (dilution 1:100).

The coverslips were mounted with Mowiol on glass slides (0.1% w/v in Tris and glycerol, Calbiochem).

Confocal imaging

Images were performed on a commercial Leica TCS SP8 STED 3× microscope equipped with a pulsed supercontinuum white light laser excitation source, using a 100× 1.4 NA oil HC PL APO CS2 objective. Images were acquired with the Leica LAS AF software. In all acquisitions the pinhole size was set to 151.6 µm size.

For the HeLa wild type samples overexpressing both PAUF-MycHis and ss-SNAP (Abberior STAR RED and JF549-SNAPligand, respectively), the imaging conditions

were as follow: The PAUF-MycHis signal was detected with excitation using a 637-nm line at 2% of the white-light laser intensity (set at 70% output power). The ss-SNAP signal was detected using excitation at 549 nm wavelength at 14% of the white-light laser intensity (set at 70% output power). The two channels were imaged sequentially, line by line, and Z-stacks of about 3 µm were performed with slices of about 300 nm thickness. Images were taken with 2 line-accumulation, with a pixel size of 72 nm, and scanning at 400 lines per second. The PAUF-MycHis signal was collected with a PMT detector with detection window from 647 – 750 nm. The detection of ss-SNAP was performed with a HyD SMD detector, with the detection window from 559 – 627 nm, in photon counting mode, gain at 10%, and gating from 0.3 to 3.8 ns.

For the HeLa BiFC samples overexpressing PAUF-SNAP (JF646-SNAPligand), the imaging conditions were as follow: The BiFC signal was detected using 514-nm wavelength excitation at 20% of the white-light laser intensity (set at 70% output power). The PAUF-SNAP signal was detected with excitation using a 646-nm line at 30% of the white-light laser intensity. The two channels were imaged simultaneously, with 2 line-accumulations, a pixel size of 89 nm, and scanning at 400 lines per second. The detection of the PAUF-SNAP signal was performed with a HyD SMD detector, with detection window 670 – 750 nm, gain at 10%, counting mode, and gating from 0.3 to 3.8 ns. For the BiFC signal, the detector was a HyD SMD, with detection window set to 524 – 570, gain at 10%, photon counting mode, and gating from 0.3 to 3.8 ns.

Image processing with Fiji (ImageJ)

For the HeLa wild type samples overexpressing both PAUF-MycHis and ss-SNAP, the z-stacks were projected using maximum intensity z-projection with Fiji. All images were smoothed using the processing option in Fiji, and the brightness and contrast were adjusted.

2.2. RESULTS

In order to determine the incubation time required for a proper accumulation of cargo proteins at the Golgi, we incubated the cells for 1 or 2 hours at 20°C. Afterwards, samples were incubated at 37°C for different times. **Figure 1** shows that 2 hours is enough for a proper accumulation of both PAUF-MycHis and ss-SNAP in the Golgi. In a few cells, it is possible to observe point-like structures containing both ss-SNAP and PAUF-MycHis. Given their distribution, their size and the perfect

colocalization of both proteins, we suggest that they correspond to ER exit sites (ERES). However, immunolabeling against ERES proteins such as Sec13 should be performed in the future to confirm this hypothesis. From 30 min of incubation at 37°C, it is possible to start observing CARTS, which are bigger and brighter than the previously mentioned point-like structures. After 1 hour, most of the overexpressing cells show CARTS. It is to be noted that there is not perfect colocalization between the carriers containing both proteins, suggesting that ss-SNAP is able to exit both through CARTS, and alternative secretion carriers.

This process was also characterized for the cargo PAUF-SNAP. In **Figure 2**, one can appreciate that, after 1 hour incubation at 37°C, signal at the perinuclear area is still not very defined, and there is quite some signal at the ER. After 2 hours, the signal is more accumulated at the Golgi. After 30 min incubation at 37°C, one can appreciate CARTS. It is to be noted that fluorescence in the ER is still present after the 20°C block, which could be problematic especially for the SPT experiments.

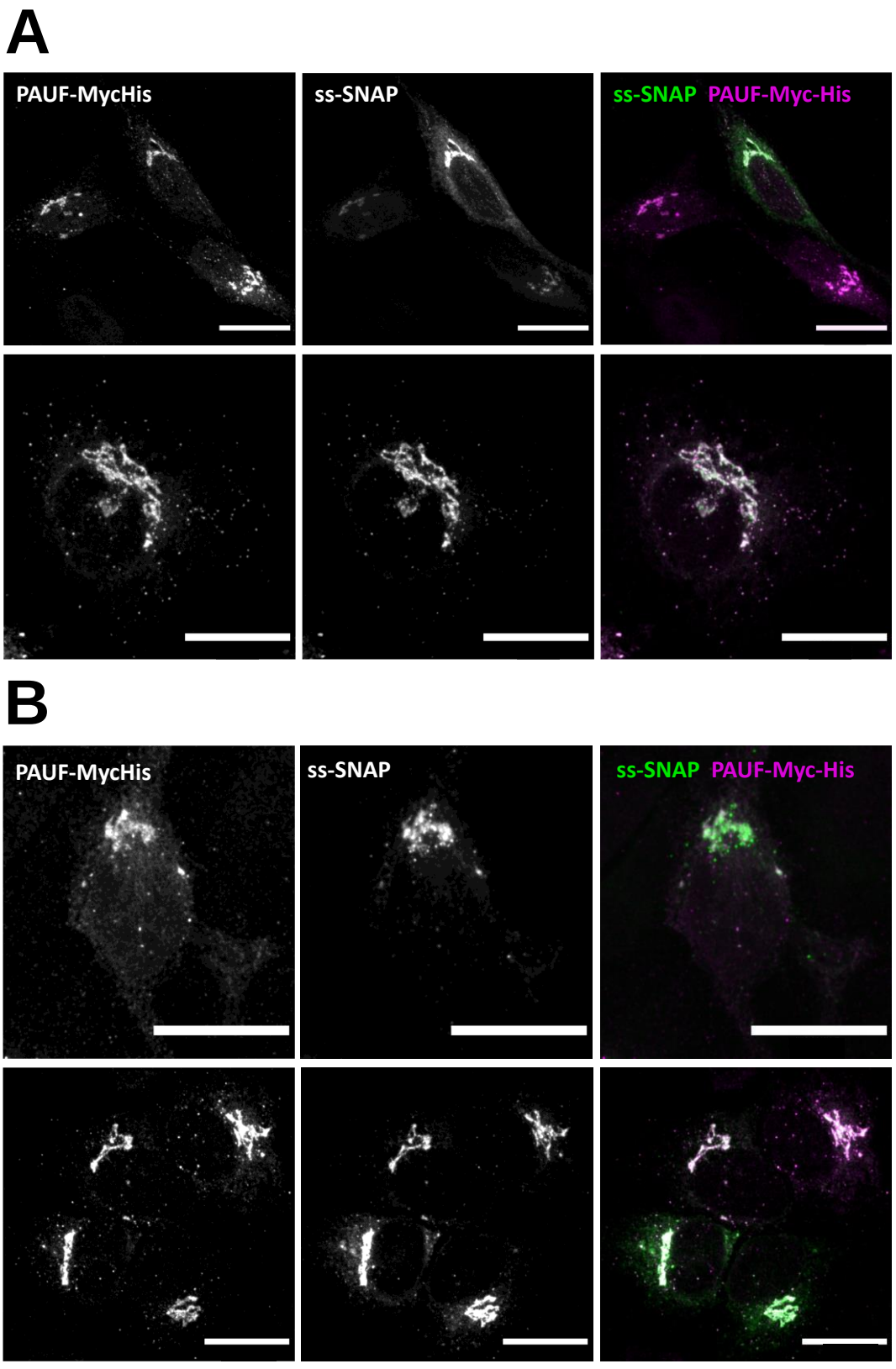
A
PAUF-MycHis
ss-SNAP
ss-SNAP PAUF-Myc-His
B
PAUF-MycHis
ss-SNAP
ss-SNAP PAUF-Myc-His

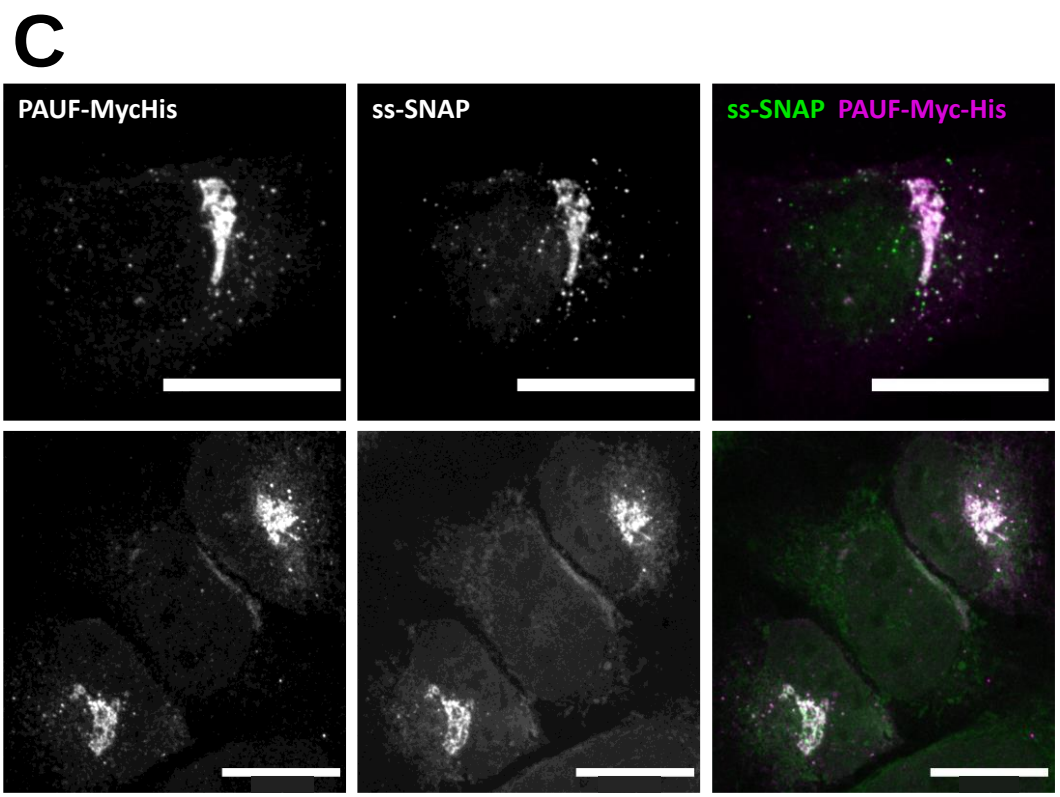

Figure 1. Secretion synchronization of PAUF-MycHis and ss-SNAP. Representative images of cells. Samples were taken after 2 hours at 20°C (**A**), after 30 min incubation at 37°C (**B**), and after 1 hour incubation at 37°C (**C**). Scale bars 20 μm.

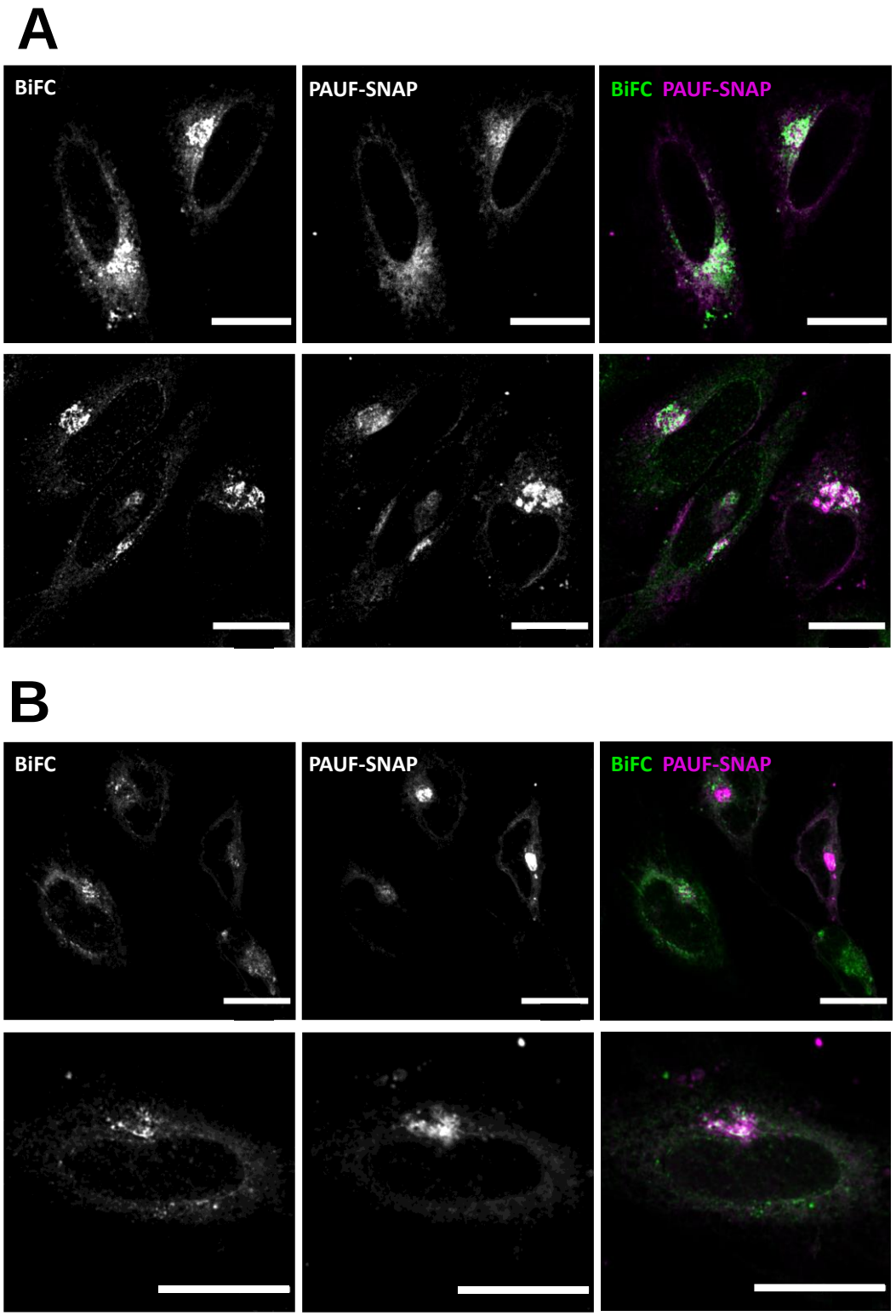
A
BiFC
PAUF-SNAP
BiFC PAUF-SNAP
B
BiFC
PAUF-SNAP
BiFC PAUF-SNAP

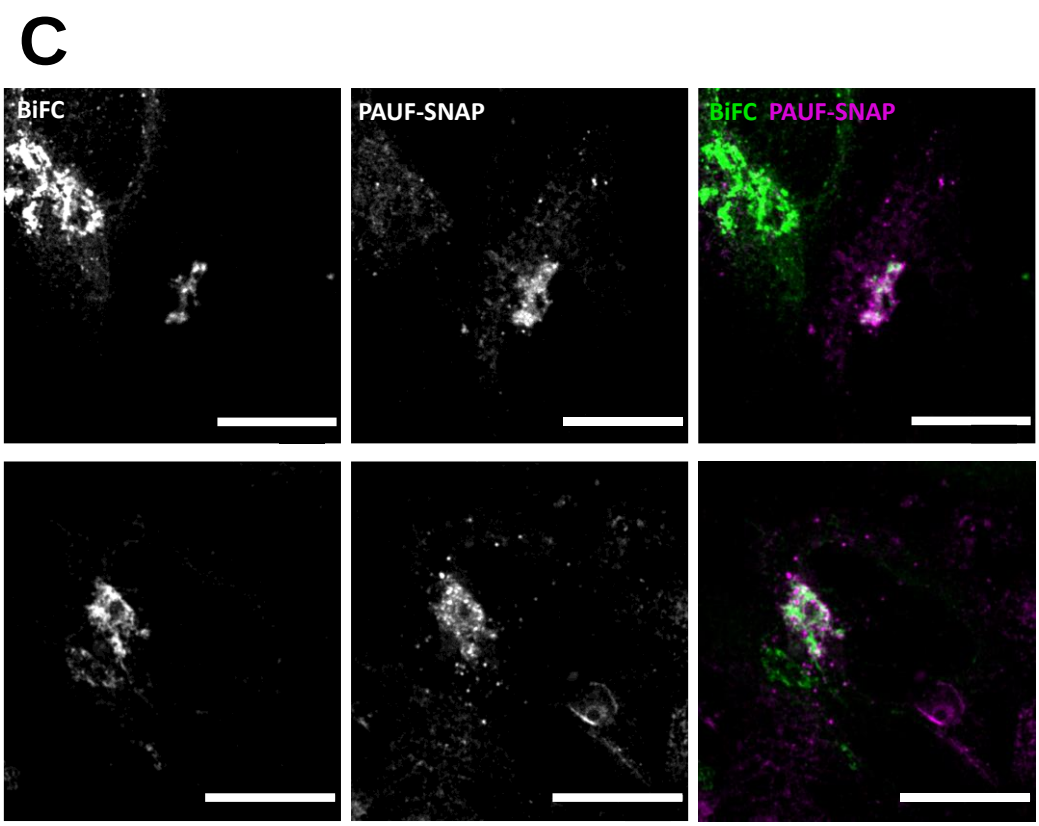

Figure 2. Secretion synchronization of PAUF-SNAP in HeLa BiFC. Representative images of cells. Samples were taken after 1 hours at 20°C (**A**), after 2 hours at 20°C (**B**), and 30 min incubation at 37°C (**C**). Scale bars 20 µm.

3. SUPER-RESOLUTION STED IMAGING OF CARTS BIOGENESIS

In order to assess whether local nanodomains of sphingomyelin and cholesterol produced by ER-Golgi MCS are resulting in accumulation of cargo protein at specific TGN sites, we analyzed the protein spatial distribution with super-resolution STED, both in fixed and live conditions. Fixed conditions allowed to obtain better resolved images, by allowing the utilization of higher laser powers, and longer acquisition times. Live-STED imaging allowed to observe the dynamics of both ER-Golgi MCS and the accumulation of cargo proteins.

3.1. METHODS

Cell culture and molecular biology

Cell culture, transfection, secretion synchronization and immunofluorescence were performed as described in **Section 2**. The origin on the plasmids and cell lines is also

described in **Section 2**. We used the HeLa BiFC cell line, and overexpressed the corresponding plasmids using X-tremeGENE 9 DNA transfection reagent (Roche), 20 hours before the experiment, and according to the manufacturers' protocol.

STED imaging of fixed samples

Immunofluorescence was performed as described in **Section 2**. The cover glasses were mounted on glass slides using ProLong Gold (Thermo Fisher Scientific). Images were performed on a commercial Leica TCS SP8 STED 3× microscope equipped with a pulsed supercontinuum white light laser excitation source, using a 100× 1.4 NA oil HC PL APO CS2 objective. In all acquisitions the pinhole size was set to 151.6 μm size.

The BiFC signal was detected in confocal mode (without STED) using 514-nm wavelength excitation at 8% of the white-light laser intensity (set at 70% output power); the PAUF-MycHis signal was detected in STED mode, where the excitation was performed using a 633-nm line at 1% of the white-light laser intensity and the depletion was performed with a second ps-pulsed laser at 775nm with a 0-ps pulse delay and used at 100% intensity (output power set to 100%). The two channels were imaged sequentially line by line, in an almost simultaneous manner to minimize the effects of mechanical drift of the system. Images were taken with multiple line accumulations (up to 16 accumulations) with a pixel size of around 10 nm, with scanning at 400 lines per second. The detection of the two channels was done with two separate HyD SMD detectors in photon counting mode and acquisition windows set to 524–607 nm (for the BiFC channel) and to 643–745 nm (for the PAUF-MycHis channel) and using time gating (gating from 0.3 ns to 6 ns). Images were acquired with the Leica LAS AF software and further deconvolved using Huygens software, to improve the spatial resolution in both the confocal BiFC channel and the STED PAUF-MycHis channel.

STED imaging of live samples

For the live-cell imaging, cells were seeded on 35 mm cell imaging dishes with glass bottom (#81218-200, Ibidi) ~24 hours before transfection. The imaging dishes had been previously coated with fibronectin by incubation with 125 μg of fibronectin for 30 minutes at 37ºC. HeLa BiFC cells were transfected with either PAUF-SNAP or ss-SNAP plasmids. 20 hours later, they were labeled with 1 μM JFX650-SNAPligand (Janelia Materials) in DMEM (10%FBS, 2.5mM L-glutamine, without antibiotics, without phenol red) for 15 min at 37°C. Samples were washed 3 times with PBS.

Then, the medium of the cells was changed to DMEM (10%FBS, 2.5mM L-glutamine, without antibiotics, without phenol red) with 25 mM HEPES pH 7.4. Cells were then incubated for 2h at 20°C. After the 20°C block, cells were washed 3 times with PBS, and the medium was changed to DMEM, and cells were imaged at 37°C during 1 hour.

Imaging was performed with the Abberior STED microscope expert line and the control software Imspector. This microscope is mounted on a U-MCZ Olympus Microscope controller, equipped with 485, 518, and 561, and 640 nm excitation lasers (all except the 405 are pulsed lasers), and 775 nm and 595 nm depletion lasers. We used the Olympus Objective UPLXApO60XO with 60× magnification, 0.15 mm working distance, 1.42 NA, and cover correction of 0.17 mm. The pinhole was always set to 1.0AU.

Samples were kept at 37°C during the whole acquisition with a custom-made incubator. The 2 channels were recorded sequentially line by line. Videos were acquired at 5 seconds per frame until bleaching, using a 30 nm pixel size, 2 µs/pixel dwell time, and no line or frame accumulations. The fluorophore JF646-SNAPligand was excited with 640 nm laser, at 15% laser power, and the depletion laser 775 nm at 2% laser power. The BIFC fluorescence was obtained with excitation with the 518 nm laser at 10% laser power. Detection was carried out with an Ultra-high-sensitivity APD. The detection windows are not specified by the Imspector software, but correspond to the pre-established channel conditions “Silicon rhodamine” and “Yellow Fluorescent Protein”.

Image deconvolution

Deconvolution processing was performed with Huygens Professional version 18.04 (Scientific Volume Imaging). For that, a theoretical point-spread function was automatically computed based on the microscope and image acquisition parameters. The deconvolution process was numerically performed using the Classic Maximum Likelihood Estimation algorithm. In brief, this algorithm assumes that the photon noise is Poisson-distributed, and the likelihood of an estimate of the actual image given the computed point-spread function and the acquired image is iteratively optimized until either a quality factor or a maximum number of iterations is reached. In our deconvolutions, we used a quality factor equal to 0.001 and a maximum 50 iterations. The signal-to-noise ratio for each acquired image was computed based on three line profiles going through regions of background signals toward regions of positive, actual signals. Typically, signal-to-noise ratios were on

the order of 7–20 for the different analyzed confocal images and 7 for the STED image.

After deconvolution of the STED images, the effective resolution obtained was ~30 nm for the PAUF-MycHis channel, in fixed samples, and ~150 nm for PAUF-SNAP in live samples.

3.2. RESULTS

We first visualized CARTS in the Vn-OSBP–Vc-VAP-A stably expressing cells (HeLa BiFC) by immunostaining the exogenously overexpressed CARTS-specific cargo PAUF-MycHis in fixed samples. Many of the putative nascent CARTS imaged by super-resolution microscopy (STED) were located in the close vicinity of the BiFC-positive perinuclear structures (see **Figure 3**, arrowheads), suggesting that CARTS form at sites immediately adjacent to the VAP-A–OSBP complex-containing ER–Golgi MCSs.

We then examined whether it is possible to appreciate differences in the protein distribution when treating the cells with 25-HC. **Figure 4** shows representative images of HeLa BiFC cells overexpressing PAUF-MycHis either treated or not with 25-HC. We were not able to appreciate major differences between the two conditions. Similarly to control cells, 25-HC-treated cells revealed heterogeneities of protein cargo distribution, as well as the appearance of some punctate structures located adjacent to the BiFC signal.

Live-STED was performed in order to visualize the dynamics of these cargo accumulations in the proximity to ER-Golgi MCS, without the need of chemical fixation of the cells. When overexpressing PAUF-SNAP in HeLa BiFC cells (see **Figure 5A**), we detected similar puncta as the ones observed in the fixed samples (**Figures 3,4**). Additionally, MCS structures move together with these puncta of cargo accumulation, sometimes even wrapping them. We can also observe fusion and fission events between these punctate structures, suggesting that they are not fully-formed carriers, but rather nanodomains of cargo accumulation still connected to the lumen of the TGN. We also observed that some of these cargo-containing buds become bigger, more rounded, and move away from the ER-Golgi MCS (**Figure 5A**, red). We propose that they correspond to newly formed CARTS that travel away from the TGN en route to the cell surface.

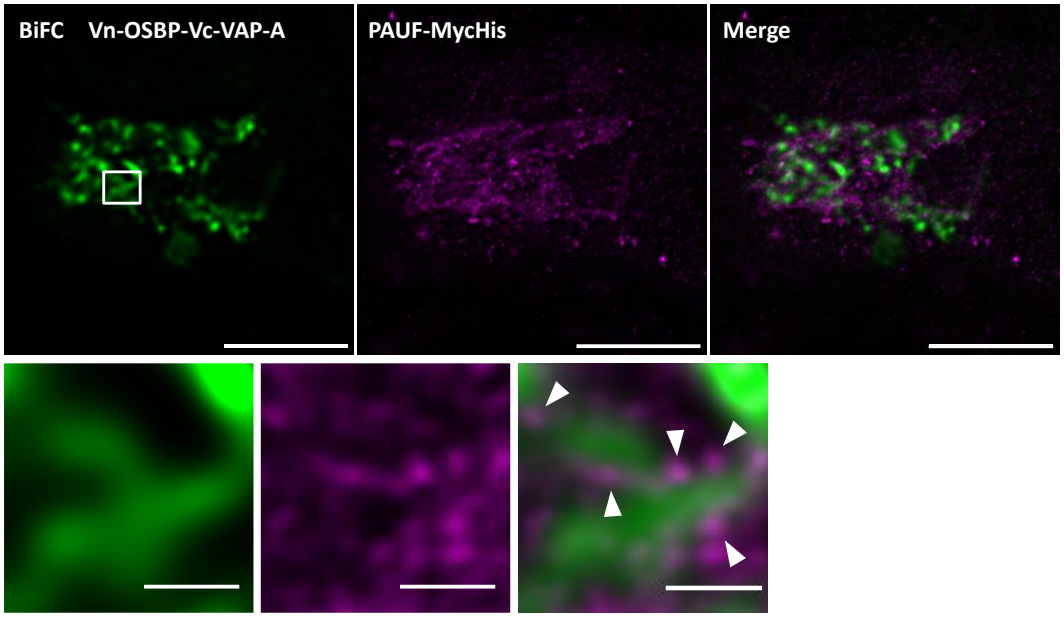

Figure 3. Super-resolution STED microscopy images of PAUF in HeLa BiFC. CARTS formation sites (PAUF-MycHis channel, imaged by STED) are in close proximity to VAP-A–OSBP–mediated ER–Golgi MCSs (BiFC channel, imaged by confocal microscopy). High magnifications of the boxed areas are shown in the bottom panels. Arrowheads indicate putative nascent CARTS located in the close vicinity of the BiFC signal of Vn-OSBP–Vc-VAP-A. Scale bars, 5 µm (top panels), 1 µm (bottom panels). (Published in Y. Wakana et al., Journal of Cell Biology (2021)[6]).

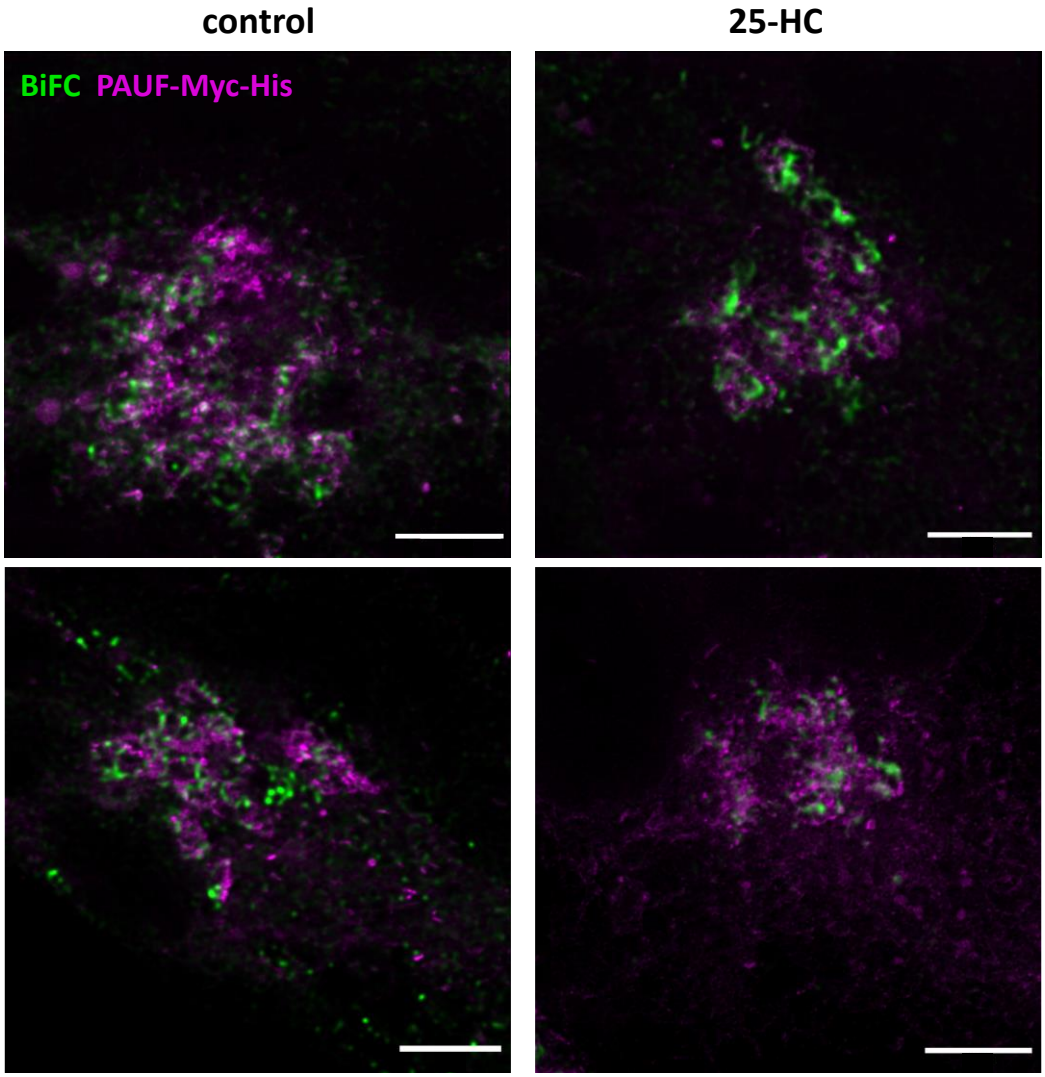

Figure 4. Super-resolution STED microscopy images of PAUF in HeLa BiFC treated with 25-HC. PAUF-MycHis channel was imaged by STED and VAP-A–OSBP–mediated ER–Golgi MCSs (BiFC channel) were imaged by confocal microscopy. Left images correspond to HeLa cells in control conditions, and right images correspond to 25-HC treated cells. Scale bars 4 µm.

We next monitored by live-cell STED microscopy how the bulk cargo protein ss-SNAP distributes within the TGN and in relation to the ER-Golgi MCS during its export. Our results revealed that ss-SNAP presents a more smeared distribution of its signal, with less punctate structures and enlarged regions of cargo accumulation (**Figure 5B**). These domains also move in synchrony with the MCS. Although many of the more rounded structures seem to be located away from the MCS, it is difficult to confirm their presence in these regions because we are not imaging the full 3D volume.

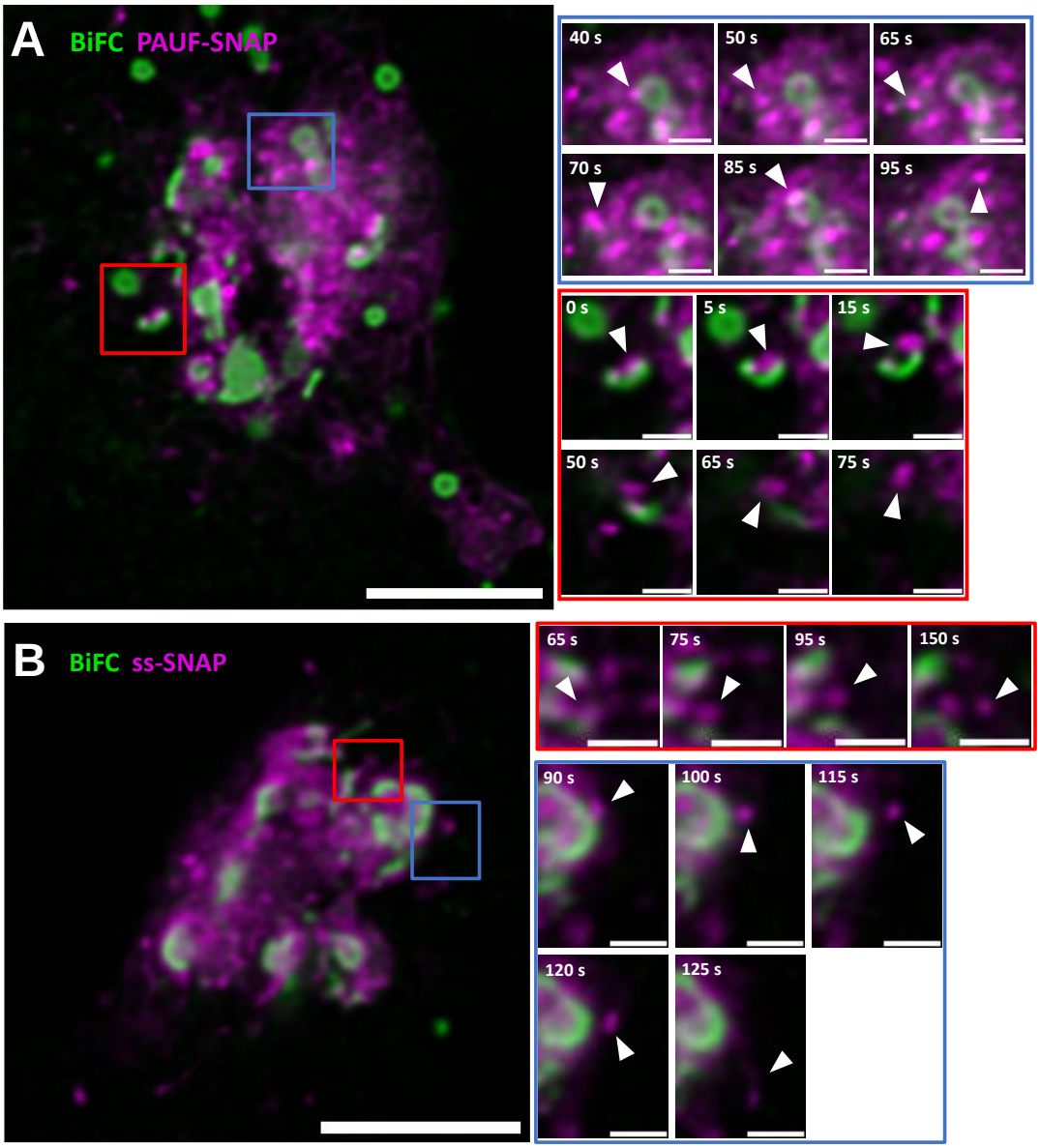

Figure 5. Live-STED imaging of PAUF-SNAP and ss-SNAP in HeLa BiFC cells. The red and blue boxes represent regions that have been zoomed in at the right. The movement of selected structures (white arrowheads) is displayed with a time sequence. Scale bar in the overall images is 5 µm, while scale bar on the zoom-ins is 1 µm. **A.** Overexpression of PAUF-SNAP on HeLa BiFC cells. Many punctate structures move together with the BiFC signal. Some move away from the BiFC signal once they get more rounded, and the BiFC signal can disappear. **B.** Overexpression of ss-SNAP on the HeLa BiFC cells. One can appreciate similar punctate structures that move together with the BiFC structures. In the second example, one can hint a tubular structure coming out.

4. SINGLE PARTICLE TRACKING TO STUDY PROTEIN SORTING AT THE TGN

So far, our data indicated that the CARTS specific protein cargo is not homogeneously distributed in the TGN, but it rather accumulates in nanodomains that many times are very close to the ER-Golgi MCS. In the following experiments we aimed to better describe the dynamics of the protein cargoes in these punctate regions, in order to shed light on the properties of these cargo heterogeneities. Moreover, the sequentially acquired BiFC images will let us link these results with the spatial organization of the MCS signal.

We hypothesize that these regions of cargo accumulation should have distinct diffusion properties. Such differences could exist independently of whether there is an active sorting mechanism, which will lead to a selective leading of cargoes into these TGN export sites; or not, where cargo proteins simply accumulate by bulk flow at sites of carrier biogenesis, and experience a crowded and confined environment. Consequently, according to our hypothesis, we predicted that the proteins within these nanodomains should exhibit a rather confined (i.e. alpha exponent between 0 and 1) and slow diffusion (diffusion coefficient in the order of 10^{-1} $\mu m^2/s$). Being able to monitor slight differences in the extent and type of motion within these nanodomains could be informative to distinguish different molecular mechanisms of cargo recruitment. A reduction of the mobility could indicate either cargo aggregation or condensation, similar to what has been observed for the Ca^{2+} and Cab45-dependent sorting mechanism,[25] or a rather stable interaction with other proteins behaving as cargo receptors, as it has been suggested for TGN46.[26] To tackle these and other questions, our aim is to investigate the spatiotemporal dynamics of cargo proteins at the TGN by using SPT.

Some of the open questions that we would like to address are:

(i) Do TGN regions of cargo accumulation have distinct diffusion properties? To test this, we need to be able to visualize and sample the diffusion properties (diffusion coefficient and alpha exponent) of the cargo proteins in space, that is, in relation to the location within the cell. The challenge arises from the generally scarce statistics of intracellular SPT. We do not only need to obtain trajectories long enough to very precisely determine their diffusion properties, but also the number of trajectories should be large enough to be able to have a good spatial sampling so we can distinguish the nanodomains of cargo accumulation. To overcome the first

challenge, we used a deep learning approach for the prediction of the diffusion coefficient and the alpha exponent that performs better with short trajectories, and that provides frame-wise diffusion values (described in **Chapter 2**, **Section 4.2**). These can be correlated to their position in space to obtain spatial information about cargo dynamics. To overcome the challenge of having a high sampling of the TGN regions, we used photoactivatable fluorescent dyes, that allowed the harvest of enough trajectories to sample all underlying molecular processes.

(ii) Do these regions have homogeneous diffusion properties? An advantage of being able to obtain the diffusion properties of the cargo proteins in space is that we can test whether proteins experience different dynamic states within this nanodomains, and if there are distinct nanodomains with distinct diffusion properties.

(iii) If the regions have homogeneous diffusion properties, do these correspond to specific sorting mechanism? Observing well-defined, homogeneous diffusion properties within these TGN regions of cargo accumulation could indicate lack of an active sorting mechanism, and therefore could be simply due to a reduction of the mobility due to the crowding within these regions. Alternatively, if cargo is sorted into those regions and retained there by an aggregation/condensation mechanism, we would also expect a similar behavior with respect to homogeneous diffusion properties. In order to distinguish between these two possibilities, we used the control ss-SNAP, that lacks a possible sorting motif, and therefore should allow the distinction between bulk accumulation of cargo (signal-independent), and specific sorting through aggregation/condensation (signal-dependent).

(iv) If the regions have inhomogeneous diffusion properties, is this a signature of a sorting mechanism? Heterogeneous diffusion properties within these nanodomains, and more specifically, the existence of immobile or highly confined proteins, might be indicative of a sorting mechanism in which there are rather immobile receptors that strongly interact with the cargo proteins. This interaction can be transient, and therefore allow the successive recruitment of more cargo proteins. These two populations of recruited proteins, one that is bound to the receptor, and the other one that is not, would have distinct mobilities.

(v) Are these regions distributed preferentially close to the ER-Golgi MCS? In Wakana et al. Journal of Cell Biology (2020) we have shown that the nascent CARTS are in very close apposition to the ER-Golgi MCS (see **Section 3**).[6] If diffusion properties of the cargoes in these buds close to the MCS were different to those located far

from the MCS, this would suggest the existence of an underlying molecular mechanism for the sorting within these regions closely located to MCS.

(vi) Does the lipid transfer at MCS trigger the formation of these nanodomains of cargo accumulation? To find out whether the MCS' lipid transfer function regulates this mechanism, we used the molecule 25-HC, which stabilizes the interaction between OSBP and VAP, and prevents the cholesterol and PI4P transfer between the membranes. TGN enrichment in cholesterol and DAG promoted by functional ER-Golgi MCS has been suggested to play a role in protein sorting.[6,27] We might expect three possible results:

(i) Disappearance of the sorting regions, due to the lack of sphingolipid-rich nanodomains. Looking at the STED images, which display these punctate structures even after treatment with 25-HC, this possibility is very unlikely.

(ii) Increase of the number of sorting regions, of conserved number of molecules. This would suggest a limit in growth of these sorting regions.

(iii) Conservation of the number of sorting regions, but of higher number of molecules.

(iv) No effect in cargo dynamics caused by 25-HC treatment. This would indicate that the ER-Golgi MCS might be regulating the formation of CARTS at the later steps of the carrier biogenesis, downstream of cargo sorting.

4.1. METHODS

Cell culture and molecular biology

Cell culture and transfection were performed as described in **Section 2**. The origin on the plasmids and cell lines is also described in **Section 2**.

Secretion synchronization

Cells were seeded on 35 mm cell imaging dishes with glass bottom (#81218-200, Ibidi) the previous day. 20 hours after transfection, cells were labeled with 1 µM PA-JF549-SNAPligand (Janelia Materials)[28] in DMEM (10% FBS, 2.5 mM L-glutamine, without antibiotics, without Phenol Red) for 15 min at 37°C and 5% CO_2, and washed 3 times with PBS previous to the 20°C block. Then they were incubated for 2 hours at 20°C in DMEM (10% FBS, 2.5 mM L-glutamine, without antibiotics, without Phenol Red) with 25 mM HEPES pH 7.4, which also served as washing time for the Janelia

fluorophore. After blocking the export at the TGN by this incubation, cells were washed again 3 times with PBS, and the medium was changed to DMEM (10% FBS, 2.5 mM L-glutamine, without antibiotics, without Phenol Red) with 25 mM HEPES pH 7.4. Cells were further incubated 30 minutes at 37°C and subsequently used for imaging.

SPT imaging

Imaging was performed on a Nikon Eclipse Ti system using a 100x oil objective with NA of 1.49, equipped with an ANDOR technology EMCCD iXon 897 camera, with a 512x512 pixels field of view, and 156.7 nm pixel size. The system has 4 laser lines of wavelength: 405 nm, 488 nm, 560 nm and 647 nm. Imaging at 37°C was achieved with a custom-built incubator.

Image sequences of ROIs of size 150x150 pixel were obtained using HILO illumination (adjusted for each sample). The illumination conditions were chosen according to the conclusions derived from **Chapter 4**:

1- Simultaneous illumination with 2% (~329 mW/cm^2)* of the 405 nm laser and 5% (~3.5 W/cm^2)* of the 560 nm laser during 20 ms, for photoactivation of the JF dye and the imaging of the BiFC signal, respectively.

2- Illumination with the 647 nm laser at 30% power (~805 W/cm^2)* for 20 seconds, for the single molecule imaging of the JF dye.

3- Repetition of the illumination sequence 15 times, i.e. imaging during 5 min.

*The laser powers were measured in epifluorescence illumination mode at the specimen side.

The frame rate was chosen according to the characterization described in **Chapter 4**, which was performed for both overexpressed proteins (PAUF-SNAP and ss-SNAP). The characterization for PAUF-SNAP was already shown in **Chapter 4**. Consequently, we used a 2% laser power of the photoactivating laser, and a 10 ms frame rate. In **Figure 6**, we show the calculated maximum achievable velocities for a linking distance in which there is an approximate 5% probability of having a wrong linking candidate. In order to maximize the detectable maximum velocity, and reduce the ratio of rejected displacements, we selected a 2% laser power for the photoactivation, and a 10 ms frame time.

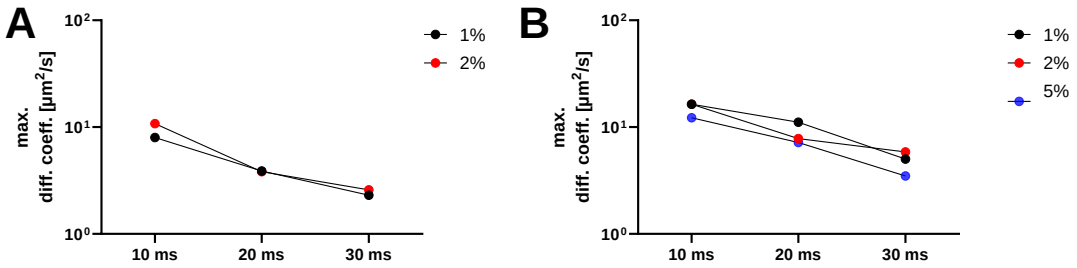

Figure 6. Selection of the frame rate and the labeling density for SPT of the proteins PAUF-SNAP and ss-SNAP labeled with PA-JF646. Living HeLa BiFC cells overexpressing either of the plasmids, labeled with PA-JF646-Halo ligand, and washed for 2 hours with PBS. The excitation was performed with continuous illumination at 30% laser power of the 647 nm laser, and photoactivation for 10 ms with the 405 nm laser at different powers every 20 seconds. The acquisition was at 10, 20 or 30 ms frame time. Detection threshold was set to SNR 2. **A.** Maximum detectable diffusion coefficient for the protein PAUF-SNAP. **B.** Maximum detectable diffusion coefficient for the protein ss-SNAP.

4.2. DEVELOPED ANALYSIS

Spot detection and tracking

Spot detection and tracking were performed with Trackit, implemented in MATLAB.[29] The spot detection was performed with a SNR thresholding value equal to 2. The tracking was performed with nearest neighbors, using a tracking radius of 5.1 px (0.8 μm) for the ss-SNAP samples, and 3.2 px (0.5 μm) for the PAUF-SNAP samples. The selection of the tracking radius is based on the previously described calibration of the framerate and the photoactivation conditions (see **Figure 6** and **Chapter 4**). These selected linking distances provide a linking error smaller than 5%. We selected a minimum tracking length of 2 frames, 1 gap frames and a minimum track length before gap of 0 frames.

Classical diffusion analysis with MATLAB

Classical TA-MSD was performed with a self-written MATLAB user interface (see **Chapter 4**). It can be found in the following Github repository link: https://github.com/JessicaAngulo/SPT_analysis_UI.git

This user interface allowed the selection of an ROI containing the perinuclear area, and therefore excludes trajectories laying outside. For each identified trajectory, we computed *(i)* the instantaneous velocity in every frame as the frame-by-frame displacement divided by the frame time and *(ii)* the diffusion coefficient (also referred to as instantaneous diffusion coefficient, D_{1-4}), which was calculated from

the TA-MSD. Specifically, for a particle trajectory with coordinate position vectors $\boldsymbol{x}_j$, composed of N time steps, the TA-MSD at time lag t_{lag} is calculated as:

$$TA\text{-}MSD\left(t_{lag} = m\Delta t\right) = \frac{1}{N-m}\sum_{i=1}^{N-m}\left[\boldsymbol{x}_j(t_i + m\Delta t) - \boldsymbol{x}_j(t_i)\right]^2 \quad (1)$$

and from here the diffusion coefficient, D_{1-4}, was computed by a linear fit of $TA\text{-}MSD\left(t_{lag}\right) = 4D_{1-4}t_{lag} + b$ using the first four time lags, $t_{lag} = m\Delta t$, for $m = 1\ to\ 4$, where Δt is the frame time. The "y" intercept (b) is also fitted for each trajectory. For these computations, we used only those trajectories with a minimum trajectory length of 12 frames.

The angle distribution was obtained by calculation of the angle formed by triplets of points in successive displacements. To that end, the two vectors ($\vec{A}$, joining points 1 and 2; and $\vec{B}$, joining points 2 and 3) were normalized to create unit vectors. The dot product between the two vectors was used to determine the cosine of the angle between them (see Equation (2)). Finally, the angle was obtained using the arccosine. The orientation was obtained by computing the cross product of both vectors (see Equation (3)), and from there the scalar that indicates the magnitude and sign of what would be the z-component of the 3D cross product. The result will be positive for counterclockwise turns, and negative for clockwise turns.

$$\vec{A}\cdot\vec{B} = |A|\cdot|B|\cdot\cos\theta \quad (2)$$

$$\left(\vec{A}\times\vec{B}\right)\cdot\hat{k} = a_x b_y - a_y b_x \quad (3)$$

where $\hat{k}$ is the unit vector in the z direction.

Diffusion analysis with STEP (Python)

We obtained the pointwise diffusion properties of the trajectories with STEP, a machine learning method able to predict the diffusion coefficient and the anomalous diffusion exponent, at each time step of the input trajectory.[30] The codes for the original publication of STEP can be found in: https://github.com/BorjaRequena/step.git. The scripts for the specific data analysis can be found in: https://github.com/JessicaAngulo/step.git.

Two models were trained by B. Requena (ICFO-Institute of Photonic Sciences, Barcelona, Spain). The details are described in **Chapter 4**, **Section 2.2**. The trajectories used in the training were generated following the procedure described in G. Muñoz-Gil et al. for the fractional Brownian motion (FBM) diffusion model.[2]

For the inference, we used only those trajectories with a minimum trajectory length of 12 frames, and located no further than 40 pixels away from the BiFC structures (the second fluorescence channel used to obtain a diffraction-limited mask of the ER-Golgi MCS regions). The initial position of each trajectory was adjusted to start at the origin (i.e., coordinate [0,0]). This means that we shifted the entire trajectory such that the starting point is at (0,0). Additionally, we scaled the displacements (the changes in position between consecutive frames) by dividing them by their standard deviation. This normalization step ensures that the variations in trajectory displacements are comparable across different trajectories, making the data more consistent for analysis.

BiFC signal detection

The detection of the BiFC fluorescent structures was performed with the same self-written MATLAB user interface, that can be found in the following repository link: https://github.com/JessicaAngulo/SPT_analysis_UI.git

Our approach includes a few user-defined parameters, such as thresholding value for the selection of the meaningful intensity, and a number of intensity levels, that will be further explained below. As one can observe in **Figure 7**, we chose this methodology over a simple thresholding, in order to be able to identify overlaying structures of different intensity. Although the detected signal is diffraction-limited and very influenced by the signal coming from other focal planes, we consider that these structures correspond, in a first-order approximation, to the MCS structures observed by STED microscopy. Therefore, we consider that it is important to assess the protein cargo dynamics with respect to the boundaries, even if these boundary positions are not exactly matching their actual position with very high accuracy.

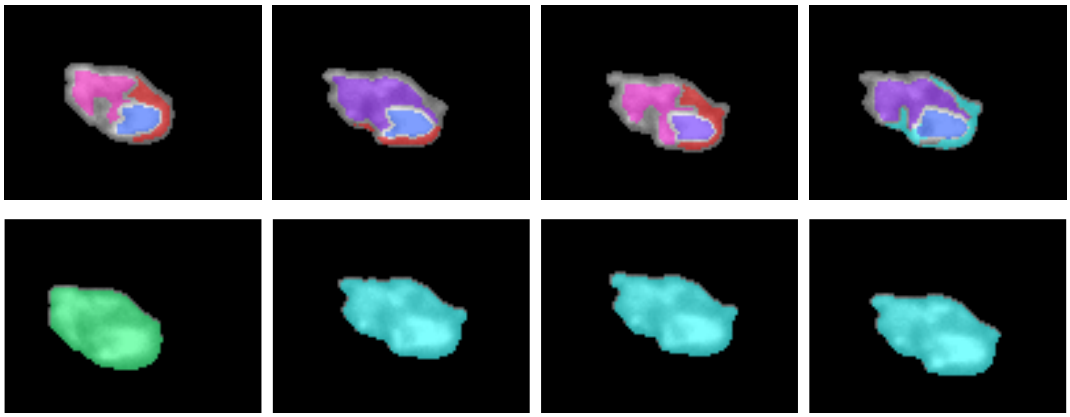

Figure 7. Analysis of the BiFC signal. These are representative images of a sequential imaging of the BiFC fluorescence. The top row shows the analysis performed. The lower row shows a simple thresholding of the signal. Different colors label the differently segmented regions.

The image processing pipeline that we built for the identification of the BiFC structures is illustrated in **Figure 8**. First, the BiFC image (contrast adjusted) is Gaussian filtered with the MATLAB function *imgaussfilt*, which uses a 2-D Gaussian smoothing kernel of standard deviation 2. Then, this filtered image is used for the user selection of an intensity threshold, which in turn is used on the original image. The thresholded image is eroded using a disk-shaped structuring element of size 3 pixels (MATLAB function *imerode*), and morphologically opened using the eroded image as mask to identify high-intensity objects (MATLAB function *imreconstruct*). This opened image is Gaussian filtered again with a kernel of standard deviation 1, and used for the identification of the regional maxima of the H-maxima transform (MATLAB function *imextendedmax*). Regional maxima are connected components of pixels with a constant intensity value, and whose external boundary pixels all have a lower value. The threshold of the local maxima regions was set to 50. The obtained binary mask is already used for the identification of the structures' boundaries, using the function *bwboundaries* ('noholes' option). These are the firstly identified BiFC structures, corresponding to the ones of highest intensity. In the following cycle, the maximum intensity regions are subtracted from the opened image, the regional maxima are identified again, and boundaries are extracted. This process is repeated as many times as selected by the user (from 1 to 3 times), allowing to identify structures of homogeneous intensity, for different intensity levels. For these results, the number of rounds was selected according to the observed intensity levels. Given that an image of the BiFC signal is taken every 20 seconds, this analysis is repeated for all image in each time-lapse movie.

The distance of all localizations to the boundaries of these identified structures is calculated using k-nearest neighbors. This function finds the closest boundary point for each localization, and computes the distance (function *knnsearch*). The sign if these distances is expressed as negative when the localization lays inside the structure. These distances are afterwards used for the link between diffusion parameters and distance to MCS.

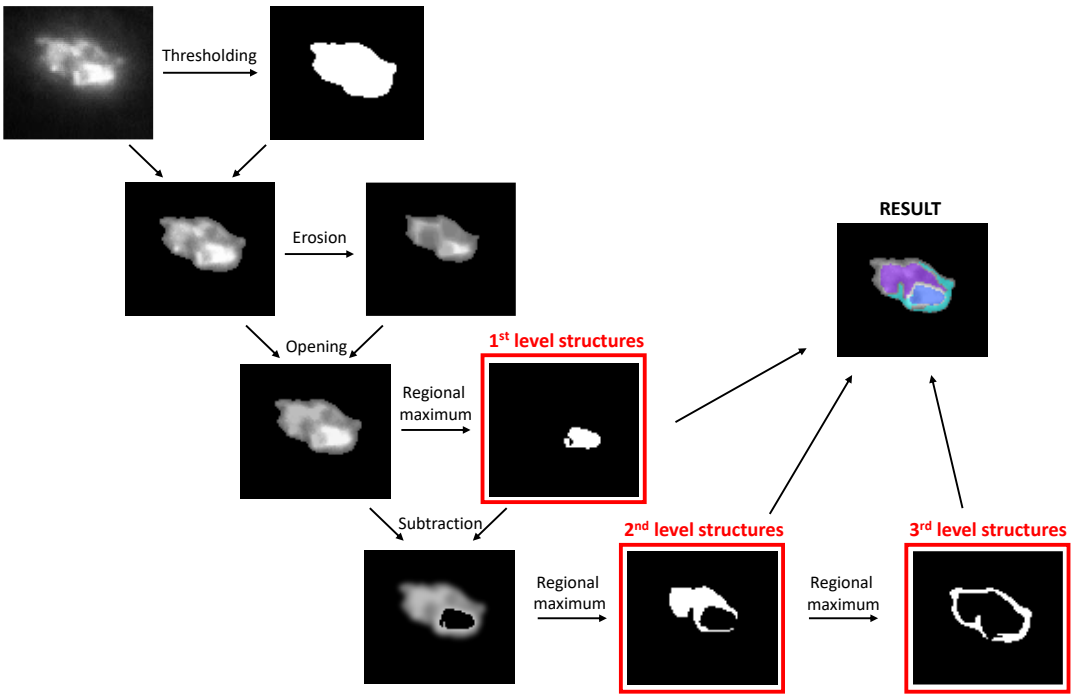

Figure 8. Analysis pipeline for the segmentation of the BiFC signal with morphological transformations. The original image (top left) is Gaussian filtered and thresholded. The selected threshold is used as a binary mask to remove background fluorescence. This processed image is eroded and morphologically opened. The result is used for the identification of regional maxima, that are in turn used for the identification of the structures boundaries. The identification of regional maxima and structure boundaries are repeated to extract structures with different intensity levels.

4.3. RESULTS

Characterization of the confined regions

Thanks to the use of photoactivation, that allowed us to harvest many trajectories; and the machine learning algorithm STEP, that provided us step-wise values for the diffusion parameters, we were able to obtain enough data to plot the diffusion properties of the collected trajectories, and reconstruct a diffusion spatial map. This analysis showed that indeed there are many regions that concentrate trajectories of

very confined motion, with anomalous diffusion exponents ranging from 0 to 0.2 in **Figure 9A**. In **Figure 9B**, we discretized the ranges of values to better visualize these 3 types of confinement: *(i)* highly confined motion, with alpha coefficient 0 to 0.2; *(ii)* subdiffusive motion, with alpha ranging from 0.2 to 0.6; and *(iii)* Brownian motion, with alphas from 0.6 to 1.2. This definition is arbitrary based on visual inspection of the trajectories and values.

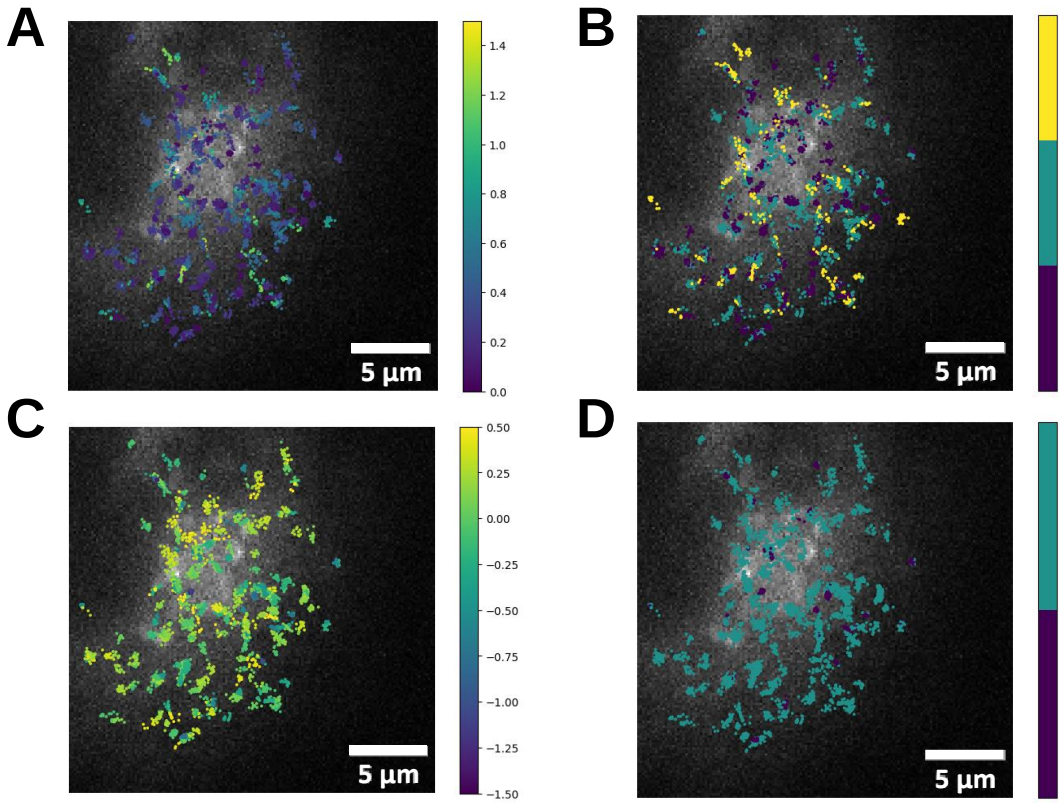

Figure 9. Diffusion maps of the cargo protein PAUF-SNAP. Representation of the framewise diffusion parameters predicted with STEP in space, on top of the grey scaled image of the ER-Golgi MCS, imaged through BiFC. **A-B**. Diffusion map colored by the framewise alpha exponents. A. Full distribution of alpha exponents. **B.** Discretization of the alpha exponents. Range from 0 to 0.2 in purple, range from 0.2 to 0.6 in blue, and values higher than 0.6 in yellow. **C-D.** Diffusion map colored by the framewise diffusion coefficients, expressed in logarithmic scale. **C.** Full distribution of the diffusion coefficients. **D.** Discretization of the diffusion coefficient. The range of values smaller than 0.3 $\mu m^2/s$ (indicated as $10^{-0.5}$ in the figure) are colored in purple, and the range of values higher than this value are colored in blue.

Although SPT has the inherent limitation of not being able to sample all the proteins at the same time, we observed that these regions of high protein confinement do many times consist in more than one trajectory (see **Figure 10**), indicating that they

are indeed regions of accumulation of cargo with characteristic diffusion properties. Moreover, we sometimes observed trajectories displaying an increase of the confinement when approaching the nanodomain (**Figure 10** insets).

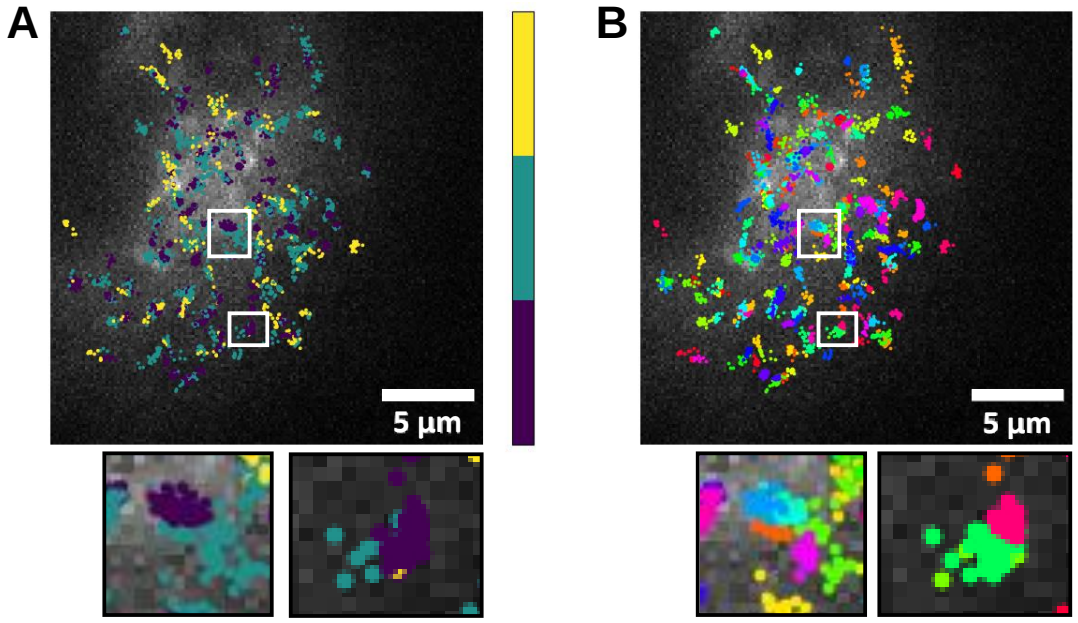

Figure 10. Representative diffusion map of PAUF-SNAP in a HeLa cell. Representation of the framewise diffusion parameters predicted with STEP in space, on top of the grey scaled image of the ER-Golgi MCS, imaged through BiFC. Insets show examples of nanodomains of high confinement that are visited by different proteins. **A.** Discretization of the alpha exponents. Range from 0 to 0.2 in purple, range from 0.2 to 0.6 in blue, and values higher than 0.6 in yellow. **B.** Spatial representation of the trajectories, each one labeled with a different color to distinguish regions with different trajectories that share alpha values.

These regions of high confinement (alpha from 0 to 0.2, purple in **Figure 10A**) have sizes of 500 to 900 nm, which is consistent with the structures observed with STED, and the described sizes of CARTS[14]. Visual inspection of their diffusion characteristics indicates that these regions have *(i)* rather homogeneous degrees of confinement (similar alpha exponents), and *(ii)* a wider distribution of diffusion coefficients (**Figure 9C, D**). Indeed, a closer inspection into the distribution of diffusion coefficients of the highly confined proteins (see **Figure 11A**, purple) and of the subdiffusive proteins (see **Figure 11A**, blue), reveals that the former displays a bimodal distribution of diffusion coefficients (with peaks at ~0.1 and 1 $\mu m^2/s$), whereas the latter follows a rather unimodal distribution with a peak at ~1 $\mu m^2/s$. Therefore, there are two types of regions of high confinement (alpha from 0 to 0.2, purple in **Figure 10A**) with two characteristic diffusion coefficients. We propose three possible hypothesis to rationalize this observation: *(i)* that the population of

proteins that follow a confined dynamics with a smaller diffusion coefficient (~0.1 $\mu m^2/s$) corresponds to an active retention by a sorting mechanism, whereas those with larger diffusion coefficient (~1 $\mu m^2/s$) correspond to cargo proteins that accumulate in bulk in nascent budding sites; *(ii)* that the two populations (high an slow diffusion coefficients) correspond to two different sorting mechanisms; or *(iii)* that both populations correspond to bulk accumulation of cargo protein (without any active sorting mechanism), with distinct degrees of packing (possible due to geometrical constrains).

In order to test if we can distinguish between these possible hypotheses, we took advantage of the control cargo protein ss-SNAP, which is the SNAP tag fused to an ER targeting signal sequence, and therefore should not have any signal for sorting into CARTS. This cargo should therefore exit the TGN by bulk export, so it is probable that it can be packed both into other carriers and CARTS. However, even if sorted into CARTS, we expected ss-SNAP to have distinct diffusion properties that would allow us to distinguish reduction of the mobility by crowding, from an active retention mechanism.

Hence, we used SPT and quantitatively analyzed the dynamics of ss-SNAP in relation with the spatial location of ER-Golgi MCS. The diffusion maps of a representative cell are shown in **Figure 12**. Similarly to PAUF-SNAP, ss-SNAP also show accumulation of confined diffusion, and the ranges of alpha coefficient and diffusion coefficient values are very similar to those of PAUF-SNAP. **Figure 11B** shows that ss-SNAP also exhibits a bimodal distribution of diffusion coefficients. Moreover, the ratio of ss-SNAP molecules in each of the dynamics states is indistinguishable from that of PAUF-SNAP (see **Figure 11C**). The selection of the ranges of alpha and diffusion coefficient are shown in **Figure 13**. In conclusion, a protein lacking possible specific sorting signals displays the same dynamics in the regions of cargo accumulation, and the ratio of molecules within these regions is also the same, one can derive that there are no characteristic diffusion properties for active sorting within these nanodomains.

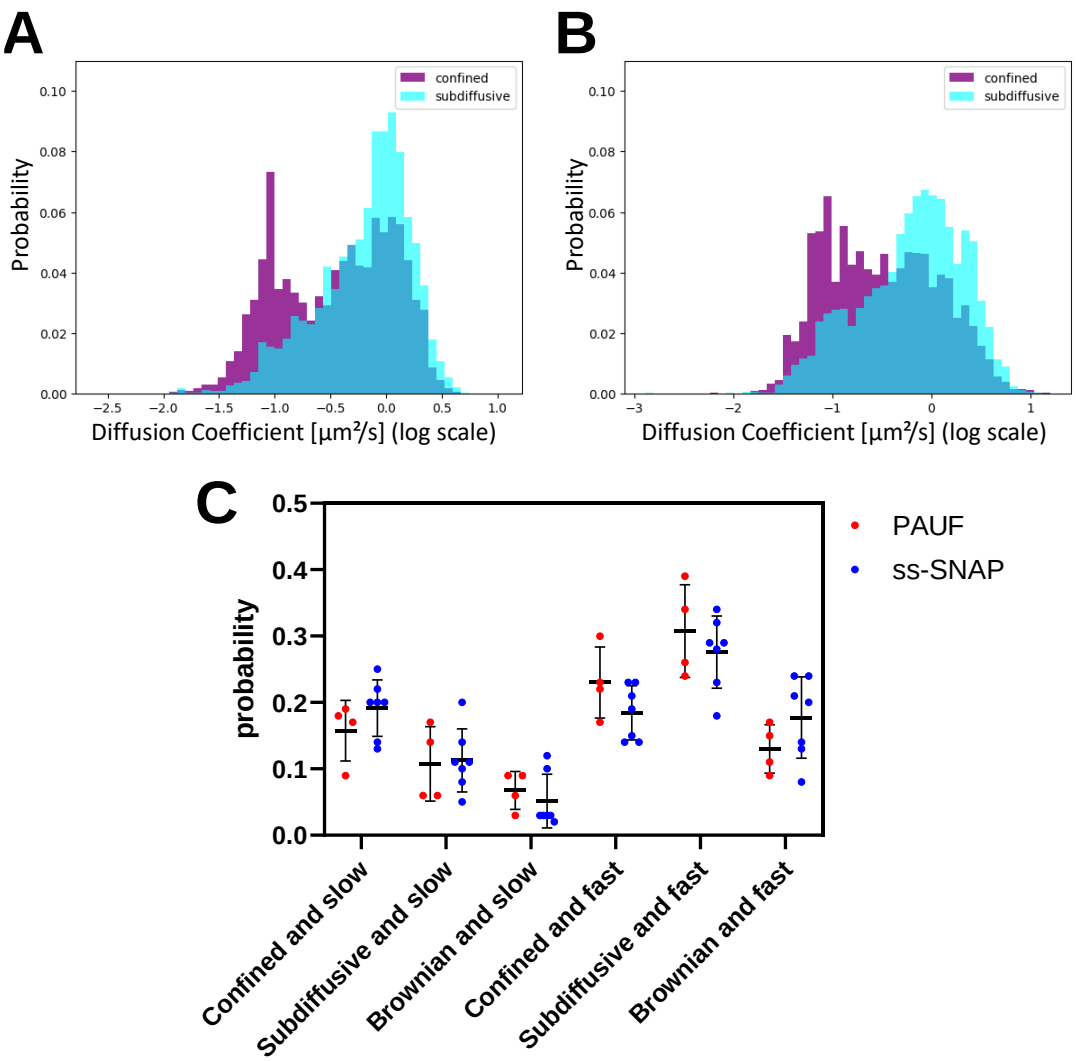

Figure 11. Diffusion properties of PAUF-SNAP and ss-SNAP. A-B. Distribution of the framewise diffusion coefficient for confined and subdiffusive molecules, expressed in logarithmic scale. Confined molecules (purple) are characterized by an alpha coefficient of 0 to 0.2. Subdiffusive molecules (blue) are characterized by an alpha coefficient of 0.2 to 0.6. **A.** Distribution for PAUF-SNAP. **B.** Distribution for ss-SNAP. **C.** Probability to be in each of the diffusion states for PAUF-SNAP and ss-SNAP. Each point represents an independent sample, each one having data from 3 to 7 cells. The probability is calculated as the fraction of step-wise diffusion values laying in the different ranges of alpha exponent and diffusion coefficient. The values are classified as "Confined" when their alpha exponent is between 0 and 0.2, "Subdiffusive" when their alpha exponent is between 0.2 and 0.6, and "Brownian" when it is larger than 0.6. They are also classified as "Slow" when their diffusion coefficient is smaller than 0.3 $\mu m^2/s$, and "Fast" when it is larger. There is no significant difference within populations when comparing PAUF-SNAP and ss-SNAP with unpaired Welch's T-test.

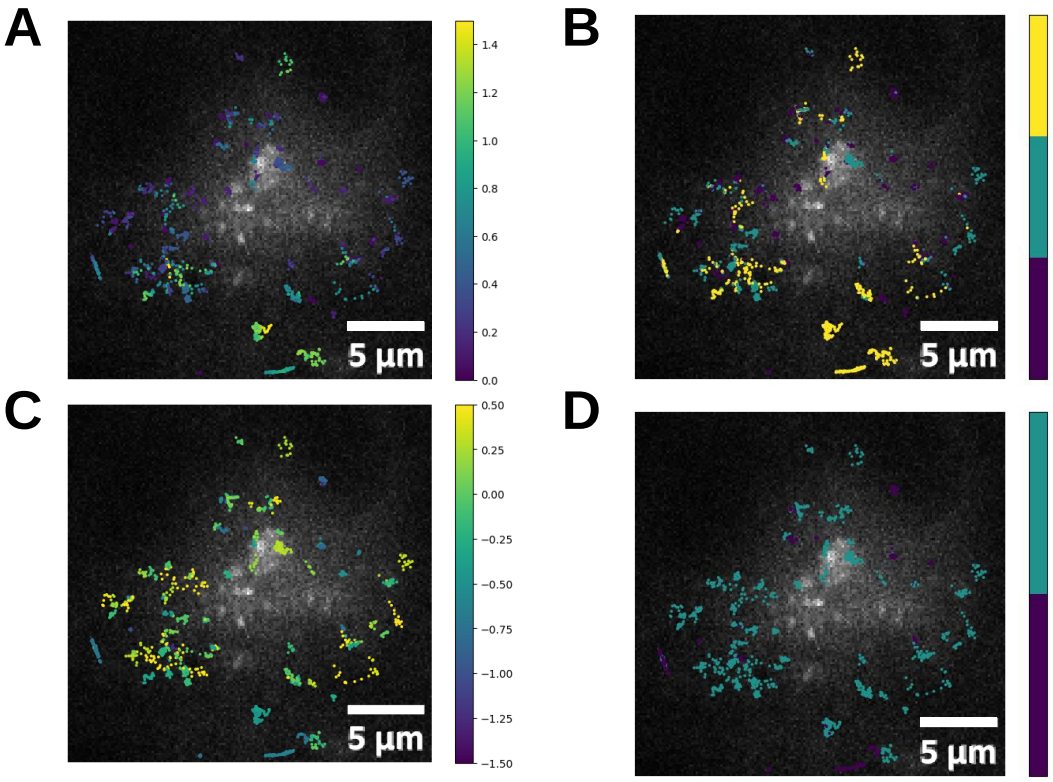

Figure 12. Diffusion maps of the cargo protein ss-SNAP. Representation of the framewise diffusion parameters predicted with STEP in space, on top of the grey scaled image of the ER-Golgi MCS, imaged through BiFC. **A-B**. Diffusion map colored by the framewise alpha exponents. **A.** Full distribution of alpha exponents. **B.** Discretization of the alpha exponents. Range from 0 to 0.2 in purple, range from 0.2 to 0.6 in blue, and values larger than 0.6 in yellow. **C-D.** Diffusion map colored by the framewise diffusion coefficients, expressed in logarithmic scale. **C.** Full distribution of the diffusion coefficients. **D.** Discretization of the diffusion coefficient. The range of values smaller than 0.3 $\mu m^2/s$ (indicated as $10^{-0.5}$ in the figure) are colored in purple, and the range of values larger than this value are colored in blue.

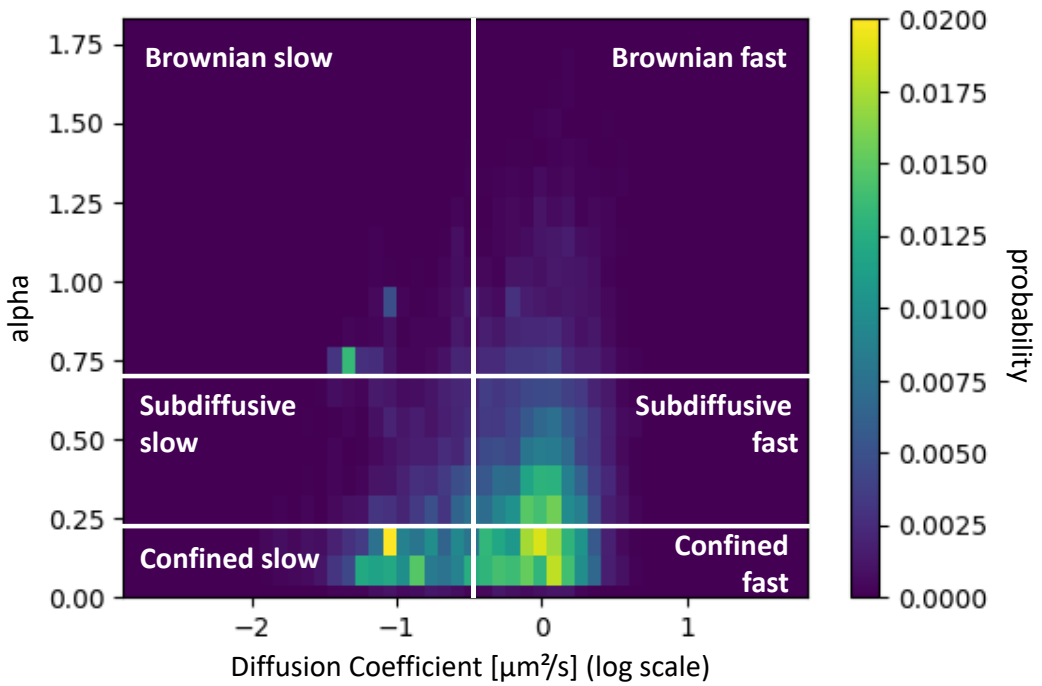

Figure 13. Histogram of the framewise diffusion coefficient versus the framewise alpha coefficient of PAUF-SNAP molecules. The diffusion coefficient is expressed in logarithmic scale. The scale bar represents the normalized probability. The values are classified as "Confined" when their alpha exponent is between 0 and 0.2, "Subdiffusive" when their alpha exponent is between 0.2 and 0.6, and "Brownian" when it is larger than 0.6. They are also classified as "slow" when their diffusion coefficient is smaller than 0.3 $\mu m^2/s$, and "fast" when it is larger.

Although we don't see statistically significant changes between the two protein cargoes, something striking is that the ratio of molecules in each of these diffusion states is very consistent between samples, even between the two different protein cargoes. This shows that each of our imaging sessions contains enough information to sample all types of diffusion populations, and that the ratio of molecules in each of these states is conserved. One could speculate that this data suggests the existence of a generalized molecular mechanism that controls the ratio of molecules that are being packed into carriers. It will be interesting in the future to investigate this possibility in more detail.

Distribution of the sorting regions with respect to the MCS

One of the main questions that we wanted to address in this thesis is whether there is spatial and functional relation between cargo sorting regions at the TGN and ER-Golgi MCS. And whether the sorting regions located closer to the MCS have different diffusion properties. If true, this would establish a connection between sorting

mechanism and cargo dynamics. In **Figure 14**, we represent the distribution of the confined particles with respect to the distance to the BiFC-positive region boundaries. There seems to be an accumulation of confined movement very close to the MCS, at locations practically in contact with the boundary (see **Figure 14A**). Only the confined motion that also has a small diffusion coefficient is enriched at MCS boundaries.

A similar accumulation of confined motion located close to MCS is present for the tracking of ss-SNAP. However, in this case there is also confinement at longer distances, around 3-4 μm (see **Figure 14B**). The fact that confined and slow motion is present both close and far away from the MCS, and both in the specific cargo PAUF and ss-SNAP, discards this type of motion as a readout of an active sorting mechanism. In conclusion, though this confined and slow motion is not characteristic of ER-Golgi MCS-associated cargo accumulations, we can say that PAUF cargo accumulations are located very close to the MCS (closer than 1 μm). We can also suggest that the control cargo ss-SNAP also visits these regions of cargo accumulation of high confinement and slow diffusion coefficient, which are very close to the MCS. However, simultaneous imaging with the two cargo proteins should be performed to confirm so.

A quantification of the number of displacements which are considered close and far, within these diffusion populations is shown in **Figure 14C**. Indeed, only for the cargo protein PAUF-SNAP, it is more probable to find confined and slow motion very close to the MCS (closer than 1 μm), than far from the MCS (from 1 to 5 μm away) (see **Figure 14C, Confined and slow**). Moreover, the confined and fast motion is more probable in PAUF-SNAP molecules that are far away from the MCS (see **Figure 14C, Confined and fast**).

Taken our data together, we can say that protein accumulations are dispersed throughout the TGN, both near and distant from the ER-Golgi MCS. However, PAUF molecules exhibiting confined and slow motion are predominantly found close to the MCS, while ss-SNAP molecules with similar diffusion characteristics are evenly distributed. This points out towards a model in which, although the recruitment of protein cargo for secretion at the TGN by CARTS is regulated upstream of the ER-Golgi MCS, these MCS influence the nucleation preference of these protein accumulations.

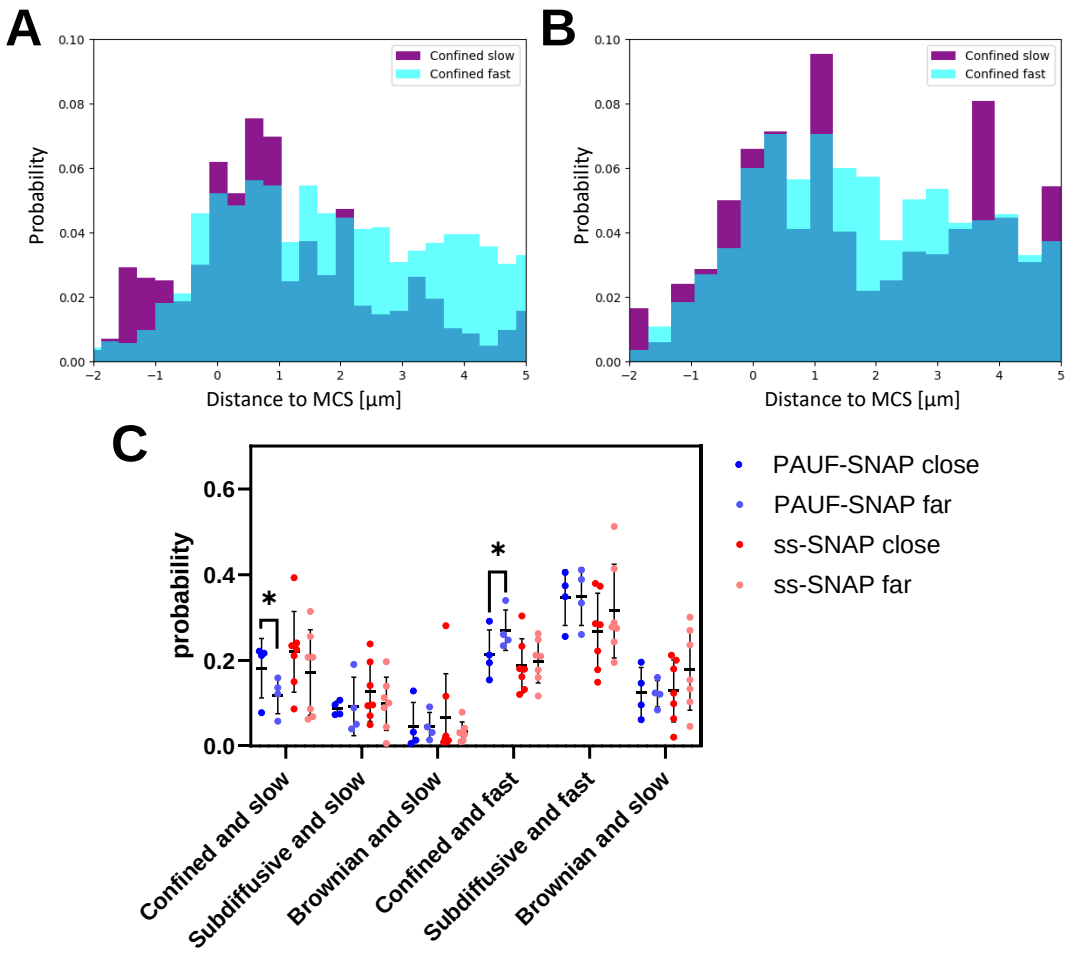

Figure 14. Distribution of the motion with respect to MCS distance. A-B. Distribution of the framewise confined motion with respect to the MCS distance. The confined motion (alpha exponent smaller than 0.2) is divided in slow motion (diffusion coefficient smaller than 0.3 $\mu m^2/s$, purple), and fast motion (diffusion coefficient higher than 0.3 $\mu m^2/s$, blue). **A.** Distribution for the protein PAUF-SNAP. **B.** Distribution for the protein ss-SNAP. **C.** Probability to be in each of the diffusion states for PAUF-SNAP and ss-SNAP. Each point represents an independent sample, each one having from 3 to 7 cells. The probability is calculated from the number of step-wise diffusion values laying in the different ranges of alpha exponent and diffusion coefficient, for displacements located close or far from the MCS. The values are considered "close" when they are located at a distance to the MCS boundaries smaller than 1 µm, and "far", when they are located between 1 and 5 µm away from the MCS boundaries. The values are classified as "Confined" when their alpha exponent is between 0 and 0.2, "Subdiffusive" when their alpha exponent is between 0.2 and 0.6, and "Brownian" when it is larger than 0.6. They are also classified as "Slow" when their diffusion coefficient is smaller than 0.3 $\mu m^2/s$, and "Fast" when it is higher. The only statistically significant differences are labeled with asterisks, and have been calculated with a paired t-test between probabilities of the same protein, and with unpaired Welch's T-test for comparisons between the two different proteins.

Diffusion properties of the confined regions after treatment with 25-HC

We have observed that PAUF-SNAP, and to a lower extent ss-SNAP, accumulates in regions of confined and slow motion very close to ER-Golgi MCS. Do these MCS play an active role in controlling cargo dynamics, and if so, how? As explained in the introduction, lipid transfer at ER-Golgi MCS has been speculated to contribute to the formation of cholesterol and sphingolipid-rich membrane nanodomains at the TGN, which could in turn serve as platforms for cargo sorting and the biogenesis of CARTS. In order to test whether lipid transfer at ER-Golgi MCS alters secretory cargo dynamics at the TGN, we used the molecule 25-HC, a cholesterol analog that inhibits the lipid transport by the ER-Golgi MCS protein OSBP, leading to stable but non-functional –regarding lipid transfer– ER-Golgi MCS. Of note, incubating HeLa BiFC cells with 25-HC led to the inhibition of CARTS formation, which implies that a larger number of cargo molecules will be in the TGN after 25-HC treatment. We expect that different possible outcomes might arise with respect to cargo dynamics in 25-HC-treated cells: *(i)* disappearance of the sorting regions (regions of cargo immobilization); *(ii)* increase in the number of sorting regions of conserved size; *(iii)* conservation of the number of sorting regions of conserved number of molecules; or *(iv)* no detectable changes with respect to non-25-HC treated cells.

HeLa BiFC cells overexpressing PAUF-SNAP were treated with 25-HC, and the dynamics of this cargo proteins was assessed by SPT. Our results revealed that MCS stabilization by 25-HC did not inhibit the formation of sorting regions of confined motion (**Figure 15**). Moreover, the distribution of the angles formed by consecutive segments of a PAUF-SNAP molecule trajectory did not change upon the addition of 25-HC (**Figure 16A**). These results disfavor the hypothesis that 25-HC might be inhibiting the formation of sphingolipid-rich nanodomains, and therefore dissolving the sorting regions. Similar results are seen for the protein ss-SNAP (see **Figure 17** and **Figure 16B**).

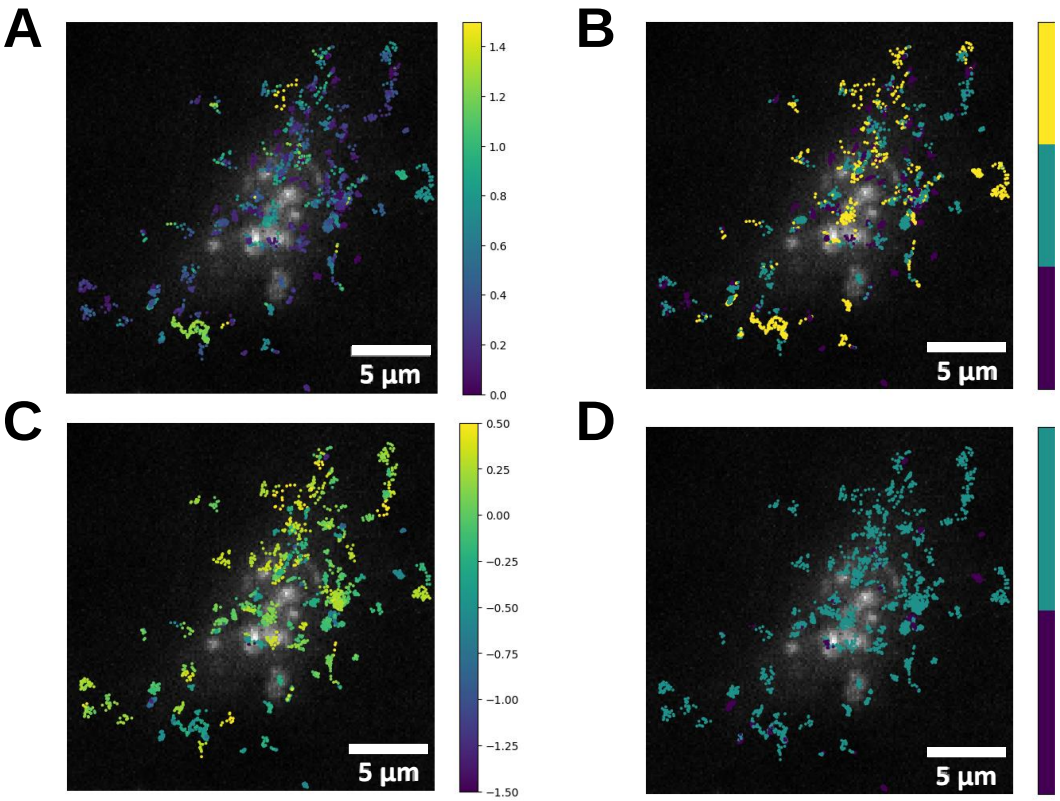

Figure 15. Diffusion maps of the cargo protein PAUF-SNAP after treatment with 25-HC. Representation of the framewise diffusion parameters predicted with STEP in space, on top of the grey scaled image of the ER-Golgi MCS, imaged through BiFC. **A-B.** Diffusion map colored by the framewise alpha exponents. A. Full distribution of alpha exponents. **B.** Discretization of the alpha exponents. Range from 0 to 0.2 in purple, range from 0.2 to 0.6 in blue, and values higher than 0.6 in yellow. C-D. Diffusion map colored by the framewise diffusion coefficients, expressed in logarithmic scale. **C.** Full distribution of the diffusion coefficients. D. Discretization of the diffusion coefficient. The range of values smaller than 0.3 $\mu m^2/s$ (indicated as $10^{-0.5}$ in the figure) are colored in purple, and the range of values higher than this value are colored in blue.

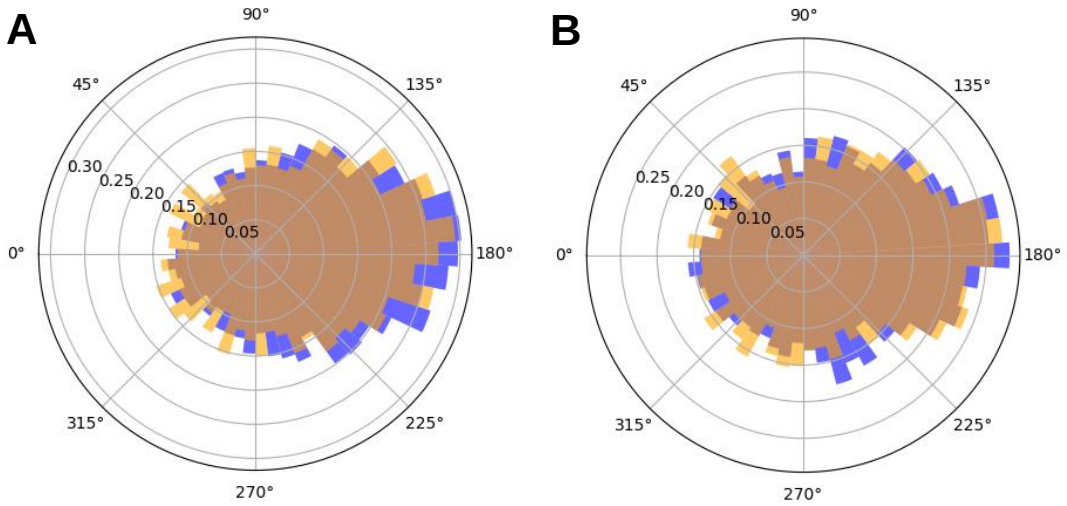

Figure 16. Angle distribution. Cells in control conditions are shown in blue, while cells treated with 25-HC are shown in orange. The angles are calculated between consecutive segments formed by triplets of points. All distributions are shifted to 180° indicating a tendency of the molecules to bounce back. This is a measure of confinement. **A.** Distribution for the protein cargo PAUF-SNAP. N(control) = 22 cells. N(25_HC) = 37 cells. **B.** Distribution for the protein cargo ss-SNAP. N(control) = 25 cells. N(25-HC) = 35 cells.

When focusing on the computed values of the diffusion coefficient of PAUF-SNAP and ss-SNAP molecules, we observed that 25-HC treatment shifted the diffusion coefficient distribution towards smaller values for both cargo proteins, a tendency perhaps more pronounced for PAUF-SNAP (**Figure 18A, C**). This data reveals that stabilizing ER-Golgi MCS slows down protein dynamics, possibly due to an increase in the number of immobile cargoes at the TGN, triggered by an active sorting mechanism. Alternatively, this slowed down dynamics could result from molecular crowding within the TGN as a consequence of the accumulation of secretory cargoes by inhibition of CARTS formation. In the future, it will be interesting to test if the dynamics of non-secretory Golgi proteins, such as glycosylation enzymes or other resident proteins, are also affected by ER-Golgi MCS stabilization. The alpha coefficient, though, doesn't change for PAUF, and slightly decreases for ss-SNAP.

We next classified the cargo molecules according to their dynamics (following the six groups of combinations of alpha coefficients and diffusion coefficients, described in **Figure 13**), and quantified the probability of having each of these types of motion. In the results, it becomes clear that the slight differences observed in the previous histograms are not statistically significant (see **Figure 19**). The same is observed for ss-SNAP. Therefore, we can conclude that the stabilization of ER-Golgi MCS and inhibition of the lipid transfer of OSBP does not result in changes in the ratio of accumulated protein, nor the diffusion properties of these accumulations.

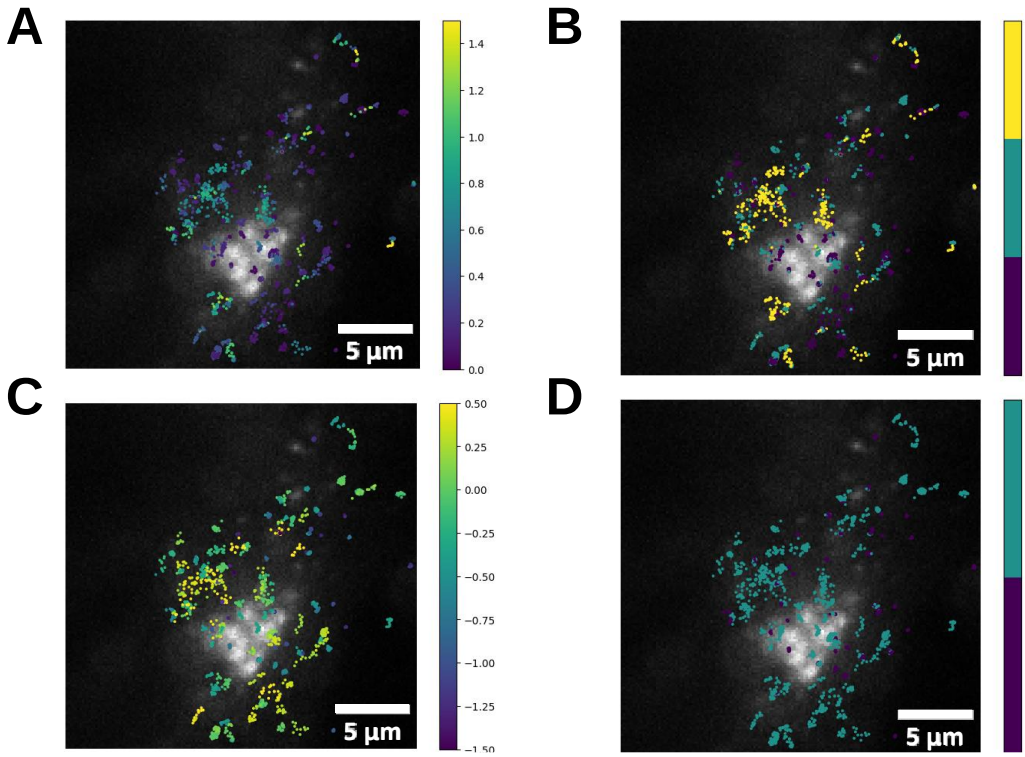

Figure 17. Diffusion maps of the cargo protein ss-SNAP after treatment with 25-HC. Representation of the framewise diffusion parameters predicted with STEP in space, on top of the grey scaled image of the ER-Golgi MCS, imaged through BiFC. **A-B.** Diffusion map colored by the framewise alpha exponents. **A.** Full distribution of alpha exponents. **B.** Discretization of the alpha exponents. Range from 0 to 0.2 in purple, range from 0.2 to 0.6 in blue, and values higher than 0.6 in yellow. **C-D.** Diffusion map colored by the framewise diffusion coefficients, expressed in logarithmic scale. **C.** Full distribution of the diffusion coefficients. **D.** Discretization of the diffusion coefficient. The range of values smaller than 0.3 $\mu m^2/s$ (indicated as $10^{-0.5}$ in the figure) are colored in purple, and the range of values higher than this value are colored in blue.

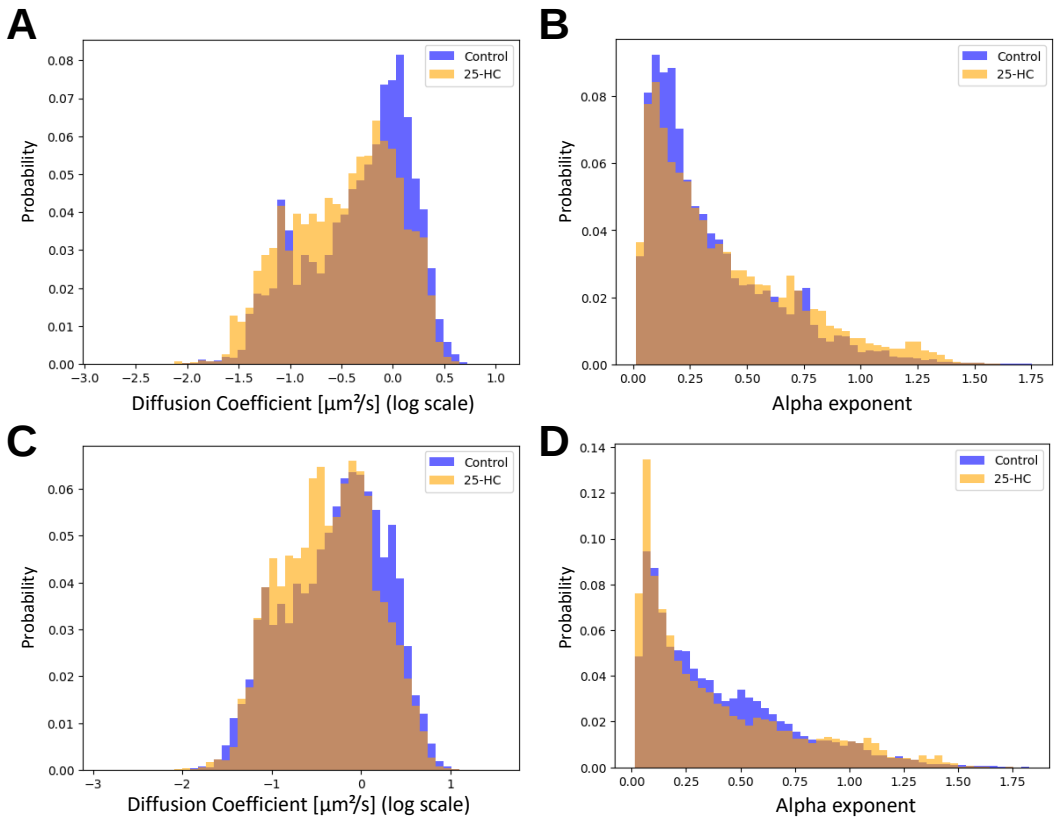

Figure 18. Stepwise diffusion coefficient and alpha coefficient distributions after 25-HC treatment. A-B. Diffusion properties of PAUF-SNAP molecules in control conditions (blue) and in 25-HC treated conditions (orange). N(control) = 22 cells. N(25_HC) = 37 cells. **A**. Diffusion coefficient stepwise values, expressed in logarithmic scale. **B.** Alpha coefficient. **C-D.** Diffusion properties of ss-SNAP molecules in control conditions (blue) and in 25-HC treated conditions (orange). N(control) = 23 cells. N(25-HC) = 35 cells. **C.** Diffusion coefficient stepwise values, expressed in logarithmic scale. **D.** Alpha coefficient.

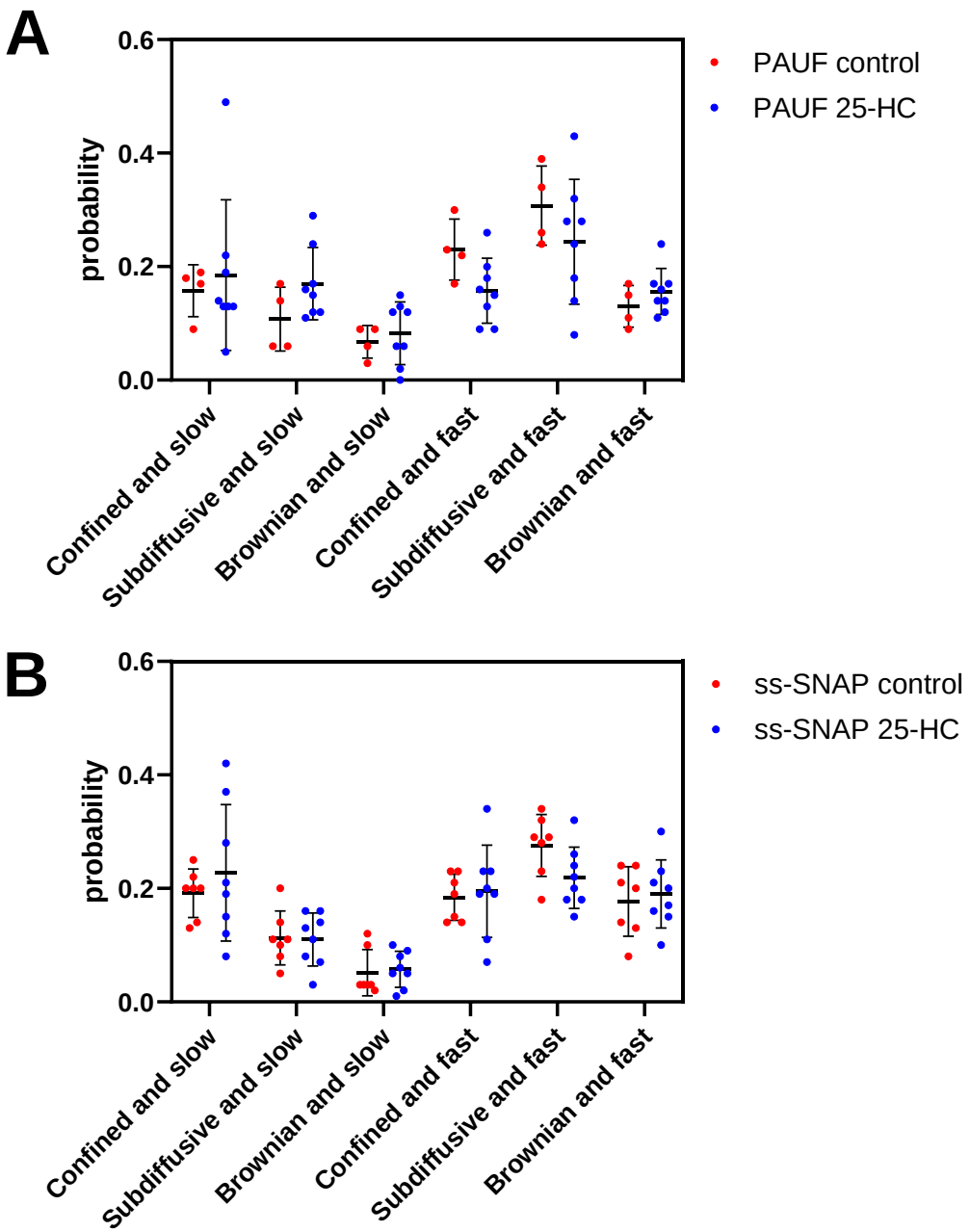

Figure 19. Probability to be in each of the diffusion states for PAUF-SNAP and ss-SNAP, in cells treated with 25-HC. Each point represents an independent sample, each one having from 3 to 7 cells. The probability is calculated from the number of step-wise diffusion values laying in the different ranges of alpha exponent and diffusion coefficient. The values are classified as "Confined" when their alpha exponent is between 0 and 0.2, "Subdiffusive" when their alpha exponent is between 0.2 and 0.6, and "Brownian" when it is larger than 0.6. They are also classified as "Slow" when their diffusion coefficient is smaller than $10^{-0.5}$, and "Fast" when it is higher. There is no significant difference within populations when comparing the control samples and the 25-HC treated samples with Welch's T-test. **A.** Probability values for the protein cargo PAUF-SNAP. **B.** Probability values for the protein cargo ss-SNAP.

We investigated whether the stabilization of ER-Golgi MCS alters cargo dynamics differently based on the proximity of the proteins to the MCS. This analysis indeed revealed some differences between cargoes localized close or far from the MCS boundaries (i.e., within or further away than 1 µm, respectively). Specifically, the observed enrichment of "confined slow" particles close to the MCS in control cells, is lost upon 25-HC treatment (**Figure 20A**). When quantifying the probability of each type of motion, we can appreciate that the preference for PAUF-SNAP molecules to be confined close to MCS is lost after 25-HC treatment (**Figure 20C**). Interestingly, this effect is specific for PAUF-SNAP, as we did not appreciate major differences for the dynamics of ss-SNAP with respect to the ER-Golgi MCS (**Figure 21A**). There seems to be an increase of the confined and fast population close to MCS (see **Figure 21B**), but this difference is not significant across samples, as shown in **Figure 21C**. In summary, based on our results, we can propose that MCS stabilization by 25-HC treatment does not alter the ratio of PAUF-SNAP or ss-SNAP molecules that are being packed in slow mobility regions, possibly representing sorting nanodomains or nascent budding sites. By contrast, for PAUF-SNAP but not for ss-SNAP, this treatment does indeed cause a change in the location of these regions, which are not so much concentrated at close apposition to ER-Golgi MCS.

Taken together, these results indicate that, upon stabilizing MCS and blocking OSBP-mediated lipid transfer with 25-HC, the ratio of molecules in the cargo accumulations remains unchanged. This suggests that the ability to recruit cargo protein is independent of the lipid-transfer function of ER-Golgi MCS. We suggest that it could be intrinsic to the protein or is regulated by other molecular machinery, but it does not seem to rely on the formation of sphingolipid- and cholesterol-rich nanodomains by MCS, as we had initially proposed. While the recruitment ratio for secretion remains constant, the addition of 25-HC disrupts the preference for cargo recruitment near the MCS. This could be the determining step controlling that the cargo accumulations result into the formation of productive, bona-fide CARTS.

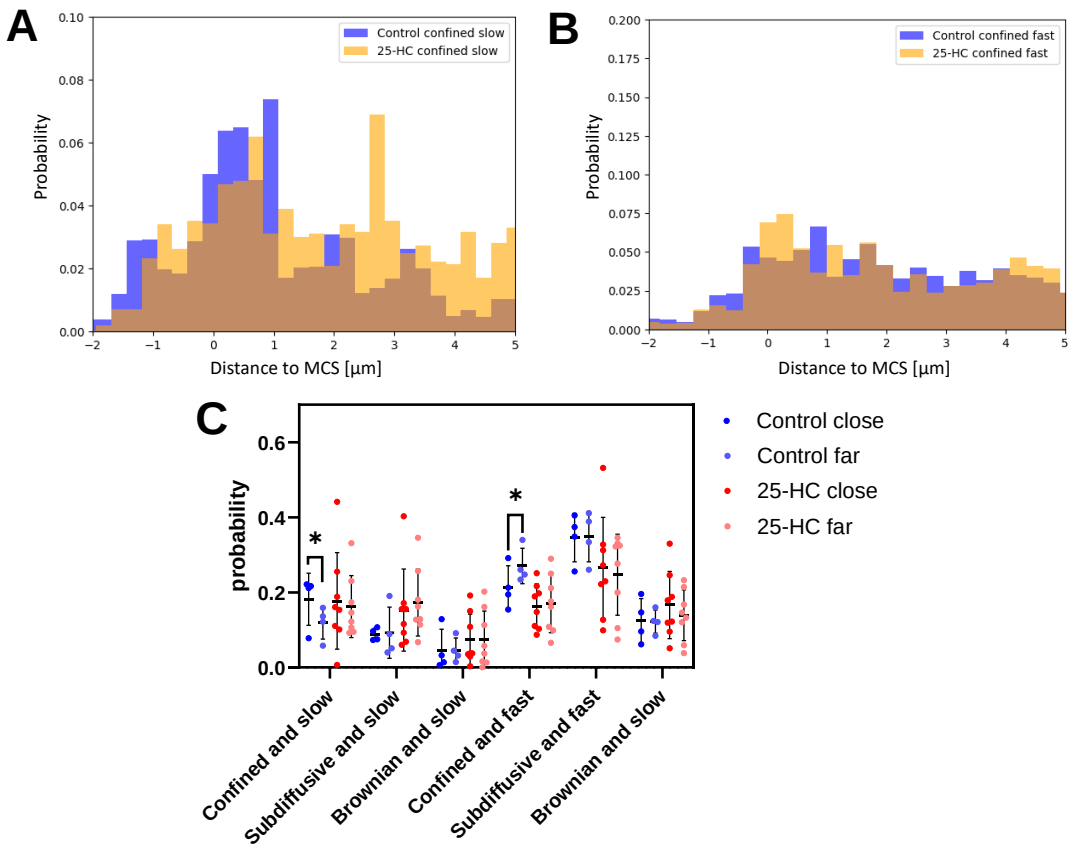

Figure 20. Distribution of the motion of PAUF-SNAP with respect to MCS distance, before and after treatment with 25-HC. A-B. Distribution of the framewise confined motion with respect to the MCS distance. The confined motion (alpha exponent smaller than 0.2) is divided in slow motion (diffusion coefficient smaller than 0.3 $\mu m^2/s$, purple), and fast motion (diffusion coefficient higher than 0.3 $\mu m^2/s$, blue). The results for the control conditions are shown in blue, and the results for the 25-HC treated conditions are shown in orange. N(control) = 22 cells. N(25_HC) = 37 cells. **A.** Distribution for the confined and slow population. **B.** Distribution for confined and fast population. **C.** Probability to be in each of the diffusion states for control (blue) and 25-HC conditions (red). Each point represents an independent sample, each one having from 3 to 7 cells. The probability is calculated from the number of step-wise diffusion values laying in the different ranges of alpha exponent and diffusion coefficient, for displacements located close or far from the MCS. The values are considered "close" when they are located at a distance to the MCS boundaries smaller than 1 µm, and "far", when they are located between 1 and 5 µm away from the MCS boundaries. The values are classified as "Confined" when their alpha exponent is between 0 and 0.2, "Subdiffusive" when their alpha exponent is between 0.2 and 0.6, and "Brownian" when it is larger than 0.6. They are also classified as "Slow" when their diffusion coefficient is smaller than 0.3 $\mu m^2/s$, and "Fast" when it is higher. The only statistically significant differences are labeled with asterisks, and have been calculated with a paired t-test between probabilities of the same protein, and with unpaired Welch's T-test for comparisons between the two different proteins.

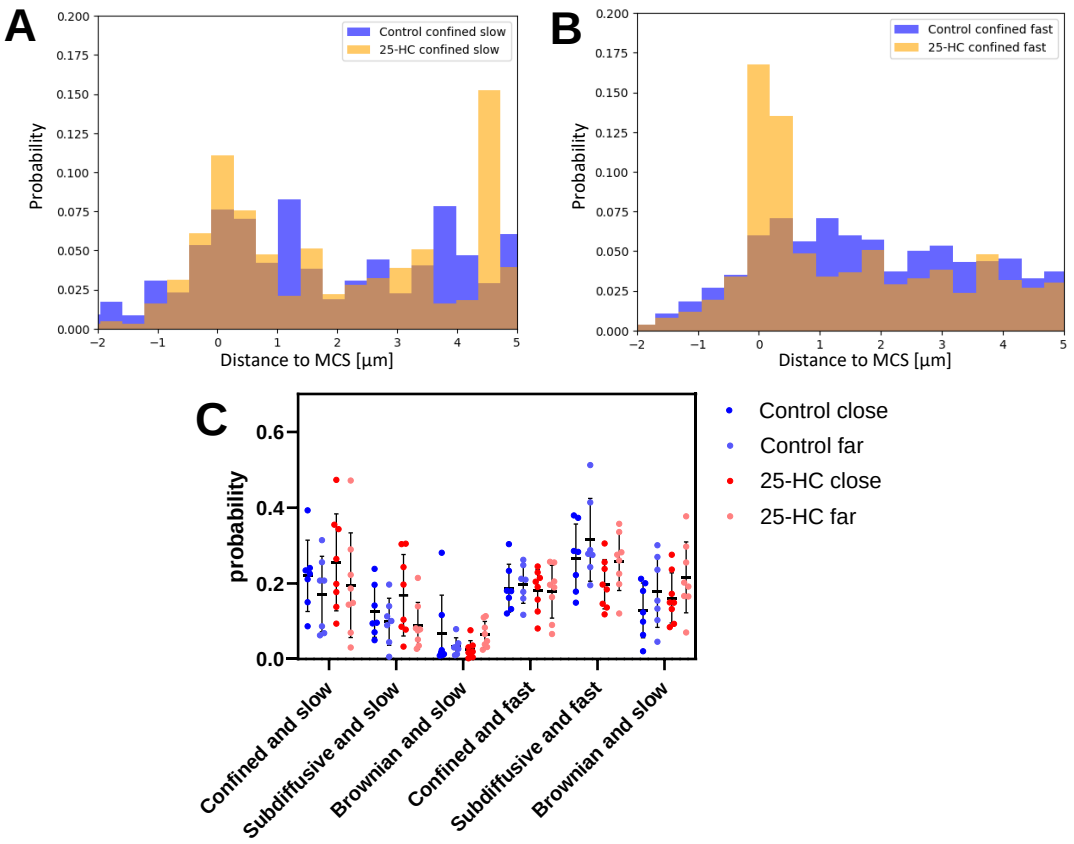

Figure 21. Distribution of the motion of ss-SNAP with respect to MCS distance, before and after treatment with 25-HC. A-B. Distribution of the framewise confined motion with respect to the MCS distance. The confined motion (alpha exponent smaller than 0.2) is divided in slow motion (diffusion coefficient smaller than 0.3 $\mu m^2/s$, purple), and fast motion (diffusion coefficient higher than 0.3 $\mu m^2/s$, blue). The results for the control conditions are shown in blue, and the results for the 25-HC treated conditions are shown in orange. N(control) = 23 cells. N(25-HC) = 35 cells. **A.** Distribution for the confined and slow population. **B.** Distribution for confined and fast population. **C.** Probability to be in each of the diffusion states for control (blue) and 25-HC conditions (red). Each point represents an independent sample, each one having from 3 to 7 cells. The probability is calculated from the number of step-wise diffusion values laying in the different ranges of alpha exponent and diffusion coefficient, for displacements located close or far from the MCS. The values are considered "close" when they are located at a distance to the MCS boundaries smaller than 1 µm, and "far", when they are located between 1 and 5 µm away from the MCS boundaries. The values are classified as "Confined" when their alpha exponent is between 0 and 0.2, "Subdiffusive" when their alpha exponent is between 0.2 and 0.6, and "Brownian" when it is larger than 0.6. They are also classified as "Slow" when their diffusion coefficient is smaller than 0.3 $\mu m^2/s$, and "Fast" when it is higher. The only statistically significant differences are labeled with asterisks, and have been calculated with a paired t-test between probabilities of the same protein, and with unpaired Welch's T-test for comparisons between the two different proteins.

5. DISCUSSION

In this chapter we firstly made use of super-resolution STED microscopy both in fixed and live conditions to characterize CARTS biogenesis. With this technique, we were able to visualize regions in the TGN of cargo accumulation. Strikingly, ER-Golgi MCS, visualized through the interaction of Vn-OSBP and Vc-VAP-A with bimolecular fluorescence complementation (BiFC), seem to be very close to these cargo accumulations, and remodel and move in synchrony with them. Aiming at gaining spatial and temporal resolution, we used SPT to characterized these regions of cargo accumulations, and try to bring light on the molecular mechanism behind.

Our SPT results indicate that:

(i) These regions of cargo accumulation are characterized by a very small alpha coefficient, that ranges from 0 to 0.2.

(ii) The cargoes in those regions display two possible ranges of diffusion coefficient, one small, centered at 10^{-1} $\mu m^2/s$, and one higher, centered at 1 $\mu m^2/s$.

(iii) The ratio of molecules in each of the diffusion states, and more importantly in the two confined types of motion (small alpha and either high or low diffusion coefficient), is highly conserved across experimental replicates and proteins. This suggests that there is a generalized and strong regulation of the amount of protein cargo that is being recruited for carrier biogenesis. This mechanism seems independent of the secretion pathway, as the ratios are conserved for both a specific cargo, and a bulk control cargo (PAUF and ss-SNAP, respectively).

(iv) The accumulations of protein are distributed all over the TGN, adjacent and far from the ER-Golgi MCS. However, the molecules of PAUF that display a more confined and slow motion are more enriched very close to the MCS, whereas the ss-SNAP molecules with the same diffusion characteristics are distributed homogeneously.

(v) Upon stabilization of MCS and block of the lipid transfer of OSBP with 25-HC, the ratio of molecules present in the cargo accumulations is conserved, indicating that the ability to form these aggregates is independent of the MCS. We propose that the accumulation of cargo protein is either an intrinsic ability of the cargo protein, or it is regulated by other means, but it does not seem to depend on the formation of sphingolipid- and cholesterol-rich nanodomains by MCS.

(vi) Although the ratio of molecules that is being recruited for secretion is constant, the addition of 25-HC dysregulates the preference of cargo recruitment at the MCS vicinity.

We therefore propose a model in which protein cargo recruitment for secretion at the TGN by CARTS is regulated upstream of the ER-Golgi MCS, which contradicts the initial hypothesis we proposed in Wakana et al, JCB (2021).[6] The amount of protein that is being recruited is extremely regulated. We suggest that this could be due to a saturation of the molecular machinery involved the formation of these protein inhomogeneities. However, ER-Golgi MCS' lipid transfer function seems to play a role in the preference of the nucleation of these protein accumulations. MCS are then also involved in the successive steps of carrier biogenesis, determining which of these recruited proteins are successfully secreted.

Possible future work would include the simultaneous visualization of both cargo proteins (PAUF and ss-SNAP), as well as of different cargo proteins, in order to elucidate whether they localize to the same regions of cargo accumulation or not. Moreover, this model of cargo recruitment is very much compatible with the previously described Cab45- and Ca^{2+}-dependent nucleation of cargoes. Therefore, it would be interesting to check whether sorting into CARTS, at least for some cargoes, depends in this mechanism and whether this Cab45-dependent sorting mechanism occurs close to the MCS. It is to be noted that a recent publication by Ramazanov et al. has shown that ER-Golgi MCS play a role in the transient Ca^{2+} transfer during cargo entry into the TGN, which would support our hypothesis.[31]

6. REFERENCES

1. Venditti, R. *et al.* Molecular determinants of ER–Golgi contacts identified through a new FRET–FLIM system. *Journal of Cell Biology* **218**, 1055–1065 (2019).

2. Hanada, K. *et al.* Molecular machinery for non-vesicular trafficking of ceramide. *Nature* **426**, 803–809 (2003).

3. Mesmin, B. *et al.* A Four-Step Cycle Driven by PI(4)P Hydrolysis Directs Sterol/PI(4)P Exchange by the ER-Golgi Tether OSBP. *Cell* **155**, 830–843 (2013).

4. Kim, Y. J., Hernandez, M.-L. G. & Balla, T. Inositol lipid regulation of lipid transfer in specialized membrane domains. *Trends Cell Biol* **23**, 270–278 (2013).

5. Wakana, Y. *et al.* CARTS biogenesis requires VAP–lipid transfer protein complexes functioning at the endoplasmic reticulum–Golgi interface. *Mol Biol Cell* **26**, 4686–4699 (2015).

6. Wakana, Y. *et al.* The ER cholesterol sensor SCAP promotes CARTS biogenesis at ER–Golgi membrane contact sites. *Journal of Cell Biology* **220**, (2021).

7. Perry, R. J. & Ridgway, N. D. Oxysterol-binding protein and vesicle-associated membrane protein-associated protein are required for sterol-dependent activation of the ceramide transport protein. *Mol Biol Cell* **17**, (2006).

8. Huitema, K., Van Den Dikkenberg, J., Brouwers, J. F. H. M. & Holthuis, J. C. M. Identification of a family of animal sphingomyelin synthases. *EMBO Journal* **23**, (2004).

9. Shemesh, T., Luini, A., Malhotra, V., Burger, K. N. J. & Kozlov, M. M. Prefission Constriction of Golgi Tubular Carriers Driven by Local Lipid Metabolism: A Theoretical Model. *Biophys J* **85**, (2003).

10. Baron, C. L. & Malhotra, V. Role of diacylglycerol in PKD recruitment to the TGN and protein transport to the plasma membrane. *Science (1979)* **295**, (2002).

11. Yeaman, C. *et al.* Protein kinase D regulates basolateral membrane protein exit from trans-Golgi network. *Nat Cell Biol* **6**, (2004).

12. Maeda, Y., Beznoussenko, G. V., Lint, J. Van, Mironov, A. A. & Malhotra, V. Recruitment of protein kinase D to the trans-Golgi network via the first cysteine-rich domain. *EMBO Journal* **20**, (2001).

13. Bossard, C., Bresson, D., Polishchuk, R. S. & Malhotra, V. Dimeric PKD regulates membrane fission to form transport carriers at the TGN. *Journal of Cell Biology* **179**, (2007).

14. Wakana, Y. *et al.* A new class of carriers that transport selective cargo from the trans Golgi network to the cell surface. *EMBO J* **31**, 3976–3990 (2012).

15. Liljedahl, M. *et al.* Protein Kinase D Regulates the Fission of Cell Surface Destined Transport Carriers from the Trans-Golgi Network. *Cell* **104**, 409–420 (2001).

16. Surma, M. A., Klose, C. & Simons, K. Lipid-dependent protein sorting at the trans-Golgi network. *Biochimica et Biophysica Acta - Molecular and Cell*

Biology of Lipids vol. 1821 Preprint at https://doi.org/10.1016/j.bbalip.2011.12.008 (2012).

17. Klemm, R. W. *et al.* Segregation of sphingolipids and sterols during formation of secretory vesicles at the trans-Golgi network. *Journal of Cell Biology* **185**, (2009).

18. Deng, Y. *et al.* Activity of the SPCA1 Calcium Pump Couples Sphingomyelin Synthesis to Sorting of Secretory Proteins in the Trans-Golgi Network. *Dev Cell* **47**, (2018).

19. Duran, J. M. *et al.* Sphingomyelin organization is required for vesicle biogenesis at the Golgi complex. *EMBO Journal* **31**, (2012).

20. Griffiths, G., Pfeiffer, S., Simons, K. & Matlin, K. Exit of newly synthesized membrane proteins from the trans cisterna of the golgi complex to the plasma membrane. *Journal of Cell Biology* **101**, (1985).

21. Saraste, J. & Kuismanen, E. Pre- and post-golgi vacuoles operate in the transport of semliki forest virus membrane glycoproteins to the cell surface. *Cell* vol. 38 Preprint at https://doi.org/10.1016/0092-8674(84)90508-7 (1984).

22. Boncompain, G. *et al.* Synchronization of secretory protein traffic in populations of cells. *Nat Methods* **9**, (2012).

23. Pereira, C. *et al.* The exocyst complex is an essential component of the mammalian constitutive secretory pathway. *J Cell Biol* **222**, (2023).

24. Grimm, J. B., Brown, T. A., English, B. P., Lionnet, T. & Lavis, L. D. Synthesis of Janelia Fluor HaloTag and SNAP-Tag Ligands and Their Use in Cellular Imaging Experiments. in *Methods in Molecular Biology* 179–188 (Springer New York, 2017). doi:10.1007/978-1-4939-7265-4_15.

25. Crevenna, A. H. *et al.* Secretory cargo sorting by Ca2+-dependent Cab45 oligomerization at the trans-Golgi network. *Journal of Cell Biology* **213**, 305–314 (2016).

26. Lujan, P. *et al.* Sorting of secretory proteins at the trans-Golgi network by human TGN46. *Elife* **12**, (2024).

27. Wakana, Y. & Campelo, F. The PKD-Dependent Biogenesis of TGN-to-Plasma Membrane Transport Carriers. *Cells* **10**, 1618 (2021).

28. Grimm, J. B. *et al.* Bright photoactivatable fluorophores for single-molecule imaging. *Nat Methods* **13**, 985–988 (2016).

29. Kuhn, T., Hettich, J., Davtyan, R. & Gebhardt, J. C. M. Single molecule tracking and analysis framework including theory-predicted parameter settings. *Sci Rep* **11**, (2021).

30. Requena, B. *et al.* Inferring pointwise diffusion properties of single trajectories with deep learning. *Biophys J* **122**, (2023).

31. Ramazanov, B. R. *et al.* Calcium flow at ER-TGN contact sites facilitates secretory cargo export. *Mol Biol Cell* **35**, (2024).

Chapter 6

Conclusions and Outlook

In this final chapter we draw some general conclusions of the thesis. The main aim of this research has been to provide new advanced fluorescence microscopy tools and to re-evaluate existing ones for a quantitative investigation of intracellular trafficking processes, particularly protein secretion. This task involved developing methods for detailed molecular characterization and objective measurements to enhance understanding and ensure accurate, reproducible results when studying protein dynamics and interactions within cells. We employed methodologies such as various fluorescence microscopy techniques, automated image analysis, and biological methods tailored to the secretory pathway. Our analyses underscore that consistent sample preparation and data processing are both key factors for accurate results.

1. CONCLUSIONS

Intracellular trafficking, particularly protein secretion, remains an area with many open questions and unresolved challenges. At each stage of the secretory pathway, existing models are continually being tested, and many processes are still not fully understood. This thesis aimed to provide tools and evaluate existing ones for a quantitative investigation of these processes using fluorescence microscopy. Such a quantitative approach offers two main benefits:

(i) Detailed quantitative characterization of molecular dynamics, interactions, and spatial distributions, which can help to provide a mechanistic understanding of the biological process under study.

(ii) Objective measurement removes subjective biases and allows for accurate comparisons between different experiments and conditions.

The set of experimental and analytical tools as well as methodologies employed in the thesis include *(i)* different fluorescence microscopy techniques, that enable a quantitative characterization of the spatio-temporal dynamics of cellular components; *(ii)* automated image analysis and quantification algorithms; and *(iii)* biological methods tailored to the study of the secretory pathway. The selection criteria for these tools were guided by three main objectives: *(i)* achieving the highest spatial and temporal resolution possible; *(ii)* enabling quantitative and automated analysis for objective and reproducible outcomes; and, when feasible, *(iii)* allowing for live-cell characterization of the biological processes under investigation.

The original results of this thesis are delineated in three chapters (**Chapters 3-5**). In **Chapter 3**, we have evaluated results obtained from fluorescence imaging in an objective and unbiased manner. Similar approaches were used in four different projects aimed at resolving specific questions in the field of protein secretion and intracellular trafficking. These projects, conducted in collaboration with scientists at ICFO and other research institutions, included: *(i)* quantification of the colocalization and proximity of structures recorded in different fluorescent channels; *(ii)* measurement of the fluorescent intensity differences at different cell compartments, and under different experimental

conditions; and *(iii)* characterization of the dynamics of different imaged particles.

We believe that when performing quantifications of microscopy images obtained by using fluorescence microscopy, several key factors need to be considered to ensure accurate, unbiased, and reproducible results. For instance, sample preparation and image acquisitions need to be consistent. On the image analysis side, one needs to understand how the data have been obtained, as well as how it has been or can be processed. Otherwise, the quantifications can lead to artifacts and misinterpretation of the results. Despite this, we want to highlight the importance of using computational approaches to extract meaningful quantitative descriptors of the microscopy data, even when they might appear obvious by eye inspection. Utilizing computational pipelines can significantly enhance the accuracy and reliability of the quantifications for many reasons: *(i)* standardization and consistency, *(ii)* efficiency and throughput, and *(iii)* allowing for more sophisticated analyses.

We have highlighted how important this is, especially when acquiring and analyzing SPT data of molecules in the secretory pathway. Over this thesis, we tried to be consistent and used these guidelines. In **Chapter 4**, we have addressed the challenges associated to performing SPT in the context of the secretory pathway. We proposed control experiments and identified parameter descriptors to maximize data quality and quantity while avoiding artifacts. Our focus included optimization of the protocols involved in labeling strategies, imaging, and data analysis. We also highlighted the considerations needed when comparing results with those from other studies, both from experimental and analytical perspectives. We hope that the experiment controls and guidelines that we proposed in this work can help get artifact-free and unbiased results, as well as help extracting more meaningful information out of SPT data.

Specifically, our work underscored the importance of selecting dyes that provide the highest brightness and photostability in our set up and specific experimental conditions. The Janelia dyes, and specially the photoactivatable dyes PA-JF646 and PA-JF549 have superior fluorescent properties, and

therefore are being widely used in SPT. In addition, we have shown the importance of finely tuning the excitation laser power, and the frame rate to have a good SNR and localization precision, and at the same time being able to follow the diffusion of the protein of study.

One of the biggest challenges when performing SPT intracellularly is the worse SNR due to the out-of-focus excitation, as compared to SPT at the plasma membrane, which limits the density of single molecules in the field of view. To overcome this, we recommend to use SPT PALM, as it allows for the collection of more data by the successive photoactivation of new molecules. The second biggest challenge is the fact that molecules get out of the imaging plane, and therefore result in shorter trajectories. We addressed this by using a machine learning algorithm, named STEP, that is able to reliably predict the diffusion coefficient and the alpha exponent of very short trajectories. STEP provides the step-wise prediction, allowing to visualize the calculated parameters in space, in the so-called diffusion maps. The disadvantages associated with this method are that: *(i)* it could overfit the training data, leading to poor analysis of new, unseen data; *(ii)* the training requires significant computational power and resources, but once a model is obtained, inference is very fast; *(iii)* as it is common for deep learning algorithms, it is difficult to interpret what the algorithm actually computes, and it is therefore difficult to identify the origin or possible biases and artifacts.

Finally, in **Chapter 5**, we applied all the established methodologies to characterize protein sorting at the TGN. Our specific goal was to understand the role of ER-Golgi MCS in the formation of TGN-derived transport carriers. Using both fixed- and live-cell super resolution fluorescence STED microscopy, we identified regions of accumulation of cargo at the TGN, adjacent to this ER-Golgi MCS. This microscopy technique, combined with deconvolution methods, allowed us to visualize ER-Golgi MCS and the protein cargo distribution with high resolution. It is to be noted that STED in fixed conditions provided higher resolution and the possibility to perform 3D imaging (not shown in this thesis), while live-STED enabled the visualization of the movement and interactions between the MCS signal and the cargo protein. However, the temporal resolution of live-STED was limited to the order of

seconds, with 1 second being the maximum temporal resolution achieved in videos of up to 30 frames.

Next, we conducted SPT experiments to monitor the dynamics of individual cargo proteins both within and outside these putative cargo sorting regions. Through quantitative characterization of the dynamics of different cargo proteins, we found that many exhibit very confined and slow motion when in close proximity to the MCS. Interestingly, while the ratio of molecules in these confined regions remained unchanged, the preferential location of these regions close to the MCS was inhibited when the ER-Golgi MCS were stabilized by the lipid transfer blocker 25-HC. Interestingly, the percentage of proteins within and outside of these cargo accumulations remained unchanged across different proteins and MCS destabilizing conditions.

We therefore proposed that protein cargo recruitment for secretion at the TGN by CARTS is regulated upstream of the ER-Golgi MCS, challenging the initial hypothesis we proposed in Wakana et al., JCB (2021).[1] The amount of protein being recruited is highly regulated, possibly due to the saturation of the molecular machinery involved in forming these protein inhomogeneities. Additionally, the lipid transfer function of the ER-Golgi MCS appears to influence the nucleation preference of these protein accumulations. Consequently, MCS also play a role in the successive steps of carrier biogenesis, determining which of these recruited proteins are successfully secreted.

2. FUTURE PERSPECTIVES

Future perspectives for this work could include:

(i) Further development of the computational pipelines for high-throughput analysis. Although we have implemented a user interface that allows the SPT analysis, we have not included the STEP analysis, as the former is developed in MATLAB and the latter is developed in Python. Seeing the recent developments in the field of deep learning, which is mostly being performed in Python, it would be useful to integrate everything into a Python web interface. Moreover, Python is a free and open source, and therefore more accessible by definition.

(ii) New biological insights. It would be interesting to apply the control experiments and the analysis described in **Chapter 4** to investigate other aspects in cell biology, not only in the field of intracellular trafficking, but also, in other cell compartments such as the nucleus and the plasma membrane. SPT in these compartments will suffer similar challenges, and therefore can profit from the enhanced experimental conditions and the more sophisticated analyses.

(iii) Multimodal approaches. Combining fluorescence microscopy with other techniques, such as electron microscopy or mass spectrometry, to gain complementary information and a more comprehensive understanding of cellular mechanisms. In this thesis, we used STED in live and fixed conditions, which allowed the 2D visualization of the protein distribution, and helped explain the results obtained with SPT. As another example, in the article by Obara et al., they performed focused ion beam-scanning electron microscopy (FIB-SEM) of ER-mitochondria MCS. They identified that the regions of confinement of the MCS protein VAP-B observed with SPT were of similar size as the MCS reconstructed from the FIB-SEM images.[2] We believe that such techniques that allow the visualization of the intracellular compartments without fixation are interesting to bring further information for the proposal of a molecular mechanism.

Regarding the research in the context of the protein sorting at the TGN and the role of ER-Golgi MCS in this process, we think that future work could include:

(i) Simultaneous visualization of multiple proteins with SPT: It would involve visualizing both PAUF-SNAP and ss-SNAP simultaneously to determine if they localize to the same regions of cargo accumulation. This would help elucidate whether different cargoes share similar sorting and accumulation mechanisms, and/or they spatially segregate in different of these Golgi subdomains. A comparison with other protein cargoes and Golgi-resident proteins could bring further information and could help define the diffusion properties of proteins being sorted, as compared to passive diffusion within the Golgi. A cargo protein that would be interesting to visualize is lysozyme C, as it has been shown to be sorted into CARTS. It has been shown that it is sorted into

SM-rich carriers by a Ca^{2+}-dependent oligomerization of the protein Cab45. Therefore, it would be interesting to visualize the distribution of the cargo lysozyme C, and study a possible relationship with ER-Golgi MCS.

(ii) Characterization of basal conditions. In this work we performed overexpression of PAUF-SNAP and the control ss-SNAP. CRISPR/Cas9 knock in of the protein tags Halo- or SNAP- could be performed on the gene encoding PAUF or other proteins of interest. This way, the expression levels would not be altered, and the experiments would be more similar to physiological conditions.

(iii) Comparative analysis across different cell types. In this thesis we always used the cell line HeLa. Extending the studies to different cell types show whether the observed mechanisms are conserved or vary across different cellular contexts. This could provide a broader understanding of cargo sorting and its regulation. Specially because it is well known that HeLa cells have several genetic and phenotypic differences from normal human cells, including aneuploidy and altered gene expression patterns. These differences can affect the interpretation and relevance of research findings to human biology.[3]

(iv) Functional studies on cargo sorting mechanisms. In order to reveal the full molecular mechanism underlying cargo sorting into CARTS, one should perform different functional studies. This could include identifying key proteins and pathways involved in the sorting process, and investigating the impact of disrupting specific components on cargo sorting and accumulation. Some interesting research lines could be:

> *(a) Inhibition of sorting into SM-rich carriers*. Over the thesis, we have seen that there seem to be links between two TGN-derived transport carrier formation pathways: CARTS and SM-rich carriers. Cab45 and the Ca^{2+} pump SPCA1 are necessary for sorting of some cargoes such as lysozyme C into SM-rich carriers.[4] Crevenna et al. showed that Cab45$^{-/-}$ cells (i.e. homozygous knock out cells), generated using CRISPR/Cas9, have a compromised sorting of lysozyme C into SM carriers. It would be interesting to find out whether the secretion of the CARTS specific cargo PAUF is also altered in these Cab45 deficient cells.

(b) Inhibition of fission by PKD2-KD. When PKD-KD is expressed, long cargo-containing tubes emanating from the TGN extend throughout the cell, due to an over-elongation of the bud and a fission defect in CARTS biogenesis.[5] It would be interesting to either express PDK2-KD by transient transfection, or alternatively, use a stable line expressing this defective protein, which shows fission defect after incubation at 20°C. When PKD-KD is expressed, long cargo-containing tubes emanating from the TGN extend throughout the cell, due to an over-elongation of the bud and a fission defect. It could be relevant to study the effect of the stabilization of ER-Golgi MCS.

(c) Ca2+ inhibition of OSBP binding. Malek et al. showed that cytoplasmic Ca^{2+} can directly interfere in the interaction between OSBP and PI(4)P at the TGN membranes. Ca^{2+} is released from the ER through pumps activated by the signaling molecule inositol 1,4,5-triphosphate (IP_3). Exogenous addition of a cell permeable IP_3 triggered the unbinding of OSBP from the TGN.[6] Thus, one could use this molecule to disrupt OSBP binding, and see in which step of CARTS formation is OSBP playing a role.

(c) Inhibition of MCS components. Knock down of the key ER-Golgi MCS components VAP-A, OSBP, and CERT have been performed by Wakana et al.[7] Therefore silencing of these molecules could be performed to study the possible changes in the TGN structure and cargo distribution with STED in live and fixed conditions.

(v) Identify the changes in the spatiotemporal dynamics in the functional studies. We have performed SPT in basal conditions for PAUF-SNAP and the control cargo ss-SNAP. To complement these results, it would be interesting to see what are the consequences regarding the protein distribution at the TGN after performing the above-mentioned experiments.

(i) Inhibition of sorting in SM carriers. One could look at the distribution of cargo in the Cab45$^{-/-}$ cells. An alteration of the distribution of PAUF at the TGN would indicate that it probably follows a similar sorting pathway.

(ii) Inhibition of fission by PKD2-KD. As already mentioned, when PKD-KD is expressed, long cargo-containing tubes emanating from the TGN extend throughout the cell, due to an over-elongation of the bud and a fission defect.[5] It has been shown that these tubes contain PAUF.[8] It would be interesting to look at the diffusion of these proteins within the tubes. For instance, one would like to know if these regions of cargo accumulation are still conserved within the tubes, to find out whether the regulation of the sorting of the proteins at the TGN is also upstream of PKD2.

(iii) Ca2+ inhibition of OSBP binding. If ER-Golgi MCS are indeed not directly involved in the sorting of the cargo proteins, but it is instead involved in the later steps of the carrier biogenesis, we should still observe the cargo protein accumulations.

(iv) Inhibition of MCS components. As we have mentioned, it could be an alternative way to alter the ER-Golgi MCS. However, in this case the MCS are not stabilized, and it is a more direct way of altering them.

(v) Interaction studies. In order to identify new interacting partners involved in the recruitment and sorting of the cargo proteins into CARTS, techniques like FRET (Förster Resonance Energy Transfer) would help study interactions between cargo proteins, Cab45, and other proteins.

3. REFERENCES

1. Wakana, Y. *et al.* The ER cholesterol sensor SCAP promotes CARTS biogenesis at ER–Golgi membrane contact sites. *Journal of Cell Biology* **220**, (2021).
2. Obara, C. J. *et al.* Motion of VAPB molecules reveals ER–mitochondria contact site subdomains. *Nature* **626**, (2024).
3. Landry, J. J. M. *et al.* The genomic and transcriptomic landscape of a hela cell line. *G3: Genes, Genomes, Genetics* **3**, (2013).
4. Crevenna, A. H. *et al.* Secretory cargo sorting by Ca2+-dependent Cab45 oligomerization at the trans-Golgi network. *Journal of Cell Biology* **213**, 305–314 (2016).

5. Liljedahl, M. *et al.* Protein Kinase D Regulates the Fission of Cell Surface Destined Transport Carriers from the Trans-Golgi Network. *Cell* **104**, 409–420 (2001).

6. Malek, M. *et al.* Inositol triphosphate-triggered calcium release blocks lipid exchange at endoplasmic reticulum-Golgi contact sites. *Nat Commun* **12**, (2021).

7. Wakana, Y. *et al.* CARTS biogenesis requires VAP–lipid transfer protein complexes functioning at the endoplasmic reticulum–Golgi interface. *Mol Biol Cell* **26**, 4686–4699 (2015).

8. Lujan, P. *et al.* Sorting of secretory proteins at the trans-Golgi network by human TGN46. *Elife* **12**, (2024).

List of Publications

Wakana, Y., Hayashi, K., Nemoto, T., Watanabe, C., Taoka, M., **Angulo-Capel, J.**, Garcia-Parajo, M. F., Kumata, H., Umemura, T., Inoue, H., Arasaki, K., Campelo, F., Tagaya, M. (2020) The ER cholesterol sensor SCAP promotes CARTS biogenesis at ER–Golgi membrane contact sites. Journal of Cell Biology. 220 (1): e202002150; doi: 10.1083/jcb.202002150

I performed STED microscopy images to visualize the distribution of the protein cargo PAUF in the TGN, and the florescence coming from the ER-Golgi MCS. I also performed specific quantifications on fluorescence microscopy images. The first quantification entailed the distances between Golgi ministacks in different channels in nocodazole-treated of HeLa cells. The distance was measured between two ER-Golgi MCS proteins: Sac1, either as a mutant variant or as wild type, and VAP-A. The second quantification was a colocalization quantification between carriers in different channels. More specifically, colocalization between the SM sensor equinatoxin-SM (EQ-SM), and the CARTS cargo PAUF.

Angulo-Capel, J.*, Lujan, P.*, Chabanon, M.*, Campelo, F., (2021) Interorganelle communication and membrane shaping in the early secretory pathway. *Current Opinion in Cell Biology*. 71:95-1002. doi: 10.1016/j.ceb.2021.01.010

*These authors contributed equally

I worked on the manuscript and the figures of this review paper.

Wong-Dilworth, L., Bregu, G., Restel, S., Rodilla-Ramirez, C., Ebeling, S., Harel, S., Leupold, P., Grimm, J., Lavis, L.D., **Angulo-Capel, J.**, Campelo, F., Bottanelli, F. (2023) Nanoscale imaging reveals the mechanisms of ER-to-Golgi transport via a dynamic tubular vesicular network. BioRxiv 2023.10.27.563951; doi: 10.1101/2023.10.27.563951

My contribution in this publication included 3 different quantifications. The first one was a quantitative measurement of the mobility of peripheral ERGIC tubular structures, as seen by live-cell confocal fluorescence microscopy; as well as a comparison of this measure between more rounded tubules, and more elongated tubules. This was

performed both in HeLa and human retinal epithelial (RPE-1) cells. The second contribution was the measurement of the movement of peripheral ERGIC tubular structures as compared to ERES. Finally, I performed a quantification of the proximity between ARF4 tubules and ERES.

Acknowledgements

It seems like it was a different Jessica who decided to start a PhD at ICFO. I was excited because I had finally achieved what I had wanted for so many years: doing a PhD. And it was much better than I had imagined: in my city, in a cool place, in the best working conditions, and in a topic I loved. Even with COVID, I never understood why many PhDs felt so demotivated.

I was naïve then, and that meant that I had enough with doing exciting experiments and learning new things. I was a weird biochemist, always fascinated by microscopes and physics, and I had finally found a place where I was not the only one. I am very grateful that my supervisors were supportive of that. They always encouraged me to learn whatever I wanted and allowed me to go in the direction that I desired. I always felt valuable and able to express my opinions. I don't give this for granted.

However, it was just a matter of time that I had to face the reality of the academic world. It was my final year, and if I wanted to decide about my future, I had to find out what this job was about. I began to realize that, in science, much of the work is aimed at building one's own name. It was very far from the idyllic view in which scientists work together to understand nature. I guess that this wild system intoxicates many people, turning them into ego machines, while others just try to survive in it.

Sometimes I wonder if my supervisors should have taught me to play that game. And for a long time I thought that by not doing so – and by not teaching me how to do my work more "publishable" – they doubted my ability to succeed. Now I see this wasn't necessarily the case, and that for them success might have meant something different.

Looking at this thesis I am convinced that I succeeded (sorry, I love bullet points): *(i)* I completed a scientific project. And now that I see how crazy the initial idea was, I am surprised how did I manage to get to conclusions. *(ii)* I believe that the methodology and the results will be useful to future researchers. *(iii)* I learned thousands of things out of my comfort zone. *(iv)* I learned a bit more about myself.

In the future, I will remind myself what success should mean. Although the academic system made me forget for a short time, it comforts me to see that the naïve Jessica already knew it, and pushed me to enjoy the PhD, making thousands of friends, helping in ICONS, and going to as many conferences as possible.

After this letter to myself, I definitely need to thank many people who accompanied me along this journey. First of all, to my supervisors and the tribunal, to make all this even possible. I hope I did not pressure to much with the corrections. I felt very praised that all of you gave me so much feedback. I definitely drove Maria and Felix crazy with the deadlines. They had an infinite patience with my mix of stress and existential crisis (although I would do it again :P).

Next, I want to thank all the members of my group. I loved how open we always were with each other, and that made me feel I was never alone. Definitely the breakfasts with Javi and Lukas made me save a lot of money on therapists. And Roger, my science buddy, made my project much more fun, having someone to share it with. This also includes the Biolab and SLN staff, that were always happy to help. Especially Merche, without whose work (and the chats at the hood) my PhD thesis would be the half of what it is today. And not to forget the amazing people that I met at Bottanelli's lab, in a moment in which I just needed to remind myself to have fun in science. Carmen was the small sister that I just needed.

The last shout out definitely needs to go to my family. Even though they may not think they contributed at all of this, they are really at the foundation. They raised me trusting in my capabilities, knowing that whatever I did would make them proud (even though I am the worse explaining what I do). This made me a good person, that wants to grow and have an impact on other people life; and the most useful part, that chooses to be where I feel valued, and quickly runs away those where I don't. Family also includes Ian, that also had an endless patience with my stress and existential crisis, and always makes me feel like a super hero capable of anything.

[ESP] Parece que fue otra Jessica la que decidió empezar un doctorado en ICFO. Estaba muy emocionada por que había conseguido o que hacia tantp tiempo quería, hacer un doctorado. Además, era mucho mejor de lo que hubiera imaginado: en mi ciudad, en un sitio super guay, en las mejores condiciones, y en un tema que me encantaba. Incluso con el COVID, no podía entender por qué había tantos estudiantes tan desmotivados.

Era inocente, i eso quería decir que tenía suficiente con hacer experimentos emocionantes y aprender cosas nuevas. Ira una bioquímica rara, a la que siempre le habían fascinado los microscopios y la física; y ahora había encontrado un lugar donde yo no era la única. Estoy muy agradecidad de que mis supervisores también tuvieran suficiente con eso. Siempre me animaron a aprender lo que fuera que se me pasaba por la cabeza, y me dejaron ir en la dirección que deseara. Siempre me sentí muy valorada y que podía expresar mi opinión. No es algo que dé por hecho.

Sin embargo, solo fue una cuestión de tiempo que tuve que enfrentarme a la realidad del mundo académico. Era mu último año, y si quería decidir sobre mi futuro, tenía que averiguar de que iba mi trabajo. Empecé a darme cuenta que, en ciencia, el trabajo es para hacer crecer tu propio nombre. Nada que ver con la visión idealizada en que los científicos trabajan juntos para entender la naturaleza. Supongo que este sistema salvaje intoxica a mucha gente, convirtiéndolos en máquinas de ego; mientras otros simplemente intentan sobrevivir.

A veces me pregunto si mis supervisores no deberían de haberme enseñado a jugar a este juego. Y durante mucho tiempo, pensé que el no hacerlo, y no enseñarme a hacer mi trabajo más "publicable", era una señal de que no creían en mi habilidad de éxito. Ahora veo que quizás ese no era el caso, y que para ellos la idea de éxito debía de ser algo diferente.

Mirando mi tesis ahora estoy convencida de que he tenido éxito (lo siento pero me encantan estos los puntos): *(i)* He completado un proyecto científico. Y la verdad ahora que veo la idea inicial, me parece increíble que fuera capaz de llegar a alguna conclusión. *(ii)* Creo que la metodología y los resultados serán útiles para futuros investigadores. *(iii)* He aprendido cientos de cosas fuera de mi zona de confort. *(iv)* He aprendido un poco más sobre mi.

En el futuro, me recordaré a mi misma que debería de significar la palabra éxito. Aunque el mundo académico me lo hizo olvidar por un tiempo corto, me reconforta ver que la Jessica inocente ya lo sabía, y me empujó a disfrutar este doctorado, haciendo cientos de amigos, ayudando en ICONS, y yendo a tantas conferencias como fue posible.

Después de esta carta a mí misma, desde luego tengo que dar las gracias a mucha gente que me ha acompañado en este viaje. Primero a mis supervisores y el tribunal, por hacer esto simplemente posible. Espero que no presionara demasiado con las correcciones. Definitivamente volví locos a Maria y a Felix, con mis fechas límite. Tuvieron una paciencia infinita con mi mezcla de estrés y crisis existencial (aunque lo haría otra vez :P).

Después, tengo que agradecerles a todos los miembros de nuestro grupo, siempre abiertos entre nosotros, lo que me hizo sentir que nunca estaba sola. Definitivamente los desayunos con Javi y Lukas me hicieron ahorrar mucho dinero en psicólogos. Y Roger, mi compañero de ciencia, hizo mi proyecto mucho más divertido, pudiéndolo compartir con alguien. Esto también incluye al Biolab y el SLN, siempre dispuestos a ayudar. Especialmente Merche, que sin su trabajo (y las charlas en la cabina) mi tesis se podría recortar a la mitad. Y no olvidar a la gente genial que conocí en el laboratorio de Francesca, en un momento en que simplemente necesitaba recordarme a mi misma pasármelo bien con la ciencia. Carme fue la hermana pequeña que necesitaba en ese momento.

La última mención, y no menos importnate, tiene que ir a mi familia (mis padres y Oscar). Aun que puedan creer que no han contribuido en esto para nada, son la base de todo. Me criaron confiando en mis capacidades, sabiendo que ellos siempre iban a estar orgullosos, hiciera lo que hiciera (aun que yo sea la peor explicando lo que sea que hago). Esto me convirtió en una buna persona, que quiere tener un impacto en la vida de otros; y lo más útil, que sabe escoger donde estar, allí donde me siento apreciada, y huir de donde no me siento así. Familia también incluye a Ian, que también ha tenido una paciencia infinita con mi estrés y crisis existencial, y siempre me hace sentir como una superhéroe capaz de cualquier cosa.